The Borexino Solar Neutrino Experiment:

Scintillator Purification and

Surface Contamination

Michael Leung

A dissertation

presented to the faculty

of Princeton University

in candidacy for the degree

of Doctor of Philosophy

Recommended for acceptance

by the department of Physics

June 2006

Abstract

The Borexino Solar Neutrino Experiment will observe the monoenergetic (862 keV) ^{7}Be neutrinos, produced in the solar reaction ^{7}Be$+e^- \to^7$ Li$+\nu_e$. These neutrinos are the second most abundant species of solar neutrinos, with an expected flux at earth of 5×10^9/cm^2/s. Using $\nu - e$ scattering in an aromatic liquid scintillator, Borexino will make the first real time measurement of the solar neutrino flux at energies less than 1 MeV.

In addition to checking Standard Solar Model and neutrino oscillation predictions at low energies, Borexino will test the MSW vacuum-matter transition, luminosity constraint, and non-standard theories such as mass varying neutrinos. The Borexino detector will also be sensitive to supernova neutrinos, geoneutrinos, reactor neutrinos, and *pep* solar neutrinos. The *pep* measurement will tightly constrain the primary *pp* solar neutrino flux whose energy is below the Borexino threshold.

With an expected rate of 35 events per day from solar ^{7}Be neutrinos, the maximum tolerable background rate is one count per day. Removal of radioactive isotopes from the liquid scintillator is essential for the experiment's success and will be achieved with purification techniques including filtration, distillation, water extraction, nitrogen stripping, and silica gel adsorption. Results from small-scale purification efficiency tests are presented. Water extraction showed moderate but inadequate removal of ^{210}Po which is a dominant background. Distillation reduced ^{210}Po by a factor of more than 500.

Online purification involves cycling over 300 m^3 of scintillator from the detector though the purification plants. Flow patterns within the detector that influence the purification efficiency were determined with numerical simulations. Poor flow in the prototype Counting Test Facility showed effectively stagnant volumes within the detector. These are not present in the larger Borexino detector.

Surface contamination in Borexino arises primarily from contact with contaminated liquids and the deposition of airborne radon progeny. Measurements of desorption rates showed that surface contaminants are transferred to the scintillator logarithmically with

time. Partitioning constants between the scintillator and surfaces were measured and air-borne deposition rate of radon progeny in a clean room environment are analyzed. The efficiency of various surface cleaning techniques was also tested.

Acknowledgments

It is a pleasure to thank the many people who have made my graduate education an enjoyable and enlightening experience and without whom this thesis would not have been possible. A special thanks to the following people whose assistance have been particularly invaluable:

My advisor Prof. Frank Calaprice for his guidance, insight, and optimism. Also for his remarkable perseverance in the face of difficult laboratory conditions and his patience and understanding when equipment was broken. Prof. Tom Shutt for his enthusiasm, interesting detector discussions, entertaining laboratory mishaps, and theory of air travel optimization. Prof. Cristiano Galbiati for help with the data acquisition electronics and for being a co-survivor of the Gran Sasso tunnel fire of 2004. Prof. Jay Benziger for being a great resource when I had chemistry and purification questions. Kevin McCarty for his willingness to help install Linux on any computer. Andrea Pocar and Beth Harding for always knowing where to find the stuff I was looking for. Domenic Schimizzi for help with the purification operations. Allan Nelson for a constant supply of jokes. Ernst deHass for various technical assistance. Joe Horvath for the use of his equipment and lab. Mike Peloso for help in the machine shop. Mike Souza for fabricating and fixing glassware. The Italy crew for building the detector. Our group secretary Helen Ju for all kinds of help, but especially tips that free food had appeared in the department which were an essential part of graduate school. Claude Champagne in purchasing making parts appear quickly, and for convincing me to order a second jar of optical coupling grease after we incorrectly assumed there was a decimal point in the price.

Professors Peter Myers, Bill Bialek, David Nice, Suzan Staggs, Mike Romalis, and Jeremy Mans for a great time teaching physics to undergrads. Asad Aboobaker for setting up Ultimate Frisbee games and BBQ's. Kevin Huffenberger for creating the Princeton Fabio Project website. Ryan Patterson for silly ideas like quarter flipping for grading. If Borexino doesn't publish a neutrino result by 2008 I'll owe you a hoagie. Tom Kornack

Contents

Chapter 1

Neutrino Physics

Neutrinos rarely interact despite their vast abundance in nature. To give a sense of scale, a person has roughly 10^{16} neutrinos passing through them each second, completely unnoticed. Nonetheless, neutrinos can still be used to probe the fundamental laws of nature. They are observed with large detectors built deep underground where there are few cosmic rays to mask their signal. Data from these measurements have led to a number of surprising discoveries about neutrinos. One such finding is a phenomenon known as neutrino oscillations, where one type of neutrino changes into another type of neutrino as it propagates.

There are three types of neutrinos (ν_e, ν_μ, and ν_τ) found in nature. They carry no charge and have a mass of less than $\sim 0.01\,\text{eV}$, which is light compared to the rest of the fundamental particles. The cross section for a neutrino to interact with an electron is on the order of $10^{-48}\,\text{m}^2$ which is also relatively tiny. These properties are reflected in the name neutrino which means "little neutral one" in Italian.

The neutrino was first postulated by Wolfgang Pauli in 1930 to reconcile the continuous energy spectrum seen in beta emission, with the conservation of energy [1]. If no neutrino were emitted, the beta decay products would have discrete energies instead of a broad spectrum. Three years later in 1933, Enrico Fermi devised a theory for beta decays which

included neutrinos that produced the correct energy spectrum. The particles were not actually observed until 1956, when Frederick Reines and Clyde Cowan detected antineutrinos from nearby nuclear reactor [2]. Early hints of unusual neutrino properties came from an experiment by Ray Davis that measured roughly a third of the neutrino flux expected from the sun [3]. The discovery of neutrino oscillations in 1998 by the Super Kamiokande experiment and confirmation by the Sudbury Neutrino Observatory in 2001 provided proof that neutrinos had a non-zero mass [4, 5]. Kamland's measurements of reactor antineutrinos also indicated oscillations [6].

This chapter will describe neutrino physics and some of the experiments that resulted in our current understanding of these particles. There will be a particular emphasis on neutrino oscillations as they relate to solar neutrinos. This will provide some of the background and motivation for the Borexino solar neutrino experiment.

1.1   Neutrino Production

Neutrinos are continuously produced through solar fusion reactions, the beta decay of radioactive isotopes, and the interaction of high-energy cosmic rays with the atmosphere. Fusion in the core of the sun produces neutrinos with a flux at earth of roughly 7×10^{10} neutrinos/cm^2/s. Terrestrial neutrino sources resulting from weak interactions include natural radioactivity, nuclear reactors whose fission products undergo beta decay, and high energy particle accelerators. Some typical neutrino producing reactions are:

Solar Fusion: $\quad\quad\quad \mathrm{p} + \mathrm{p} \rightarrow {}^2\mathrm{H} + \mathrm{e}^+ + \nu_e$

Beta Decay: $\quad\quad\quad \mathrm{n} \rightarrow \mathrm{p} + \mathrm{e}^- + \bar{\nu}_e$

$\quad\quad\quad\quad\quad\quad\quad {}^A_Z\mathrm{X} \rightarrow e^+ + \nu_e + {}^{A}_{Z-1}\mathrm{Y}$

Electron Capture: $\quad {}^A_Z\mathrm{X} + \mathrm{e}^- \rightarrow \nu_e + {}^{A}_{Z-1}\mathrm{Y}$

Cosmic Rays: $\quad\quad\quad \pi^+$ or $K^+ \rightarrow \mu^+ + \nu_\mu$

$\quad\quad\quad\quad\quad\quad\quad\quad\quad \mu^+ \rightarrow \mathrm{e}^+ + \nu_e + \bar{\nu}_\mu$

$\quad\quad\quad\quad\quad \pi^-$ or $K^- \rightarrow \mu^- + \bar{\nu}_\mu$

$\quad\quad\quad\quad\quad\quad\quad\quad\quad \mu^- \rightarrow \mathrm{e}^- + \bar{\nu}_e + \nu_\mu$

Source	Type	Average Energy	Intensity
Sun	ν_e	$0.55\,\text{MeV}$	10^{38}/s total
Nuclear Reactor	$\bar{\nu}_e$	$4\,\text{MeV}$	3×10^{19}/GW/s [7]
Cosmic Rays	ν_e, ν_μ	$1\,\text{GeV}$	$1/\text{cm}^2$/s
Supernova	all	$15\,\text{MeV}$	10^{57}/collapse
Cosmic ν Background	all	$164\,\mu\text{eV}$	$3 \times 10^{12}\,/\text{cm}^2$/s [8]
Geoneutrinos	$\bar{\nu}_e$	$0.5\,\text{MeV}$	$4 \times 10^6\,/\text{cm}^2$/s [9]

Table 1.1: Various sources of neutrinos. The sun produces neutrinos during nuclear fusion. Fission in nuclear reactors also produces neutrinos. There are roughly 440 nuclear reactors producing about $373\,\text{GW}$ of power globally. High energy cosmic rays hitting the atmosphere produce a neutrino flux of about $1/\text{cm}^2$/s at sea level. Neutrinos produced in the Big Bang that have since cooled now comprise the cosmic neutrino background. Geoneutrinos are produced by the decay of uranium, thorium, and potassium in the ground.

Here X or Y represent a nucleus with atomic mass A and atomic number Z. The fluxes from different sources of neutrinos are listed in Table 1.1. The neutrino fluxes at earth are shown in Figure 1.1.

It is predicted that there is a cosmic neutrino background (CNB) similar to the cosmic microwave background (CMB) but with a blackbody temperature of $1.9\,\text{K}$. These neutrinos were created during the big bang and have cooled as the universe has expanded. They account for the majority of the neutrinos in the universe though they have yet to be observed due to their low energy.

In the early universe neutrinos were in equilibrium with the cosmic plasma. Because they only interact weakly neutrinos came out of equilbrium at later times with their temperature falling with the scale factor as a^{-1}. When the temperature of the universe was of order the electrom mass, electrons and positrons began to annihilate increasing the photon temperature. Since neutrinos decoupled slightly before this time they did not receive any of this energy. Relations between the temperature of the CNB and CMB can be derived from the entropy density which scales as a^{-3}. Massless bosons contribute $2\pi^2 T^3/45$ to the energy density per spin state, and massless Fermions contribute $7\pi^2 T^3/180$ or 7/8 of the boson contribution. Before annihilation the Bosons are photons with 2 spin states, and
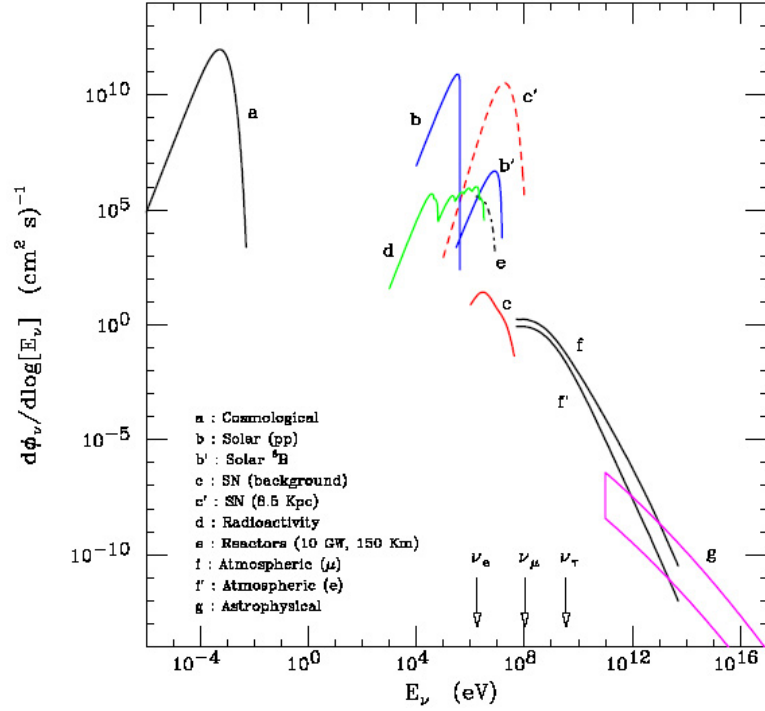
Figure 1.1: The neutrino energy spectra at earth from various sources. From reference [10].

the Fermions are electrons and positrons with 2 spin states each, and three generations of neutrinos and antineutrinos with one spin state each. The entropy at a_1 before annihilation is

$$s(a_1) = \frac{2\pi^2}{45}T_1^3[2 + \frac{7}{8}(2 + 2 + 3 + 3)] = \frac{43\pi^2}{90}T_1^3 \tag{1.1}$$

where T_1 is the temperature at a_1. After annihilation there are no electrons and positrons and the temperatures of the photons and neutrinos are different. The entropy density after annihilation at a_2 is

$$s(a_2) = \frac{2\pi^2}{45}\left[2T_\gamma^3 + \frac{7}{8}6T_\nu^3\right] \tag{1.2}$$

where T_γ is the photon temperature and T_ν is the neutrino temperature [11]. The entropy at the two times is related by

$$s(a_1)a_1^3 = s(a_2)a_2^3 \tag{1.3}$$

and the neutrino temperature evloves according to the relation

$$a_1 T_1 = a_2 T_\nu(a_2). \tag{1.4}$$

The ratio of the cosmic neutrino temperature to the photon temperature is

$$T_\nu = \left(\frac{4}{11}\right)^{1/3} T_\gamma = 0.714\, T_\gamma \tag{1.5}$$

where $T_\gamma = 2.726\,\mathrm{K}$ [8, 12]. The density of each species of CNB neutrinos is related to the temperature of the CMB by

$$n_\nu = \frac{6\zeta(3)}{11\pi^2} T_\gamma^3 \tag{1.6}$$

where $\zeta(3) \approx 1.202$ [12]. The cosmic neutrinos have a density of $336\,\mathrm{neutrinos/cm^3}$ with an equal contribution from all three species. This gives a flux of $3 \times 10^{12}\,\mathrm{neutrinos/cm^2/s}$. The relationship between the number density of neutrinos to photons in the cosmic background is

$$\frac{n_\nu}{n_\gamma} = \frac{9}{11} \tag{1.7}$$

where n_γ is the photon density [8]. Since the energy density of massless particle scales as T^4 the ratio of the energy densities of neutrinos and photons is

$$\frac{\rho_\nu}{\rho_\gamma} = 3\frac{7}{8}\left(\frac{4}{11}\right)^{\frac{4}{3}} = 0.681 \tag{1.8}$$

where ρ_γ and ρ_ν represents the energy densities of the photons and neutrinos respectively. Cosmic neutrinos have a similar number density and energy density to photons. However, cosmic neutrinos have not yet been observed due to their low energy.

Constraints from WMAP and other surveys limit the cosmic density of neutrinos from above and terrestrial measurements provide a lower bound [13].

$$7 \times 10^{-4} < \Omega_\nu < 0.02 \tag{1.9}$$

where Ω_ν is the contribution of neutrinos to the total density of the universe. The density of baryons is $\Omega_B = 0.04$, dark matter $\Omega_D = 0.23$, and dark energy $\Omega_\Lambda = 0.73$. For a flat universe $\sum \Omega_i = 1$, with a critical density of $\rho_c = 9.9 \times 10^{-30}\,\mathrm{g/cm^3}$. The universe has been measured to be flat to within two percent.

1.2 Standard Model

Much of particle physics can be explained by a theory of particle interactions called the Standard Model. The Standard Model identifies the fundamental particles and provides a method of calculating their interaction cross sections with exceptional accuracy. Since its formulation, it has been an invaluable tool and provided tremendous predictive power by theorizing new particles that were later observed. Despite its remarkable success, we now know that the Standard Model is not entirely correct and there are a number of observed phenomena it cannot describe. Among these phenomena is the physics of neutrinos. Experiments have observed that one type of neutrino can change into another type of neutrino, a process known as neutrino oscillations. This can only happen if neutrinos have a nonzero mass. According to the Standard Model, the neutrino's mass is equal to zero. The masses of the neutrinos have yet to be precisely determined. Only upper bounds have been set for each of the masses, though these limits are much lower then the masses of other particles. Neutrino oscillation probabilities can indicate differences in squares of the masses between the three types of neutrinos, but not their absolute magnitude.

The Standard Model classifies particles into two groups based on their spin, the intrinsic angular momentum held by a particle. Bosons have spin in integer units of $\hbar$ (0,1,2...) and Fermions have half integer spin in units of $\hbar$ (1/2, 3/2, 5/2...). There are 12 fundamental Fermions that are the building blocks of matter and 4 fundamental Bosons which are force carriers. These are shown in Table 1.2 and Table 1.2.

Neutrinos interact through the weak force by coupling to the massive W and Z bosons. The strength of the interaction is governed by the Fermi constant G_F. They also interact gravitationally but since this force is negligibly small, neutrinos are measured exclusively through weak interactions. Interactions involving the charged W bosons are called Charged Current (CC) reactions and interactions with the neutral Z boson are called Neutral Current (NC) reactions. Experimentally, neutrinos are detected through scattering off electrons or interactions with nuclei. Feynman diagrams for CC electron scattering, NC electron scattering, CC quark (inverse beta decay), and NC quark interactions are shown in Figures

Quark	Charge [e]	Mass [MeV/c^2]	Lepton	Charge [e]	Mass [MeV/c^2]
u	$+\frac{2}{3}$	~ 3	ν_e	0	$< 3 \times 10^{-6}$
d	$-\frac{1}{3}$	~ 6	e^-	-1	0.511
c	$+\frac{2}{3}$	~ 1250	ν_μ	0	< 0.19
s	$-\frac{1}{3}$	~ 105	μ^-	-1	105.7
t	$+\frac{2}{3}$	$\sim 1.74 \times 10^5$	ν_τ	0	< 18.2
b	$-\frac{1}{3}$	~ 4250	τ^-	-1	1777.0

Table 1.2: Fundamental Fermions in the Standard Model have a spin of $\frac{1}{2}\hbar$ [14]. Quarks are always bound in colorless combinations which leads to uncertainty in their mass. Composite particles containing quarks are called hadrons which include mesons (quark and anitquark pairs) and baryons (3 quark combinations). The most common baryons are protons which contain $p = (u, u, d)$ and neutrons which contain $n = (u, d, d)$.

Particle	Symbol	Charge [e]	Mass [GeV/c^2]	Interaction
Photon	γ	0	0	Electromagnetic
W Boson	W^+	$+1$	80.4	Weak
W Boson	W^-	-1	80.4	Weak
Z Boson	Z^0	0	91.2	Weak
Gluon	g	0	0	Strong
Higgs	H^0	0	> 115	-

Table 1.3: Fundamental Bosons in the Standard Model [14]. Each has a spin of $1\hbar$, except for the Higgs which is spin 0. There are 8 types of gluons. Quarks and gluons carry color charge and gluons interact exclusively with quarks. There are three types of color charge (red, green, blue) plus their anticolors. A neutral, massless, spin $2\hbar$ graviton responsible for the gravitational force is not included in the SM, and has yet to be observed.

Neutrino Flavor	Mass [eV]	Magnetic Moment $[\mu_B]$
ν_e	< 3	$< 1.8 \times 10^{-10}$
ν_μ	$< 1.90 \times 10^5$	$< 7.4 \times 10^{-10}$
ν_τ	$< 1.82 \times 10^7$	$< 4.2 \times 10^{-7}$

Table 1.4: Limits on neutrino masses and magnetic moments [14]. The Bohr Magneton is defined as $\mu_B = \frac{e\hbar}{2m_e}$. In SI units $\mu_B = 9.27 \times 10^{-24} \, \text{Am}^2$.

1.2 and 1.3. Charged current electron scattering can only occur with electron neutrinos. Neutral current scattering involves all three flavors of neutrinos. Thus an electron neutrino is usually more likely to interact than a muon or tau neutrino.
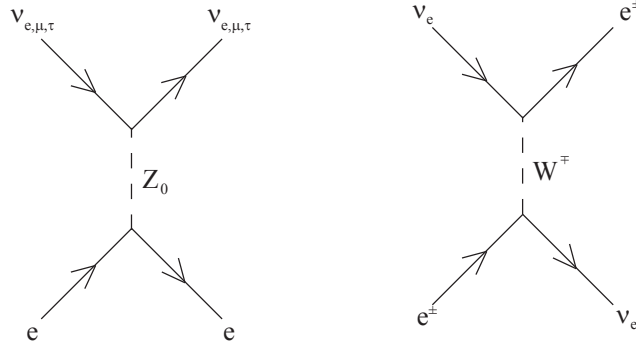
Figure 1.2: First order Feynman diagrams for ν-e scattering. All neutrino flavors scatter via the neutral current reaction (left) while only the electron neutrino can interact through a charged current interaction (right). Due to the interference of the two amplitudes, the cross section of electron neutrinos is about five times larger than for muon or tau neutrinos at 1 MeV.

Current experimental upper limits on neutrino masses [14, 15, 16, 17] and magnetic moments [18, 19] are shown in Table 1.2. The limit for the electron neutrino mass came from measuring the endpoint of the beta energy spectrum of tritium decay. The limit for the muon and tau neutrino masses were found from observing decays of muons and taus respectively. The relative masses of the Fermions are illustrated in Figure 1.4.
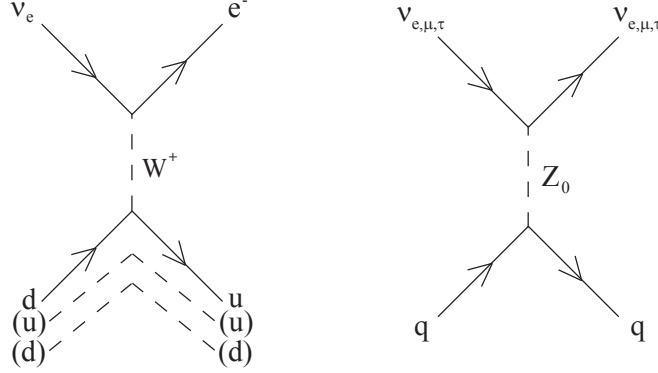
Figure 1.3: First order Feynman diagrams for neutrino nucleon interactions. The interaction on the left shows inverse beta decay $\nu_e + n \rightarrow e^- + p$. The two spectator quarks that do not take place in the interaction are shown in parenthesis. The neutral current interaction on the right applies to all quarks and neutrino flavors.

Cosmic microwave background (CMB) radiation is a highly uniform distribution of photons with a blackbody spectrum of $2.7\,\mathrm{K}$ that fills the universe. Tiny deviations in its temperature and angular distribution provide a wealth of cosmological information. Features in the angular power spectrum of the CMB are influenced by massive particles such as neutrinos. Power spectrum calculations for different neutrino mass are shown along with data in Figure 1.5. With the Wilkinson Microwave Anisotropy Probe (WMAP) measurements of the power spectrum, an upper limit can be placed on the sum of the neutrino masses [20].

$$\sum_{i=1}^{3} m_i < 0.71\,\mathrm{eV} \tag{1.10}$$

The sum only includes light neutrino species that decouple while they are still relativistic. The neutrino's mass is constrained with cosmological data setting an upper limit and below from oscillation data which sets a limit of $\sim 0.05\,\mathrm{eV}$. A sky map of the cosmic microwave background is shown in Figure 1.6.

The number of neutrino flavors has been determined by measurements of the width of the Z^0 boson at LEP [21]. It found that the number of neutrino species with a mass less
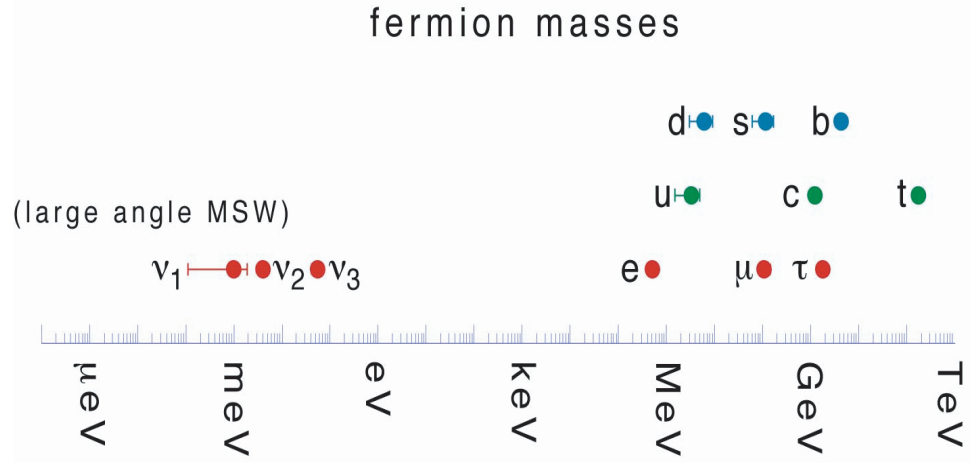
Figure 1.4: The Fermion masses. Red dots represent leptons and blue or green dots represent quarks. The neutrino masses are small compared to the rest of the Fermions.

than $45\,\mathrm{GeV}$ is

$$N_\nu = 2.991 \pm 0.011 \tag{1.11}$$

A plot of the cross sections for different numbers of neutrino species and the experimental data is shown in Figure 1.7.
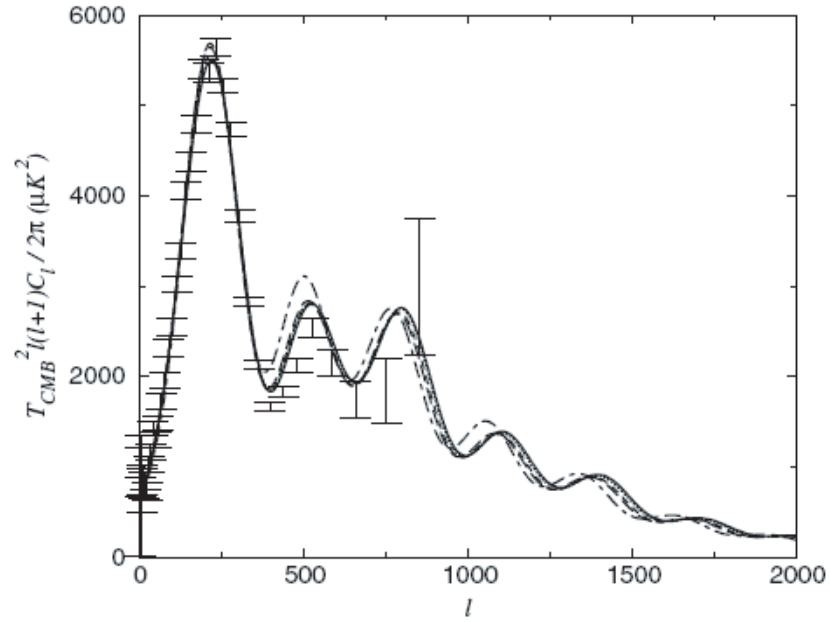
Figure 1.5: The cosmic microwave background power spectrum from WMAP. The sky temperature is expanded in spherical harmonics $\Delta T(\theta, \phi) = \sum\limits_{m,l} a_{ml} Y_{ml}(\theta, \phi)$. The amplitude at multipole l measures the root-mean-square fluctuation on an angular scale of $180°/l$. The power spectra for neutrino mass per flavor are $m_\nu = 0$(——), $m_\nu = 0.1$(.......), $m_\nu = 0.3$(- - - - -), $m_\nu = 0.5(-----)$, $m_\nu = 3\,\mathrm{eV}$ $(\cdot - \cdot - \cdot -)$. From reference [20].
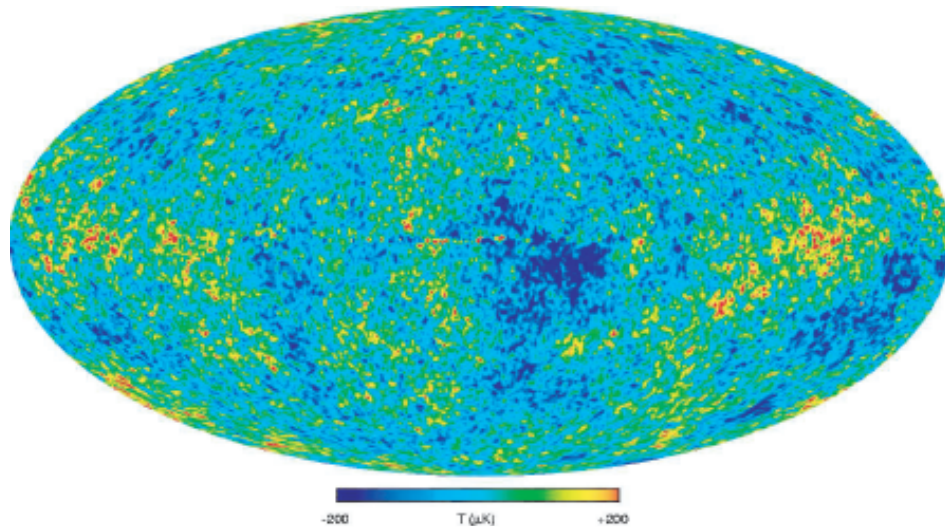
Figure 1.6: A map of the cosmic microwave background produced by the WMAP satellite with the hot and cold regions are indicated by the different colors. The average temperature is $2.7\,\mathrm{K}$ and the total temperature difference from the hottest to coldest region is $400\,\mu\mathrm{K}$. A similar background of cosmic neutrinos with a temperature of $1.9\,\mathrm{K}$ has yet to be observed. From reference [20].
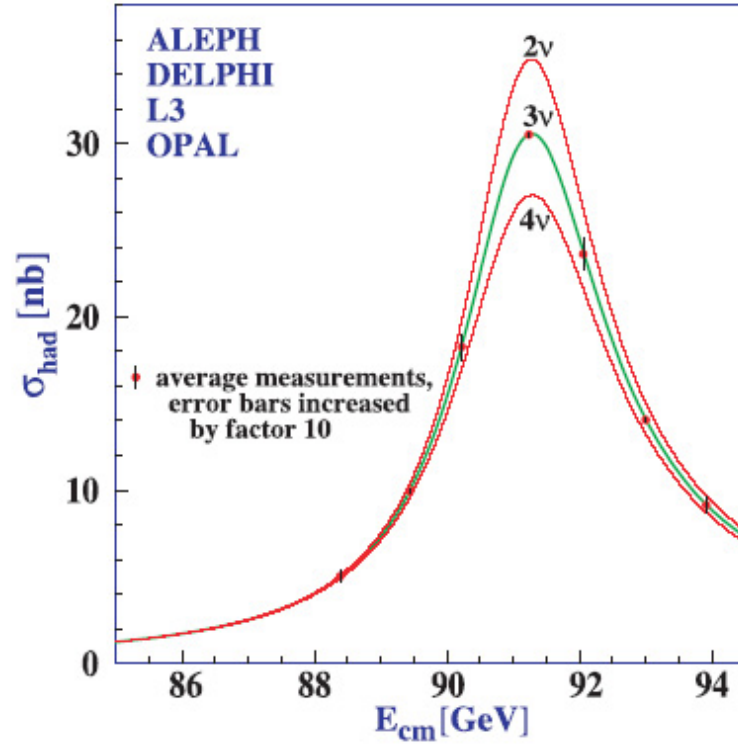
Figure 1.7: A plot of the cross section for e^+e^- annihilation into hadronic final states near the Z pole. Curves show the expected cross sections for different numbers of light neutrinos. Data indicate there are exactly three flavors of light active neutrinos. This plot uses the combined data from the ALEPH, DELPHI, L3, and OPAL Collaborations [14].

1.2.1   Neutrino Cross Section

The cross section of a particle is its the effective area for scattering. It determines the interaction rate with other particles. Cross sections depend on the types of forces involved, the energy of the particles, and their spin. A differential cross section contains information regarding the distribution of the products. The total cross section is attained by integrating the differential cross section. The differential cross section for electron neutrino scattering in energy is

$$\frac{d\sigma}{dT} = \frac{2G_F m_e}{\pi} \left[g_L^2 + g_R^2(1 - T/E_\nu)^2 + g_L g_R m_e T/E_\nu^2 \right] \tag{1.12}$$

where T is the electron recoil energy, and E_ν is the incoming neutrino energy. The couplings g_L and g_R are defined as

$$g_L = \frac{1}{\sqrt{2}}(g_V - g_A) \tag{1.13}$$

$$g_R = \frac{1}{\sqrt{2}}(g_V + g_A) \tag{1.14}$$

where for weak interactions $g_V = 1$ and $g_A = 1.23$.

The cross section of a neutrino is small compared to other particles because it interacts exclusively though the weak force. The following are approximate total neutrino cross sections for various electron scattering interactions. They are of order $10^{-49}\,\mathrm{m}^2$ or 10^{-21} barns for $1\,\mathrm{MeV}$ neutrinos.

Electron neutrino - electron scattering (ν_e, e)

$$\sigma_{(\nu_e e^- \to \nu_e e^-)} \approx 9.5 \times 10^{-49}\mathrm{m}^2 \left(\frac{E_\nu}{1\mathrm{MeV}} \right) \tag{1.15}$$

Electron antineutrino - electron scattering $(\bar{\nu}_e, e)$

$$\sigma_{(\bar{\nu}_e e^- \to \bar{\nu}_e e^-)} \approx 4.0 \times 10^{-49}\mathrm{m}^2 \left(\frac{E_\nu}{1\mathrm{MeV}} \right) \tag{1.16}$$

Muon/tau neutrino - electron scattering $(\nu_{\mu,\tau}, e)$

$$\sigma_{(\nu_{\mu,\tau} e^- \to \nu_{\mu,\tau} e^-)} \approx 1.6 \times 10^{-49}\mathrm{m}^2 \left(\frac{E_\nu}{1\mathrm{MeV}} \right) \tag{1.17}$$

Muon/tau antineutrino - electron scattering $(\bar{\nu}_{\mu,\tau}, e)$

$$\sigma_{(\bar{\nu}_{\mu,\tau} e^- \to \bar{\nu}_{\mu,\tau} e^-)} \approx 1.3 \times 10^{-49}\mathrm{m}^2 \left(\frac{E_\nu}{1\mathrm{MeV}} \right) \tag{1.18}$$

Interaction	σ/σ_0	Relative Size
$\nu_e + e^- \to \nu_e + e^-$	$1 + 4\sin^2\theta_W + \frac{16}{3}\sin^4\theta_W$	2.2
$\bar{\nu}_e + e^- \to \bar{\nu}_e + e^-$	$\frac{1}{3} + \frac{4}{3}\sin^2\theta_W + \frac{16}{3}\sin^4\theta_W$	0.922
$\nu_\mu + e^- \to \nu_\mu + e^-$	$1 - 4\sin^2\theta_W + \frac{16}{3}\sin^4\theta_W$	0.362
$\bar{\nu}_\mu + e^- \to \bar{\nu}_\mu + e^-$	$\frac{1}{3} - \frac{4}{3}\sin^2\theta_W + \frac{16}{3}\sin^4\theta_W$	0.309
$\nu_\mu + e^- \to \nu_e + \mu^-$	4	4
$\bar{\nu}_\mu + e^- \to \bar{\nu}_e + \mu^-$	$\frac{4}{3}$	$\frac{4}{3}$

Table 1.5: The cross sections for electron-neutrino interactions in the limit $E_\nu \gg m_\mu^2/2m_e$ and $-q^2 \ll m_W^2$. Cross sections are stated in units of $\sigma_0 = G_F m_e E_\nu/2\pi$. Cross sections for ν_τ are the same as those for ν_μ. The Fermi coupling constant $G_F/(\hbar c)^3 = 1.17 \times 10^{-5}\,\mathrm{GeV}^{-2}$, E_ν is the incoming neutrino energy, $m_e = 9.1 \times 10^{-31}\,\mathrm{kg}$ is the electron mass, and the Weinberg angle is $\sin^2\theta_W = 0.2317$. The vector and axial couplings for weak interactions are $g_V = 1$ and $g_A = 1.23$. From reference [22].

Interaction	Channel	σ_{tot}
$\nu_e + n \to e^- + p$	CC, IE	$\frac{G_F^2 E_\nu^2 (\hbar c)^2}{\pi}(g_V^2 + 3g_A^2)\left(1 + \frac{Q}{E_\nu}\right)$ $\times \sqrt{1 + 2\frac{Q}{E_\nu} + \frac{Q^2 - m_e^2}{E_\nu^2}}$
$\bar{\nu}_e + p \to e^+ + n$	CC, IE	$\frac{G_F^2 E_\nu^2 (\hbar c)^2}{\pi}(g_V^2 + 3g_A^2)\left(1 - \frac{Q}{E_\nu}\right)$ $\times \sqrt{1 + 2\frac{Q}{E_\nu} + \frac{Q^2 - m_e^2}{E_\nu^2}}\,\theta(E - Q)$
$\nu_{e,\mu,\tau} + n \to \nu_{e,\mu,\tau} + n$	NC, ES	$\frac{G_F^2 E_\nu^2 (\hbar c)^2}{\pi}(1 + 3g_A^2)$
$\nu_{e,\mu,\tau} + p \to \nu_{e,\mu,\tau} + p$	NC, ES	$\frac{G_F^2 E_\nu^2 (\hbar c)^2}{4\pi}(16\sin^4\theta_W - 8\sin^2\theta_W + 1)$ $\times (1 + 3g_A^2)$

Table 1.6: The cross sections for neutrino-nucleon interactions. ES and IE refer to elastic scattering and inelastic scattering, respectively. NC and CC refer to neutral current and charged current reactions. Cross sections for ν_τ are the same as those for ν_μ. For nucleon interaction the formulae are only valid for energies less than 1GeV. The nucleon mass difference $Q = 1.3\,\mathrm{MeV}$. The Heaviside step function $\theta(E - Q)$ is zero for $E < Q$ and 1 for $E > Q$. The Fermi coupling constant is $G_F/(\hbar c)^3 = 1.17 \times 10^{-5}\,\mathrm{GeV}^{-2}$, E_ν is the incoming neutrino energy, $s = 2m_e E_\nu$, $m_e = 9.1 \times 10^{-31}\,\mathrm{kg}$ is the electron mass and the Weinberg angle is $\sin^2\theta_W = 0.2317$. From reference [22].
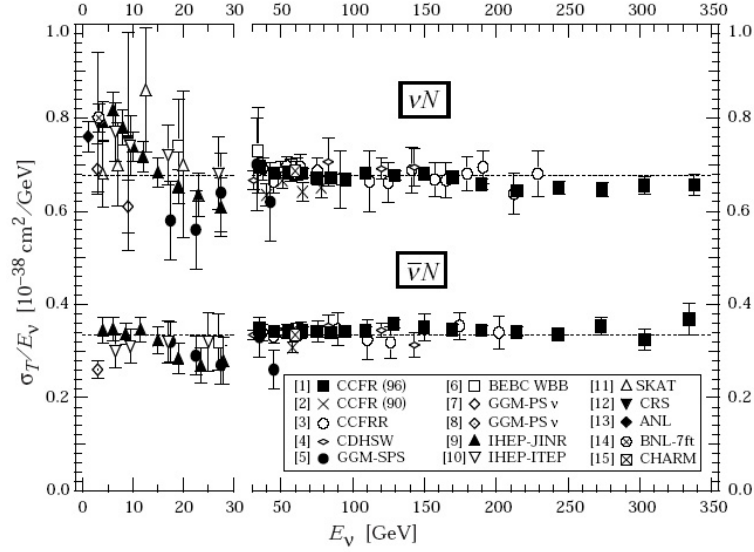
Figure 1.8: Measurements of the total charged current cross section for muon neutrino and muon antineutrino nucleon interactions. The average cross section is $\frac{\sigma_{\nu_\mu}}{E_\nu} = (0.677 \pm 0.014) \times 10^{-38}\,\mathrm{cm^2/GeV}$, and $\frac{\sigma_{\bar{\nu}_\mu}}{E_\nu} = (0.334 \pm 0.008) \times 10^{-38}\,\mathrm{cm^2/GeV}$ [14].

Explicit cross sections for neutrino-electron interactions are given in Table 1.5.

If neutrinos have a magnetic moment as expected since they have mass, the cross section will have an additional term for processes where an electron can be scattered by the exchange of a photon.

$$\frac{d\sigma}{dT} = \frac{2G_F m_e}{\pi}\left[g_L^2 + g_R^2(1 - T/E_\nu)^2 + g_L g_R m_e T/E_\nu^2\right] + \mu_\nu^2 \frac{\pi\alpha^2}{m_e^2}\frac{1 - T/E_\nu}{T} \qquad (1.19)$$

where μ_ν is the neutrino magnetic moment and $\alpha = e^2/\hbar c$ is the fine structure constant.

1.3 Neutrino oscillations

Neutrinos are always created in a flavor eigenstate (e, μ, τ) through weak interactions. Each flavor eigenstate can be equivalently described as a superposition of mass eigenstates generically labeled (m_1, m_2, m_3). As a neutrino propagates the composition of each of these mass

eigenstates evolves over time. When a neutrino is later observed, the probability of it being a particular flavor is determined by the mixture of these eigenstates. Oscillations can occur between different flavors of neutrino only if their flavor and mass eigenstates do not coincide.

The following neutrino oscillation analysis has assumed that

- Neutrinos propagate with a definite momentum which is the same for all mass eigenstates.

- The different mass eigenstates have different energies, determined by the energy-momentum dispersion relations.

- Neutrinos are relativistic, implying that their kinetic energy is much larger than the mass eigenstates (times c^2).

The probability that a neutrino of one flavor is later measured as a different flavor is

$$P(\nu_e \rightarrow \nu_\mu) = |\langle \nu_\mu | \nu_e(t) \rangle|^2 \tag{1.20}$$

For simplicity, take the case of two flavor oscillations. The relationship between the flavor and mass eigenstates is given by

$$\begin{pmatrix} |\nu_e\rangle \\ |\nu_\mu\rangle \end{pmatrix} = \begin{pmatrix} \cos\theta & \sin\theta \\ -\sin\theta & \cos\theta \end{pmatrix} \begin{pmatrix} |\nu_1\rangle \\ |\nu_2\rangle \end{pmatrix} \tag{1.21}$$

where the angle θ is the mixing angle between the flavor and mass eigenstates. Thus when an electron neutrino is created it evolves over time like

$$|\nu_e(t)\rangle = e^{-iE_1 t/\hbar} \cos\theta |\nu_1\rangle + e^{-iE_2 t/\hbar} \sin\theta |\nu_2\rangle \tag{1.22}$$

where $E_1 = \sqrt{p_1^2 c^2 + m_1^2 c^4}$ and $E_2 = \sqrt{p_2^2 c^2 + m_2^2 c^4}$, $c = 3 \times 10^8$ m/s is the speed of light. For oscillations to occur the neutrino must be created in a state of definite momentum $p_1 = p_2 = p$, . Typically the energy of a neutrino is much greater than the rest mass implying $\gamma = \frac{E}{m_o c^2} = \frac{\sqrt{p^2 c^2 + m_o^2 c^4}}{m_o c^2} \gg 1$. This condition holds for all observed neutrinos.

Because the neutrino mass is small compared to its momentum the energies can be Taylor expanded in units where $\hbar = c = 1$ to

$$E_1 \simeq p + \frac{m_1^2}{2p} \text{ and } E_2 \simeq p + \frac{m_2^2}{2p}. \tag{1.23}$$

Since the ν_μ state is

$$\langle \nu_\mu | = -\sin\theta \langle \nu_1 | + \cos\theta \langle \nu_2 | \tag{1.24}$$

we find the amplitude squared

$$|\langle \nu_\mu | \nu_e(t) \rangle|^2 = - \left| \langle \nu_1 | \sin\theta\cos\theta e^{-\frac{it}{\hbar}(p+\frac{m_1^2}{2p})} | \nu_1 \rangle + \langle \nu_2 | \cos\theta\sin\theta e^{-\frac{it}{\hbar}(p+\frac{m_2^2}{2p})} | \nu_2 \rangle \right|^2. \tag{1.25}$$

Define $\Delta m^2 = m_1^2 - m_2^2$, and let $pc = E_\nu$ and $t = L/c$ since the neutrinos are highly relativistic. Note that $\langle \nu_i | \nu_j \rangle = \delta_{ij}$. The probability of an electron neutrino of energy E_ν becoming a muon neutrino at a distance L away is then

$$P(\nu_e \to \nu_\mu) = |\langle \nu_\mu | \nu_e(t) \rangle|^2 = \sin^2 2\theta \sin^2 \left(1.27 \Delta m^2 \frac{L}{E_\nu} \right) \tag{1.26}$$

with Δm^2 in eV^2, L in meters and E_ν in MeV. To demonstrate neutrino oscillations one would like to make measurements varying the neutrino energy and distance of the detector from the source. The $\sin^2\theta$ term governs the overall amplitude of the oscillations. If $\theta = 45$ then mixing is maximal and if $\theta = 0$ then no mixing occurs. For a given energy, the oscillations are a periodic function of distance. An oscillation length in vacuum can be defined as

$$L_v = \frac{4\pi E_\nu}{\Delta m^2} \approx 2.47 \frac{E_\nu}{\Delta m^2} \text{m} \tag{1.27}$$

when E_ν is in [MeV] and Δm^2 is in [eV^2].

1.3.1 Three flavor vacuum oscillations

In general neutrinos of all three mass and flavor eigenstates can mix. Formally this is represented as

$$\begin{pmatrix} \nu_e \\ \nu_\mu \\ \nu_\tau \end{pmatrix} = U_{MNS} \begin{pmatrix} \nu_1 \\ \nu_2 \\ \nu_3 \end{pmatrix} \tag{1.28}$$

The matrix U (Maki-Nakagawa-Sakata) for the parameterization of neutrino mixing is

$$U_{MNS} = \begin{pmatrix} U_{e1} & U_{e2} & U_{e3} \\ U_{\mu1} & U_{\mu2} & U_{\mu3} \\ U_{\tau1} & U_{\tau2} & U_{\tau3} \end{pmatrix} \tag{1.29}$$

$$= \begin{pmatrix} 1 & 0 & 0 \\ 0 & c_{23} & s_{23} \\ 0 & -s_{23} & c_{23} \end{pmatrix} \times \begin{pmatrix} c_{13} & 0 & s_{13}e^{i\delta} \\ 0 & 1 & 0 \\ -s_{13}e^{i\delta} & 0 & c_{13} \end{pmatrix} \times \begin{pmatrix} c_{12} & s_{12} & 0 \\ -s_{12} & c_{12} & 0 \\ 0 & 0 & 1 \end{pmatrix} \tag{1.30}$$

$$= \begin{pmatrix} c_{13}c_{12} & c_{13}s_{12} & S_{13}e^{i\delta} \\ -c_{23}s_{12} - s_{13}s_{23}c_{12}e^{i\delta} & c_{23}c_{12} - s_{13}s_{23}s_{12}e^{i\delta} & c_{13}s_{23} \\ s_{23}s_{12} - s_{13}c_{23}c_{12}e^{i\delta} & -s_{23}s_{12} - s_{13}c_{23}s_{12}e^{i\delta} & c_{13}c_{23} \end{pmatrix} \tag{1.31}$$

where $c_{ij} = \cos\theta_{ij}$ and $s_{ij} = \sin\theta_{ij}$ and δ is the Dirac phase. If neutrinos are Majorana type particles then the matrix U_{MNS} is multiplied by diag$(1, e^{\phi_1}, e^{\phi_2})$.

$$U_{MNS} \to \begin{pmatrix} c_{13}c_{12} & c_{13}s_{12} & S_{13}e^{i\delta} \\ -c_{23}s_{12} - s_{13}s_{23}c_{12}e^{i\delta} & c_{23}c_{12} - s_{13}s_{23}s_{12}e^{i\delta} & c_{13}s_{23} \\ s_{23}s_{12} - s_{13}c_{23}c_{12}e^{i\delta} & -s_{23}s_{12} - s_{13}c_{23}s_{12}e^{i\delta} & c_{13}c_{23} \end{pmatrix} \begin{pmatrix} 1 & 0 & 0 \\ 0 & e^{\phi_1} & 0 \\ 0 & 0 & e^{\phi_2} \end{pmatrix} \tag{1.32}$$

where and ϕ_1 and ϕ_2 are two Majorana phases.

The probability (in units of $\hbar = c = 1$) for a neutrino of flavor α to be measured as a neutrino of flavor β a distance of L away is

$$P(\nu_\alpha \to \nu_\beta) = |\langle \nu_\alpha | e^{-i(\mathbf{p}\cdot\mathbf{x})t} | \nu_\beta \rangle|^2 = \sum_{i,j=1}^{3} U_{\alpha i} U_{\beta j}^* U_{\beta i}^* U_{\alpha j} e^{-i\Delta m_{ij}^2 L/2E} \tag{1.33}$$

where $\Delta m_{ij}^2 = m_i^2 - m_j^2$, and $\mathbf{p}$ and $\mathbf{x}$ are the momentum and position 4-vectors. The oscillation length is

$$L_{ij} = \frac{4\pi E_\nu}{\Delta m_{ij}^2}. \tag{1.34}$$

To describe the neutrino mixing we need to know three mixing angles θ_{12}, θ_{23}, and θ_{13}, the complex phase δ, and two mass differences squared. One of the Δm_{ij}^2 is determined by the condition

$$\Delta m_{12}^2 + \Delta m_{23}^2 + \Delta m_{31}^2 = 0. \tag{1.35}$$

Fundamentally, the goal is to know the nine parameters θ_{12}, θ_{13}, θ_{23}, m_1, m_2, m_3, δ, ϕ_1, and ϕ_2. The absolute neutrino masses m_1, m_2, and m_3 cannot be determined by oscillations, but their actual values are of great significance.

1.3.2 Matter-enhanced oscillations

In matter neutrinos have their oscillation amplitude enhanced due to forward scattering off electrons. This theory was worked out by Mikheyev-Smirnov-Wolfenstein and is known as the MSW effect [23, 24]. An electron neutrino interacts through the $W^{\pm}$ and Z bosons while the muon and tau neutrino only interact with the Z. Since the electron neutrino has both the CC and NC interactions it has a larger cross section. The difference in forward scattering amplitudes of neutrinos off electrons is

$$f_{(\nu_e, e)}(0) - f_{(\nu_{\mu,\tau}, e)}(0) = -\frac{G_F p}{\sqrt{2}\pi} \tag{1.36}$$

where p is the neutrino momentum. This difference in forward scattering amplitudes between the ν_e and $\nu_{\mu,\tau}$ results in a difference in phase. The MSW effect can affect solar neutrinos as they exit the sun or as they cross earth at night. A solar MSW effect will produce a change in the overall survival probability. If there is an effect from earth it will show up as a day/night asymmetry.

The index of refraction n_α for a neutrino of flavor α is a function of the electron number density N_e and the forward scattering amplitude $f_\alpha(0)$ for elastic interactions [24].

$$n_\alpha = 1 + \frac{2\pi N_e f_\alpha(0)}{p^2} \tag{1.37}$$

The difference in the indicies of refraction is

$$n_{\nu_e} - n_{\nu_{\mu,\tau}} = \frac{2\pi N_e}{p^2}[f_{(\nu_e, e)}(0) - f_{(\nu_{\mu,\tau}, e)}(0)] = \frac{\sqrt{2}G_F N_e}{p}. \tag{1.38}$$

The electron neutrino wavefunction gains an additional phase with respect to the other neutrino flavors

$$|\nu_e\rangle \propto e^{i\sqrt{2}N_e G_F x}. \tag{1.39}$$

	Vacuum	Matter
Hamiltonian	H_0	$H_0 + V$
Eigenstates	ν_1, ν_2	ν_{1m}, ν_{2m}
Eigenvalues	m_1, m_2	m_{1m}, m_{2m}
Eigenvalues	$m_1^2/2E$, $m_2^2/2E$	H_{1m}, H_{2m}

Table 1.7: Neutrino eigenstates in are modified in matter. The mixing in matter is determined with respect to the eigenstates in matter. $V = V_e - V_{\mu,\tau} = \sqrt{2}G_F N_e$

The oscillation length in matter can be defined as

$$L_m = \frac{2\pi}{\sqrt{2}G_F N_e} = \frac{1.7 \times 10^7}{\rho \langle Z/A \rangle} \text{m} \tag{1.40}$$

with ρ in [g/cm^3]. In the core of the sun the oscillation length $L_m \approx 200\,\text{km}$ and in the earth $L_m \approx 10^4\,\text{km}$. The mixing angle in matter is

$$\sin^2 2\theta_m = \frac{\sin^2 2\theta}{(\cos 2\theta - L_v/L_m)^2 + \sin^2 2\theta} \tag{1.41}$$

which has a resonance for

$$L_v/L_m = \cos 2\theta. \tag{1.42}$$

Regions with a critical electron density

$$\rho_c = \frac{\cos 2\theta \Delta m^2}{2\sqrt{2}G_F E_\nu} \tag{1.43}$$

result in maximal mixing where $\sin^2 2\theta_m = 1$.

Matter modifies the neutrino Hamiltonian. The new states in matter are denoted by a subscript m shown Table 1.7. These states in matter are a function of the electron density. Otherwise the formalism is the same.

If the density is non-uniform $N_e \to N_e(x)$ then the Hamiltonian will depend on time. The mixing will be a function of the local density $\theta \to \theta(N_e(x))$. This will mean ν_{1m} and ν_{2m} are no longer eigenstates of propagation and transitions $\nu_{1m} \leftrightarrow \nu_{2m}$ will occur. If the density change is slow then the change is adiabatic and the transitions $\nu_{1m} \leftrightarrow \nu_{2m}$ can be neglected. The adiabatic condition is

$$\frac{\left| \frac{d\theta_m}{dt} \right|}{H_2 - H_1} \ll 1 \tag{1.44}$$

In the two neutrino case the survival probability for an electron neutrino $P_{ee}^{2\nu}$ is

$$P_{ee}^{2\nu} = \frac{1}{2}(1 + \cos 2\theta_m^0 \cos 2\theta) \tag{1.45}$$

where θ is the vacuum mixing angle and θ_m^0 is the mixing angle at the neutrino production point x_0 [25]. The mixing angle in matter θ_m is given be equation 1.41. Neutrino conversion can be described by instantaneous matter eigenstates ν_{1m} and ν_{2m}. Then the evolution of a neutrino in an arbitrary state $|\nu\rangle = \psi_{1m}|\nu_{1m}\rangle + \psi_{2m}|\nu_{2m}\rangle$ is

$$i\frac{d}{dx}\begin{pmatrix} \psi_{1m} \\ \psi_{2m} \end{pmatrix} = \begin{pmatrix} -\frac{\Delta(x)}{4E} & -i\dot{\theta}_m(x) \\ i\dot{\theta}_m(x) & \frac{\Delta(x)}{4E} \end{pmatrix} \begin{pmatrix} \psi_{1m} \\ \psi_{2m} \end{pmatrix} \tag{1.46}$$

where the adiabatic split $\Delta(x)$ is

$$\Delta(x) = \Delta m^2 \sqrt{(\cos 2\theta - 2EV(x)/\Delta m^2)^2 + \sin^2 2\theta} \tag{1.47}$$

$$\dot{\theta}_m(x) = \frac{d\theta_m(x)}{dx} = \frac{E\Delta m^2 \sin 2\theta}{\Delta(x)^2}\frac{dV(x)}{dx}. \tag{1.48}$$

The adiabatic condition is met when the off diagonal elements are much smaller than the diagonal elements. The solution is $\Psi_m^{ad}(x) = S^{ad}(x, x_0)\Psi_m(x_0)$ or more explicitly

$$\begin{pmatrix} \psi_{1m}^{ad}(x) \\ \psi_{2m}^{ad}(x) \end{pmatrix} = \begin{pmatrix} e^{i\Phi(x)} & 0 \\ 0 & e^{-i\Phi(x)} \end{pmatrix} \begin{pmatrix} \psi_{1m}(x_0) \\ \psi_{2m}(x_0) \end{pmatrix} \tag{1.49}$$

where

$$\Phi(x) = \frac{1}{4}\int_{x_0}^{x} \Delta(x')dx'. \tag{1.50}$$

An electron neutrino would evolve like

$$\nu(x) = \cos\theta_m^0 e^{i\Phi(x)\nu_{1m}} + \sin\theta_m^0 e^{-i\Phi(x)\nu_{2m}}. \tag{1.51}$$

For the non-adiabatic case the off diagonal elements are no longer zero allowing for transitions between the instantaneous eigenstates. The evolution matrix is then

$$S^{na} = \begin{pmatrix} e^{i\Phi(x)} & c(x)e^{i\Phi(-x)} \\ -c^*(x)e^{i\Phi(x)} & e^{-i\Phi(x)} \end{pmatrix} \tag{1.52}$$

where $|c(x)| \ll 1$ along the trajectory. The condition

$$i\frac{d}{dx}c(x) = -\frac{\Delta(x)}{2E}c(x) - i\dot{\theta}_m(x) \tag{1.53}$$

leads to the solution

$$c(x) = -\int_{x_0}^{x} \frac{d\theta_m(x')}{dx'} \exp\left[-i\int_{x}^{x'} \frac{\Delta(x'')}{2E}dx''\right] dx'. \tag{1.54}$$

Integrating by parts to remove the exponential from the integral results in

$$c(x_f) = -i\frac{2e^2\Delta m^2 \sin 2\theta}{\Delta(x)^3} \frac{dV(x)}{dx} \exp\left[-i\int_{x_f}^{x} \frac{\Delta(x')}{2E}dx'\right]. \tag{1.55}$$

In the sun the survival probability with an adiabatic violation is

$$P_{ee} = \frac{1}{2}[1 + (1 - 2P_c)\cos 2\theta_m^0 \cos 2\theta] \tag{1.56}$$

where $P_c = |c(x_f)|^2$ is the probability of the $\nu_{2m} \to \nu_{1m}$ transition. The probability of a non-adiabatic transition P_c is

$$P_c = \frac{1}{16\pi^2} \frac{L_m^2(x_0)}{h^2(x_0)} \left[\frac{2EV(x_0)\Delta m^2 \sin 2\theta}{\Delta(x_0)^2}\right] \tag{1.57}$$

where the height density $h(x)$ is

$$h(x) = V(x)\left[\frac{dV(x)}{dx}\right]^{-1} \tag{1.58}$$

and the oscillation length in matter L_v is

$$L_m(x) = \frac{4\pi E}{\Delta(x)} \tag{1.59}$$

Because $L_m(x) \ll h(x)$ there are many oscillations before the potential changes significantly. Thus the non-adiabatic average out except at the endpoints of the trajectory. Since the potential at the surface of the sun goes to zero the transition probability is mostly dependent on the production point. For the LMA parameters

$$P_c = (10^{-9} - 10^{-7})(\frac{E}{10\,\text{MeV}})^2 \tag{1.60}$$

K	pp	^{8}B	^{13}N	^{15}O	^{17}F	^{7}Be	pep	hep
$\bar{V}_K[10^{-12}\,\text{eV}]$	4.68	6.81	6.22	6.69	6.74	6.16	5.13	3.96
$\Delta V_k^2/\bar{V}_K^2$	0.109	0.010	0.054	0.013	0.012	0.029	0.076	0.165

Table 1.8: Solar neutrino MSW parameters. From [25].

The probability of a non-adiabatic transition in the sun is negligible for the entire solar neutrino production region.

For adiabatic evolution, survival depends on the electron density at the production point. The neutrino flux at earth is dependent on the survival probability averaged over neutrino production region. Since the sun is symmetric P_{ee} is a function of the production point r. The survival probability averaged over the production region P_K is

$$P_K = \frac{\int G_K(r)P_{ee}(r)dr}{\int G_K} \tag{1.61}$$

for $K = pp, pep$, Be, N, C, O, F, B, *hep*, and where G_K is the source distribution of K neutrinos. The average potential in the production region is

$$\bar{V}_K = \frac{\int G_K(r)V(r)dr}{\int G_K}. \tag{1.62}$$

Expanding around $\bar{V}_K$ the average survival probability P_K can be expressed as

$$P_K = \frac{1}{2} + \frac{1}{2}(1-\delta_K)\cos 2\theta_m(\bar{V}_K)\cos 2\theta \tag{1.63}$$

where

$$\delta_K = \frac{3}{2}\frac{(2E\bar{V}_K/\Delta m^2)^2\sin^2 2\theta}{[(\cos 2\theta - 2E\bar{V}_K/\Delta m^2)^2 + \sin^2 2\theta]^2}\frac{\Delta V_K^2}{\bar{V}_K^2} \tag{1.64}$$

and

$$\Delta V_K^2 = \frac{\int G_K(V(r)-\bar{V}_K)^2 dr}{\int G_K dr}. \tag{1.65}$$

Values for $\bar{V}_K$ and $\Delta V_k^2/\bar{V}_K^2$ can be found in Table 1.8.

Regeneration refers to the conversion of a muon or tau neutrino back into an electron neutrino in earth. The MSW effect in earth is relatively weak due to the comparatively low electron densities involved. The survival probability with regeneration is

$$P_{ee}^{2\nu} = \frac{1}{2}(1 + \cos 2\theta_m^0\cos 2\theta) - \cos 2\theta_m^0 f_{reg} \tag{1.66}$$

The regeneration effect can be modeled by considering an earth made of spherical shells each with constant density. Neutrinos accumulate an adiabatic phase as they cross each shell and non-adiabatic corrections at the boundary between each shell.

$$f_{reg} = \frac{2E \sin^2 2\theta}{\Delta m^2} \sin \Phi_0 \sum_{i=0}^{n-1} \Delta V_i \sin \Phi_i \tag{1.67}$$

where the adiabatic phase Φ_i acquired between $-L_i/2$ and $L_i/2$ is

$$\Phi_i = \int_{-L_i/2}^{L_i/2} \frac{\Delta(x)}{4E} dx \approx \int_{-L_i/2}^{L_i/2} \left[\frac{\Delta m^2}{4E} - \frac{1}{2}\cos 2\theta V(x) + \frac{E \sin^2 2\theta}{2\Delta m^2} V^2(x) \right] dx \tag{1.68}$$

Calculation have shown that f_{reg} is about 1.5% for $10\,\text{MeV}$ neutrinos [25].

To summarize LMA-MSW conversion, the survival probability of a solar neutrino is primarily dependent on the local electron density at its production point in the sun, vacuum mixing on its way to earth, and regenerative effects during passage through earth. This survival probability in the two neutrino case is given by

$$P_{ee} = \frac{1}{2} + \frac{1}{2}(1 - \delta_K)\cos 2\theta_m(\bar{V}_K)\cos 2\theta - (1 - \delta_K)\cos 2\theta_m(\bar{V}_K)f_{reg} \tag{1.69}$$

where K represents the component of the solar neutrino spectrum and the other terms are as defined above.

In general all three neutrino flavors should be taken into account in the MSW effect. Solar neutrinos experiments are only sensitive to the electron neutrino survival probability $P_{ee}^{3\nu}$. This is because the sun produces only electron neutrinos, and solar neutrino detectors cannot distinguish between muon and tau neutrinos. The probability for conversion to muon neutrinos $P_{e\mu}$ or tau neutrinos $P_{e\tau}$ only appears in the form $P_{e\mu} + P_{e\tau}$[26]. $P_{ee}^{3\nu}$ is related to the survival probability for effective two neutrino oscillations P_{ee} by

$$P_{ee}^{3\nu} = \cos^4 \theta_{13} P_{ee} + \sin^4 \theta_{13} \tag{1.70}$$

where P_{ee} is the two neutrino survival probability that is defined in equation 1.69.

The effective Hamiltonian for neutrinos propagating in matter is

$$H = \begin{pmatrix} \frac{\Delta m^2 \cos 2\theta_{12}}{4E} - \frac{\sqrt{2}G_F \cos^2 \theta_{13} n_e}{2} & \frac{\Delta m^2 \sin 2\theta_{12}}{2E} \\ \frac{\Delta m^2 \sin 2\theta_{12}}{2E} & -\frac{\Delta m^2 \cos 2\theta_{12}}{4E} + \frac{\sqrt{2}G_F \cos^2 \theta_{13} n_e}{2} \end{pmatrix}. \tag{1.71}$$

The ratio of the oscillation length in matter to the oscillation length in vacuum β is

$$\beta = \frac{2\sqrt{2}G_F \cos^2\theta_{13} n_e E}{\Delta m^2} \tag{1.72}$$

or in more useful units

$$\beta = 0.22 \cos^2\theta_{13} \left[\frac{E}{1\,\mathrm{MeV}}\right] \left[\frac{\mu_e \rho}{100\,\mathrm{g/cm^3}}\right] \left[\frac{7\times 10^{-5}\,\mathrm{eV}}{\Delta m^2}\right] \tag{1.73}$$

where $\mu_e = \frac{\rho}{n_e m_p}$ is the mean electron molecular weight, and ρ is the total density. In the sun $\mu_e = 1.18$.

The daytime survival probability of solar neutrinos with the LMA solution can be approximated by

$$P_{ee}^{3\nu} \approx \cos^4\theta_{13}\left(\frac{1}{2} + \frac{1}{2}\cos 2\theta_{12}^M \cos 2\theta_{12}\right). \tag{1.74}$$

Recall that the mixing angle in matter is

$$\cos 2\theta_{12}^M = \frac{\cos 2\theta_{12} - \beta}{\sqrt{(\cos 2\theta_{12} - \beta)^2 + \sin^2 2\theta_{12}}} \tag{1.75}$$

where β is calculated where the neutrino is produced [26]. The value of β from equation (1.72) determines weather the oscillations are vacuum dominated or matter dominated. If $\beta < \cos 2\theta_{12}$ which is about 0.4 for solar neutrinos then vacuum averaged oscillations dominate. The survival probability in this case is

$$P_{ee}(\mathrm{Vacuum}) = \cos^4\theta_{13}\left(1 - \frac{1}{2}\sin^2 2\theta_{12}\right). \tag{1.76}$$

If $\beta > 1$ the the survival is matter dominated and

$$P_{ee}(Matter) = \cos^4\theta_{13}\sin^2 2\theta_{12}. \tag{1.77}$$

The survival is fairly constant in these regions and only exhibits a strong energy dependence when $\cos 2\theta_{12} < \beta < 1$. The critical energy for ^{7}Be neutrinos is 2.2 MeV. Since the energy of ^{7}Be neutrinos is below the critical energy they are dominated by vacuum oscillations and are not influenced significantly by the MSW effect. This is shown qualitatively in Figure 1.9.
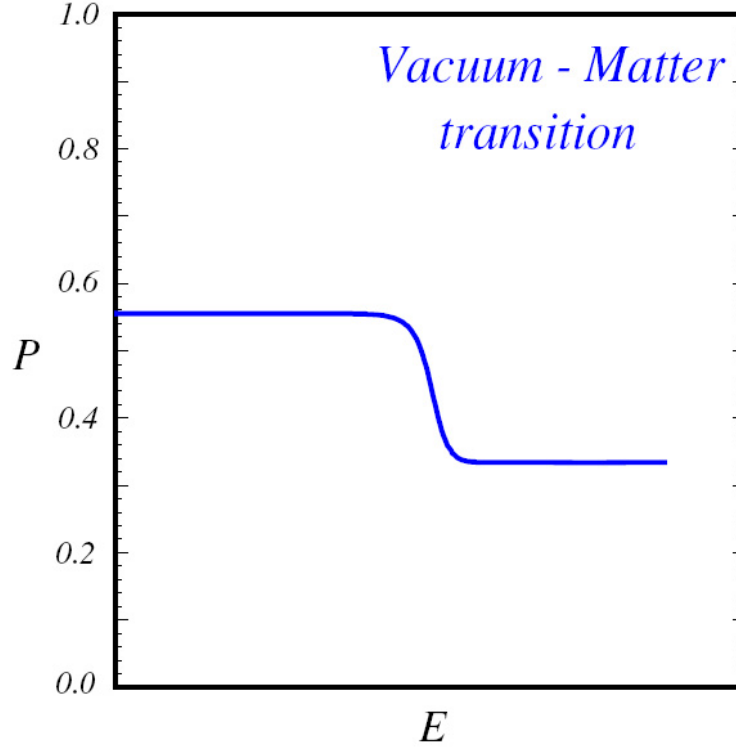
Figure 1.9: The electron neutrino survival probability as a function of energy [26]. The critical energy β given in equation (1.72) determines which type of oscillations dominate. Above this energy matter enhanced MSW oscillations are important (right), and below this energy vacuum averaged oscillations dominate (left). For the ^{7}Be solar neutrinos $\beta = 2.2\,\text{MeV}$. Since the energy of ^{7}Be neutrinos is $862\,\text{keV}$ their survival probability is dominated by vacuum averaged oscillations.

1.4 Dirac and Majorana neutrinos

According to the standard model there are only left-handed neutrinos and right-handed antineutrinos. The chirality refers to the helicity of a particle which is its spin vector projected on its direction of travel

$$\vec{h} = \frac{\vec{s} \cdot \vec{p}}{|\vec{p}|}. \tag{1.78}$$

A spin 1/2 particle will have either positive or negative helicity depending on whether its spin is parallel or antiparllel to its motion. For a massless particle which must travel at the

speed of light, the helicity is the same as the particles spin. For a massive particle helicity will depend on the frame of reference since an observer can move to a frame traveling faster than a massive particle, making its momentum negative and thus changing the sign of its helicity. Thus neutrinos are massless in the Standard Model. In the Standard Model for V-A coupling the current 4-vector is

$$j_\mu = \bar{\nu}\gamma_\mu(1 - \gamma_5)e = 2\bar{\nu}_L\gamma_\mu e_L \tag{1.79}$$

where the left and right handed particles and antiparticles of the neutrino field are

$$\nu = \begin{pmatrix} \chi_R \\ \chi_L \end{pmatrix} \tag{1.80}$$

In the chiral representation

$$\gamma_0 = \begin{pmatrix} 0 & -1 \\ -1 & 0 \end{pmatrix}, \quad \gamma_i = \begin{pmatrix} 0 & \sigma_i \\ -\sigma_i & 0 \end{pmatrix}, \quad \gamma_5 = \begin{pmatrix} 1 & 0 \\ 0 & -1 \end{pmatrix}. \tag{1.81}$$

where the σ_i are the Pauli spin matrices

$$\nu_L \equiv \frac{1 - \gamma_5}{2}\nu = \begin{pmatrix} 0 & 0 \\ 0 & 1 \end{pmatrix}\begin{pmatrix} \chi_R \\ \chi_L \end{pmatrix} = \begin{pmatrix} 0 \\ \chi_L \end{pmatrix} \tag{1.82}$$

and $\gamma_5\nu_L = -\nu_L$ for left handed chirality. The Dirac equation

$$(i\gamma^\mu\partial_\mu - m)\nu = 0 \tag{1.83}$$

with massless neutrinos reduces to the two component Weyl equation

$$(\partial_0 - \vec{\sigma} \cdot \vec{\nabla})\chi_L = 0. \tag{1.84}$$

Thus weak interactions in the SM involve only two components of the neutrino field. The Dirac mass term is

$$\mathcal{L}_{Dirac} = m_D(\bar{\nu}_L\nu_R + \bar{\nu}_R\nu_L) = m_D\bar{\nu}\nu \tag{1.85}$$

where $\nu = \nu_L + \nu_R$.

For Majorana type neutrino there are both left and right handed neutrinos and anti-neutrinos

$$(i\gamma^\mu\partial_\mu - m)\nu = 0 \qquad \text{particle} \tag{1.86}$$

$$(i\gamma^\mu\partial_\mu - m)\nu^c = 0 \quad \text{anitparticle} \tag{1.87}$$

where

$$\nu = \begin{pmatrix} \chi_R \\ \chi_L \end{pmatrix}, \quad \nu_c = \begin{pmatrix} -i\sigma^2\chi_L^* \\ i\sigma^2\chi_R^* \end{pmatrix}. \tag{1.88}$$

The Majorana condition is $\nu = \nu^c$ which implies

$$\begin{aligned} \chi_R &= -i\sigma^2\chi_L^* \\ \chi_L &= i\sigma^2\chi_R^* \end{aligned} \tag{1.89}$$

A Majorana neutrino is its own antiparticle. Thus one can have a two component neutrino with Majorana mass. The Majorana equation is

$$(\partial_0 - \vec{\sigma}\cdot\vec{\nabla})\chi_L + m\sigma^2\chi_L^* = 0 \tag{1.90}$$

The Majorana mass term is

$$\mathcal{L}_{Majorana} = -\frac{1}{2}m_M(\bar{\nu}_L\nu_L^c + \bar{\nu}_L^c\nu_L) = -\frac{1}{2}m_M\bar{\nu}\nu \tag{1.91}$$

where $\nu = \nu_L + \bar{\nu}_L^c$. A Majorana neutrino will violate lepton number conservation. According to Noether's Theorem this would imply a loss of global gauge invariance. A massive Majorana neutrino can have neither a magnetic nor electric dipole moment.

1.5 Neutrino CP Violation

All field theories fundamentally preserve CPT symmetry (Charge conjugation, Partiy, and Time reveral). CPT symmetry says that physics is identical under charge conjugation where particles are replaced with their antiparticles, parity where the coordinate system is inverted, and time reversal where time is run backwards. Neutrinos may violate charge conjugation

parity (CP) symmetry. This would produce a difference in oscillation probabilities between particle and antiparticle

$$\Delta P_{CP} = P(\nu_e \to \nu_\mu) - P(\bar{\nu}_e \to \bar{\nu}_\mu) = 4 J_{CP} f_{CP} \tag{1.92}$$

with

$$f_{CP} = \sin \Delta_{12} + \sin \Delta_{23} + \sin \Delta_{31} \tag{1.93}$$

and

$$J_{CP} = \sin \theta_{12} \sin \theta_{23} \sin \theta_{13} \cos \theta_{12} \cos \theta_{23} \cos^2 \theta_{13} \sin \delta \tag{1.94}$$

where $\Delta_{ij} = \Delta m_{ij}^2 \frac{L}{2E}$ [27]. CP violation can only be observed if the mixing angles, particularly θ_{13} are non zero. If neutrinos violate CP they would also violate T as well.

1.6   The Standard Solar Model

Fusion in the core of the sun releases a huge amount of energy. This energy primarily takes the form of neutrino emission and the kinetic energy of the nuclear products formed in the reactions. The nuclear products are thermalized producing heat and which is then radiated away as photons. The fusion energy is generated by consuming a portion of the mass of the particles that are fusing together. The intense pressure and high density required for the fusion reactions to occur is provided by the gravitational force due to the sun's mass. A radiative pressure generated by fusion counteracts the gravitational force and prevents the sun from collapsing. The primary fusion cycle which burns hydrogen is shown in Figure 1.10. It can be summarized by the following reaction

$$4p \to \alpha + 2e^+ + 2\nu_e + 26.7 \, \text{MeV}. \tag{1.95}$$

There are heavier elements left over from previous star formation that are also present in the sun. These include carbon, nitrogen, and oxygen and their reactions are known as the CNO cycle shown in Figure 1.11.
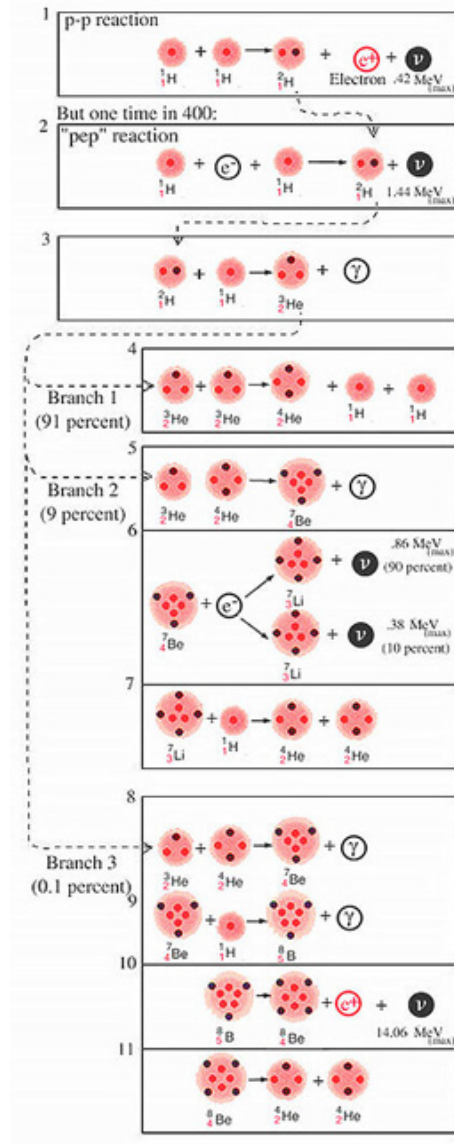
Figure 1.10: The primary solar fusion cycle converts 4 protons into helium, 2 positrons, and 2 electron neutrinos. Figure from [28].
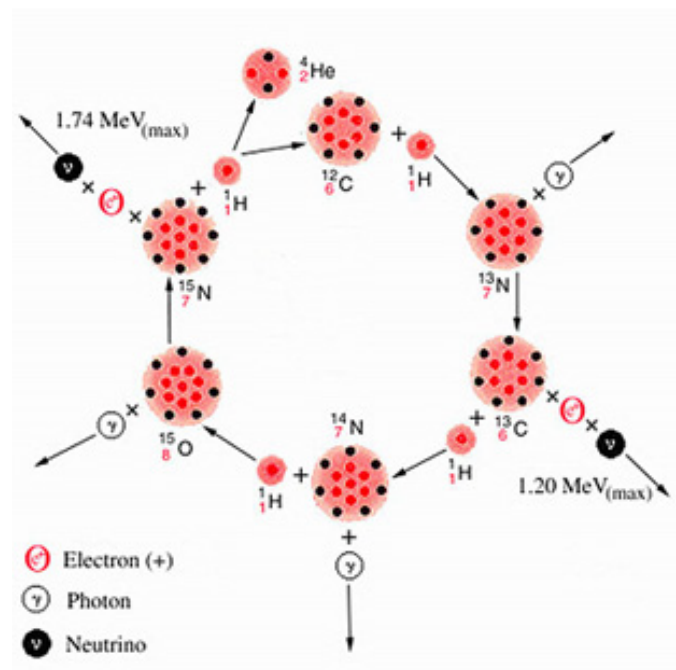
Figure 1.11: The CNO cycle in the sun results in the release of two neutrinos. Figure from [28].

Reaction	Source $[\nu_e]$	Flux $[\mathrm{cm}^{-2}\mathrm{s}^{-1}]$	Q [MeV]	E_{ν_e} [MeV]
$p + p \rightarrow ^2\mathrm{H} + e^+ + \nu_e$	pp	5.94×10^{10}	1.422	≤ 0.420
$p + e^- + p \rightarrow ^2\mathrm{H} + \nu_e$	pep	1.40×10^8	1.422	1.422
$^7\mathrm{Be} + e^- \rightarrow ^7\mathrm{Li} + \nu_e$	$^7\mathrm{Be}$	4.86×10^9	0.862(90%) 0.383(10%)	0.862(90%) 0.383(10%)
$^8\mathrm{B} \rightarrow ^8\mathrm{Be}^* + e^+ + \nu_e$	$^8\mathrm{B}$	5.79×10^6	17.980	≤ 15
$^3\mathrm{He} + p \rightarrow ^4\mathrm{He} + e^+ + \nu_e$	hep	7.99×10^3	19.795	≤ 18.8
$^{13}\mathrm{N} \rightarrow ^{13}\mathrm{C} + e^+ + \nu_e$	$^{13}\mathrm{N}$	5.71×10^8	2.221	≤ 1.199
$^{15}\mathrm{O} \rightarrow ^{15}\mathrm{N} + e^+ + \nu_e$	$^{15}\mathrm{O}$	5.03×10^8	2.754	≤ 1.732
$^{17}\mathrm{F} \rightarrow ^{17}\mathrm{O} + e^+ + \nu_e$	$^{17}\mathrm{F}$	5.91×10^6	2.762	≤ 1.740

Table 1.9: Neutrino producing reactions in the sun and the resulting flux at earth 1 AU away. An AU is an Astronomical Unit which is the average earth sun distance and equals 1.5×10^{11} meters. Measurements of the solar neutrino spectrum can provide information about specific fusion reactions that take place in the core of the sun. This information can then be correlated with measurements of temperature, luminosity, spectroscopy, or helioseiemic activity [29].

Several of the fusion reactions in the sun produce electron neutrinos. They are summarized in Table 1.6. Neutrinos are a useful tool for illuminating the solar fusion process because they can probe specific fusion reactions in the sun and the neutrinos free stream out from the sun's core providing real time information. Photons produced in the sun's core through specific gamma emitting reactions and black body radiation scatter a huge number of times before reaching the sun's surface. They only show the combined energy released from the reactions and yield the information only after a significant time delay of $10^5 - 10^6$ years. The energy spectrum from solar neutrinos at earth is shown in Figure 1.12.

Fusion reactions and thus solar neutrino fluxes are extremely sensitive to the temperature of the sun. Each flux depends on the central temperature of the sun ($\phi \propto T_c$). For the $^7\mathrm{Be}$ neutrinos, $\phi(^7\mathrm{Be}) \propto T_c^{11}$ [31].

The temperature in the core of the sun is 1.56×10^7 K and decreases monotonically to 5770 K at the surface. The radius of the sun is 6.96×10^5 km. The density at the center of the sun is $150\,\mathrm{g/cm}^3$ and decreases to roughly zero at the surface.
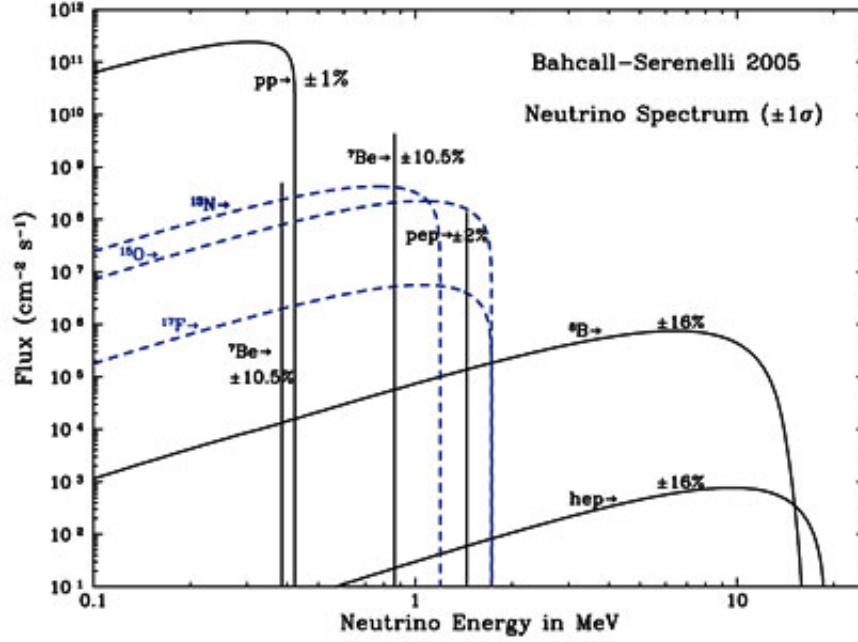
Figure 1.12: The solar neutrino energy spectrum at earth. The units for continuum sources are number of neutrinos $\mathrm{cm}^{-2}\mathrm{s}^{-1}\mathrm{MeV}^{-1}$ and for monoenergetic neutrino lines are number of neutrinos $\mathrm{cm}^{-2}\mathrm{s}^{-1}$. Figure from [30].

Neutrino Flux	Temperature Dependence
$\phi(\mathrm{pp})$	$1 - 0.08(T_c/T_{ssm})^{13}$
$\phi(\mathrm{pep})$	$T_c^{-1.4}$
$\phi(^7\mathrm{Be})$	T_c^{11}
$\phi(^8\mathrm{B})$	T_c^{25}
$\phi(^{13}\mathrm{N})$	T_c^{20}
$\phi(^{15}\mathrm{O})$	T_c^{20}
$\phi(^{17}\mathrm{F})$	T_c^{23}

Table 1.10: The temperature dependence of various solar neutrino fluxes. T_c is the temperature in the core of the sun and $T_{ssm} = 15.64 \times 10^{16}\,\mathrm{K}$ [31].

1.7 Neutrino Experiments

The first neutrino detectors used a large mass of material to capture neutrinos on nuclei changing one atom into another. Typically chemical means were used to separate the few new atoms from the bulk material, and the new atoms were usually radioactive to allow for easy detection. These types of measurements are referred to as radiochemical experiments. The reaction used can be generically described as an inverse beta decay.

$$\nu_e + {}^A_Z X = {}^A_{Z+1} Y + e^-$$ (1.96)

where X and Y are different atoms with the same atomic number. There is a minimum neutrino energy needed for the reaction to occur

$$E_{threshold} = (m_Y + m_e - m_X)c^2.$$ (1.97)

Another common method of detecting neutrinos is with scintillator. Scintillator refers to a material that converts the energy of a particle into light. The number of photons produced by a scintillator is proportional to the energy of the particle. The light can be measured with photomultiplier tubes (PMTs). Good PMTs are sensitive to single photons. By using the PMTs to count the number of photons produced, the energy or the event can be determined. A clever trick is to use a series of events with known energies that are spaced closely in time as a signature for a neutrino event. This coincidence of events is unlikely to be produced randomly by background.

The high sensitivity of PMTs allows them to measure Cherenkov radiation as well. Cherenkov radiation is a shockwave of light produced when a charged particle moves faster than the speed of light in a material. This is allowed because the index of refraction $n > 1$ reduces the velocity of light to $v = c/n$. This phenomenon is similar to the sonic boom produced when a object travels faster than the speed of sound. The result is a cone of light that can be measured by the phototubes. Cherenkov radiation is convenient because it can provide a wealth of information including the type, energy, location, and direction of the particle. When neutrino interactions can produce sufficiently high energy particles this method can be employed.

One of the primary difficulties when designing a neutrino detector is achieving a low rate of non-neutrino events. If uncontrolled these background events can swamp the relatively low neutrino rate by many orders of magnitude. Background events can come from cosmic rays, external radioactivity, and radioactivity inside the detector. Though these sources vary in nature depending on the location of the experiment and the materials being used, the background events are always a significant concern.

Cosmic rays are produced when high energy particles that stream through the universe in all directions hit earth's atmosphere. They are composed of 90% protons, 9% alphas, and 1% electrons. The initial interaction produces primarily pions and kaons that decay or interact further producing a shower of particles. Some of these are absorbed in the atmosphere but many reach sea level. The muon flux at sea level is about $1 \, \text{muon/cm}^2/\text{s}$. Muons are particularly troublesome because they are charged meaning an active detector will see all the muons that pass through and very massive which makes them hard to shield against. In addition they can also cause atoms in the material of the detector to break apart making radioactive spallation products or the bump nuclei into an excited state which then decays. The most effective way to reduce the cosmic ray flux is to go deep underground or underwater. Units of meters water equivalent (mwe) are used to describe cosmic ray shielding in a way that is independent of the material. The muon flux as a function of depth is shown in Figure 1.13.

External radioactivity results from radioactive elements that are naturally present in the environment. This could be uranium and thorium in the ground or radon in the air. They produce alpha, beta, gamma and neutron emissions. They are usually stopped or reduced by placing shielding material immediately around the detector. Alphas are completely stopped within a cm of material. Betas and gammas are more penetrating with higher energy particles going further but they can be stopped with a reasonable amount of material depending on its density.

Internal activity results from radioactive elements that are present in the detector. All material is radioactive at some level and it is impossible for a material to be completely pure. Careful material selection is important for reducing background.
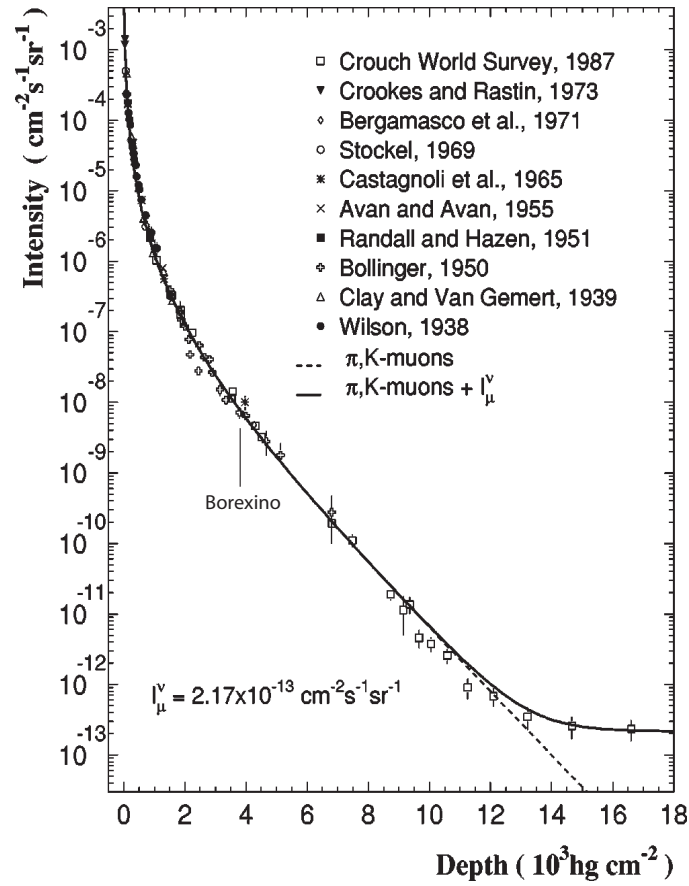
Figure 1.13: The muon flux from cosmic rays as a function of depth. The units hg/cm^2 is equal to a mwe. From reference [32]

1.7.1 Solar Neutrino Experiments

The Homestake Experiment led by Ray Davis in 1970, was the first solar neutrino experiment [3]. Homestake was a radiochemical experiment that observed the new elements produced when neutrinos were captured in a nucleus. The detector mass consisted of 615 tons of liquid perchloroethylene (C_2Cl_4). It utilized the reaction $\nu_e + ^{37}Cl \rightarrow e^- + ^{37}Ar$. The neutrino capture reaction on Chlorine is only sensitive to neutrinos above and energy threshold $E_{th} = 814$ keV. Periodically the radioactive isotope ^{37}Ar was extracted from the tank with a helium gas purge and then trapped on a charcoal filter. The argon atom then decays through electron capture $^{37}Ar + e^- \rightarrow \nu_e + ^{37}Cl$ with $t_{1/2} = 35$ days. The rate of argon decays indicated how many neutrinos were captured in the detector. Homestake measured about 1/3 of the neutrino rate expected from theory. This deficit of solar neutrino became known as the "Solar Neutrino Problem".

The Russian (formerly Soviet)-American Gallium Experiment - SAGE uses 50 tons of gallium to capture neutrinos [33]. The gallium capture reaction is $\nu_e + ^{71}Ga \rightarrow e^- + ^{71}Ge$ with an energy threshold of $E_{th} = 233$ keV. ^{71}Ge has a half life of $t_{1/2} = 11.43$ days. The Gallex experiment and its second generation experiment GNO also use neutrino capture on 30 tons of Gallium. Together they recorded a rate of 70.8 ± 4.5 statistical ± 3.8 systematic SNU. The expected rate was 128 ± 9 SNU. A SNU is a solar neutrinos unit is defined as 10^{-36} neutrino captures per target atom per second.

These radiochemical experiments rely on separating and measuring the radioactive products of a neutrino interaction. They yield no real time information about when individual neutrino interactions occurred, the neutrino's directionality, or its energy except that it is higher than the threshold. Temporal information is limited to the frequency of extraction.

The Sudbury Neutrino Observatory (SNO) uses 1000 tons of heavy water (D_2O) to detect neutrinos [5, 34]. Heavy water is the same as normal water except the hydrogen atoms are replaced by by deuterium which contains one proton and one neutron. SNO uses 9700 PMT's to detect light produced by three different types of neutrino events.

1.) Charged current reaction (CC) $\nu_e + {}_1^2\text{D} \rightarrow p + p + e^-$

2.) Neutral current reaction (NC) $\nu_{e,\mu,\tau} + {}_1^2\text{D} \rightarrow p + n + \nu_{e,\mu,\tau}$

3.) Electron Scattering (ES) $\nu_{e,\mu,\tau} + e^- \rightarrow \nu_{e,\mu,\tau} + e^-$

The CC reaction produces a high energy electron that creates Cherenkov radiation. The threshold for the CC reaction is $E_{th} = 2.3\,\text{MeV}$. The NC reaction has an energy threshold $E_{th} = 1.4\,\text{MeV}$. The neutron produced by NC processes will be captured by a nucleus producing gamma rays. The gamma rays will scatter electrons that can be detected by their Cherenkov radiation. The NC reaction is equally sensitive to all 3 neutrino flavors. The ES reactions were also detected by the Cherenkov radiation produced by the scattered electron. SNO was able to distinguish between the three types of neutrino interactions. SNO demonstrated convincingly that all the solar neutrinos were accounted for when the all the neutrino flavors were observed and that solar neutrino oscillations were taking place. Data from the SNO are shown in Figure 1.14.

The next generation of solar neutrino experiments will measure solar neutrinos with better energy resolution and a lower energy threshold. This will allow for real time measurements of the most intense *pp* neutrino flux which also has the lowest energy. Some of these experiments are MOON (Molybdenum Observatory of Neutrinos) which will use neutrino capture in ^{100}Mo, LENS (Low-Energy Neutrino Spectrometer) that will capture neutrinos on ^{176}Yb, and HERON (HElium Roton Observation of Neutrinos) an ambitious experiment which will measure the scintillation as well as the phonons and rotons produced when a neutrino interacts with superfluid liquid helium.

Solar neutrinos are a good probe of electron neutrino mixing. The parameters m_{12} and θ_{12} are often referred to as $m_{\odot}$ and $\theta_{\odot}$ indicating they are determined from solar neutrino data.

1.7.2   Atmospheric Experiments and Neutrino Telescopes

Cosmic rays stream through the universe with a very broad range of energies. The cosmic ray spectrum is shown in Figure 1.15. The source of the highest energy cosmic rays, which
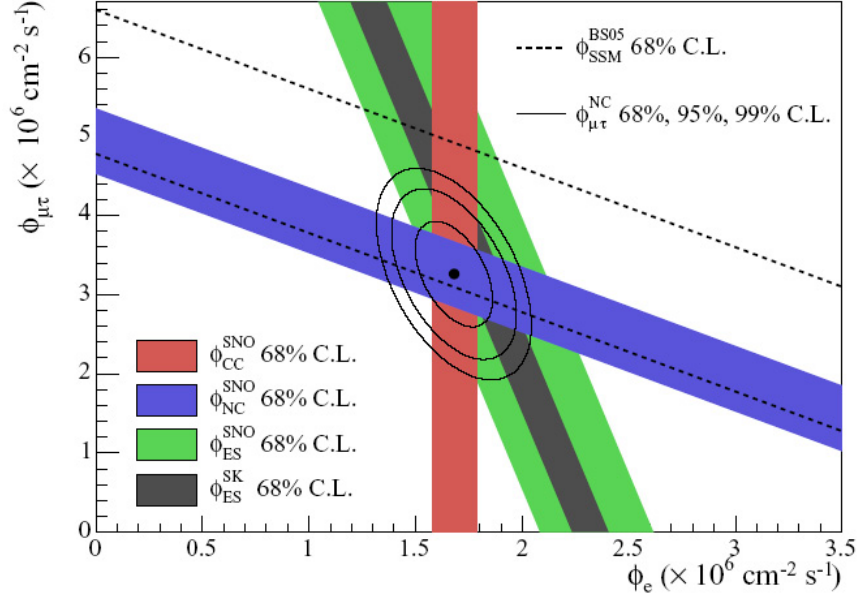
Figure 1.14: The ^{8}B solar neutrino fluxes measured by the SNO and Super K experiments. The colored bands indicate the CC, NC, and ES measurements. The Solar Standard Model flux prediction is shown by the dashed lines. The non zero flux of muon and tau neutrinos is a result of oscillations. From reference [34].

are over 1000 times more energetic than what accelerators can produce on earth, is still unknown. These cosmic rays collide with the earth's atmosphere, composed of 78% N_2, 21% O_2 and 1% Ar, producing showers of secondary particles. There is a relatively uniform spatial distribution of cosmic rays though some distortions arise from earth's magnetic field. Many of the reactions between cosmic rays and the atmosphere produce neutrinos. The spectrum of atmospheric neutrinos produced from cosmic rays is shown in Figure 1.16.

Atmospheric neutrinos are convenient because many are of high enough energy to produce Cherenkov radiation. This allows for the determination of neutrino direction and thus the distance the neutrino traveled since it was created. For example, downward neutrinos were created in the atmosphere above the detector whereas upward neutrinos must have traveled across the diameter of earth. Atmospheric neutrinos can probe baselines from to
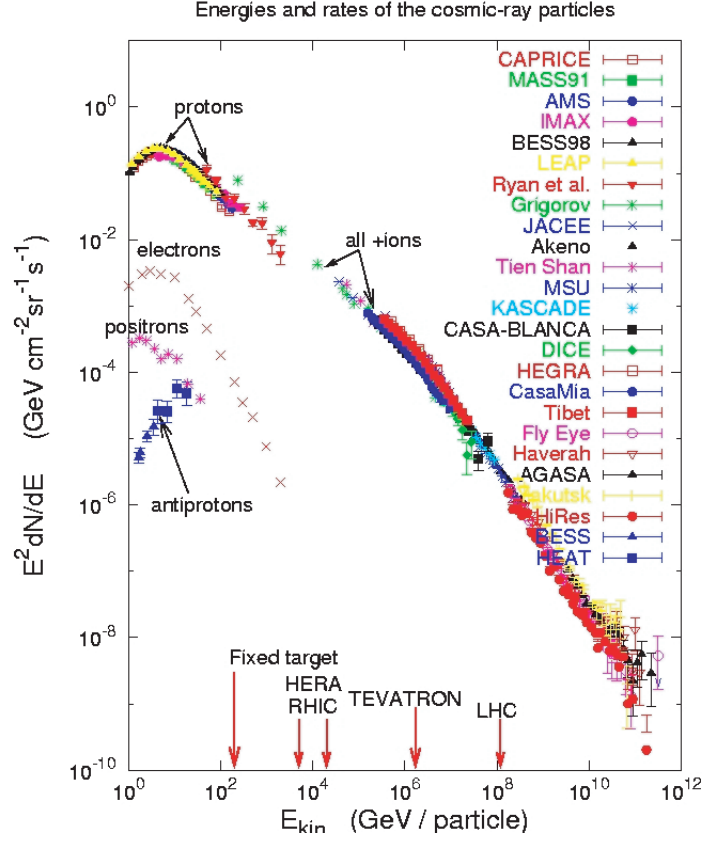
Figure 1.15: The energy spectrum of the cosmic ray flux. These particles interact with the atmosphere producing neutrinos. The source of the highest energy cosmic rays above the 10^{20} eV range is still unexplained. From reference [35].

3×10^5 m, the atmosphere's thickness containing 99% of its mass, to 1.2×10^7 m, the diameter of earth. These neutrinos cover a range of energies which allows for a probe of spectral distortions.

Super-Kamiokande is a gigantic 50 kton water Cherenkov detector located in Mount Ikena, Japan. It uses 13000 PMTs to view Cherenkov light produced by atmospheric neutrinos. The experiment saw a muon neutrino survival probability dependent on L/E, which was predicted by oscillation theory. The data currently places the tightest constraint on the $\nu_\mu \leftrightarrow \nu_\tau$ neutrino oscillation parameters [4]. The experiment also measured the ^{8}B
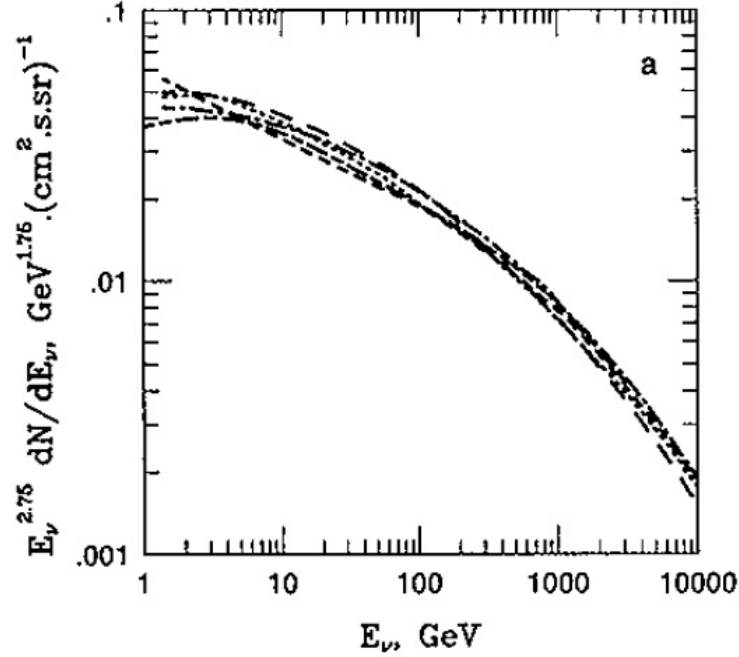
Figure 1.16: The angle averaged atmospheric neutrino flux $\nu_\mu + \bar\nu_\mu$ as calculated by Volkova, Butkevich, Mitsui, and Honda. From reference [36].

and *hep* solar neutrino fluxes [37].

ICARUS is 600 ton liquid argon detector. It is a Time Projection Chamber (TCP), which detects events by applying an electric field and drifting electrons and ions to a wire grid where they can be read out. It is essentially a modern bubble chamber that can identify particles by their tracks as well as resolving their energy.

Neutrino detectors that can pinpoint the highest energy processes in the universe are called neutrino telescopes. The Antarctic Muon And Neutrino Detector Array (AMANDA) and a larger version called IceCube which will span a cubic kilometer, are two high energy neutrino detectors located at the south pole. They use the ice to stop neutrinos and have arrays of PMTs buried in the ice shelf to observe the events. They are capable of measuring very high energy neutrinos in the PeV (10^{15} eV) range which are some the highest energy particles observed. These neutrinos can shed light on the sources of high energy cosmic

rays. Candidate sources are black holes, supernova, active galactic nuclei, and gamma-ray bursters. There are three other experiments, ANTARES, NESTOR, and NEMO, that submerge the PMT's deep under water in the Mediterranean Sea. Both water and ice are convenient detector choices because they are available in large quantities and are free. The tradeoff between them is that ice scatters light more than sea water but has a longer absorption length. This gives ice detectors better energy resolution while water detectors have better directional resolution. Since the detectors see only upward going neutrinos, the Antarctic detectors will observe the northern hemisphere while the Mediterranean detectors will observe the southern hemisphere.

Atmospheric neutrinos are a good probe of muon neutrino mixing. The parameters m_{23} and θ_{23} are often referred to as m_{atm} and θ_{atm}.

1.7.3   Reactor and Accelerator Experiments

Reactor experiments observe electron antineutrinos produced by fission products in nuclear reactors. These reactors produce fluxes of roughly 10^{19} $\bar{\nu}_e$ per second per gigawatt of thermal power into a 4π solid angle. The neutrinos have energies mostly below $10\,\mathrm{MeV}$ with an energy spectrum shown in Figure 1.17. Reactor experiments observe events with an inverse
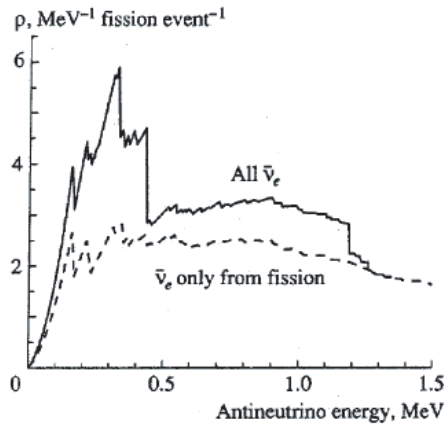
Figure 1.17: The $\bar{\nu}_e$ spectrum produced by nuclear reactors. From reference [38].

beta decay reaction

$$\bar{\nu}_e + p \rightarrow e^+ + n \tag{1.98}$$

which has a threshold of $= 1.804\,\mathrm{MeV}$. The signature is the release of $1.02\,\mathrm{MeV}$ of energy when the positron annihilates an electron followed by a delayed energy release from neutron capture. The first successful experiment to detect neutrinos by Reines and Cowan at the Savannah River nuclear reactor in South Carolina used this detection method. Detectors can be placed various distances from reactors ranging from meters to hundreds of kilometers.

Kamland is the largest of the reactor experiments. It measures anti-electron neutrinos produced by the nuclear power plants in Japan which have an average distance of $180\,\mathrm{km}$. The experiment observed a reduced rate or disappearance of reactor neutrinos as a sign of oscillations [6]. There was also a distortion of the energy spectrum indicating that the oscillations were dependent on the energy of the neutrino [39]. Two other reactor experiments, using the CHOOZ reactor in France and the Palo Verde Nuclear Generating Station in Arizona, measure reactor neutrinos with baselines of about a kilometer [40, 41].

Accelerator experiments produce neutrinos by firing a high energy particle beam at a target. This produces many different particles, some of which are neutrinos or particles that decay into neutrinos. MiniBoone uses a $8\,\mathrm{GeV}$ proton beam at FermiLab to produce a beam of muon neutrinos. Other experiments use neutrino beams produced with the CERN Super Proton Synchrotron in Switzerland or KEK in Japan. Accelerator experiments measure neutrinos that have higher energies than reactor neutrinos, typically in the multi-GeV range. The K2K experiment uses a 12 GeV proton accelerator at KEK to fire a beam of muon neutrinos at the Super Kamiokande detector. MINOS experiment uses the Main Injector at Ferimlab Illinois to create a beam of neutrinos that is measured in the Soudan mine in Minnesota, $735\,\mathrm{km}$ away. The CERN Neutrinos to Gran Sasso (CNGS) sends a neutrino beam from CERN to Gran Sasso, Italy $730\,\mathrm{km}$ away. OPERA, located at Gran Sasso, will look of the appearance of tau neutrinos in the muon neutrino beam.

1.7.4 Double Beta Decay

Normal double beta decay ($2\nu\beta\beta$) occurs when two electrons and two anti-neutrinos are emitted by the nucleus of an atom.

$$\,^A_Z X \rightarrow\,^A_{Z+2} Y + 2e^- + 2\bar{\nu}_e \tag{1.99}$$

This type of double beta decay conserves lepton number with $\Delta L = 0$, since electrons have lepton number $L = 1$ and antineutrinos have $L = -1$. This process has been observed in 9 isotopes with long half lives between $10^{19} - 10^{25}$ years.

   Experiments are looking for a special mode of decay where no neutrinos are emitted called neutrinoless double beta decay ($0\nu\beta\beta$).

$$\,^A_Z X \rightarrow\,^A_{Z+2} Y + 2e^- \tag{1.100}$$

This reaction violates lepton number conservation with $\Delta L = 2$. Neutrinoless double beta decay would be proof that neutrinos are Majorana particles implying a neutrino is its own antiparticle.

   Neutrinos are too difficult to detect to use as an indication of rare types of decays. Instead, experiments search for signs of neutrinoless double beta decay in the energy spectrum of the electrons, which is easily observable. Neutrino emission will result in a continuous energy spectrum while a neutrinoless double beta decay will result in a discreet peak at the end point of the energy spectrum equal to the total energy of the decay. This is a result of the full energy of the decay being imparted to the electrons. There are currently experiments or proposals to look for the following decays:

$$0\nu\beta\beta \text{ searches} \begin{cases} ^{48}\text{Ca} \rightarrow\,^{48}\text{Ti} + 2e^- \\ ^{76}\text{Ge} \rightarrow\,^{76}\text{Se} + 2e^- \\ ^{100}\text{Mo} \rightarrow\,^{100}\text{Ru} + 2e^- \\ ^{136}\text{Xe} \rightarrow\,^{136}\text{Ba} + 2e^- \\ ^{150}\text{Nd} \rightarrow\,^{150}\text{Sm} + 2e^- \end{cases} \tag{1.101}$$

The decay rate of $0\nu\beta\beta$ is related to the nuclear matrix element and an effective neutrino

mass [42].

$$\Gamma^{0\nu\beta\beta} = \frac{1}{T_{1/2}^{0\nu\beta\beta}} = \frac{G^{0\nu}}{m_e^2}|M^{0\nu}|^2\langle m_\nu\rangle^2 \qquad (1.102)$$

where $G^{0\nu}/m_e^2$ is a phase space factor. The Majorana neutrino mass is greater than or equal to

$$\langle m_\nu\rangle = \sum_i m_i U_{ei}^2 = m_1 U_{e1}^2 + m_1 U_{e3} + m_1 U_{e3} \qquad (1.103)$$

where the elements of U include the Majorana phases. The nuclear matrix element is

$$M^{0\nu} = M_{GT}^{0\nu} + (\frac{g_V}{g_A})^2 M_F^{0\nu} \qquad (1.104)$$

where $M_{GT}^{0\nu}$ is the Gamow-Teller contribution, $M_F^{0\nu}$ is the Fermi contribution, and g_V and g_A are the vector and axial vector form factors. The largest uncertainty comes from the nuclear matrix element $|M^{0\nu}|$ which is difficult to compute. The matrix is most often calculated using the nuclear shell model or quasiparticle random phase approximation.

1.8   Oscillation Results

Data from all the neutrino measurements can be used to find best-fit values for the oscillation parameters which include the squares of the mass differences and the mixing angles. It turns out that solar neutrinos with energies below $11\,\mathrm{MeV}$ and a baseline of about $10^{11}\,\mathrm{m}$ are a good probe of Δm_{12}^2 and θ_{12}. Atmospheric neutrinos with higher energies and shorter baseline are useful for looking at Δm_{23}^2 and θ_{23}. The fits for solar neutrino mixing parameters are shown in Figure 1.18.

The results from all experiments are summarized in Figure 1.19. Currently the LSND experiment is in conflict with the other data. If confirmed it will indicate the existence of a sterile neutrino.

Values for Δm^2 and $\sin^2 2\theta$ are presented in Table 1.11.
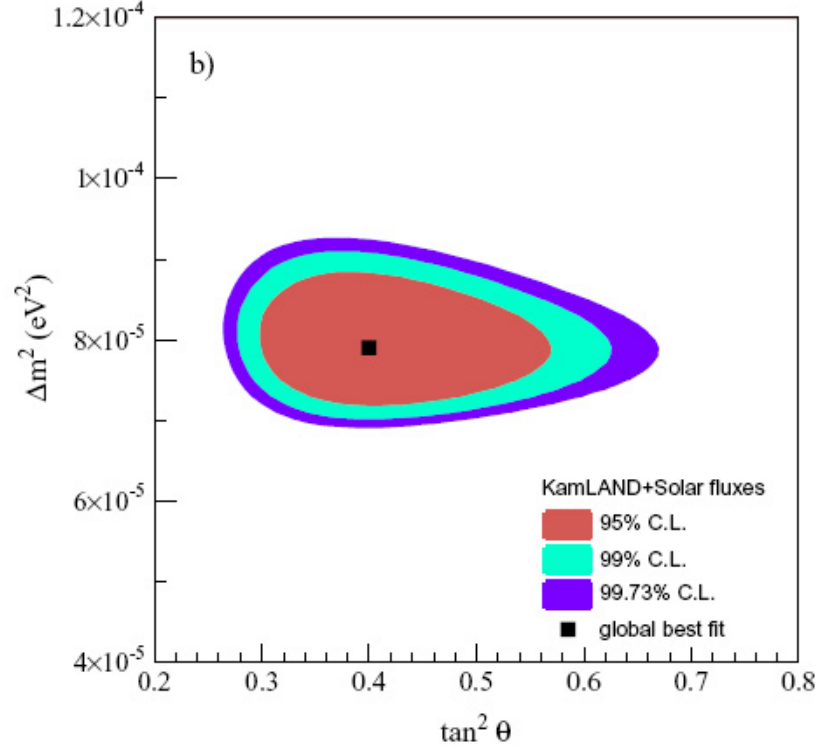
Figure 1.18: The constraints on neutrino mass and mixing parameters for Δm_{12}^2 and θ_{12} from solar and KamLAND data. The best fit point is $\Delta m_{12}^2 = (7.9 \pm 0.6) \times 10^{-5}\,\mathrm{eV}^2$ and $\tan^2\theta_{12} = 0.40 \pm 0.10$ [39].

1.9 Open Questions

In the last decade, neutrino experiments have rapidly improved our basic understanding of the neutrinos. However, there are currently several neutrino properties that are either poorly constrained or unknown. These include:

1) The value of θ_{13} which governs the amplitude of mixing between the electron and tau neutrino states. This angle is known to be small and possibly zero. Experiments have shown $\sin\theta_{13} < 0.05$ which means $\theta_{13} < 10°$. An improved limit on θ_{13} will be achieved with reactor experiments with km scale baselines and accelerator experiments with $100\,\mathrm{km}$ or longer baselines.

$i, j =$	12	23	13
$\Delta m_{ij}^2 [\text{eV}^2]$	$(8.2 \pm 0.4) \times 10^{-5}$	-	$(2.6 \pm 0.4) \times 10^{-3}$
$\sin^2 2\theta_{ij}$	0.8	0.96	<0.05

Table 1.11: Current limits on neutrino oscillation parameters.

2) The mass ordering or hierarchy problem. Are the mass eigenstates ordered $m_1 < m_2 < m_3$ in the normal hierarchy or is the hierarchy inverted. Equivalently, the mass ordering is a question of whether there is a normal hierarchy with $\Delta m_{23}^2 > 0$ or an inverted hierarchy with $\Delta m_{23}^2 < 0$. This is illustrated in Figure 1.20. The absolute scale of neutrino mass is also unknown. There are upper bounds on the mass from beta endpoint measurement and cosmological data but no direct mass measurements to date. Double beta decay experiments will address this question.

3) ^{7}Be solar neutrinos must exist according to the solar standard model which is widely believed to be valid. However, the ^{7}Be line has yet to be directly measured. If the high energy flux from Super-K and SNO is subtracted from the integrated measurements of SAGE, GALLEX, and GNO, the remainder is accounted for entirely by the *pp* flux. There seems to be none left over for ^{7}Be. Real time measurements of the low energy *pp* neutrinos are also lacking. There is a relationship between the luminosity of the sun and neutrino flux that can be checked once all the solar neutrino fluxes are measured. The total light output must be the sum of the energy output from the fusion reactions which the neutrino spectrum reveals.

4) Are neutrinos Majorana or Dirac in nature? This will determined if the neutrino is its own antiparticle. An observation of neutrinoless double beta decay will definitively show that neutrinos are Majorana particles.

5) The LSND result is currently inconsistent with other neutrino measurements unless neutrinos oscillate into a sterile non-interacting flavor. The MiniBooNE experiment will verify or refute this result.

There are a number of experiments that have been proposed to further study neutrinos.

The next generation of neutrino and dark matter detectors will utilize cryogenic noble gases. Some of the gases (and experiments) being proposed are Helium (Heron), Neon (CLEAN), Argon (ICARUS), and Xenon (XMASS). Noble gases are advantageous because they are easily purified. Since noble gases are the least reactive elements, impurities are easily filtered out on charcoal traps or frozen out when the liquid is cooled. These experiments are designed to make real time measurements of the solar pp neutrino flux.

To achieve higher neutrino fluxes there is a plan to build a neutrino super-beam. This would be based on a mega-Watt class proton driver that would be used to produce an intense neutrino beam. Detectors at long and short baselines would be placed in the path of the beam permitting precision flux measurements.

Precision flux measurements on the order of 1% are now required to place tighter limits on oscillation parameters and constrain theories. It is with these measurements that the next generation of neutrino experiments will answer these questions and guide future research. A discussion of the physics that was learned from the Borexino experiment is given in section 2.3.
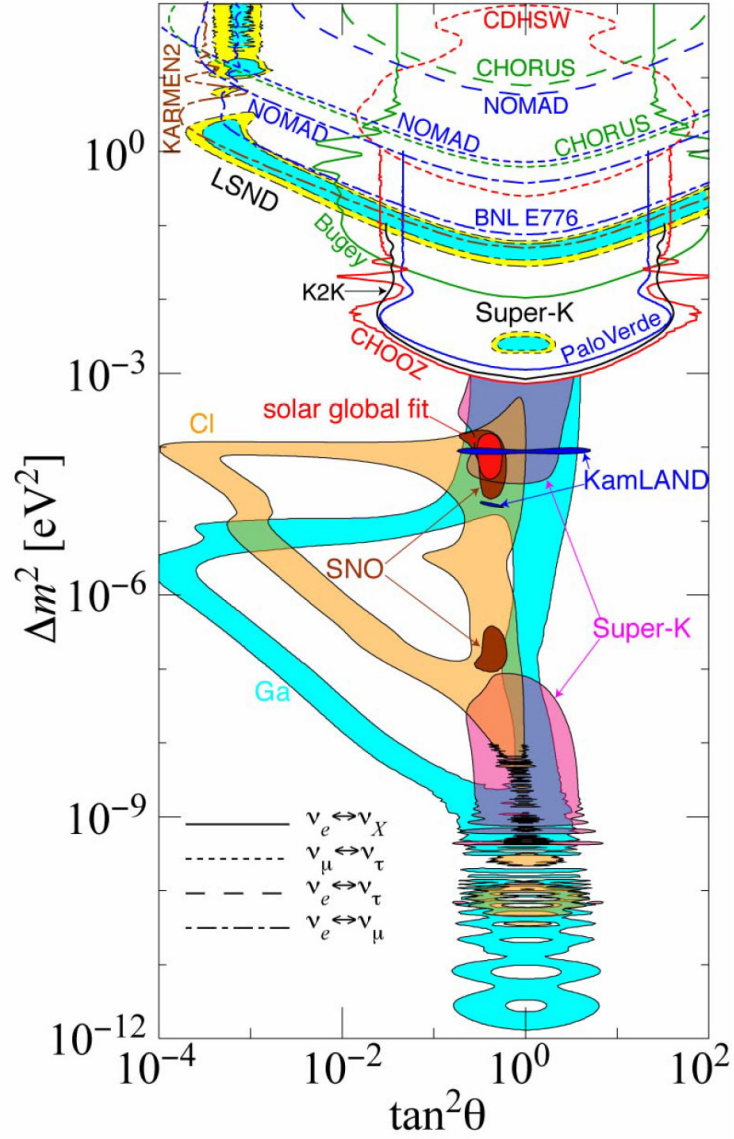
Figure 1.19: This plot by H. Murayama shows the allowed regions of Δm^2 and $\tan^2\theta$. The shaded sections mark allowed regions at the 90% confidence level. This summarizes the best estimates of the neutrino parameters from all neutrino experiments. The x-axis is plotted in $\tan^2\theta$ in order to show the full range of $0 < \theta < 90$ [14].
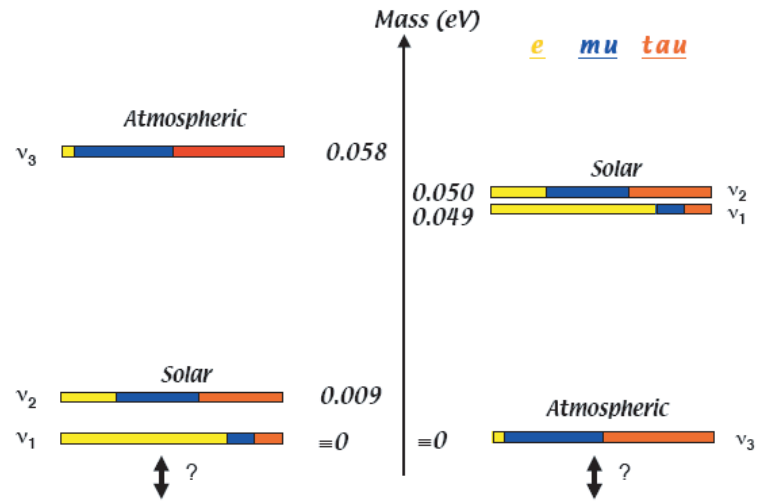
Figure 1.20: There are two possibilities for the arrangement of neutrino mass. The normal hierarchy is shown on the left and the inverted hierarchy is shown on the right. In addition to not knowing the ordering of the masses the zero of the scale is not known either [43].

Borexino Experiment

The Borexino Experiment is designed to measure the monoenergetic ^{7}Be solar neutrino line[1]. These 862keV neutrinos, which are produced when a beryllium nucleus captures an electron, travel radially outward from the sun in all directions. At earth the predicted flux from ^{7}Be neutrinos is $4.86 \times 10^9/\text{cm}^2/\text{s}$. At earth the survival probability is 66% for the ^{7}Be neutrinos. According to the current best fits to oscillation parameters, there will be 35 electron-neutrino scattering events per day from ^{7}Be in the Borexino detector fiducial volume of 100 tons.

Borexino will detect neutrino interactions inside 100 tons of liquid scintillator that converts the energy deposited by the neutrinos into light. The perimeter of the detector is instrumented with photomultiplier tubes (PMTs) that can measure the intensity and arrival time of this light. From this information the energy, position, and time of the events within the detector can be reconstructed. While the energy and rate of the neutrino events is the most physically interesting information, the position of the events ensures that the detector background is well understood. Neutrino events should be uniformly distributed over the volume of the detector while many types of background events such as radioactivity from materials or surfaces can be identified by their spatial distribution.

---

[1]The name Borexino was originally conceived in 1987, when the project was going to measure ^{8}B solar neutrinos with a ^{11}B target in the form of trimethylborate($C_3H_9BO_3$). The proposal evolved to instead measure the more intense ^{7}Be neutrino line with pseudocumene, but the name remained.

With a sufficient number of events, the neutrino energy spectrum and the neutrino flux can be determined. Essentially all the physics of the Borexino experiment is found from the characteristics of these two quantities.

The energy spectrum produced from electrons scattered by monoenergetic neutrinos will be almost flat up until the maximum recoil energy. This sharp cutoff is a distinctive feature of a monoenergetic neutrino source. Some backgrounds can be identified and rejected due to features in their energy spectra.

Two temporal changes in the neutrino flux are indicative of a successful neutrino oscillation measurement. The first will be a sinusoidal signal with a period of one year due to the eccentricity of the earth's orbit around the sun. The change in earth-sun distance will modulate the flux due to the $1/r^2$ dependence. The second signal, if present, will be another time varying rate with a period of one solar day due to the MSW effect because neutrinos have to pass through the earth at night. These two periodic patterns will be distinct from backgrounds in the detector.

The Borexino detector is primarily sensitive to electron neutrinos. It is able to observe muon and tau neutrinos as well, but with a sensitivity reduced by about a factor of five. If the electron neutrinos produced by the sun change into muon or tau neutrinos they will be mostly missed by the detector resulting in a lower rate.

Borexino will observe neutrino events in an energy window from 250-800 keV. To clearly see the neutrino signal, the number of background events in this window should be low compared to the neutrino interaction rate. Background events arise from many sources both internal and external to the detector. The most significant background is from radioactive elements that decay in the scintillator, producing energetic particles which mimic neutrino events in the detector. There are several methods through which certain types of non-neutrino events can be identified and rejected. However, extremely low background levels are ultimately required for a successful measurement to be made. If not carefully controlled, the background event rate will exceed the neutrino rate by many orders of magnitude. In order to achieve such strong suppression of background the Borexino detector is heavily shielded and the components are carefully selected for their high radiopurity. In addition

all the parts are meticulously cleaned. Details on backgrounds can be found in Chapter 3.

2.1 ^{7}Be Neutrinos

The primary goal of Borexino is to extract information about neutrino oscillation parameters and probe the fusion process in the sun. Borexino will measure the monoenergetic 862 keV ^{7}Be solar neutrino line. There is also a second ^{7}Be line at 383 keV with roughly a tenth of the intensity. The ^{7}Be neutrinos are the second most intense flux after that of the primary pp fusion reaction. The fusion reaction that produces the ^{7}Be neutrinos is

$$^7\text{Be} + e^- \rightarrow ^7\text{Li} + \nu_e \tag{2.1}$$

which is a two body electron capture reaction. This reaction occurs 90% of the time. The capture to an excited state of lithium occurs 10% of the time where a 477.6 keV gamma is emitted.

$$^7\text{Be} + e^- \rightarrow ^7\text{Li} + \nu_e + \gamma \tag{2.2}$$

However, this gamma is absorbed in the sun and not seen by the detector. The rate of the electron capture reaction on ^{7}Be in the sun is

$$R(^4\text{Be} + e^-) = 5.6 \times 10^{-9} \frac{\rho}{\mu_e} T_6^{-1/2} \times [1 + (0.004 T_6 - 16)] \ \text{s}^{-1} \tag{2.3}$$

where $\mu_e = 5 \times 10^{-4}$ amu is the electron mean molecular weight and T_6 is the temperature in units of 10^6 K, and ρ is a density [44]. The decay scheme of ^{7}Be is shown in Figure 2.1.

The width of the ^{7}Be neutrino lines is a few keV is due to thermal effects like Doppler broadening from ^{7}Li nuclei, the thermal energy of the electron and ^{7}Be nuclei at capture, and the ionization of the ^{7}Be in the sun [45]. There is a predicted energy shift of 1.29 keV which depends on the core temperature of the sun. Conservation of energy implies that

$$E_i - E_f = \Delta M + K(e) + K(^7\text{Be}) - K(^7\text{Li}) + a(^7\text{Be}) - a(^7\text{Li}) - E_\nu \tag{2.4}$$

where E_i and E_f are the energies in the initial and final states, $K(e)$ and $K(^7\text{Be})$ are the kinetic energies of the electron and ^{7}Be nucleus before the collision, $K(^7\text{Li})$ is the energy
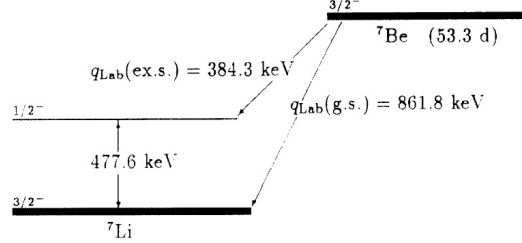
Figure 2.1: The ^{7}Be decay scheme. 10.3% of the decays are to the excited state and 89.7% of the decays go to the ground state.

of the recoiling ^{7}Li nucleus, E_ν is the neutrino energy, and a refers to the atomic binding energies of the particles. The difference in the nuclear rest mass energies ΔM is

$$\Delta M = m_e + M(^7\text{Be}) - M(^7\text{Li}) = 862.10 \,\text{keV} \tag{2.5}$$

The neutrino energy is evaluated for solar decays to produce the line shapes shown in Figure 2.2 and Figure 2.3.

The ^{7}Be reaction occurs in the core of the sun at less than 0.3 of a solar radius. This corresponds to a region with a radius of $\sim 2 \times 10^6$ km. Comparing this region where neutrinos are produced in the sun to the vacuum oscillation length of 26 km for the 862 keV line and 11.5 km for 384 keV line, we see that the solar production region is much greater than an oscillation wavelength. Production is incoherent over a region much larger than a wavelength so vacuum oscillations due to differences in path length cannot be observed. The flux that is measured is the average of the vacuum oscillations.

2.2 Day/Night and Seasonal Variations

There will be a seasonal variations of the neutrino flux due to the change of the radius of earth's orbit around the sun. The orbit of earth can be described by an ellipse

$$r = \frac{r_0}{1 + \epsilon \cos\theta} \tag{2.6}$$
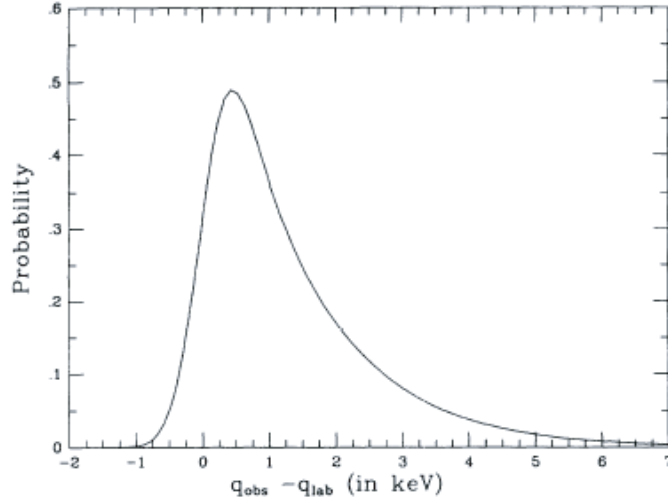
Figure 2.2: The shape of the $862\,\text{keV}$ ^{7}Be neutrino line. The solar neutrino has a peak in the distribution at $q_{peak} = 862.27\,\text{keV}$. The laboratory decay peaks at $q_{lab} = 861.84\,\text{keV}$.

where r is the distance of earth from the sun, $r_0 = 1.496 \times 10^{11}\,\text{m}$ is the average earth-sun distance, and the orbit eccentricity $\epsilon = 0.0167$. The maximum radius of earth's orbit is $1.52 \times 10^{11}\,\text{m}$ and the minimum radius is $1.47 \times 10^{11}\,\text{m}$ with a total variation of about 3% in radius. The maximum difference in path length is $5 \times 10^9\,\text{m}$ [46]. This distance is much greater than the ^{7}Be oscillation length, however, any oscillatory signal is already lost due to the large production region in the sun. The expected Borexino signal from seasonal variations is shown in Figure 2.4.

The change in the neutrino signal over a day is given by the asymmetry parameter

$$A = \frac{D - N}{D + N} \tag{2.7}$$

where D is the daytime flux and N is the flux at night. At night a neutrino has to pass through earth which has a radius of $6.371 \times 10^6\,\text{m}$. The asymmetry would result from ν_e regeneration in earth due to the MSW effect. The MSW effect is expected to be small because the energy of the ^{7}Be neutrinos is below the critical energy of $2.2\,\text{MeV}$. In this
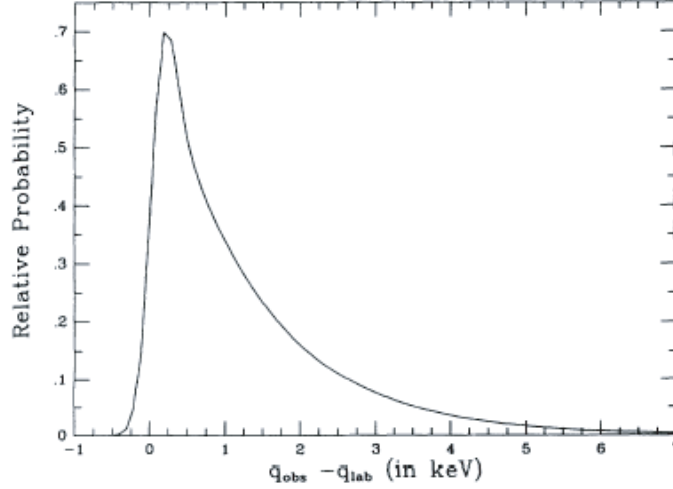
Figure 2.3: The shape of the 384 keV ^{7}Be neutrino line. The solar neutrino has a peak in the distribution at $q_{peak} = 384.47$ keV. The laboratory decay peaks at $q_{lab} = 384.28$ keV.

regime vacuum averaging effects dominate and the survival probability is

$$P_{ee}(^7\text{Be}) = \cos^4 \theta_{13}(1 - \frac{1}{2} \sin^2 2\theta_{12}) \approx \frac{2}{3}. \tag{2.8}$$

2.3 Physics Potential

There has yet to be a direct precision real time measurement of the ^{7}Be solar neutrinos. At present there are low energy measurements of the integrated solar neutrino flux from chemical experiments. They have little timing resolution and no energy resolution above threshold. Measurements of higher energy solar neutrinos such as ^{8}B have been made with Cherenkov detectors such as SNO and SuperK where the background is low due to the higher energies and ability to image rings. A sub-MeV real time solar neutrino experiment has yet to be carried out.

Current experiments provide a poor constraint on the ^{7}Be neutrino flux which is about $\pm 40\%$ at 1σ [26]. If Borexino makes a 10% measurement of the ^{7}Be neutrino flux it will
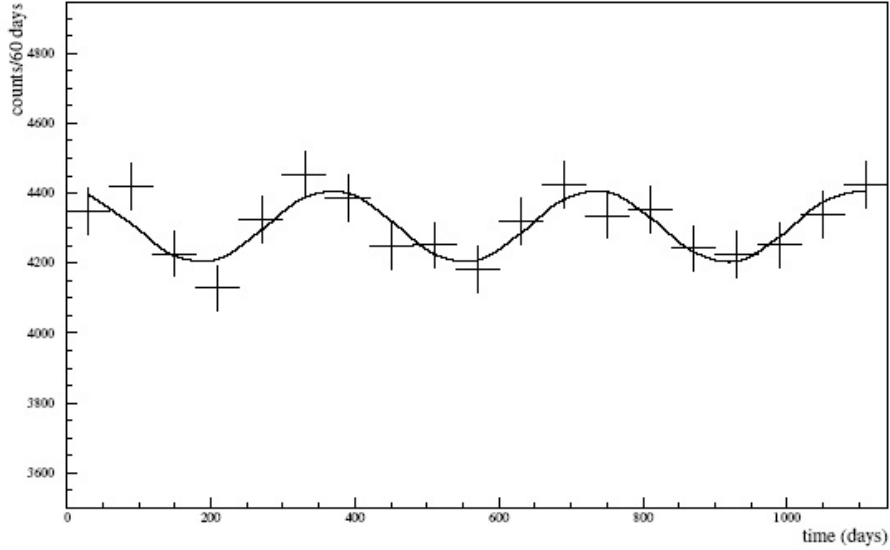
Figure 2.4: The seasonal variation expected in the ^{7}Be neutrino flux. Simulated data is binned in 60 day periods. The variation is due solely to the $1/r^2$ effect from the change in the radius of earth's orbit. Changes in flux due to vacuum oscillations are not observed when the orbit radius changes because the ^{7}Be production region in the sun is greater than an oscillation length. However vacuum oscillations will result in a constant overall reduction in the flux intensity. Figure from [47].

provide a factor of four improvement and improve the *pp* flux uncertainty by a factor of 2.5 due to the luminosity constraint. A 3% measurement will provide another factor of two improvement in the uncertainties. For Borexino to make a 10% measurement it will need about 3 years of data.

The theoretical uncertainty in flux of ^{7}Be neutrinos is currently 10%. There are tighter limits on the *pp* and *pep* solar neutrino fluxes which are uncertain to 1% and 2% respectively. A direct measurement of the ^{7}Be flux at the 3% level will provide a much tighter constraint.

Solar neutrinos give real time information about the fusion process in the core of the sun as neutrinos can exit the sun quickly without significant scattering. By contrast a photon in the core of the sun scatters repeatedly and takes about 10^6 years to reach the surface. However, if the sun is stable over this time scale then the solar luminosity is directly related

to the sum of the neutrino fluxes. In this circumstance, the luminosity constraint provides a prediction of the total number of solar neutrinos that are expected.

$$\frac{L_\odot}{4\pi(\text{AU})^2} = \sum_i \alpha_i \Phi_i \tag{2.9}$$

where $L_\odot$ is the solar luminosity at earth, 1 AU is the average earth sun distance, and α_i is the energy from the fusion reaction producing neutrino flux Φ_i [48]. Currently measurements indicate that the *pp* flux provides all the neutrinos required by the luminosity constraint and the ^{7}Be neutrinos are unnecessary. This was one of the main motivations for the Borexino experiment. Solar neutrino predictions and flux measurements are compared in Figure 2.5. If the solar luminosity does not match the neutrino flux this will indicate the sun is evolving over million year time scales.
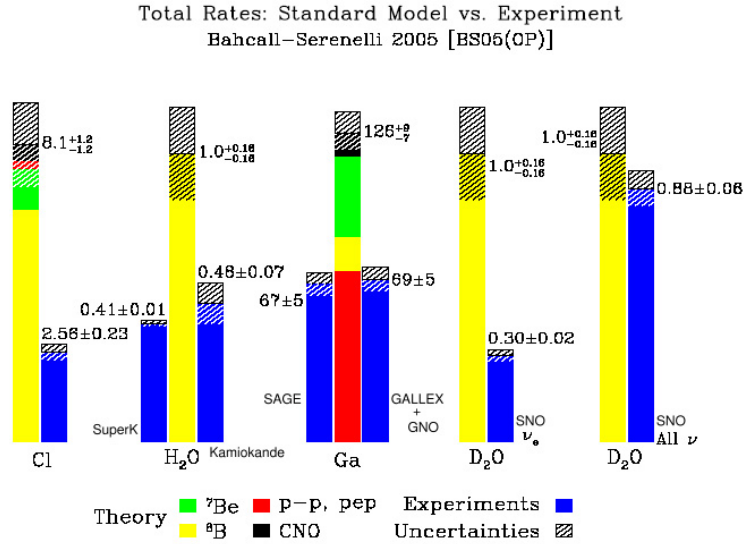
Figure 2.5: A comparison of the theoretical neutrino fluxes and measurements. Fluxes were calculated from the standard solar model and standard model of electroweak interactions. Experiments until SNO all measured a deficit of solar electron neutrinos. SNO showed all the solar neutrinos were accounted for by measuring all three flavors. The gallium measurements from SAGE, GALLEX, and GNO all show a deficit of solar neutrinos. Their result is entirely accounted for by the predicted *pp* flux which has a small uncertainty [49].

Borexino will also measure the CNO neutrinos and the pep neutrinos if backgrounds in

an extended higher energy window from 1-3 MeV are sufficiently low. These neutrinos have higher energies than the ^{7}Be neutrinos but a lower overall flux. The main background in this region is from the decay of ^{11}C which is produced by cosmogenic muons interacting with ^{12}C in the scintillator. It has been shown that this background can be tagged and subtracted by observing a triple coincidence from the cosmic muon, neutron capture, and ^{11}C decay [50, 51]. The production reaction is

$$\mu + ^{12}\text{C} \rightarrow ^{11}\text{C} + n \tag{2.10}$$

with a number of secondary particles produced as well. The neutron is captured on a hydrogen atom after $\sim 250\,\mu$s in pseudocumene releasing a γ with 2.2 MeV.

$$n + ^1_1\text{H} \rightarrow ^2_1\text{D} + \gamma \tag{2.11}$$

^{11}C is a positron emitter with a half life of 29.4 min and an endpoint energy of 0.96 MeV.

$$^{11}\text{C} \rightarrow ^{11}\text{B} + e^+ + \nu_e \tag{2.12}$$

The positron annihilates an electron in the scintillator releasing 1.02-1.98 MeV.

Pep solar neutrinos have energies up to 1.42 MeV though the total flux is 35 times less than that of the ^{7}Be neutrinos. These should be observable in Borexino in an extended high energy window up to 1.3 MeV. The *pep* neutrinos are interesting because their measurement will tightly constrain the primary *pp* flux. The two are directly related by the ratio of their cross sections. The *pp* neutrinos which are the lowest energy and most intense component of the solar flux have yet to be measured by a precision real time experiment. The energy of the *pp* neutrinos is two low for Borexino to measure directly as it is hidden under the intrinsic ^{14}C background from the scintillator.

CNO neutrinos are produced during the carbon, nitrogen, oxygen cycle. During this cycle ^{13}C emits a neutrino with an endpoint energy of 1.20 MeV and the ^{15}N neutrino has an endpoint energy of 1.74 MeV. These will also be visible to Borexino with the ^{11}C background subtraction.

Borexino will also be able to determine if the expected vacuum-matter transition takes place. Current real time measurements of high energy neutrinos from SuperK and SNO

are all in the MSW dominated ($\beta > 1$) region. The ^{7}Be neutrinos measured by Borexino are expected to be in the vacuum averaged ($\beta < \cos 2\theta_{12}$) region. This would give them a higher survival probability than the higher enery solar neutrinos. Thus Borexino can test a fundamental prediction of MSW oscillation theory.

Borexino will also have the potential to detect neutrinos from other sources besides the sun. These include supernova neutrinos, geoneutrinos, and neutrinos from radioactive sources. They are described below.

A type II supernova produces about 10^{46} J of energy. Roughly 99% of the energy is carried away by $\sim 10^{57}$ neutrinos released over $\sim$10 seconds when the star collapses. If a supernova appears in our galaxy the neutrinos will be visible in detectors on earth. Neutrinos from supernova will reach earth hours before light does because the supernova is transparent to neutrinos much sooner than it is for photons. Thus the identification of supernova neutrinos can be used as an early warning system to alert astronomers that a collapse took place and tell them where to look [52]. Supernova SN1987A had about 20 neutrino events that were observed by two detectors. Borexino will be incorporated in a network of neutrino detectors used to observe supernova [53]. A supernova at 10 kpc will result in 110 events in Borexino. A Parsec is equal to 3.08×10^{16} m or 3.26 light years.

Geoneutrinos are produced by radioactive elements in earth. The sources of these antineutrino are primarily the ^{238}U and ^{232}Th chains, and ^{40}K [54]. Their measurement will help determine what percent of earth's heat (which is between 30-40 TW) is generated from radioactive decays. It will also provide information about the chemical composition of the whole earth which is otherwise inaccessible. Geochemical analysis is limited by the deepest hole which is about 10 km and only penetrates the crust, and seismology only provides information about the earth's density. The heat output of earth and the neutrino luminosity are related by the total mass of the radioactive elements.

$$H_R = 9.5M(\text{U}) + 2.7M(\text{Th}) + 3.6M(^{40}\text{K}) \tag{2.13}$$

$$L_\nu = 7.4M(\text{U}) + 1.6M(\text{Th}) + 27M(^{40}\text{K}) \tag{2.14}$$

where H_R is the total heat output in [TW], M is the mass in [10^{17} kg], and L_ν is the total

neutrinos flux in $[10^{24}\,\bar{\nu}_e/\text{s}]$. Estimates put the geoneutrino flux at about $4 \times 10^6\,\bar{\nu}_e/\text{cm}^2/\text{s}$. Borexino expects to observe about 10-30 geoneutrinos per year at energies up to $3.3\,\text{MeV}$ [55]. Borexino also expects to observe about 10 antineutrinos per year from nuclear reactors in Europe.

A possible neutrino magnetic moment can be probed by Borexino with a strong radioactive source. The two most promising sources are ^{51}Cr for neutrinos and ^{90}Sr for antineutrinos. A $10^{16}\,\text{Bq}$ source placed under the detector will provide sensitivities of $\mu_{\nu_e} \sim 10^{-11}\mu_B$.

A precision flux measurement will also allow Borexino to test new theories about neutrino mass. Mass Varying Neutrinos (MaVaNs) [13, 56] have been proposed to explain the currently similar densities of cold dark matter and dark energy. $\frac{\rho_{CDM}}{\rho_\Lambda} = \frac{1}{3}$ despite the ratio's $1/a^3$ dependence on the cosmic scale factor which would cause the densities vary dramatically over the life of the universe. MaVaNs couple to a scalar field call the acceleron and the MaVaN mass is a function of the local neutrino density. This allowing the neutrino density ρ_ν to track the dark energy density ρ_Λ to within 10^3 over the history of the universe. MaVaNs would aslo modify the solar neutrino survival probability as shown in Figure 2.6. This would be detectible by Borexino as an enhanced day night signal.
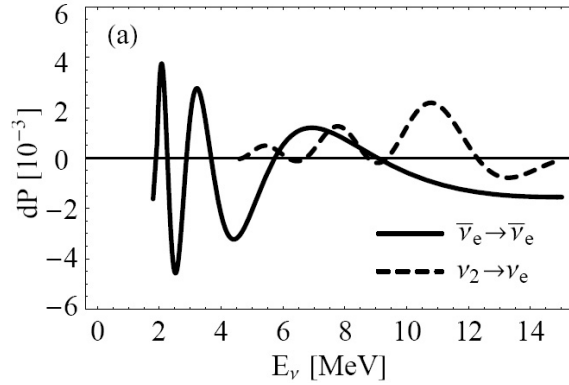
Figure 2.6: Mass Varying Neutrinos or MaVaNs would modify the solar neutrino survival probability. The difference in survival probibility of MaVaNs from the standard model $dP = P_{SM} - P_{MaVaN}$ is plotted versus neutrino energy. Solar neutrinos reach earth in a mostly ν_2 mass eigenstate shown by the dashed line. MaVaNs would enhance regeneration in earth giving a larger day/dight effect than the standard model [56].

2.4   Detector Description

The Borexino detector in located underneath the Gran Sasso Mountains in Italy. It is in one of three excavated experimental caverns in the Laboratori Nazionali del Gran Sasso (LNGS) or Gran Sasso National Laboratory shown in Figure 2.7. The LNGS is one of four labs managed by the Istituto Nazionale di Fisica Nucleare (INFN) or National Institute of Nuclear Physics. Though the laboratory is located almost a kilometer above sea level it is still shielded by the tallest peak in the Apennines, having a rock overburden of 1400 m. This corresponds to 3800 meters water equivalent (mwe) which significantly reduces the cosmic ray flux. The Gran Sasso rock has a density of $2.71\,\mathrm{g/cm^3}$ with a mean nuclear charge Z equal to 9.4. The underground labs are accessed through an exit off a 10 km freeway tunnel that runs from Teramo to L'Aquila. The geographic coordinates of LNGS are latitude 13°34'30.0", longitude 42°27'10.0", elevation 936.45 m over sea level [57]. The Borexino detector and Counting Test Facility are shown in Figure 2.8.

Borexino will observe electron recoils from neutrino interactions. The differential scattering cross section of electron neutrinos off electrons is

$$\frac{d\sigma}{dT_e} = \frac{m_e G_F}{2\pi}[(g_V + g_A)^2 + (g_V - g_A)^2(1 - \frac{T_e}{E_\nu})^2 + (g_A^2 - g_V^2)\frac{m_e T_e}{E_\nu^2}] \tag{2.15}$$

where G_F is the Fermi coupling constant, E_ν is the incoming neutrino energy, T_e is the electron recoil energy, m_e is the electron mass, and θ_W is the Weinberg angle.

$$\sin^2\theta_W = 0.2317 \tag{2.16}$$

The vector and axial vector couplings are

$$(\nu_e, e) \quad g_V = (2\sin^2\theta_W + \tfrac{1}{2}) \quad g_A = +\frac{1}{2} \tag{2.17}$$

$$(\nu_{\mu,\tau}, e) \quad g_V = (2\sin^2\theta_W - \tfrac{1}{2}) \quad g_A = -\frac{1}{2} \tag{2.18}$$

The maximum kinetic energy of the recoil electron that occurs when the scattering angle $\theta = 0$ with respect to the incoming neutrino is

$$T_{max} = \frac{E_\nu}{1 + m_e/2E_\nu}. \tag{2.19}$$
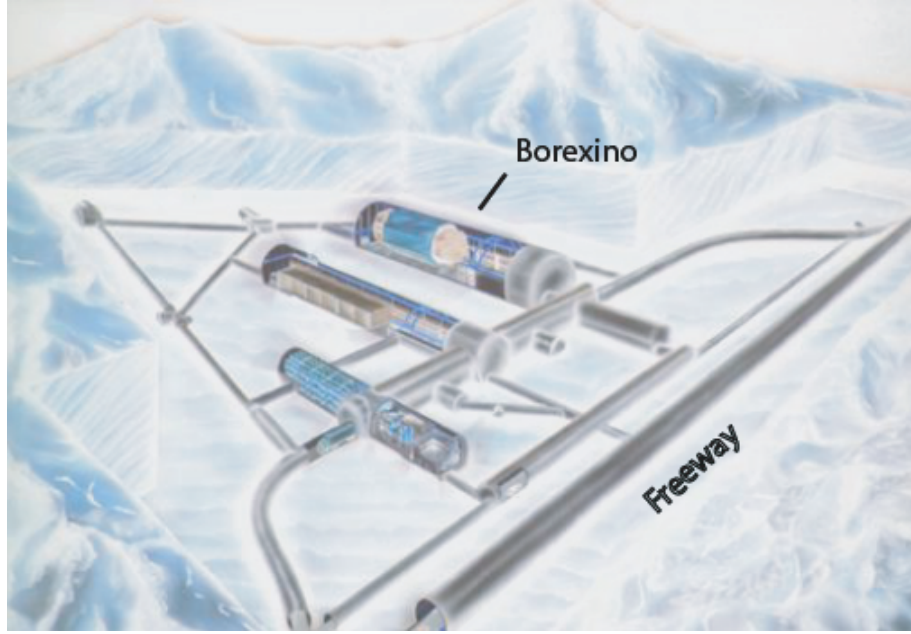
Figure 2.7: The underground experimental halls at the Gran Sasso National Laboratory (LNGS) in Italy. Borexino is located in Hall C which it shares with the OPERA experiment. Lab access is through a 10 km freeway tunnel which has a special entrance and exit for the labs.

For the ^{7}Be neutrinos with an energy $E_\nu = 862$ keV we find the maximum electron recoil energy $T_{max} = 665$ keV.

The neutrino event rate is determined by the flux of neutrinos and the number of target atoms. The theoretically predicted ν_e flux from ^{7}Be is $\phi_{Be} = (4.86 \pm 0.12) \times 10^9$cm^{-2}s^{-1} [29]. The cross section for a (ν_e, e) interaction with $E_\nu = 862$ keV is $\sigma = 5.79 \times 10^{-45}$ cm^2. Borexino will have a 100 ton fiducial volume containing $N_e = 3.31 \times 10^{31}$ electrons, 6.03×10^{30} protons, and 4.53×10^{30} ^{12}C nuclei.

$$\text{Event rate} = \phi \sigma N_e = 1.7 \times 10^{-4}\,\text{s}^{-1} = 80/\text{day} \qquad (2.20)$$

Some of these will fall below the energy window of 250-800 keV. The total event rate in the Borexino energy window with no oscillations is 50 events/day. With the current values of
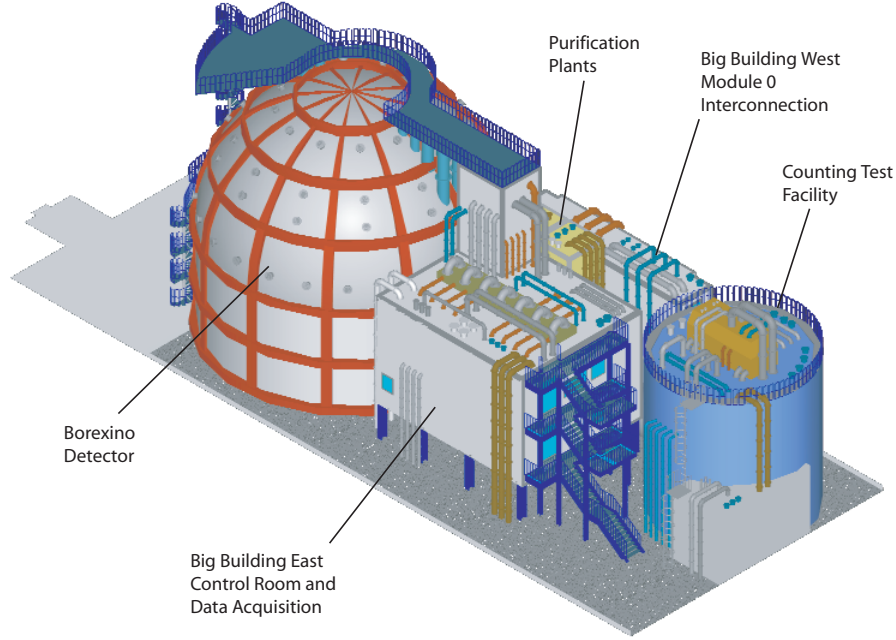
Figure 2.8: The layout of the Borexino experiment in Hall C of the Gran Sasso National Laboratory. Borexino detector is the large dome shown on the left. The Counting Test Facility housed in the blue cylindrical structure is shown on the right.

the neutrino oscillation parameters, Borexino will observe 66% of the expected neutrinos or 35 events per day from ^{7}Be. The resulting spectrum is shown in Figure 2.9. Cross sections for other solar neutrinos are shown in Table 2.4.

The vacuum oscillation length for ^{7}Be neutrinos is 26 km for the 862 keV line and 11.5 km for the 384 keV line. The production region in the sun where the ^{7}Be reaction takes place is much larger than the oscillation length of the neutrinos. The oscillations are thus out of phase with each other and cannot be distinctly observed by changing the path length. The Borexino detector will instead measure the solar electron neutrino flux averaging over oscillations to other flavors. These vacuum averaged oscillations result in 66% of the original electron neutrino flux for ^{7}Be neutrinos.

Borexino will not retain directional information from Cherenkov radiation. The velocity

Source	E_ν	T_e	$\sigma(\nu_e, e)$	$\sigma(\nu_\mu, e)$
	[keV]	[keV]	$[10^{-46}\,\mathrm{cm}^2]$	$[10^{-46}\,\mathrm{cm}^2]$
pp	≤ 420	261	11.6	3.28
^{7}Be	862	665	57.9	12.8
^{7}Be	384	231	19.2	5.08
^{8}B	≤ 15000	14500	594	106

Table 2.1: The total cross sections for neutrino-electron scattering from solar neutrinos. E_ν is the neutrino energy, T_e is the maximum electron recoil energy, and $\sigma(\nu_e, e)$ and $\sigma(\nu_\mu, e)$ are the cross sections for electron-neutrino and muon-neutrino scattering respectively [58].

threshold required to produce Cherenkov light is

$$v > c/n \tag{2.21}$$

where v is the velocity of the particle, $c = 3 \times 10^8\,\mathrm{m/s}$ is the speed of light in vacuum, and n is the index of refraction. For the scintillator in Borexino $n = 1.505$. A more useful form of the Cherenkov condition is

$$\gamma > \frac{n}{\sqrt{n^2 - 1}} \tag{2.22}$$

where $\gamma = \frac{1}{\sqrt{1 - \frac{v^2}{c^2}}}$ is the ratio of a particle's total energy to its rest mass. For the Borexino scintillator γ must be greater than 1.338 for Cherenkov production to occur. For electrons with energies between 250-800 keV, γ ranges from 1.49-2.3. Thus all recoil electrons in the Borexino energy window will produce Cherenkov radiation. The number of Cherenkov photons emitted per length is determined by

$$\frac{dN}{dl} = 2\pi\alpha \left[1 - \frac{1}{n^2 \beta^2} \right] \int \frac{d\lambda}{\lambda^2} \tag{2.23}$$

where N is the number of photons, λ is the wavelength of light, $\beta = v/c$, the fine structure constant $\alpha = e^2/\hbar c \approx 1/137$, and l is the path length of the electron. The integral is over the wavelengths that the PMTs are sensitive to. The total number of photons emitted is

$$N = 2\pi\alpha l \left(\frac{1}{\lambda_2} - \frac{1}{\lambda_1} \right) \left(1 - \frac{1}{\beta^2 n^2} \right) \tag{2.24}$$

Borexino spectrum after Neutrino 2004
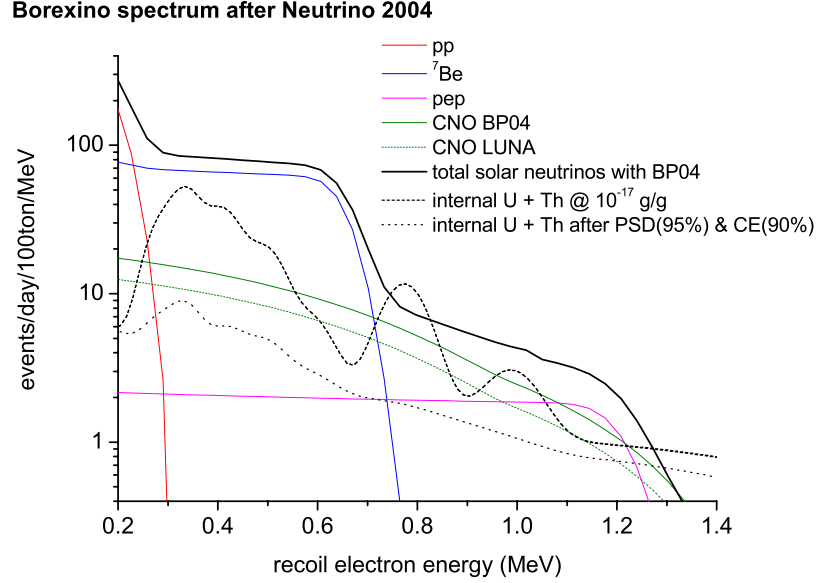
Figure 2.9: The expected electron recoil spectrum in Borexino from solar neutrinos is shown by the solid black line. The ^{7}Be electron recoil spectrum shown in blue drops off sharply at about $700\,\mathrm{keV}$. This prominant feature helps distinguish ^{7}Be neutrinos from background. The expected background from the uranium and thorium chains before and after cuts are made are shown by the dashed black lines for comparison.

where λ_1 and λ_2 bound the wavelengths of interest [59]. In Borexino the ultraviolet Cherenkov emission will be absorbed by the scintillator and reemitted isotropically providing no directional information. Only the visible light will reach the phototubes directly. Once the quantum efficiency and geometrical PMT coverage is accounted for only several photoelectrons will be observed, which is not enough to image a ring. Generally the energy a charged particle loses to Cherenkov radiation is two or three orders of magnitude less than the energy lost to ionization or excitation.

2.5   Detector Design

The design philosophy of Borexino is to have layered shielding with the background getting progressively lower towards the center of the detector. Materials will be progressively cleaner the closer they are to the scintillator. The interior of the detector can then be made relatively free of background. A diagram of the Borexino detector is shown in Figure 2.10.

2.5.1   Water Shield and Muon Veto

The Borexino detector is housed in a domed cylindrical enclosure 18 m diameter and 16.5 m tall. The outermost layer of the Borexino detector is a 2 m thick shield of ultra pure water. Its purpose is to absorb external radioactivity such as neutrons and γ's from the rocks, and serve as a muon veto. Inside this water tank is a stainless steel sphere (SSS). The stainless steel sphere is 13.7 m in diameter and supported by 20 legs which suspend it in the middle of the water tank. The steel is 8-10 mm thick and separates the water from the scintillator. It will also serve as a structural support for the PMTs. The SSS was constructed from curved plates that were brought underground and welded in place. The surface was pickled and passivated to remove particulates and prevent rusting. The SSS is required to be leak tight while feeding through the electrical signals and power for the many PMTs, as well as various monitoring devices. The inner surface has the requirement that it not reflect light too strongly as this would hinder the event reconstruction and adversely affect the α/β discrimination. Its matte finish diffusely reflects roughly 40% of the incident light.

The purpose of the moun veto is to identify mouns passing into the detector so those events can be ignored. It allows prompt events to be subtracted from the data, and determines the moun flux which is proportional to the rate of cosmogenic production. The outer moun veto is designed to detect muons passing through the water tank. It consists of PMTs mounted on the outside of the SSS and on the bottom of the detector submerged in high purity water. These PMTs detect Cherenkov light that is emitted when muons pass through the water. The inner moun veto is composed of PMT on the inside of the SSS with out light concentrators giving them a wider field of view. They can detect Cherenkov

light from mouns that enter the SSS but do not go through the fiducial volume or enter the active region. There is a combined efficiency of over 99.98% for detecting mouns passing through the detector.

2.5.2 Nylon Vessels

There are two concentric spherical nylon vessels inside the SSS with diameters of $11.5\,\mathrm{m}$ and $8.5\,\mathrm{m}$, each $125\,\mu\mathrm{m}$ thick called the outer vessel (OV) and inner vessel (IV) respectively. They separate the active scintillator from the inactive buffer and act as barriers for contaminants. The nylon vessels had to be chemically resistant to water, as well as the pseudocumene based scintillator and buffer solutions. Leak tightness was also required to prevent mixing. In addition the nylon vessels also served as a barrier to radioactive noble gases.

The vessels were fabricated from sheets of extruded nylon that were cut and bonded with Resorcinol. The index of refraction of the vessels had to match the scintillator to reduce reflections while maintaining transparency for wavelengths of 350-450 nm to allow light to reach the PMTs. They also have to withstand a positive or negative buoyant load due to thermal gradients of up to 5°C.

Because the inner nylon vessel is the closest non-scintillator material to the fiducial volume, it has some of the strictest purity and cleanliness requirements. There are four ways that the vessel can produce background events in the scintillator.

1. Intrinsic Activity - Radioactive contaminants trapped in the bulk material can decay producing events in the scintillator. Since there is scintillator on the inside only, roughly half of these decays will be seen. Most of the events will be near the surface except for gamma emissions which can reach the fiducial volume. The nylon must have a small mass and be extremely pure to reduce its total activity.

2. Diffusion - External contaminants can diffuse through the nylon vessel. In this case thicker is better. Radon is of the most concern since other contaminants have much lower diffusion constants.

3. Emanation - Bulk contaminants can diffuse out of the nylon into the scintillator. This is only a problem for radon produced by radium in the nylon. Other impurities which are solids at room temperature are essentially stationary.

4. Adsorption - Contaminants can bind to the nylon surface. This can create a thin adsorbed layer with a high activity. This results from exposure to air or liquids that have not been purified. While producing surface events these contaminants can also desorb into the purified scintillator. A significant fraction of the total contamination will generally reside on surfaces.

These mechanisms will be described in further detail in the following chapters.

B o r e x i n o   E x p e r i m e n t

Rope tendons

External water tank 18m φ

Stainless steel sphere 13.7m φ
(1 3 2 0   m   3   P C)

Nylon outer vessel 11.0 m φ

Nylon inner vessel 8.5m φ

Fiducial volume 6.0m φ

2200 Thorn EMI 8" PMTs
(1800 with light collectors
400 without light collectors)

208 PMTs in water for
External Muon Detector

Water

Buffer

Scintillator

Steel plates in
concrete for extra
shielding -
10m x 10m x 10cm
4m x 4m x 4cm

Figure 2.10: Borexino will detect ^{7}Be solar neutrinos in a 100 tons of high purity liquid scintillator. The Borexino detector is heavily shielded from external background. Gamma rays and neutrons in the rock around the detector are blocked by a 2 m water shield and activity from the photomultiplier tubes (PMTs) are absorbed by a 2.6 m inactive buffer inside the stainless steel sphere. PMTs located in the water tank are used as a muon veto. Two nylon vessels slow the diffusion of radon and other contaminants into the inner region of the detector.

Figure 2.11: A prototype of the inner and outer nylon vessels inflated in Jadwin Gym at Princeton University in 2001.

2.5.3   Liquid Scintillator

Borexino will use over 1000 tons of pseudocumene separated into three regions within the stainless steel sphere. The two outer regions will serve as an inactive buffer while the inner region will contain active scintillator. The innermost 100 tons will be used as the fiducial volume. The buffer is a solution with $5\,\mathrm{g/L}$ of DMP in pseudocumene while the scintillator is a solution of $1.5\,\mathrm{g/L}$ of PPO in pseudocumene.

The liquid scintillator in the active volume of the detector converts the kinetic energy of particles into visible light. Taking into account the geometrical coverage of the PMTs and their quantum efficiency, the detector will register $\sim$400 photoelectrons/MeV for beta events. The liquid scintillator base is 1,2,4-trimethylbenzene, more commonly called pseudocumene. The molecule is shown in Figure 2.12. Its chemical formula is $C_6H_3(CH_3)_3$ and it has a molecular weight of $120.2\,\mathrm{g/mol}$ with 66 electrons per molecule. The properties of pseudocumene are listed in Table 2.2.
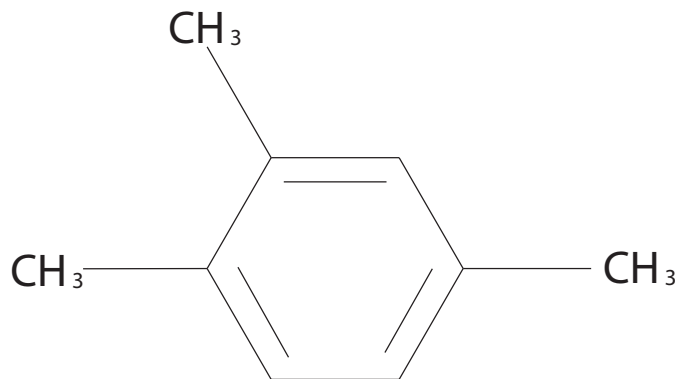
Figure 2.12: Pseudocumene is an aromatic hydrocarbon that produces scintillation light when excited. Its molecular weight is $120.2\,\mathrm{g/mol}$ and it has 66 electrons per molecule.

A wavelength shifter is added to the pseudocumene to shift the light from UV to longer wavelengths so it can pass through the glass faces of the PMTs and propagate through the scintillator without being absorbed. Borexino will use $1.5\,\mathrm{g/L}$ of $C_{15}H_{11}NO$ or 2,5-diphenyloxazole, commonly known as PPO. Its structure is shown in Figure 2.13. Properties

Name	1,2,4-Trimethylbenzene
Common name	Pseudocumene
Molecular formula	C_9H_{12}
Chemical structure	$C_6H_3(CH_3)_3$
Appearance	Colorless liquid
Odor	Aromatic
Molecular weight	$120.2\,g/mol$
Electrons	66 per molecule
Melting point	$-43.8°\,C$
Boiling point	$169°\,C$
Vapor density	4.15
Vapor pressure	$2.03\,mm\,Hg$ at $25°\,C$
Density	$876\,kg/m^3$ at $25°\,C$
Dynamic Viscosity	$5.9 \times 10^{-4}\,kg/m/s$
Kinematic Viscosity	$6.7 \times 10^{-7}\,m^2/s$
Heat Capacity	$1734\,J/kg/K$ @ $21.1°\,C$
Flash point	$48°\,C$
Explosive limits	0.9-6.4 vol% in air
Water solubility	0.9978 mole fraction [60]
Aqueous activity coefficient at saturation γ_{iw}^{sat}	1.3×10^5
Excess free energy at saturation	$29.2\,kJ/mol$
Index of refraction	1.505
Light yield (β, γ radiation)	$4500\,photons/MeV$
Quantum Efficiency	$\sim 40\%$
Peak emission wavelength	$290\,nm$
Decay time (liquid)	$21.8\,ns$ [61]
Decay time (gas)	$40\,ns$ [62]
Dielectric Constant	2.4
Ionization Energy	$8.26\,eV$
LD50	$5\,g/kg$
TWA	$25\,ppm$

Table 2.2: Properties of pseudocumene. Data from various MSDS and references [63, 64, 65, 66, 60]. LD50 is the lethal dose for 50% of a population. TWA stand for time weighted average which is the average occupation exposure limit over an 8 hour period.

of PPO are shown in Table 2.3. PPO was chosen because of its high quantum efficiency, short decay time, optical properties, and solubility. The concentration of the PPO in the scintillator is low enough that charged particles interact almost exclusively with the pseudocumene molecules which are excited to an higher electronic or ionized state. The PPO can be excited by having a pseudocumene molecule in an excited state transfer its energy to the PPO in a non-radiative process or by absorbing the light emitted by the pseudocumene. In pseudocumene about 95% of the energy is transferred to the PPO in a non-radiative process.
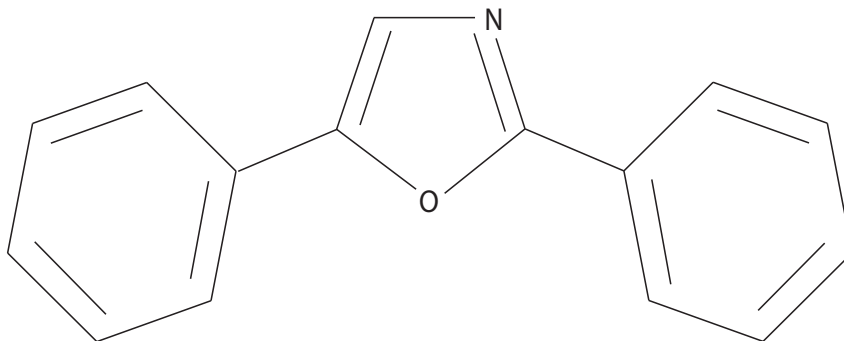
Figure 2.13: PPO is added to the pseudocumene at $1.5\,\mathrm{g/L}$. PPO emits light in the visible portion of the spectrum where it has a long mean free path in the scintillator and can pass through the PMT glass. It also reduced the decay time of the scintillator by a factor of ten, and improves the quantum efficiency dramatically. PPO is a white powder at room temperature but will crystallize if melted and frozen.

The scintillator mixture was chosen to have a large light yield, emission in the sensitive range of the PMTs, a long mean free path, good α/β discrimination, and short decay time for good position resolution. Properties of the scintillator are shown in Table 2.4. The scintillator emission spectrum and the quantum efficiency of the PMTs can be seen in Figure 2.14. Scintillators typically have efficient energy transfer from the solvent to the solute. This improves the quantum efficiency significantly from that of pseudocumene because the energy is transferred to PPO before the pseudocumene can deexcite through

Name	2,5-Diphenyloxazole
Common name	PPO
Molecular formula	$C_{15}H_{11}NO$
Appearance	White powder
Odor	Odorless
Molecular weight	221.27 g/mol
Melting point	72° C
Boiling point	360° C
Density	1060 kg/m^3
Decomposition Temperature	335 ° C
Decay time	1.78 ns [61]
LD50	750 mg/kg
TWA	10 mg/m^3

Table 2.3: Properties of PPO which is added to pseudocumene at a concentration of 1.5 g/L $(6.8 \times 10^{-4}$ M). LD50 is the lethal dose for 50% of a population. TWA stand for time weighted average which is the average occupation exposure limit over an 8 hour period.

Light yield (β event)	1.2×10^4 photons/MeV
Peak emission	370 nm
Absorption length (380 nm)	5.1 m
Fluorescence decay time	3.5 ns
Alpha quenching	$Q(E) = 20.3 - 1.3E$ [MeV]

Table 2.4: Properties of scintillator composed of pseudocumene + 1.5 g/L PPO [74]. The alpha quenching factor $Q(E)$ gives the reduced beta equivalent energy of an alpha decay.

internal quenching or some other non-radiative process. It also makes the decay time of the scintillator closer to that of the quickly decaying solute than the slowly decaying solvent. The most comprehensive references on scintillators are three books by J. Birks [67, 66, 62] and a series of 13 papers on "The Energy Transfer in Organic Systems" by the same author [68, 69, 70, 71, 72, 73].

The scintillation mechanism is best understood in terms of transitions between different electronic states of the molecules. In an aromatic molecule three electrons from the carbon are sp^2 hybridized in σ bonds. The fourth π election can orbit around the six carbon ring. The energy levels of typical organic scintillator with a π electron system are shown
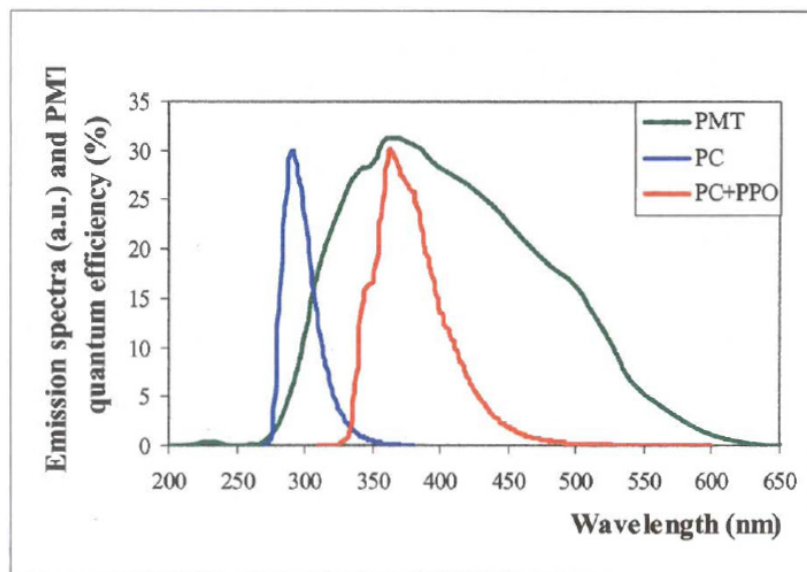
Figure 2.14: The emission spectrum of pseudocumene (PC) shown in blue and the emission spectrum of pseudocumene + PPO at $1.5\,\text{g/L}$ shown in green. The spectra are given in arbitrary units though the pseudocumene + PPO mixture has a much higher light yield than pure pseudocumene. The quantum efficiency of the photomultiplier tube (PMT) is shown in green. The addition on PPO to the pseudocumene shifts the emission spectrum to a range where the PMT had its peak quantum efficiency of 32% at $370\,\text{nm}$ [74].

in Figure 2.15. Though both σ and π electron systems are present in aromatic molecules only the π electrons are responsible for fluorescence. There are two π electron systems in aromatic molecules, singlet states S where the electrons are paired in an antiparallel spin 0 configuration and triplet states T which have electrons in a parallel spin $1\,\hbar$ configuration and are at slightly lower energy. The singlet ground state S_0 can hold two electrons. The exited states have an additional degeneracy corresponding to orbits in both directions around the ring and can hold up to four electrons each [75].

Fluorescence occurs for transitions from the S_1 state to the S_0 ground state. This typically take place on time scales on order of 10-100 ns. Phosphorescence between the T_1 and S_0 states can take up to a few seconds. Triplet states T_i cannot be populated by photonic absorption because the transition is spin forbidden, however, they can be populated

by ion recombination, slow electron excitation, and collisions between excited molecules. Triplet states decay very slowly to the ground state S_0 through spin-orbit coupling. Delayed fluorescence can occur if two molecules in the T_1 state collide and produce one molecule in the S_1 state and one in the S_0 state. The molecule in the S_1 state then decays in the normal manner. The delay is determined by the frequency with which molecules in the T_1 state collide.
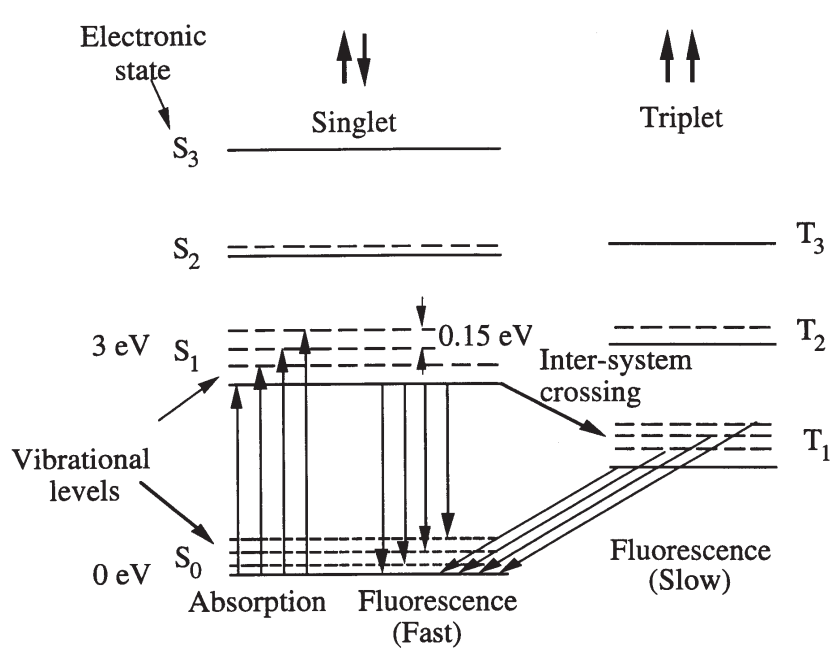
Figure 2.15: The typical π electronic energy levels from an organic molecule. S_0 is the ground state and S_1, S_2, S_3 are the excited singlet states. T_1, T_2, and T_3 are the excited triplet states. There is no triplet ground state. The dashed lines are the vibrational sublevels. Slow fluorescence is also known as phosphorescence. Figure from [67].

Energy transfer within the pseudocumene can be modeled as a combination of competing processes shown in Table 2.5. The aromatic molecules in their ground state are represented by X, molecules in their first singlet excited state by X^*, and molecules in higher singlet excited states by X^{**}. Dimers or excimers consist of two molecules bound in an excited state and are represented by D^* and D^{**}. Dimers do not exist in their ground state because

Process	Description	Rate [s^{-1}]
$X + h\nu \rightarrow X^{**}$	Photon Excitation	I_γ
$X + C \rightarrow X^{**}$	Charged Particle Excitation	I_c
$X^{**} \rightarrow X^*$	Internal Conversion	$k_{xh}[X^{**}]$
$X^{**} \rightarrow X'$	Internal Quenching	$k_{ih}[X^{**}]$
$X^{**} + X \rightarrow D^{**}$	D^{**} Formation	$k_{jh}[X][X^{**}]$
$D^{**} \rightarrow D$	Internal Conversion	$k_{dj}[D^{**}]$
$D^{**} \rightarrow 2X'$	Internal Quenching	$k_{ij}[D^{**}]$
$X^* \rightarrow X + h\nu_x$	Fluorescence	$k_{fx}[X^*]$
$X^* \rightarrow X$	Internal Quenching ground	$k_{ix}[X^*]$
$X^* \rightarrow X'$	Internal Quenching triplet	$k_{ix}[X^*]$
$X^* + X \rightarrow D^*$	D^* Formation	$k_{dx}[X][X^*]$
$D^* \rightarrow 2X + h\nu_d$	D^* Fluorescence	$k_{fd}[D^*]$
$D^* \rightarrow 2X'$	Internal Quenching	$k_{id}[D^*]$
$D^* \rightarrow X^* + X$	D^* Dissociation	$k_{xd}[D^*]$

Table 2.5: Energy transfer in an aromatic scintillator. The quantum yield of a scintillator material is determined by the rate of the fluorescence processes relative to internal quenching or other processes that produce no light. The quantities in brackets represent concentrations. The states are: ground state X, first excited state X^*, higher excited state X^{**}, triplet excited state X', and dimer D. Pseudocumene in the vapor phase at 1.8 torr has a fluorescence quantum yield $\Phi_f = 0.55$, a radiative decay rate $k_{fx} = 13.8 \times 10^6$/s, and a radiationless decay rate $k_{ix} = 11.2 \times 10^6$/s [62]. Table from [75].

they become dissociated molecules. Molecules that do not contribute to fluorescence are denoted X' or $2X'$, for single or paired molecules. These can be molecules in the lowest excited triplet state T_1, or photodissociated molecules.

When a charged particle deposits its energy in the scintillator the molecules are excited or ionized. When ions recombine they form triplet states about 75% of the time due to the 3:1 ratio of triplet to singlet states. Electron excitations can occur for the π, σ, and carbon $1s$ electron states and will depend on their relative cross sections. Non ionizing π electron excitations almost all go into the first three excited singlet states. The higher excited states rapidly decay to the S_1 state through internal conversion, dissipating their energy into vibrational or rotational degrees of freedom. While there are many ways pseudocumene can transfer energy internally, most of the energy is transferred to PPO before the

pseudocumene has a chance to deexcite from the S_1 state through fluorescence or internal quenching. A pseudocumene molecule in an excited state can rapidly transfer its energy to an adjacent pseudocumene molecule through excitation migration or molecular diffusion. Energy transfer between aromatic molecules in the second excited state occurs on the order of 10^{-11} s and energy transfer for the first excited state take place around 10^{-9} s [68]. The rapid transfer allows the deposited energy to move quickly in a random walk between pseudocumene molecules until a PPO molecule is found or the energy is dissipated though another process.

Excitation migration is partly due to the resonant transfer of energy between solvent molecules in the scintillator. The excited state energy can thought of as oscillating between two molecules. The frequency of energy migration n between two solvent molecules due to multipole-multipole exchange can be described quantitativly by

$$n = \frac{4}{h}uA \tag{2.25}$$

where h is Plank's constant, $A \approx 0.1$ is a constant, and $u \approx 3.7 \times 10^{-4}$ eV is the resonant interaction energy of a typical aromatic hydrocarbon [67]. The diffusion for excitation migration Λ is

$$\Lambda = \frac{N}{6}nR^2 \tag{2.26}$$

where N is the number of nearest neighbors, and R is the intermolecular distance. For aromatic hydrocarbons $N = 8$, $R = 0.5$ nm, the excitation diffusion constant $\Lambda = 10^{-4}$ cm^2/s. The total excitation migration in the solvent is due to $(D + \Lambda)$ where D is the standard molecular diffusion constant.

Energy is transferred primarily from the first excited π singlet state S_1 of pseudocumene to the singlet π state of PPO which is at a lower energy [67]. It occurs mostly through long range dipole-dipole interactions instead of collisions. Pseudocumene excitation energy migrates until it reaches a location where energy is transferred to the PPO by exchange, dipole-dipole, or multipole-multipole interaction. The rate constant k for a dipole-diple transfer between molecules X and Y with a separation R is

$$k = \frac{1}{\tau_{ox}} \left(\frac{R_0}{R} \right)^6 \tag{2.27}$$

where R_0 is the critical transfer distance when the probability of excitation transfer and deexcitation of X through some other process are of equal probability, and τ_{ox} is the decay time of the solvent in the absence of the solute. The values of R_0 tends to be on the range of tens of angstroms. Higher order quadrupole and octapole transfers depend on R^{-6} and R^{-8} respectively. The overall rate of excitation energy transfer to the solute from non-radiative processes is

$$k_{txy} = 2\pi(D + \Lambda)\frac{N_A}{1000}R_0\left(1 + \frac{R_0}{\sqrt{\tau_{ox}(D + \Lambda)}}\right) \tag{2.28}$$

where N_A is Avogadro's number.

The scintillation process described above involves the transfer of energy from the solvent (pseudocumene) to the solute (PPO), and subsequent fluorescence emission. These and other energy transfer processes are shown in Table 2.6. Fluorescence competes with the processes that dissipate energy nonradiatively. The relative rates depend on the concentration of the solvent, excited state concentrations, and temperature. The overall efficiency of the scintillation process will decrease with increasing temperature. The lower light output is a result of the reduction of the solvent-solute energy transfer efficiency with temperture [76].

The time dependence of scintillation emission is a function of the concentration of molecules in the first excited singlet state. For a single component system in the absence of impurity quenching, excimer formation, or energy transfer, the excited state concentration $[X^*]$ is

$$\frac{d[X^*]}{dt} = -(k_{fx} + k_{ix})[X^*] = -k_{ox}[X^*] \tag{2.29}$$

where k_{fx} and k_{ix} are the rate constants for fluorescence and internal quenching respectively [71]. The fluorscence response function is then

$$I_{ox}(t) = k_{fx}[X^*] = k_{fx}[X_0^*]e^{-k_{ox}t} \tag{2.30}$$

assuming a delta function excitation creating an initial concentration of excited atoms $[X_0^*]$ and a decay time $\tau_{ox} = 1/k_{ox}$. The fluorescence response function of the binary scintillator containing an additional component Y is more complicated than the simple

Process	Description	Rate [s^{-1}]
$X + C \to X^*$	Charged Particle Excitation	I_c
$X + \gamma \to X^*$	Gamma Excitation	I_γ
$X^* \to X + h\nu_x$	Fluorescence	$k_{fx}[X^*]$
$X^* \to X$	Internal Conversion	$k_{ix}[X^*]$
$X^* + X \to 2X$	Concentration Quenching	$k_{cx}[X^*][X]$
$X^* + Y \to X + Y^*$	Excitation Transfer	$k_{txy}[X^*][Y]$
$h\nu_x + Y \to 2X$	Radiative Transfer	$k_{rxy}[Y]I_{\nu_x}$
$Y^* \to Y + h\nu_y$	Fluorescence	$k_{fy}[Y^*]$
$Y^* \to Y$	Internal Conversion	$k_{iy}[Y^*]$
$Y^* + Y \to 2Y$	Concentration Quenching	$k_{cy}[Y^*][XY]$
$X^* + Q \to X + Q$	Impurity Quenching	$k_{qx}[X^*][Q]$
$Y^* + Q \to Y + Q$	Impurity Quenching	$k_{qy}[Y^*][Q]$

Table 2.6: Energy transfer in an binary scintillator solution. The solvent X (pseudocumene), solute Y (PPO), and quencher Q (DMP, oxygen, etc.). Quenchers can be oxygen or other impurities in the solution. The quantities in brackets represent in the rate column represent concentrations. The states are: ground state X, first excited state X^*, higher excited state X^{**}. Table from [69].

decaying exponential of a unitary system. If there is complete mixing of X^* and Y due to excitation transfer or molecular diffusion then Stern-Volmer kinetics apply. This is applicable to the pseudocumene PPO scintillator solution. In this case the energy transfer rate is independent of time. If X^* and Y were stationary the Förster kinetics would apply and the transfer rate would decrease with time. This is only the case in crystals or high viscosity liquids.

The concentrations of X^* and Y^* with Stern-Volmer kinetics are determined by

$$\frac{d[X^*]}{dt} = -(k_{ox} + k_{yx}[Y])[X^*] = -k_x[X^*] \tag{2.31}$$

$$\frac{d[Y^*]}{dt} = k_{yx}[Y][X^*] - (k_{fy} + k_{iy})[Y^*] = k_{yx}[Y][X^*] - k_{oy}[Y^*] \tag{2.32}$$

where k_{yx} is the rate parameter for non-radiative transfer, and k_{fy}, k_{iy}, and k_{oy} are the rates for fluorescence, internal quenching, and total decay of Y respectively [71]. Here other energy transfer mechanisms are ignored. The fluorescence functions are then

$$I_x(t) = k_{fx}[X_0^*]e^{-k_x t} \tag{2.33}$$

$$I_{xy}(t) = k_{fy}[Y^*] = \frac{k_{fy}k_{yx}[X^*][Y]}{k_x - k_{oy}}(e^{-k_{oy}t} - e^{-k_x t}). \tag{2.34}$$

The pulse shape is determined by I_{xy} which is the difference of exponentials. When

$$k_x = k_{ox} + k_{yx}[Y] < k_{oy} \tag{2.35}$$

the rise time is determined by $\tau_x = 1/k_x$ and the decay time is determined by $\tau_{oy} = 1/k_{oy}$. The decay time τ_x is depends on the concentration of Y as

$$\tau_x = \frac{1}{k_x} = \frac{1}{k_{ox} + k_{yx}[Y]} \tag{2.36}$$

so decay time τ_x can be reduced by increasing $[Y]$. For the Borexino scintillator $k_{yx} \approx 5 \times 10^{10}/\text{mol/s}$, and $\tau_{oy} = 1.6\,\text{ns}$.

The time dependence of the Borexino scintillation intensity is determined by a competition between different processes that dissipate energy. In the above scenario which only included energy transfer to the solute and fluorescence decay, the pulse shape was found to be proportional to the difference of a fast rising exponential and a slower decaying exponential. However this neglects complications which arise from energy density effects along the particle track which modify the pulse shape. These differences in pulse shape can be used to identify the type of radiation exciting the scintillator.

Pulse Shape Discrimination

The time dependence of scintillation emissions for different types of radiation is a function of their specific energy loss in the scintillator. This changes the pulse shape which can be used to distinguish the particles. The final pulse shape that also depends on the PMT response function and electronics though these can be designed so the critical features of the pulse shape are preserved.

Quenching refers to de-excitation through non-photonic processes. Quenching reduces the number of photons produced and thus lowers the observed event energy. It also affects the timing of the scintillation emission which allows for pulse shape discrimination. The scintillation decay has a fast ($\sim$ns) and slow ($\sim \mu$s) component. Quenching causes the ratio

of the fast to slow components of the scintillation decay curve to change depending on the incomming particles mass. Light emission for the fast component is strongly repressed when heavy particles deposit their energy over a short distance resulting in a high specific energy density. The slow component of the decay is nearly independent of the energy deposited per path length and thus nearly the same for all types of radiation.

Reduction of the fast component of the scintillation decay results from ionization quenching. High densities of ionized molecules interact with excited solvent molecules reducing them to their ground state without the emission of a photon. A majority of the primary π excitations are produced in the S_2 and S_3 states and it is believed that ionization quenching is strongest for these states. Ionization quenching competes with internal conversion of the S_2 and S_3 to the S_1 state.

The ionization density depends on the energy deposited along the track of the particle $B\frac{dE}{dx}$, where B is a constant determined by the average ionization potential of the particular scintillator. In the simplest form the fluorescence L is expressed as

$$\frac{dL}{dx} = S\frac{dE}{dx} \tag{2.37}$$

where S is the absolute scintillator efficiency, and x is the particle range. Accounting for unimolecular ionization quenching with a quench parameter k then the equation for emission becomes

$$\frac{dL}{dx} = \frac{S\frac{dE}{dx}}{1 + kB\frac{dE}{dx}}. \tag{2.38}$$

For electrons with small $\frac{dE}{dx}$ this reduces back to equation 2.37. For heavy alpha particles with large $\frac{dE}{dx}$ the light emission can be approximated as

$$\frac{dL}{dx} = \frac{S}{kB} \tag{2.39}$$

which is constant. Typical values of kB are on order of $10\,\mathrm{mg\,cm^2/MeV}$ in organic scintillators. In a liquid a $665\,\mathrm{keV}$ electron has a range of a few mm in scintillator while a $5\,\mathrm{MeV}$ alpha particle has a range of a few μm. It should aslo be noted that while ionization quenching has a large effect on the primary light yield, it does not significantly change the decay time of the scintillator.

The slow component of the scintillation decay is a result of collisions between molecules in the lowest π triplet excited state T_1. The two triplets annihilate forming a molecule in the singlet state.

$$X' + X' \rightarrow X^* + X \tag{2.40}$$
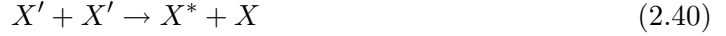
where X' is a molecule in the triplet state, X^* is a molecule in the singlet excited state. The triplet-triplet annihilation is a bimolecular process that depends on the square of density of triplets. Once in the X^* state the molecule can decay in the normal manner. Triplet states are formed mainly from the recombination of ions but there are also contributions to the triplet state population from intersystem crossing and excitation from slow secondary electrons. The slow component of the scintillator decay is roughly independent of the type of radiation.

The time dependence of scintillator emission depends mostly on the density of singlet states in space and time. Assume that the density of excited molecules along the particle track is cylindrically symmetric for a single component scintillator. The prompt component of scintillator emission depends on the singlet concentration $c_s(r, t)$ in the S_1 state.

$$\frac{\partial c_s(r, t)}{\partial t} = D_s \nabla^2 c_s(r, t) - \frac{1}{\tau_f} c_s(r, t) \tag{2.41}$$

where D_s is the singlet diffusion constant and τ_f is the fluorescense decay time [77]. With some initial population of the singlet state this will lead to a simple exponential decay over time. The intensity will be

$$I_s(t) = k_f N_s(0) e^{-t/\tau_f} \tag{2.42}$$

where k_f is the rate parameter for fluorescense emission and $N_s(0)$ is the total number of singlets produced at $t = 0$.

The slow component is a bit more complicated because delayed singlets can be created during the collision of two triplets. It also depends on the density of delayed singlets $c_s'(r, t)$ and is described by

$$\frac{\partial c_s'(r, t)}{\partial t} = D_s \nabla^2 c_s'(r, t) - \frac{1}{\tau_f} c_s'(r, t) + k_u c_t^2(r, t) \tag{2.43}$$

where k_u is the rate constant for the production of delayed singlets from two triplets and the initial condition $c'_s(r, 0) = 0$ applies since there are no delayed singlets in the initial state.

The triplet density is required to find the delayed singlet density as it depends on $c_t^2(r, t)$. The analysis is simplified because the production of molecules in the triplet state from intersystem crossing is small. When this source of triplets is neglected the triplet concentration is described by

$$\frac{\partial c_t(r, t)}{\partial t} = D_T \nabla^2 c_t(r, t) - \frac{1}{\tau_p} c'_s(r, t) - \chi_u c_t^2(r, t) \tag{2.44}$$

where D_T is the diffusion constant for triplets, τ_p is the phosphorescence decay time, and χ_u is the rate of bimolecular annihilation with $|\chi_u| > 2k_u$. A gaussian distribution can be assumed for the initial condition $c_T(r, 0) = c_T(0)e^{(r/r_0)^2}$. The distribution of triplet states is cylindrically symmetric along the path of high energy particles. However, a sufficiently low energy electron will deposit its energy in a spherical volume called a spur. Thus it is necessary to solve the system in these two limits. Time scales of interest for pulse shape discrimination are much shorter than the phosphorescence decay time ($t \ll \tau_p$) allowing the decay term $\frac{1}{\tau_p} c'_s(r, t)$ to be ignored. Only the annihilation and diffusion terms need to be considered. In the diffusion limit there will be a relaxation time $t_d = r_0^2/4D_T$. In the annihilation limit the relaxation time is $t_u = 1/(\chi_u c_t(0))$. The process with the smaller relaxation time will dominate. The ratio

$$\frac{t_d}{t_u} = \frac{r_0^2 \chi_u c_t(0)}{4D_T} \tag{2.45}$$

governs the relative importance. For particles with high specific energy loss such as alpha's, annihilation will dominate initially until the triplet density decreases enough that diffusion takes over. The initial density can be expressed as

$$c_t(0) = \frac{1}{\pi r_0^2 W_T} \frac{dE}{dx} \tag{2.46}$$

where $W_T \approx 60\,\text{eV}$ is the average energy needed to produce a triplet excitation. When the annihilation is diffusion limited

$$\chi_u = 8\pi D_T \rho \tag{2.47}$$

where $\rho \approx 10^{-7}$ cm is the interaction distance. There is a critical specific energy

$$\left(\frac{dE}{dx}\right)_c = 300\,\text{MeV/cm} \tag{2.48}$$

below which diffusion is the dominant mechinism for the triplet concentration reduction and above which annihilation dominates [77].

The total intensity of the delayed fluorescense can be found in cases of high and low specific energy deposition. For times where $t \gg \tau_f$ the delayed intensity for a high specific energy loss (cylindrical symmetry) is

$$I'(t) = \frac{k_f k_u \tau_f}{2\chi_u t_u} \frac{N_T(0)}{\left[1 + \frac{t_d}{2t_u}\ln\left(1+\frac{t}{t_d}\right)\right]^2 \left(1+\frac{t}{t_d}\right)} \tag{2.49}$$

where $N_T(0)$ is the total number of triplets formed along the particle track. For a low specific energy loss the delayed intensity with $t \gg \tau_f$ is

$$I'(t) = \frac{k_f k_u \tau_f}{2\chi_u t_u} \frac{N_T(0)}{\left\{1 + \frac{t_d}{\sqrt{2t_u}}\left[1 - \left(1+\frac{t}{t_d}\right)^{-\frac{1}{2}}\right]\right\}^2 \left(1+\frac{t}{t_d}\right)^{\frac{3}{2}}} \tag{2.50}$$

where there is a different dependence on t. These formulas for intensities of high and low specific energy deposition match well with experimental measurements of sctinillator decay curves. However, the overall effect on the delayed components of the scintillator pulse is small compared with the effect on the prompt emission from ionization quenching. It is mainly the difference in the prompt component of the emissions that allows for alpha/beta separation.

Most alphas decay at an energy around several MeV, which is above the neutrino window. However, quenching of the light yield for alpha particles causes the signal to fall in the neutrino energy window. The quenching of light emitted by alphas relative to betas is due to the higher stopping power $\frac{dE}{dx}$ of alphas [67]. The quenching factor in the Borexino scintillator is

$$Q(E) = 20.3 - 1.3E \tag{2.51}$$

where E is in [MeV]. The quenched energies of some common alpha emitters are shown in Table 2.5.3.

Isotope	$t_{1/2}$	E [MeV]	Quenched Energy [keV]	Quenching Factor Q
^{210}Po	138.4 days	5.30	396±10	13.4±0.3
^{222}Rn	3.82 days	5.49	410±6	13.4±0.2
^{218}Po	3.10 min	6.00	483±6	12.4±0.2
^{214}Po	164.3 μs	7.68	751±7	10.2±0.1

Table 2.7: Alpha quenching measurements in pseudocumene + PPO [78]. The apparent energy reduction of an alpha with kinetic energy E is given by the quenching factor $Q(E) = 20.3 - 1.3E$ [MeV]. Note that the quenched energies put these alpha decays in the neutrino energy window.

	τ_1	τ_2	τ_3	τ_4	q_1	q_2	q_3	q_4
β-γ	3.57	17.61	59.50	-	0.895	0.063	0.042	-
α	3.25	13.49	59.95	297.10	0.630	0.178	0.119	0.073

Table 2.8: The decay parameters of the Borexino scintillator found by fitting the decay curve to the function $f(t) = \sum_{i=1}^{4} \frac{q_i}{\tau_i} e^{-t/\tau_i}$. The units of τ are [ns]. Measurements from [79].

In practice, the decay curve of the a scintillator can often be expressed as a sum of exponentials.

$$f(t) = \sum_{i=1}^{n} \frac{q_i}{\tau_i} e^{-t/\tau_i} \qquad (2.52)$$

where q_i is the weight of each term, and τ_i is the mean decay time. The weights are normalized to one

$$\sum_i q_i = 1. \qquad (2.53)$$

Decay characteristics for the Borexino scintillator are shown in Table 2.8.

2.5.4 Inner and Outer Buffer

Inside the SSS there are two additional buffers to protect the fiducial volume and reduce the overall count rate. The outer buffer is the volume between the SSS and the outer nylon vessel where the PMTs are located, and the inner buffer is the volume between the inner and outer nylon vessels. Without these buffers, gamma decays due to impurities in the

PMT glass would overwhelm the electronics. Like the water shield, these buffers absorb gamma radiation before it can reach the inside of the detector.

The buffer solution is composed of pseudocumene that has been quenched to suppress light emission when energy is deposited in the region. While the buffer emits little light of its own, it transmits light produced in the inner volume, allowing it to reach the PMTs. The only significant light emission in the buffer is from Chrenkov radiation.

A quencher will be added to the pseudocumene to prevent scintillation in the buffer region. An amount of $5\,\mathrm{g/L}$ of dimethyl 1,2-benzenedicarboxylate, commonly known as dimethylphthalate or DMP, will be used to make the buffer solution. The chemical formula of DMP is $C_{10}H_{10}O_4$. It structure is shown in Figure 2.16. Properties of DMP are listed in Table 2.9. Light output in the buffer region is suppressed by a factor of $\sim$10 relative to
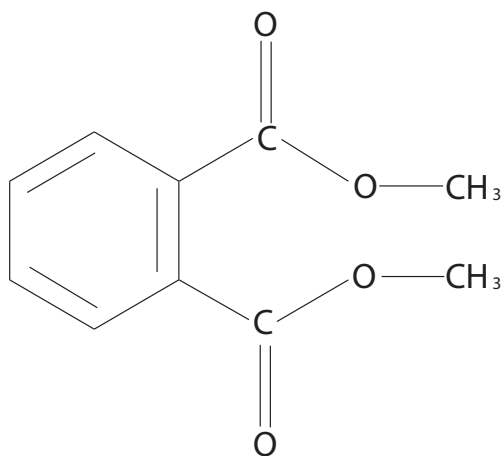
Figure 2.16: Dimethyl 1,2-benzenedicarboxylate more commonly known as DMP is mixed with pseudocumene at $5\,\mathrm{g/L}$ to form a buffer solution. The buffer quenches the scintillation light output by about a factor of 10. However, the buffer solution will transmit scintillation light produced in the inner volume.

pure pseudocumene [80].

DMP was chosen because it did not chemically degrade the pseudocumene or nylon, had good quenching efficeincy, was transparent in at the wavelengths of interest, and was stable

Name	Dimethyl 1,2-benzenedicarboxylate
Synonym	Dimethylphthalate
Common name	DMP
Molecular formula	$C_{10}H_{10}O_4$
Chemical structure	C_6H_4-1,2-$(COOCH_3)_2$
Appearance	Colorless oily liquid
Odor	Slight aromatic odor
Molecular weight	194.2 g/mol
Melting point	5.5° C
Boiling point	284° C
Density	1190 kg/m^3
Relative vapor density (Air=1)	6.7
Vapor pressure	4.19×10^{-3} mm Hg at 20° C
Flash point	146 ° C
Explosive limits	0.9-8 vol% in air
Auto-ignition temperature	490° C
Water Solubility	0.43 g/100 mL at 20° C
LD50	6800 mg/kg
TWA	5 mg/m^3

Table 2.9: Properties of dimethlyphthalate or DMP. DMP is commonly used as a plasticizer and insect repellant.

over long time periods [80]. The quenching efficieny is determined by the Stern-Volmer equation

$$\Phi([Q]) = \frac{\Phi_0}{1 + K_Q[Q]} \tag{2.54}$$

where $[Q]$ is the concentration of quencher, Φ_0 is the maximum quantum yield without quencher, and K_Q is the quenching constant. The lifetime of the scintillator is also related the concentration of quencher by

$$\tau([Q]) = \frac{\tau_0}{1 + \tau_0 k_q[Q]} \tag{2.55}$$

where τ_0 is the lifetime in the absence of quencher, and quenching rate constant $k_Q = K_Q/\tau_0$. For DMP in pseudocumene $k_q = 2.3 \times 10^{10}/\text{mol/s}$. The queching as a function of DMP concentration is shown in Figure 2.17.

Figure 2.17: The yield ratio Y_{PC}/Y_{PC+DMP} as a function of DMP concentration in pseudo-cumene. Data were obtained using a ^{207}Bi source [80].

2.5.5 Photomultiplier Tubes

The purpose of a photomultiplier tube is to convert light into an electrical signal, in this case a current. The process begins by converting 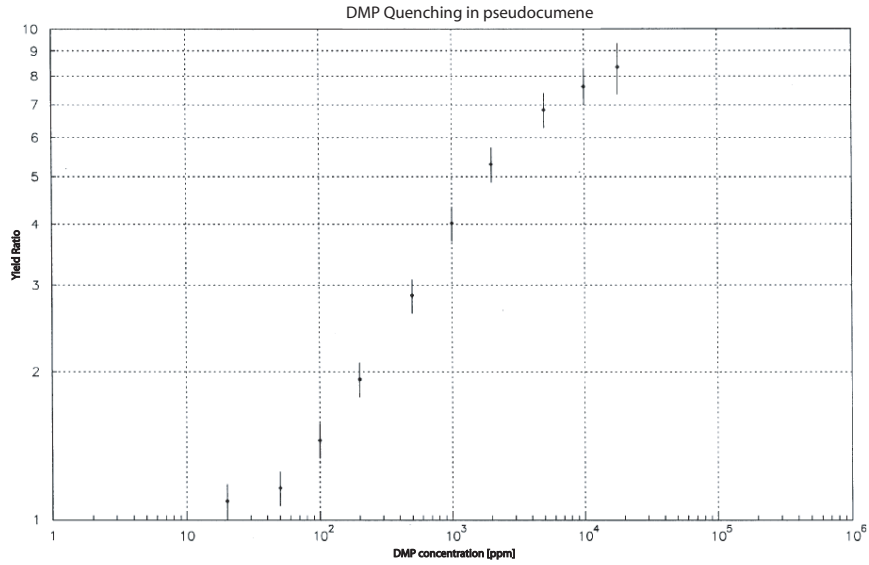a photon into an electron with a photocathode. The photocathode is a thin film of metal coated inside the window of a PMT that uses the photoelectric effect to absorb a photon and free an electron. The electron is then accelerated by a large electric field into a series of dynodes. As the electron hits each dynode it knocks out many more electrons. These new electrons are all accelerated by the next dynode in the chain and the process repeats. After several stages there are a large number of electrons which results in an amplification of the original signal. When the electrons are collected on the final dynode they become a current.

The Borexino detector will utilize 2200 PMTs with a 20.3 cm diameter to observe 300 tons of active scintillator. Of the 2200 PMTs, 1800 will be modified with light collectors which will focus them on the active volume while screening outside events. These light collectors are similar to Winston Cones [81]. There are 400 PMTs without light cones that will function as an internal muon veto. An external muon veto will be made from 200 additional PMTs observing the water shield. These PMTs will observe Cherenkov radiation produced as muons pass through the water. These occurrences are noted and the events produced in the detector during this time are excluded.

The geometrical phototube coverage for Borexino is 34% [82]. For a 1 MeV event about 400 of the PMTs will produce a single photoelectron signal. A picture of the photomultiplier tubes mounted on the stainless steel sphere is shown in Figure 2.18. Properties of the Borexino PMTs are shown in Table 2.10.

A special glass with low levels of impurities was used for the PMT faces. Even so, the PMTs and their light collectors are the two least lowest purity materials used in Borexino in terms of their ^{238}U, ^{232}Th, ^{40}K content. Coupled with their relatively close proximity to the fiducial volume, gammas emitted by radioactive impurities in the glass of the PMTs and the light collectors the dominant background contribution accounting for over 2/3 of the rate in the neutrino window [63].
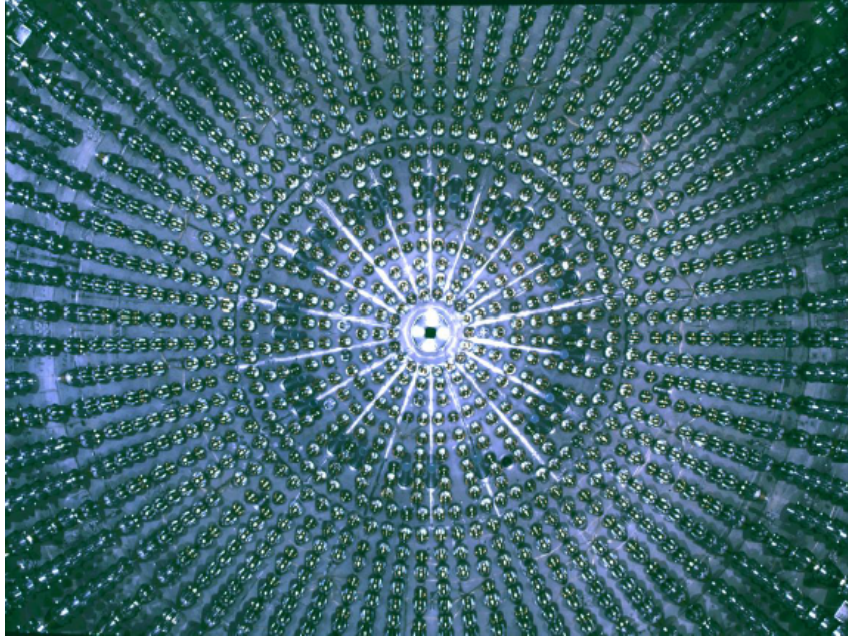
Figure 2.18: The photomultiplier tubes mounted in the stainless steel sphere before the nylon vessels are installed. This shot was taken looking vertically up from the bottom of the stainless steel sphere.

2.5.6   Purification Skids

Borexino will purify scintillator with industrial scale purification skids. They will remove contaminants with four processes: filtration, vacuum distillation, water extraction, and nitrogen stripping. There are 50 nm filters that will reduce particulates suspended in the scintillator. Vacuum distillation will separate impurities with a higher boiling point than the scintillator. Water extraction is effective for removing polar molecules and metal ions. It also hydrates the scintillator. Nitrogen stripping will remove gases such as oxygen, which will quench the light output of the scintillator, and radioactive noble gases like radon, argon, and krypton. For the extraction processes where the scintillator is in contact with water or

Property	Value
Gain	10^7
Operating voltage	$\sim 1400\,\mathrm{V}$
Cathode diameter	$19\,\mathrm{cm}$
Cathode material	SbCsK
Dynodes	12
Face material	Schott 8346 Glass
Peak quantum efficiency	32% @ $370\,\mathrm{nm}$
Peak to valley ratio	>2
Transit time	$15\,\mathrm{ns}$
Timing jitter	$1\,\mathrm{ns}$
Dark noise rate	$1\,\mathrm{kHz}$
After pulsing	2.5%
Total activity	$1.2 \times 10^9 \gamma/\mathrm{day}$

Table 2.10: Properties of the Electron Tubes Limited (formerly Thorn-EMI) 9351 photomultiplier tubes [83]. The total activity is for all PMTs based on impurity levels of $3 \times 10^{-8}\,\mathrm{g/g}$ ^{238}U, $1 \times 10^{-8}\,\mathrm{g/g}$ ^{232}Th, and $2 \times 10^{-5}\,\mathrm{g/g}$ K$_{nat}$, with a total PMT mass of $9 \times 10^3\,\mathrm{kg}$ [63].

nitrogen, great care must be taken that the materials are pure enough that they themselves do not contaminate the scintillator. A more detailed discussion in presented in Chapter 3.

2.5.7 Data Acquisition System

The electronics and data acquisition system for Borexino are designed to perform the following functions:

- Trigger the detector when a specified threshold is reached.

- Measure the energy of an event by summing PMT signals.

- Capture relative timing information from individual PMTs for position reconstruction.

- Record delayed coincidence events for event discrimination and analysis.

The data acquisition system for Borexino will read and process the signals from 2422 photomultiplier tubes. A trigger will occur when the number of internal PMTs hits within a $50\,\mathrm{ns}$ window exceeds a given threshold [84]. A typical PMT pulse is $\sim 15\,\mathrm{ns}$. The number

of PMTs and the time window for the trigger are chosen to minimize the rate of events from the dark noise of the PMTs (about 1 kHz) and low energy background while still capturing as many neutrino events as possible. The trigger rate above 250 keV is expected to be well below 1 Hz. The data acquisition system will record data from 1 μs before a trigger to about 5 μs after the trigger.

The electronics for Borexino will power the PMTs, decouple the high voltage from the signal which is on the same cable, amplify the signal, and integrate the PMT signal to find the energy. A copy of the signal is used for timing information. Timing information is processed with a time to digital converter with a resolution of 0.5 ns [85]. The pulse from a PMT will be read with a charge analog to digital converter (ADC). The Borexino data acquisition hardware is illustrated in Figure 2.19.
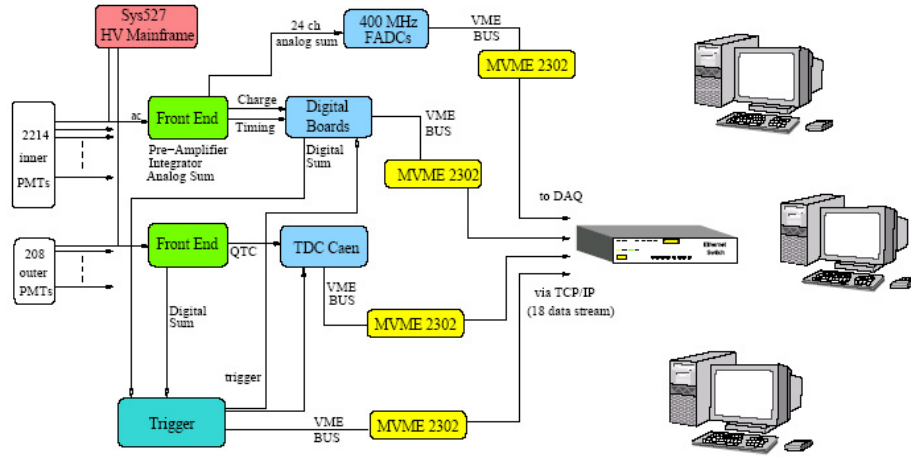

Figure 2.19: A diagram of the Borexino electronics and data acquisition system [86].

2.5.8 Detector Resolution

The Borexino detector will measure the position, energy, time, and pulse shape of each event. The uncertainty in these parameters is determined by the resolution of the detector. To give a rough idea of the detector resolution, a 1 MeV event will have an energy resolution

of $\sim 8\%$ and a position resolution of about $12\,\mathrm{cm}$ [82].

Determining whether events lie inside or outside the fiducial volume of the detector depends on good spatial resolution. Accurate knowledge of the fiducial volume is important because it is directly related to the neutrino rate. The spatial distribution of events within the fiducial volume aids in the identification of impurities which are often non-uniform in space. There are two methods of finding the location of an event in the detector. One is based on the timing of photons arriving at the different PMTs and the other is based on the charge that each PMT measures. For Borexino the timing information provides better spatial resolution.

The position of an event is determined by the maximum likelihood method. The likelihood function gives the probability that an event occurred at position x_0 at time t_0 given a pattern of PMT hits at positions x_i and t_i.

$$L(x_0, t_0; \{(x_i, t_i)\}) = \prod_{i=1}^{N} p\left(t_i - t_0 - \frac{n|x_i - x_0|}{c}\right) \frac{R - |x_0|\cos\theta_i}{|x_i - x_0|^3} \tag{2.56}$$

where R is the distance from the center of the detector to the PMTs, θ_i is the angle between a radial vector to the event and the ith PMT, and p is the scintillator response function. For a gaussian shaped pulse

$$p(\tau_e) = \frac{e^{-\tau_e^2/2\sigma^2}}{\sqrt{2\pi\sigma^2}} \tag{2.57}$$

where τ_e is an independent random variable relating the time of scintillator emission to the time of the event [87].

Using timing information to resolve event positions at the center of the detector a resolution of

$$\delta r = \left(\frac{Nn^2}{3c^2\sigma^2} + \frac{4N}{3R^2}\right)^{-1/2} \approx \sqrt{\frac{3}{N}} \frac{c\sigma}{n} \tag{2.58}$$

is obtained, where N is the number of PMTs hit, n is the index of refraction, R is the detector radius, and σ is the timing dispersion.

The energy resolution of the detector is determined by the number of photoelectrons measured by the PMTs. The variance in the number of photoelectrons σ_μ is

$$\sigma_\mu = \sqrt{\mu} \tag{2.59}$$
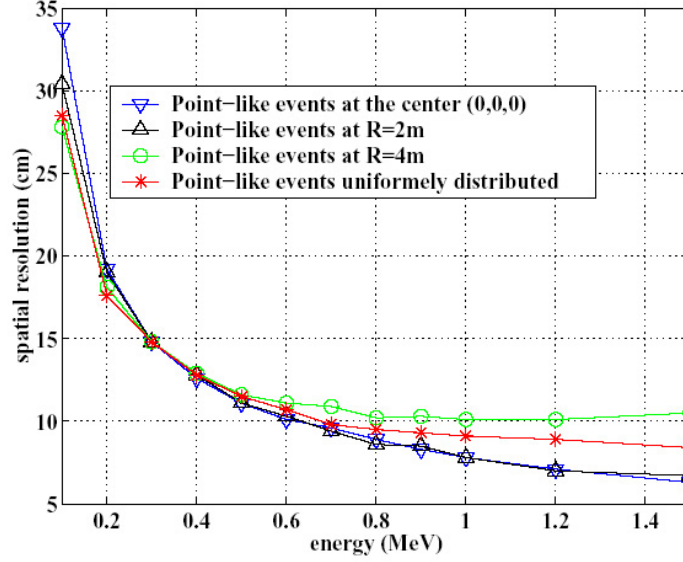
Figure 2.20: The spatial resolution of the Borexino detector from a Monte Carlo simulation of point like events. Resolution is plotted as a function of energy for various positions. The position resolution in Borexino ranges from 8-18 cm over different positions and energies [63].

where μ is the number of photoelectrons. The fractional variance in the energy dE/E then goes like $1/\sqrt{\mu}$. The energy resolution as a function of position is shown in Figure 2.21.

Alpha/beta separation was tested in a Borexino air run (with air and no scintillator in the stainless steel sphere) using a small liquid scintillation source that contained radon. The source was suspended in a small quartz vial in the center of the Borexino detector prior to installation of the nylon vessels. A number of different alpha/beta separation techniques were tested, including the tail to total ratio, a linear Gatti classifier, a likelihood test, a Kolmogorov test, and the Support Vector Machine (SVM) [88, 79]. The best separation was based on the SVM method. The SVM involved mapping the inputs into a high dimensional space and then applying a standard linear transformation. When separating a population there are two quantities of relevance: the capture efficiency for selecting the sample, and the contamination from the other species. These quantities are not normally the same for both samples. A higher capture efficiency implies more contamination from the other
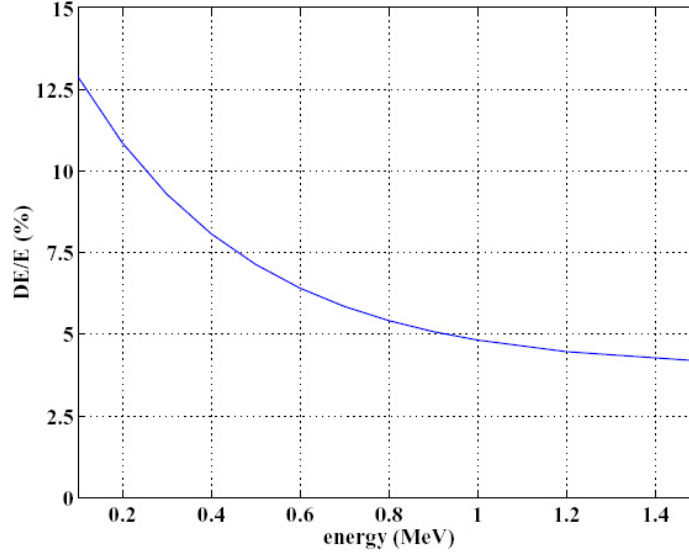
Figure 2.21: The energy resolution of the Borexino detector shown for simulated point like electron events as a function of energy. The energy resolution ranges from 5-10% in the neutrino window. Figure from [63].

species. Some results from the air run are shown in Table 2.11 and Table 2.12. A plot of the alpha/beta separation with the SVM is shown in Figure 2.22.

2.6 Calibration and Monitoring

Photomultiplier tubes can be calibrated individually with laser pulses fed to the PMTs through fiberoptics. Each PMT has a separate fiber, usually attached to the edge of its light cone. The fibers are made of Teflon coated quartz. The laser is a Hamamatsu PLP-02 which has a FWHM of 50 ps. They will allow the rise time of the PMTs to be synchronized to within 0.5 ns. Jitter of the PMTs is typically 1 ns which will dominate timing resolution. The single photoelectron peak will be used to calibrate the gain of the PMTs to within 5%.

A system of cameras and light diffusers is used to monitor the shape and position of the nylon vessels in the sphere. Teflon light diffusers attached to the vessel surface can be used to monitor the vessel position and the position resolution of the detector. They are

Method	5%	3%	1%
Primary SVM	98.4	97.7	93.1
Global SVM	98.4	97.5	91.9

Table 2.11: Alpha/beta separation in an air run using the SVM for a source at the center of the Borexino detector. This table shows the beta efficiency for a given alpha contamination shown in the top row. For example a 1% alpha contamination with the Primary SVM will allow 93.1% of the betas to be captured. A good alpha/beta separation technique will reject a high percentage of the alpha events while only loosing a small percentage of the beta events in the process. A timing coincidence was used to independently identify the alpha and beta events [88].

Method	95%	97%	99%
Primary SVM	0.4	1.9	5.6
Global SVM	1.1	1.9	5.7

Table 2.12: Alpha/beta separation in an air run using the SVM for a source at the center of the Borexino detector. This table shows the alpha contamination for a given beta efficiency shown in the top row. For example a 99% beta efficiency with the Primary SVM will have a 5.6% alpha contamination [88].
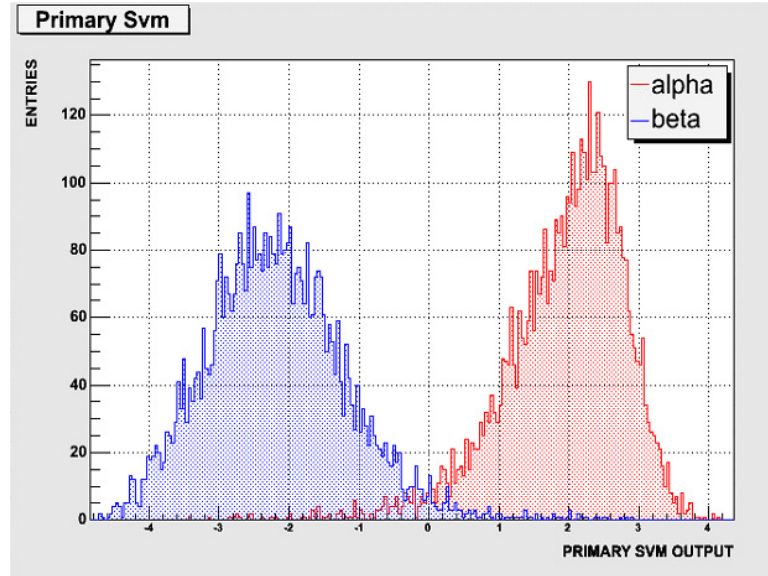
Figure 2.22: Alpha-beta discrimination with the Primary SVM. The beta population is shown in blue and the alpha population in red. This data was obtained by placing a small scintillator vial at the center of the air filled Borexino detector [88].

essentially points of a few millimeters in diameter that scatter light from optical fibers in all directions.

A camera system was installed in the stainless steel sphere to observe the nylon vessels. The combination of seven CCD cameras can resolve the position of an object in the sphere such as the light diffusers to a resolution of a few cm. In air the resolution was measured to be 1.36 cm. The cameras reside behind glass domes to protect them from the pseudocumene. To view the vessels directly the cameras require lights to be turned on inside the sphere meaning they cannot be used while the phototubes are powered.

There are eight optical fibers attached to the outside of the inner vessel with no light diffusers. They are pointed inward to excite the PPO with 355 nm light. These are used to simulate surface events.

2.6.1 Radioactive Calibration Sources

The detector electronics and performance were tested by observing radioactive sources. These provide a high data rate so that a good statistical sampling can be acquired in a short period of time. This allows a calibration of the position and energy resolution of the detector by selecting a source with known isotopes and positioning it precisely within the detector. Sources can be inserted and positioned in the inner vessel through the top of the detector. The system, which consists of a rod with a hinge, can move the source vertically and azimuthally when the arm is bent. A source consisting of a small sample of radon-loaded scintillator was used to calibrate the detection in an air run before the detector was filled with scintillator.

The calibration source for Borexino was a small quartz vial containing scintillator spiked with radon. This source provided a way to test the alpha/beta separation through the ^{214}Bi-^{214}Po coincidence. The sample of α and β decays was separated by analyzing the pulse shape and compared against the known decays based on their timing sequence.

MCi sources of ^{90}Sr and ^{51}Cr under the detector will produce known fluxes of neutrinos which can be used to calibrate the detector. These can also be used to look for a neutrino magnetic moment.

2.7 Counting Test Facility

In order to verify the design and technical feasibility of the Borexino experiment a small-scale prototype was designed and built. The Counting Test Facility (CTF) contains $4.2\,\mathrm{m}^3$ of scintillator in a $1000\,\mathrm{m}^3$ water shield being observed by 100 PMTs with 21% geometrical coverage. The CTF contains its own small purification plant located on top of the detector. It succeeded in its primary goals of measuring the scintillator photon yield, the ^{14}C content of the scintillator, and the concentration of ^{238}U, ^{232}Th, ^{85}K, ^{39}Ar [87].

The CTF also solved the problem of measuring low backgrounds with good sensitivity. There are many other techniques for determining impurities such as gas chromatography mass spectroscopy, neutron activation analysis, and nuclear magnetic resonance. These

methods have sensitivities in the 10^{-12} range at best while Borexino needs purity at the 10^{-18} level. This leaves six orders of magnitude where there is limited knowledge about the quantity and type of impurities. The CTF helped to bridge this gap without requiring the full-scale detector.
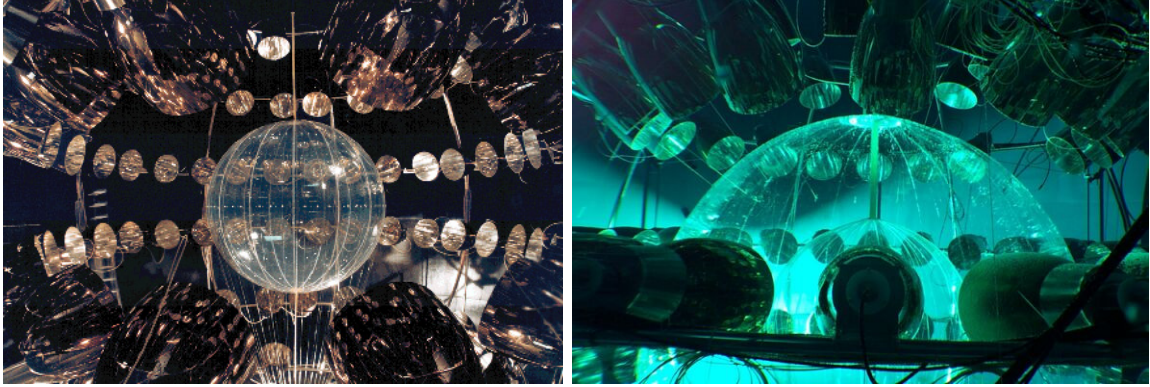
Figure 2.23: The CTF I is observed by 100 PMTs (left). The CTF III has a second nylon vessel to reduce radon diffusion (right). The phototubes are mounted on an open support frame submerged in water.

2.8   Borexino Status

Borexino has completed its main construction phase. Commissioning of the plants and filling operations are expected to start shortly. The detector should be fully operational and begin taking data in 2006. The counting test facility has been running since 2001. Its next operation will test the distillation unit of the Borexino skids.

Competition from the KamLand experiment is close behind. KamLand was originally designed to measure reactor neutrinos but has a fiducial volume 3.6 times larger than Borexino. The detector has a high background event rate of several hundred Hertz, but the experiment has added a purification system to clean its scintillator. It is expected to begin taking solar neutrino data about the same time as Borexino.

Internal and External Radioactive Backgrounds

New physics is often discovered by pushing the limit on some physical parameter. In the case of Borexino it is the low rate of background events at low energies. With the current large mixing angle-MSW oscillation parameters, Borexino expects to observe 0.35 neutrino events per day per ton from ^{7}Be in the energy window. Because there are so few events it is desirable to have a total background event rate that is very small. In any case the total background rate should not be significantly larger than the neutrino rate. The net rate of background events that cannot be identified and vetoed or removed through cuts during analysis should be less than the neutrino rate. In other words the signal to noise ratio should be greater than one, $S/N > 1$. Naturally, the larger S/N is, the better. After designing the experiment to increase the signal by having a large target mass with a maximal cross section, given the constraints that neutrinos are being measured, the only way to increase the S/N ratio is to reduce background.

Reducing backgrounds is especially difficult for Borexino because of the low energies involved. There are many radioactive elements that have decays at lower energies which must be removed from the detector. Generally the lower the energy threshold is, the higher

the rate of background. High-energy neutrino experiments can image Cherenkov rings to determine the direction the neutrino came from. If they came from the sun, an accelerator or some other localized source then the directionality can be used to identify the signal. This cannot be done by Borexino since the electrons scattering from ^{7}Be do not produce enough Cherenkov light for their direction to be determined. The scintillation light observed by Borexino is emitted isotropically and no directional information is retained. The length of the particle tracks from the scattered electrons in Borexino are also short compared with the spatial resolution of the detector of about 10 cm, which prevents the particle track from being resolved.

With scintillation events there is some ability to distinguish charged particles based on their mass. Heavier particles produce a pulse with a longer tail as a result of quenching and non-photonic decays. This allows alpha particles to be distinguished from beta particles or gamma radiation.

The big challenge for the Borexino experiment is to deal with the large number of radioactive isotopes that decay with energies in or above the region of interest. Borexino must create an environment in the detector whose activity is more than 13 orders of magnitude below the ambient environment. This is an extremely non-trivial task. An enormous effort by the collaboration was put into identifying, measuring, and analyzing the sources of background and their contribution. In some cases the required levels of purity were so low that available measurement techniques did not have the required sensitivity. New measurements devices such as the Counting Test Facility were developed to meet these needs. The purities and properties of a huge number of substances were measured to find suitable construction materials.

3.1 External Backgrounds

External backgrounds are those in which the radiation originates in the outside environment as well as in materials within the detector close to the fiducial volume. In this context they will include everything except the intrinsic scintillator contamination. Borexino must deal

Element	$t_{1/2}$ [10^9 years]	Elemental Abundance [ppm]	Natural Abundance [Percent]	Activity [Bq/kg]
^{238}U	4.468	2.7	99.27	35.6
^{235}U	0.704	2.7	0.72	1.60
^{232}Th	14.05	10.7	100	40.1
^{40}K	1.277	20900	0.0117	652
^{87}Rb	47.5	90	27.83	82.6

Table 3.1: Naturally occurring radioactive isotopes [89]. The elemental abundance is the total amount of an element in earth's crust, including all isotopes. The natural abundance is the percentage of each isotope for a given element. The activity is given in Bq/kg of dirt. The average activity in the earth's crust is about $1\,$kBq/kg of dirt [90]. The average density of the earth's crust is $2.7\,$g/cm^3. *Borexino can tolerate at most 9 μg of dirt in the fiducial volume.*

with all types of backgrounds including α, β, γ, n, and μ. Some are easily absorbed like α particles, while others like muons easily penetrate the detector shielding and must be tagged and subtracted from the data.

The basic idea is to shield external activity from the fiducial volume. This is done by placing high purity material around the detector to absorb the radiation before it reaches the interior. In the case of muons which can take many kilometers of rock to stop, the detector shielding is used to observe the muons as they pass through so the event can be identified.

The earth's crust contains a number of radioactive elements. The relative concentrations vary with location and are dependent on the rock type. A sampling of the more prevalent naturally occurring radioactive elements in earth's crust is given in Table 3.1.

There are also a number of radioactive isotopes present in the atmosphere. Naturally occurring radioactive elements in the atmosphere are shown in Table 3.2. The amount of radon present can vary widely because it emanates from the ground and depends strongly on local conditions. These levels of naturally occurring radioactivity require the Borexino detector to be vacuum tight to prevent dirt or air from entering the detector. Borexino can tolerate at no more than $10\,$cm^3 of ambient air in the detector.

Element	$t_{1/2}$ [years]	Source	Activity [Bq/m^3]
^{222}Rn	0.01	Natural	30
^{85}Kr	10.8	Anthropogenic	1
^{39}Ar	269	Cosmogenic ^{40}Ca$(n,\alpha)^{37}$Ar	0.011

Table 3.2: Radioactive isotopes in the atmosphere. The radon rate is the average indoor activity. The activities per volume of pure Ar or Kr gas accounting for the natural abundance of the isotopes are, 10^6 Bq ^{85}Kr/m^3 Kr and 1 Bq ^{39}Ar/m^3 Ar [91].

3.1.1   Ambient Activity at LNGS

The local radioactivity levels can vary significantly from earth's average activity. Measurements were made to determine the ambient radioactivity in the underground labs at LNGS where Borexino is located. The neutron flux from the rock walls at LNGS was measured to be 3.8 n/cm^2/s. Of these 77% are thermal neutrons which have energies of about 0.025 eV. These neutrons are primarily produced from fission and $(\alpha,$ n$)$ reactions. The detector is hit by 3×10^6 n/day. The 2 m water shield attenuates the neutron flux by a factor of 10^8. Fast neutrons $(> 0.5$ eV$)$ must be moderated before they can be easily captured because the cross section for neutron capture decreases rapidly with energy. Neutrons are best moderated by a low A material, which is generally something with a high density of hydrogen atoms. Low A materials are preferable because momentum is most effectively transferred during collisions of similar mass.

The underground Gran Sasso labs have a radon activity of 100 Bq/m^3 in air and 10^4 Bq/m^3 in water [92]. The radon air activity would reach 2000 Bq/m^3 were it not for a continuous venting of the halls with fresh outside air piped in through the highway tunnel. This air supply is essential to maintain safe working conditions. Radon contamination is one of the reasons the detector must remain leak tight to air. The leak tightness specification of $< 10^{-8}$ atm cm^3/s comes from ^{85}Kr. Radon is especially dangerous for Borexino because it is more soluble in pseudocumene than in air.

The gamma flux from the walls of Hall C at LNGS has been measured and the flux from

Isotope	Energy [MeV]	Flux $[10^7/m^2/day]$	$\mu(H_2O)$ [1/cm]	$I(2\,m\;H_2O)$ $[1/m^2/day]$
^{40}K	1.460	3.8	0.058	320
^{214}Bi	1.120	1.4	0.066	26
^{214}Bi	1.764	1.7	0.053	390
^{228}Ac	0.911	0.48	0.074	2
^{208}Tl	2.614	1.35	0.044	2000

Table 3.3: Gamma flux from the rocks in Hall C at the LNGS and its reduction by the 2 m water buffer between the water tank and stainless steel sphere. μ is the mass attenuation coefficient in water for a gamma of the given energy and I is the gamma flux after being attenuated by two meters of water shielding. There is an additional shielding from a pseudocumene based buffer which further reduces the total gamma rate from outside the hall to less than one count per day in the fiducial volume. The two meters of water will reduce a 1 MeV gamma flux by about 10^6 [93].

the most common elements is shown in Table 3.3.

Cosmic ray muons still reach the detector despite the rock shielding from the mountain of 3800 mwe. The flux in Hall C is $1.2\,\mu/m^2/hr$ meaning 4500 muons enter the SSS per day. These muons will produce Cherenkov light and scintillation within the detector that will fall within the neutrino window. Fortunately these muons can be detected with an efficiency of over 99.98%, meaning the veto will miss less than 1 muon per day.

Being able to tag muons efficiently only solves part of the problem. These muons also interact with the scintillator and water to produce neutrons and cosmogenic nuclides. The cosmogenic isotopes they generate inside the scintillator often have long half lives, some of which cannot be correlated with the passage of a muon through the detector. Since these cosmogenic isotopes reside within the active volume, they are discussed in the Section 3.1.3 on internal backgrounds.

3.1.2 Shielding Physics

Shielding is typically bulky and often expensive, so it is important to choose the right material and use no more than necessary. In underground laboratories space is extremely

valuable. This section will describe the process through which radiation is absorbed. Recall that the fiducial volume of Borexino is shielded by at least $2.15\,\mathrm{m}$ of high purity water, $2.6\,\mathrm{m}$ of an inactive pseudocumene based buffer, and $1.25\,\mathrm{m}$ active scintillator.

Gamma rays emitted in the rock are almost completely absorbed by the water shield. The attenuation of gammas is a result of photoelectric adsorption at low energies ($<1\,\mathrm{MeV}$), Compton scattering at intermediate energies (1-3 MeV), and pair production at high energies ($>3\,\mathrm{MeV}$). The linear attenuation coefficient μ [cm^{-1}] is the probability per unit length that the photon will be removed by the sum of these processes. The attenuation scales with the mass attenuation coefficient μ/ρ [cm^2/g] according to

$$I = I_0 e^{-(\mu/\rho)\rho t} \tag{3.1}$$

where the term ρt is the mass thickness of the absorber. For water the mass attenuation coefficient is shown in Figure 3.1. The highest energy gamma from a naturally occuring element is $2.6\,\mathrm{MeV}$ produced by ^{208}Tl. A $2.6\,\mathrm{MeV}$ gamma flux will be reduced by a factor of 6600 after passing through $2\,\mathrm{m}$ of water.

Photoelectric absorption occurs when a photon is absorbed by an atom which emits an electron, usually from the K shell. The energy of the photoelectron is

$$E_{e^-} = h\nu - E_b \tag{3.2}$$

where E_b is the binding energy of the electron. The cross section scales roughly as

$$\sigma \propto \frac{Z^n}{E_\gamma^{3.5}} \tag{3.3}$$

where n is between 4 and 5 [95]. The cross section depends on the electron binding energy with respect to the photon energy. Sharp increases in the cross section are often present once the photon energy drops below the electron binding energy. High Z materials are best for absorbing photons.

Compton scattering is the interaction between a photon and an electron in a material. It results in a gamma being scattered at an angle θ with respect to its original direction. The energy of the scattered photon $E' = h\nu'$

$$h\nu' = \frac{h\nu}{1 + \frac{h\nu}{m_0 c^2}(1 - \cos\theta)} \tag{3.4}$$
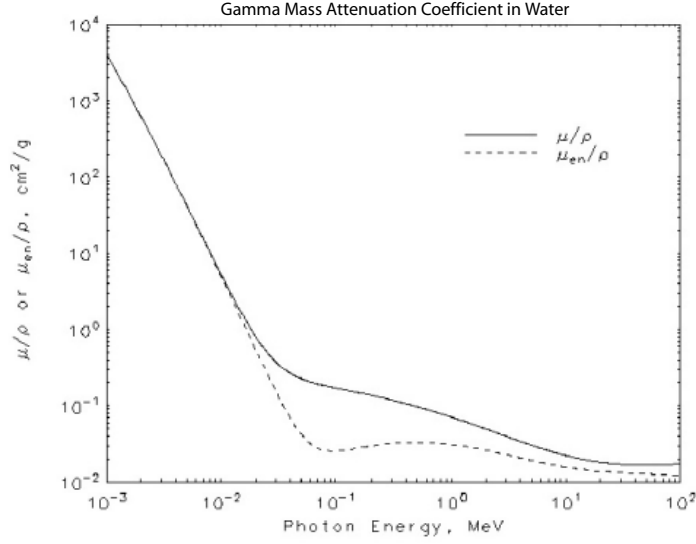
Figure 3.1: The mass attenuation coefficient μ/ρ [cm^2/g] for water as a function of photon energy [MeV]. μ_{en}/ρ is the mass energy-absorption coefficient. The mass energy-absorption coefficient is a dosimetric quantity related to the energy deposited per unit mass. Water has a density of $\rho = 1$ g/cm^3. Borexino has a two meter water shield that will effectively absorb gammas emitted from the outside environment [94].

where h is Planck's constant and ν is the frequency of the photon. The differential scattering cross section of Compton scattered photons is

$$\frac{d\sigma}{d\Omega} = Zr_0^2 \left(\frac{1}{1 + \alpha(1 - \cos\theta)}\right)^2 \left(\frac{1 + \cos^2\theta}{2}\right) \left(1 + \frac{\alpha^2(1 - \cos\theta)^2}{(1 + \cos^2\theta)[1 + \alpha(1 - \cos\theta)]}\right) \quad (3.5)$$

where $\alpha = h\nu/m_0c^2$ and $r_0 = \frac{e^2}{4\pi\epsilon_0 m_0 c^2} = 2.8 \times 10^{-15}$ m is the classical electron radius [95]. The higher the energy, the more the photon is scattered in the forward direction.

Pair production is the process of a photon scattering off a nucleus to form an electron and a positron ($\gamma + Z \rightarrow Z + e^- + e^+$). It can occur if the energy of the photon is greater than $2m_0c^2 = 1.02$ MeV, which is twice the electron rest mass. It also requires momentum to be transferred to a nucleus. The cross section scales roughly as the square of the atomic number and increases with photon energy. A full calculation of the cross section can be found in [96].

The energy loss of a charged particle due to scattering off atomic electrons is given by the Bethe formula

$$-\frac{dE}{dx} = \frac{4\pi e^4 z^2 NZ}{m_e v^2}\left(\ln\frac{2m_e v^2}{I} - \ln\gamma^{-2} - \beta^2\right) \tag{3.6}$$

where e and m_e are the electron charge and rest mass, v and z the velocity and charge of the primary particle, $\gamma^2 = \frac{1}{1-\beta^2}$, $\beta^2 = \frac{v^2}{c^2}$, N and Z are the number density and atomic number of the absorber, and I is the average excitation and ionization potential of the absorber [95]. The energy loss scales as the charge of the primary particle squared. In the non-relativistic limit the energy loss scales inversely with the incoming particle's energy. Absorbers should be made of materials with large heavy nuclei that have a high density.

The range of a charged particle can be approximated with the Bragg-Kleeman rule which relates the range between two different materials [67]. Air is often used as the reference.

$$r = \frac{\rho_{air}\sqrt{A}}{\rho\sqrt{A_0}}r_{air} \tag{3.7}$$

where r_{air} is the range in air, ρ is the density, and $\sqrt{A}$ is defined as

$$\sqrt{A} = \frac{n_1 A_1 + n_2 A_2 + \cdots}{n_1\sqrt{A_1} + n_2\sqrt{A_2} + \cdots}. \tag{3.8}$$

Here n_i are the atomic fractions of the constituent elements with atomic weights A_i.

The energy loss due to ionization and excitation for fast electrons is

$$-\left(\frac{dE}{dx}\right)_c = \frac{2\pi e^4 NZ}{m_0 v^2}\left[\ln\frac{m_0 v^2 E\gamma^2}{2I^2} - (\ln 2)\left(\frac{2}{\gamma} - \frac{1}{\gamma^2}\right) + \frac{1}{\gamma^2} + \frac{1}{8}\left(1 - \frac{1}{\gamma}\right)^2\right] \tag{3.9}$$

where the variables are defined below equation 3.6. For highly relativistic particles bremsstrahlung radiation also contributes to energy loss according to

$$-\left(\frac{dE}{dx}\right)_r = \frac{NEZ(Z+1)e^4}{137m_0^2 c^4}\left(4\ln\frac{2E}{m_0^2 c^2} - \frac{4}{3}\right). \tag{3.10}$$

This is not an issue for most naturally occurring beta emitters.

Neutrons are more difficult to absorb because they are uncharged. They are also more dangerous because they can enter the detector unnoticed. The usual method for stopping neutrons is to moderate high energy neutrons with a low Z material (something containing
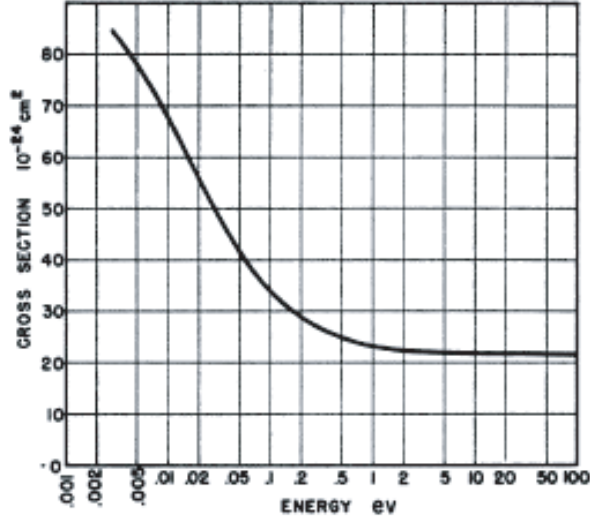
Figure 3.2: The total neutron cross section per hydrogen atom of water [97].

a lot of hydrogen) and then capture them in a nucleus once they are slowed. A plot of the neutron cross section is shown in Figure 3.2.

The attenuation lengths of different types of radiation for typical energies are shown in Table 3.4. The ranges of alpha and beta particles in water is shown in Figure 3.3. Except for muons, the shielding effectively protects Borexino from external radiation. However, events in the fiducial volume can be produced by impurities in the detector materials which have less shielding to penetrate.

Particle	Energy [MeV]	Range in H_2O [m]
α	<10	10^{-3}
β	<5	2.55
γ	<2.6	0.25
μ	~1000	$\gg 10$

Table 3.4: Attenuation lengths for external radiation. The energy listed is roughly the maximum amount of energy that can be released for each type of decay. The range given for gammas is actually an attenuation length, which is the scale for the exponential reduction in intensity. Alpha and beta particles all stop within a short distance of the given range. The water shield in Borexino is 2 m thick.

Figure 3.3: The range of α (top) and β (bottom) particles in water as a function of energy [MeV]. The attenuation of γ particles in water is shown in Figure 3.1.

3.1.3 Cosmogenics

Muons that pass through the stainless steel sphere produce Cherenkov light. Those that pass through the inner vessel produce scintillation light as well. Muons also produce hadronic showers in liquids which are a source of neutrons in the detector. When the neutrons are thermalized they are captured on hydrogen and release an energetic 2.216 MeV gamma.

$$n + p \rightarrow\, ^2\mathrm{H} + \gamma \qquad\qquad (3.11)$$

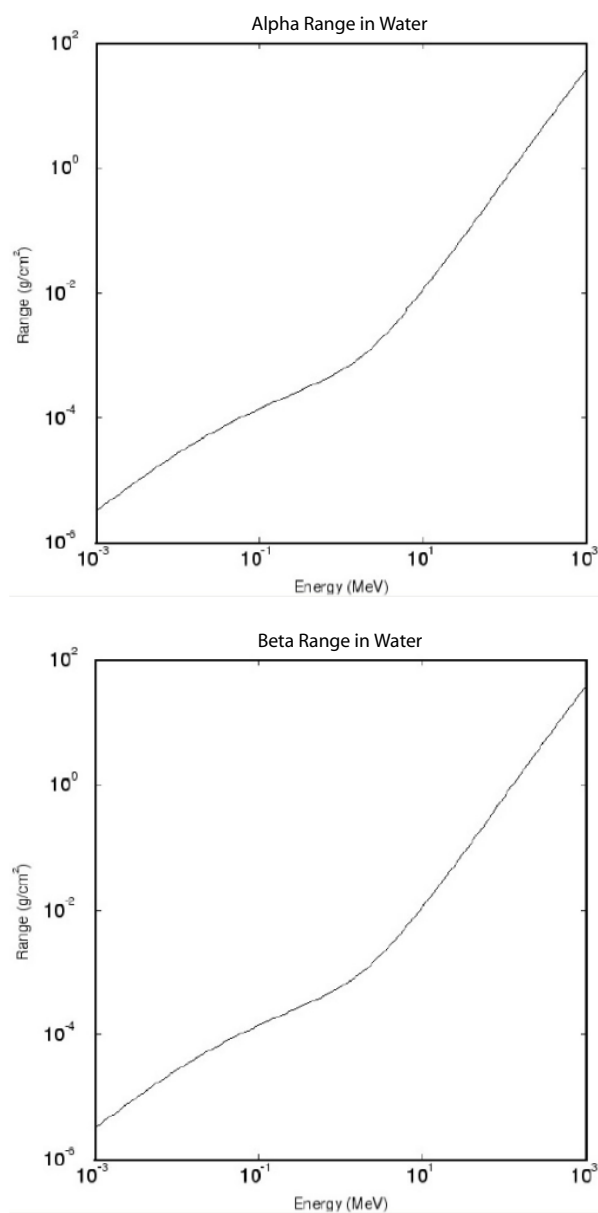The neutron capture time is about $300\,\mu$s in pseudocumene so these events are closely correlated with the preceding muon event and can be rejected [98]. The energy released in neutron capture is also above the window for ^{7}Be neutrinos.

Muons present a problem for Borexino even though they are efficiently tagged by the muon veto with an efficiency of better than 99.98%. Around 5000 muons per day enter the SSS some of which interact with nuclei in the scintillator. Muons can break apart nuclei producing a spectrum of products whose masses are less than the original nucleus. Some of these will be radioactive isotopes. Aside from ^{1}H which cannot fragment, ^{12}C is by far the most abundant nucleus in the scintillator for muons to interact with. This means the range of isotopes produced has an upper limit of 12 amu. The list of harmful isotopes produced includes ^{6}He, ^{8}He, ^{8}Li, ^{9}Li, ^{11}Li, ^{7}Be, ^{11}Be, ^{8}B, ^{12}B, ^{9}C, ^{10}C, ^{11}C. Many of these cosmogenics that decay a short time after they are created and can be correlated with the preceding muon event and rejected. The four long lived cosmogenically produced elements in Borexino with half-lives greater than one second are ^{7}Be, ^{11}Be, ^{10}C, ^{11}C. They are summarized in Table 3.5.

3.1.4 Material Activity

The purity of materials used to shield the detector and structural components was carefully considered during the detector design. Of particular concern were γ emitters since gammas had comparably long attenuation lengths and could reach the fiducial volume. α and β emissions are absorbed in relatively short distances ($\sim$10 cm) in solids and liquids.

Isotope	$t_{1/2}$	E [MeV]	Decay
^{7}Be	53.3 days	0.478	^{7}Be $+ e^- \to\, ^7$Li $+ \gamma$
^{11}Be	13.8 sec	<11.5	^{11}Be $\to\, ^{11}$B$+e^- + \bar{\nu}_e$
^{10}C	19.3 sec	<1.9	^{10}C $\to\, ^{10}$B$+e^+ + \nu_e + \gamma$
^{11}C	20.4 min	<0.99	^{11}C $\to\, ^{11}$B$+e^+ + \nu_e$

Table 3.5: Cosmogenic isotopes produced by muons in Borexino with half lives greater than one second.

Component	^{238}U [g/g]	^{238}Th [g/g]	K_{nat} [g/g]	^{60}Co [mBq/kg]
Nylon rings - extruded	3.0×10^{-11}	5.0×10^{-11}	1.3×10^{-7}	-
Steel flanges	1.5×10^{-10}	9.2×10^{-10}	1.5×10^{-7}	15
Steel pipes	1.5×10^{-10}	7.0×10^{-10}	2.6×10^{-7}	10
Steel OV mount rings	1.4×10^{-10}	2.1×10^{-9}	1.3×10^{-7}	20
Steel OV flanges	1.6×10^{-10}	3.3×10^{-9}	7.0×10^{-8}	2

Table 3.6: Measured radiopurity of the end region components that contribute most to the background. K_{nat} refers the the concentration of natural potassium. ^{40}K, the only naturally occurring radioactive potassium isotope is 0.0117% of K_{nat}. Results of measurements of other materials that were not selected for use in the experiment can be found in reference [99].

The amount of tolerable bulk contamination depends on the energy of the gamma decays and the distance from the fiducial volume. Lower energy gammas are absorbed more easily and can be located closer to the fiducial volume. A enormous effort was made to measure and catalogue the impurities in every material used in the construction of the Borexino detector. The impurities of some of these materials are listed in Table 3.6. Monte Carlo simulations were used to predict the contribution of each component to background events in the fiducial volume. The contributions from the different components are shown in Table 3.7. The backgrounds from the PMTs and associated light collectors dominate and are several time larger than other contributions. Their contribution is reduced by moving them to a larger radius, but this results in reduced geometrical coverage or a large number of PMTs.

Component	Position [m]	Mass [kg]	All NW	pep	200t NW	pep	100t NW	pep
Nylon rings	4.25	5.2	124	107	2.2	1.5	0.15	0.18
Nylon hubs	4.25	0.44	16	14				
Steel flanges	4.9	3.4	63	29	1.5	1.5	0.3	0.06
Steel pipes	4.9-5.6	6.9	66	30	2.5	1.7	0.7	0.18
IV rope attachment	5.45	3.7	3.6	1.4	0.14	0.09	0.02	0.02
Steel OV mount rings	5.5	7.76	13	6	0.3	0.3	0.06	0.011
Steel OV flanges	5.5	11.3	6	2	0.2	0.15	0.03	0.004
Steel OV tubes	5.5	2.6	2	1	0.07	0.05	0.01	0.001
4 pipe load cells	5.2	0.6	3.5	1.6	0.09	0.09	0.02	0.003
6 string load cells	5.4	0.8	2.3	1.1	0.06	0.06	0.01	0.002
Temperature sensors	>4.9		9	4	0.4	0.1	0.04	0.003
IV nylon film	4.25	32	199	95	1.5	0.8	0.03	0.011
Ropes	4.25	4.5	173	101	1.4	0.7	0.02	0.007
Phototubes	6.5		1280	651	25	26	0.6	0.4
Light Cones	6.3		896	494	18	18	0.6	0.4
Stainless Steel Sphere	6.85		496	207	10	9	0.2	0.2

Table 3.7: Gamma background in Borexino from the various components of the end region. The background is expressed as rate in events/day in the 250-800 keV energy window and in the 800-1300 keV energy window for *pep* neutrinos [63].

3.2 Internal Backgrounds

Internal backgrounds include any decay that occurs inside the fiducial volume. They are a result of radioactive isotopes in the liquid scintillator.

The most important aspect of Borexino is the purity of its liquid scintillator. This ultra high purity scintillator will allow it to make a real time measurement of low energy neutrinos. By eliminating sources of radioactive background in the target mass the rare interactions of neutrinos will become visible. We are able to run on-line purification of the scintillator.

The main technical challenge facing Borexino is the identification and elimination of radioactive impurities in the liquid scintillator. Fortunately, there is a vast array of empirical data compiled about radioactive isotopes. Data on naturally occurring isotopes and their typical abundances indicate what to expect. And knowledge of how each isotope decays, the energies of those decays, and their half lives facilitates the identification.

The difficulty in identifying isotopes statistically in the liquid scintillator stems largely from the experiment's success in making it pure. With very few events one has very little data to analyze and extract information from.

A wide range of other methods exist to determine the composition of a sample. These include chemical reactions, atomic spectroscopy, mass spectroscopy, neutron activation analysis, and others. All these methods face some limit in their sensitivity. That is to say that there is some concentration below which these methods can provide no information. While these methods are employed, Borexino is ultimately interested in purities that exceed the sensitivities of these methods by several orders of magnitude. One of the main functions of the CTF is to help bridge this gap. The sensitivities of several methods used to analyze the compositions of samples are shown in Table 3.8.

As a rough guide, the experiment can tolerate no more than one count per day in the fiducial volume from any given source. The rate of background events from radioactive isotopes produced in the detector is given by the number of atoms in the detector divided

Technique	Sensitivity	Uses
Neutron Activation Analysis (NAA)	0.1 ppb	Excitable nucleui
Mass Spectroscopy (MS)	1 ppt	Molecules and elements
Residual Gas Analyzer (RGA)	10^{-13} Torr	Gas samples

Table 3.8: The sensitivity of different measurement techniques used to analyze the composition of samples. The sensitivities are approximate showing the limits of what has measured with high end detectors under ideal conditions. The actual sensitivity limits in each case depend on a number of factors like the elements and materials involved.

by their mean life.

$$A(t) = \sum_i \frac{N_i}{\tau_i} = A_I(0)e^{-t/\tau} \tag{3.12}$$

where N_i is number of isotope atoms of species i. The mean life τ is related to the decay constant by $\tau = \frac{1}{\lambda}$. In a certain sense decays are useful because they decrease the number of radioactive nuclei over time. The amount of a given isotope as a function of time is

$$N(t) = N_o e^{-t/\tau} \tag{3.13}$$

where N_o is the initial number of atoms present at $t = 0$. The commonly used half life is related to the mean life by

$$t_{1/2} = \tau \ln 2. \tag{3.14}$$

Most isotopes with mean lives of less than a day will quickly decay away to a level where they are negligible, assuming they were not initially present in a huge quantity. If they are not replenished by some mechanism they can be ignored. Isotopes with mean lives much longer than the duration of the experiment will produce a background that is nearly constant in time.

3.2.1   Radioactive Isotopes

Some radioactive isotopes in nature are part of a decay chain. The two most common are the ^{238}U and ^{232}Th chains. If either of these elements is present in the scintillator they will produce a series of radioactive progeny that will produce a background in the detector. The

activity from a series of decays is described by the Bateman equations [67]. They assume that the initial condition is one where there are N_o atoms of the first element and none of the products. The activity of the element n in the chain is

$$A_n = N_o \sum_{i=1}^{n} c_i e^{-\lambda_i t} \tag{3.15}$$

where the coefficient c is

$$c_i = \frac{\prod_{j=1}^{n} \lambda_j}{\prod_{i=j}^{n} {}'(\lambda_j - \lambda_i)} \tag{3.16}$$

where in the lower product the prime indicates the term $i = j$ is excluded.

Secular equilibrium occurs on time scales that are long compared to the sum of the half lives in the chain. In secular equilibrium all the elements in the chain have the same activity. If secular equilibrium is reached the concentrations of elements in the decay chains can be converted to an equivalent amount of ^{238}U or ^{232}Th. This gives a standard way of describing the concentration of all elements in the chain. However care must be taken to identify factors that can break equilibrium. This is frequently done by high mobility of radon. Once equilibrium has been broken, describing the chain with equivalent amounts of ^{238}U or ^{232}Th is no longer valid. The required purity levels for different radioactive isotopes is shown in Table 3.9. A brief description of these isotopes is given below.

^{238}U Chain

Uranium is naturally abundant in the earth's crust at a level of 1.8 ppm with 99% of that uranium being the 238 isotope. It is a long-lived radioactive isotope with a half life of 4.46×10^9 years that undergoes 14 decays (8 alpha and 6 beta) before reaching stable ^{206}Pb. The final uranium concentration of the scintillator must be below $10^{-17} - 10^{-18}$ g/g(scintillator) for the background requirement of Borexino to be met. Uranium is a problem because of the long half-lifes of itself and its progeny. The uranium chain is shown in Figure 3.4.

| Isotope	$t_{1/2}$	Decay	Source	Ambient Value	Level Needed
^{14}C	5715 y	β	Cosmogenic	$\frac{^{14}\text{C}}{^{12}\text{C}} < 10^{-12}$	$\frac{^{14}\text{C}}{^{12}\text{C}} \leq 10^{-18}$
^{7}Be	53.28 d	EC	Cosmogenic	$3 \times 10^{-2}\,\text{Bq/ton}$	$< 10^{-6}\,\text{Bq/ton}$
^{222}Rn	3.82 d	α	Air	$100\,\text{Bq/m}^3$	$< 1\,\mu\text{Bq/ton}$
^{210}Pb	22.6 y	β	Radon	Time dependent	
^{238}U	4.5×10^9 y	α	Dust	$2 \times 10^{-5}\text{g/g}$	$< 10^{-16}\text{g/g}$
^{232}Th	1.4×10^{10} y	α	Dust	$2 \times 10^{-5}\text{g/g}$	$< 10^{-16}\text{g/g}$
^{40}K	1.2×10^9 y	EC	Dust	$2 \times 10^{-6}\text{g/g}$	$< 10^{-13}\text{g/g}$
^{39}Ar	268 y	β	Air	$13\,\text{mBq/m}^3$	$< 100\,\text{nBq/m}^3$
^{85}Kr	10.73 y	β	Air	$1.4\,\text{Bq/m}^3$	$< 100\,\text{nBq/m}^3$

Table 3.9: The Borexino purity requirements. Mass fraction are given in grams of isotope per gram of scintillator. The activity of any radioactive isotope must be less than $100\,\text{nBq/m}^3$. For ^{14}C the requirement is that $\frac{^{14}\text{C}}{^{12}\text{C}} < 10^{-18}$.

^{232}Th Chain

The second most common decay chain begins with ^{232}Th which has 6 ppm abundance in earths crust. ^{232}Th goes through a series of 10 decays (6 alpha and 4 beta) before reaching ^{208}Pb. Thorium is an alpha emitter with a half life of 1.4×10^{10} years. The ^{232}Th decay chain is shown in Figure 3.5.

^{226}Ra

Radium was discovered in 1898 by Marie Curie. A Curie is defined as the decay rate of 1 gram of ^{226}Ra or 3.7×10^{10} Bq. The intrinsic radium content of materials causes them to emanate radon. The interior of a block of the material far from the surface will have radon concentration that is equal to the radium activity A_{Ra}. Roughly speaking only radon that is produced within a distance $l_D = \sqrt{D/\lambda_0}$ reaches the surface, where D is the diffusion constant of radon in the material and λ_0 the decay constant of radon. For humidified nylon $l_D = 0.2$mm.
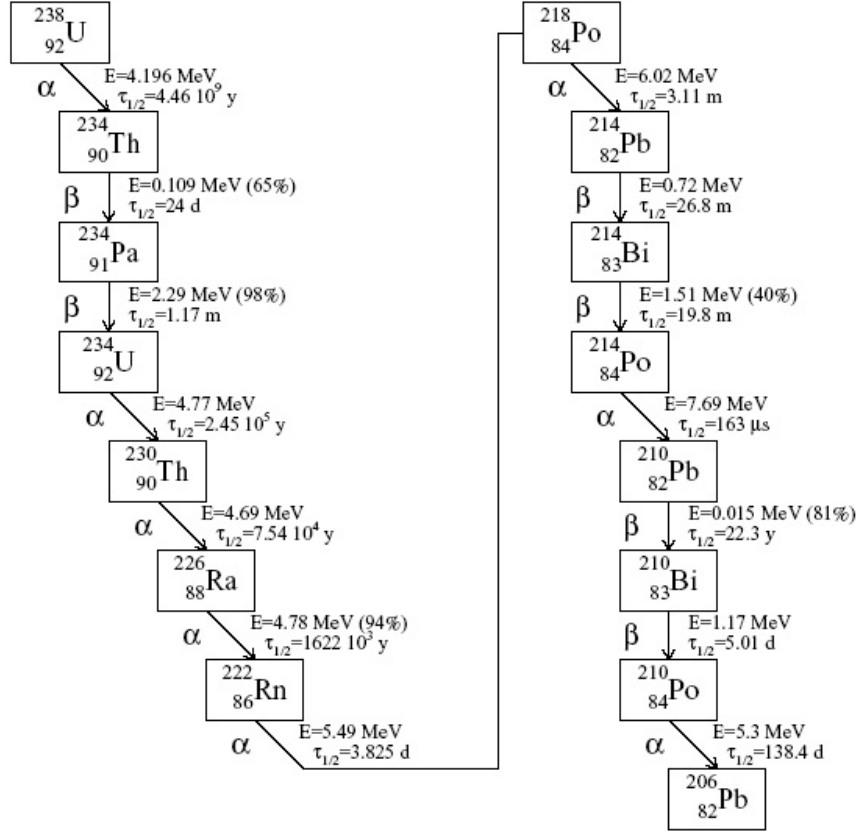
Figure 3.4: The ^{238}U decay chain.

^{222}Rn

Radon decays produce most of the activity in air. It is also the main source of radioactive exposure for humans. Its properties are typical of a noble gas, being essentially non-reactive and having a large diffusion constant making it highly mobile. A lot of effort has been put into understanding and reducing radon contamination in Borexino. Measurements have been made of radon diffusion through nylon and the partitioning of radon between nylon, pseudocumene, and water [63, 91]. Radium embedded in steel also produces radon that can emanate from the surface. Problems arising from the deposition of radon progeny on surfaces are described in Section 5.4.
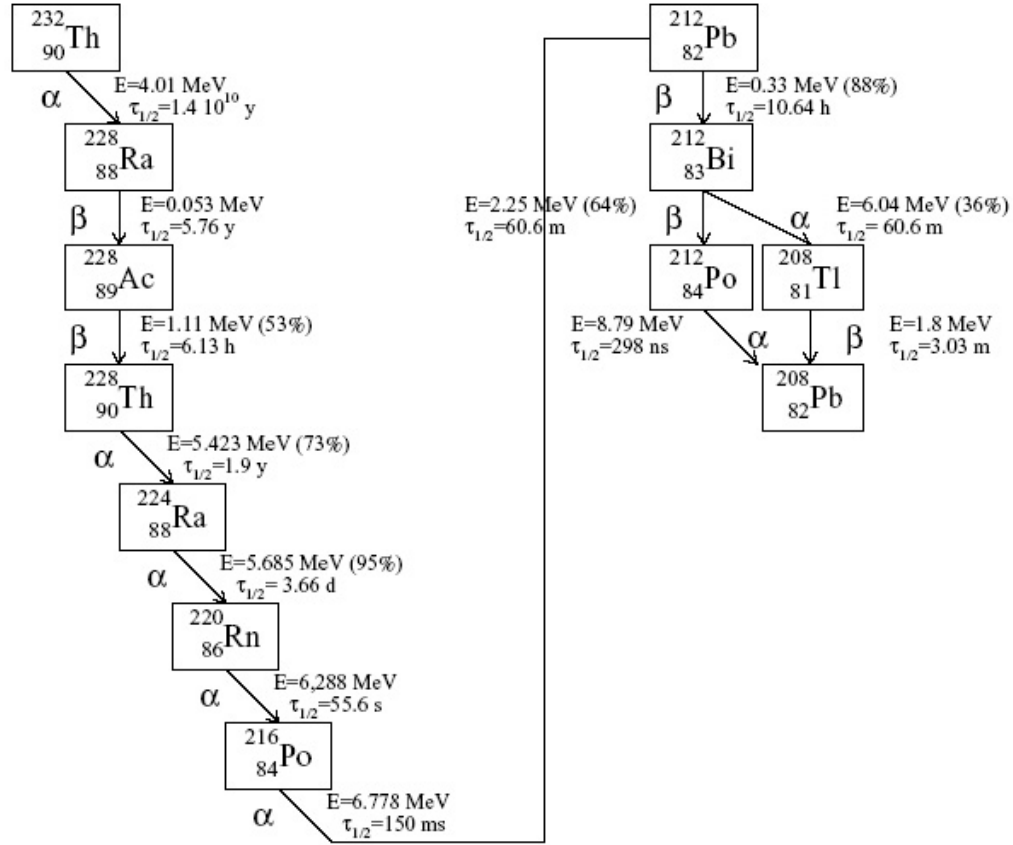
Figure 3.5: The ^{232}Th decay chain.

Though radon has a 3.8 day half-life, it undergoes a quick series of decays until it reaches ^{210}Pb which has a half-life of 22.6 years. In order to get to ^{210}Pb there is a very short-lived isotope of ^{214}Po which decays with a half life of 163 μs. Because this decay happens so fast it can be correlated with the previous decay of ^{214}Bi to form a tagged event. The number of these coincidences reveals the amount of radon in the scintillator. Once the total number of decays from the radon chain are known they can be subtracted as background from the total scintillator rate.

Radon must be removed from the ground water at LNGS before it can be used for water extraction. The solubility of radon in water is shown in Figure 3.6. The solubility of radon
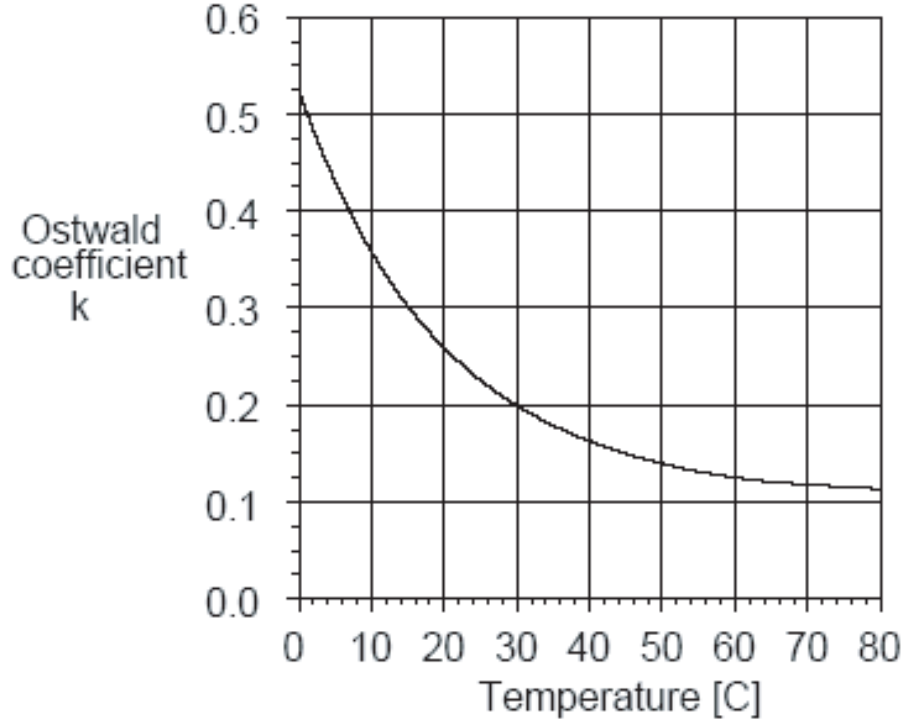
Figure 3.6: The radon solubility in water. $k = C_w/C_a$ is the Ostwald coefficient which is the ratio of the volume concentration in water to the concentration in air.

in pseudocumene is shown in Figure 3.7. Compared to water, radon is highly soluble in pseudocumene. Radon solubility was measured in pseudocumene in a temperature range from 290-301 K. The solubility χ, when defined as the mole fraction of radon in air to the mole fraction in pseudocumene is

$$\chi = \exp[2342.2/T - 10.717] \tag{3.17}$$

where T is the temperature in Kelvin [100]. At 285 K, which is the temperature of the underground labs at LNGS the, solubility is 0.082 meaning the radon favors the PC by a factor of 12.2:1.

Figure 3.7: The radon solubility in pseudocumene as a function of temperature. The solubility χ is the ratio of the mole fraction in liquid to the mole fraction in air [100].

^{210}Pb

Lead is a byproduct of radon. It has a low energy 15 keV beta decay and a 22.3 year half life. Though the decay energy of ^{210}Pb is well below the threshold for the experiment, it produces two radioactive elements that have decays at 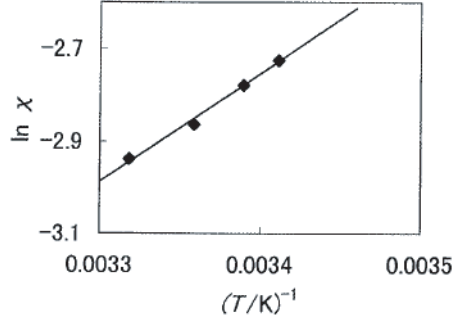energies of interest, ^{210}Bi and ^{210}Po. These isotopes will be continually produced as long as ^{210}Pb is present in the detector.

^{210}Po

Polonium is highly reactive and also toxic. It alpha decays with an energy of 5.4 MeV and a half life of 138.38 days. CTF III data indicate that there is a significant ^{210}Po contamination on the nylon vessel and in the scintillator. It is most likely due to ^{210}Pb contamination because there is more ^{210}Po activity than ^{214}Bi-Po activity which would be present if radon was the source.

^{14}C

While most impurities can be chemically removed from the scintillator ^{14}C is a special case because carbon is itself a part of the scintillator. Pseudocumene has the chemical formula C_9H_{12}. To remove the ^{14}C one would have to do an isotropic separation based on the mass

difference of the ^{14}C and ^{12}C which is impractical for a large volume of liquid. Fortunately the endpoint of ^{14}C is 156.5 keV which is below the Borexino energy window. However the finite energy resolution of the detector means that some of these decays are reconstructed with energies above the 200keV cutoff. Since there is no way to remove ^{14}C and the half life of 5717 years is too long for it to decay away, the raw material the scintillator is produced with must have a low initial ^{14}C concentration. This was ensured by selecting petroleum deposits that had been deep underground for millions of years preventing cosmogenic production of new ^{14}C from ^{14}N while allowing the existing ^{14}C in it to decay away.

^{11}C

This radioactive isotope of carbon is produced by cosmogenic muon interactions. It has a half life of 20.3 minutes decaying through EC with and energy of 1.982 MeV. ^{11}C is a problem for measuring the higher energy *pep* neutrinos. Since the production of ^{11}C occurs only along the muon track, vetoing a region around this track for a period after the muon passes through can eliminate these events with out drastically reducing the detector live time [50].

^{39}Ar

^{39}Ar which has a half life of 268 years, is commonly used for dating ground water. ^{39}Ar is produced cosmogenically from ^{40}Ar. Argon is a concern because it is present in the nitrogen used for a cover gas and sparging operations.

^{85}Kr

^{85}Kr is produced by cosmic ray interactions with ^{84}Kr which has a 57% isotopic abundance. However, atomic tests and nuclear reactor reprocessing centers have increased the activity many orders of magnitude over the natural background. ^{85}Kr is a 687 keV beta emitter with a 10.73 year half-life. Krypton is also present in the nitrogen used for a cover gas and sparging operations.

Nylon Vessel Radon Analysis

Borexino uses the nylon vessels as a barrier to prevent radon from reaching the fiducial volume. The effectiveness of the barrier is determined by the reduction of the radon concentration across a thin nylon membrane. Diffusion in an isotropic, homogenous media is governed by Fick's Law

$$\vec{\Phi} = -D\nabla\rho \tag{3.18}$$

where $\vec{\Phi}$ is the flux, D is the diffusion constant, and ρ is the density of radon. This can be combined with the continuity equation

$$\nabla \cdot \vec{\Phi} = -\frac{\partial\rho}{\partial t} \tag{3.19}$$

to get the diffusion equation

$$\frac{\partial\rho}{\partial t} = D\nabla^2\rho. \tag{3.20}$$

When dealing with radon there is a source term A_{Rn} due to the decay of radium embedded in the material, and a loss due to radon decay equal to its decay constant times density.

$$\frac{\partial\rho}{\partial t} = D\nabla^2\rho - \lambda_0\rho + A_{\text{Ra}} \tag{3.21}$$

where λ_0 is the decay constant of radon. There will be a steady state solution on time scales much longer than the radon mean life of 5.5 days if the system is left undisturbed. In this case the radon density is constant in time

$$\frac{\partial\rho}{\partial t} = 0. \tag{3.22}$$

The nylon vessels in Borexino exhibit spherical symmetry so the equation can be solved in spherical coordinates

$$0 = \left[\frac{\partial^2}{\partial r^2} + \frac{2}{r}\frac{\partial}{\partial r} - \frac{1}{l_D^2}\right]\rho + \frac{A_{\text{Ra}}}{D} \tag{3.23}$$

where the diffusion length $l_D = \sqrt{D/\lambda_0}$ is the average distance a radon atom will travel before it decays. Let the inner vessel have radius R_1 with thickness d, and the outer vessel have radius R_2 with thickness d, and the sphere have inner radius R_3. At the boundaries

$r_i \in \{R_1, R_1 + d, R_2, R_2 + d\}$ where the pseudocumene and the nylon are in contact, the flux must be equal.

$$D_{pc}\frac{\partial \rho_{pc}(r_i)}{\partial r} = D_{ny}\frac{\partial \rho_{ny}(r_i)}{\partial r} \tag{3.24}$$

where subscripts PC and Ny refer to pseudocumene and nylon respectively. At the sphere there is a constant inward flux due to emanation. Also the ratio of the density at either side of the boundaries is equal to the solubility.

$$\rho_{PC}(r_i) = S\rho_{Ny}(r_i) \quad \forall \; i \tag{3.25}$$

where S is the solubility between pseudocumene and nylon. These boundary conditions can be used to solve the differential equation whose solutions are spherical Bessel functions of the first kind $J_n(r)$.

It is perhaps more intuitive to examine the one-dimensional case of radon diffusion across a nylon barrier of thickness d. We want to find the radon concentration on one side of a nylon film given a radon concentration ρ_0 on the other side. Take the case where there is no radium in the nylon, $A_{\mathrm{Ra}} = 0$. The diffusion equation can then be written as

$$\frac{\partial \rho}{\partial t} = \frac{\partial^2 \rho}{\partial x^2} - \lambda_0 \rho. \tag{3.26}$$

Under steady state conditions ($\frac{\partial \rho}{\partial t} = 0$), the radon concentration within the nylon barrier is

$$\rho(x) = S\rho_0 \frac{\sinh[(d-x)/l_D]}{\sinh(d/l_D)} \tag{3.27}$$

where S is the relative solubility of the nylon and $l_D = \sqrt{D/\lambda_0}$. The permeability of a barrier is the product of the diffusion constant and relative solubility

$$P = DS \tag{3.28}$$

If the atoms decay then a modification can be made to get an effective permeability

$$P_{\mathrm{eff}} = DS\frac{d}{l_D \sinh d/l_D}. \tag{3.29}$$

The flux in one dimension the flux Φ can be found at both edges of the barrier. The flux entering the barrier is

$$\Phi_{in} = \frac{\rho_0 DS}{l_D}\coth(d/l_D) = \rho_0\frac{P_{\mathrm{eff}}}{d}\cosh\alpha d \tag{3.30}$$

and more interestingly the flux exiting the barrier is

$$\Phi_{out} = \frac{\rho_0 DS}{l_D \sinh d/l_D} = \rho_0 \frac{P_{\text{eff}}}{d}. \tag{3.31}$$

The time T taken to cross the barrier is

$$T = \frac{d^2}{6D} \tag{3.32}$$

The barrier attenuation factor χ is the ratio of the radon concentration on either side of the membrane. In steady state for a spherical geometry the attenuation factor is

$$\chi = \frac{\rho_{in}}{\rho_0} = P_{\text{eff}} \frac{3}{Rd\lambda} \tag{3.33}$$

where R is the radius of the vessel and $R \gg d$. This solution assumes that the radon inside the vessel is instantaneously mixed. In Borexino the radon concentration in inner volume will be reduced by at least 10^7 from the level in the outer buffer with the two nylon vessels. With this reduction the fiducial volume can tolerate up to $1 \, \text{Bq/m}^3$ of radon in the outer buffer.

Emanation is taken into account when the activity of ^{226}Ra is no longer negligible. Steady state conditions are again assumed since observations can be made after periods much longer than the radon decay time.

$$D \frac{\partial^2 \rho}{\partial x^2} - \lambda \rho + A_{\text{Ra}} = 0 \tag{3.34}$$

Analyzing the situation with a semi-infinite slab of material that extends from $+\infty$ to $x = 0$, where $\rho = 0$ for $x \leq 0$ and $\rho = A_{\text{Ra}}/\lambda_{\text{Rn}}$ as $x \to \infty$. Solving to find the radon density in the slab $(x \geq 0)$

$$\rho(x) = \frac{A_{\text{Ra}}}{\lambda_{\text{Rn}}}(1 - e^{-x/l_D}) \tag{3.35}$$

The flux of radon out of the surface is then the radium activity divided by the diffusion length

$$\Phi = D \frac{\partial \rho}{\partial x}\bigg|_{x=0} = l_D A_{\text{Ra}} \tag{3.36}$$

The nylon vessels are an effective barrier against the diffusion of radon and other noble gases into the fiducial volume. However, the nylon vessels will emanate radon even in the

absence of an external source. The emanation radon from the nylon vessels as a function of humidity is shown in Figure 3.8. Emanation in nylon increases with humidity because humidity increases the diffusion constant. From a radiopurity perspective one would like the nylon to be as dry as possible, but the strength of the nylon increases with humidity. Analysis of the mechanical strength required to withstand a buoyant load and radiopurity concerns indicates that the nylon should be kept at 30% relative humidity. Diffusion constants and diffusion lengths for radon in different materials are shown in Table 3.10.
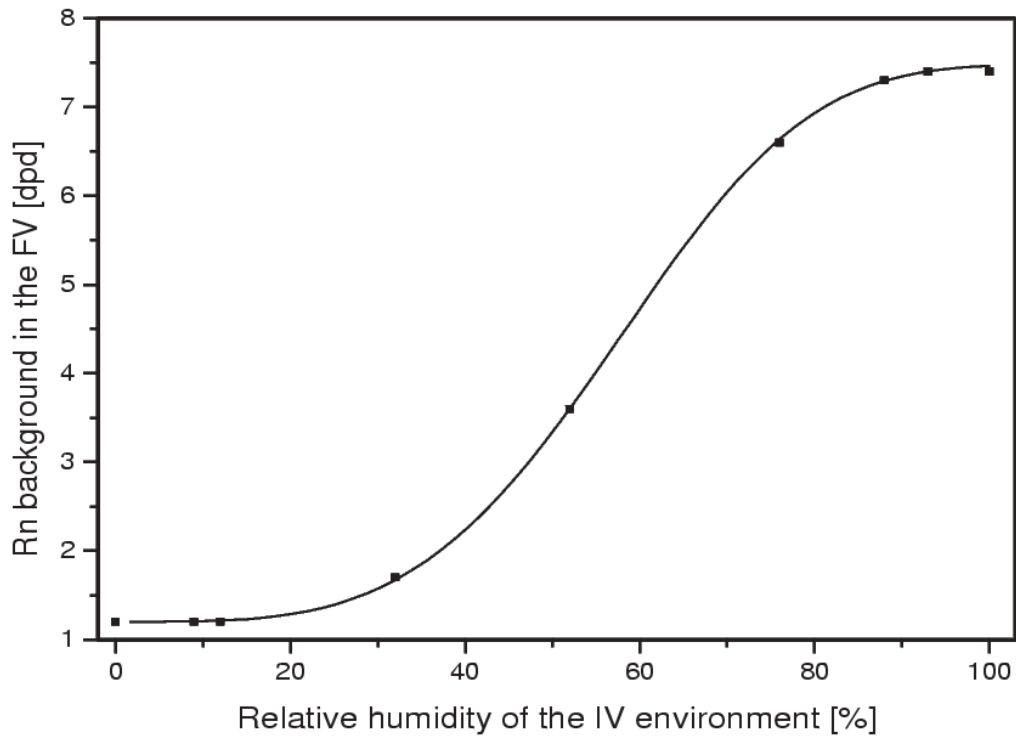

Figure 3.8: The activity in the fiducial volume in decays per day due to radon emanation from the inner nylon vessel assuming complete mixing of the scintillator. This is a worst case scenario since it is expected that Borexino will run in a static condition where mixing is minimal [101].

Material	D	l_D
	[cm^2/s]	[cm]
Pseudocumene	2×10^{-5}	3
Nylon (Dry)	$\sim 10^{-12}$	7×10^{-4}
Nylon (Wet)	$\sim 10^{-9}$	2×10^{-2}
Water	2×10^{-5}	3
Air	0.1	230

Table 3.10: Diffusion constants for ^{222}Rn. The diffusion length $l_D = \sqrt{D/\lambda_0}$ is the mean distance a radon atom will travel before it decays. The mean life for radon $\tau = \frac{1}{\lambda_0} = 4.77 \times 10^7$ s [102].

3.3 Radioactive Background Summary

The stringent cleanliness requirements for Borexino permit no more than 9μg of dirt or dust in the detector assuming dust contains ppm levels of uranium and thorium, and less than $10\,\text{cm}^3$ of air due to the presence of ^{39}Ar and ^{85}Kr. The limit on the amount of air necessitates a thorough gas purging of the detector after assembly and leak tightness of $10^{-8}\,\text{mbar L/s}$. External activity is absorbed by 6 m of layered of shielding composed of high purity water and an inactive pseudocumene based buffer. Two nylon vessels in the buffer act as barriers against the diffusion of contaminants such as radon and other noble gases.

High sensitivity composition analysis is required to determine trace levels of radioactive isotopes present in materials. Many of the measurements and techniques developed by Borexino are also useful in other low background experiments looking for neutrinos, dark matter, or neutrinoless double beta decay. In the future, identifying low levels of radioactive elements will be key to reducing backgrounds.

Scintillator Purification

The most technically difficult aspect of the Borexino experiment is the production of a large, ultra high purity target mass for neutrinos. The purification methods for Borexino must achieve high purification factors, even at extremely low scintillator contamination levels. In order to produce a large target mass thousands of cubic meters of liquid scintillator must be purified in a reasonable amount of time. This requires a purification system that uses a favorable partitioning to transfer contaminants from the scintillator to a material it is in contact with. After the scintillator is depleted of contaminants, it is extracted for use in the detector.

The Borexino purification plants were specially designed to produce a high purity pseudocumene based scintillator. This required the typical chemical resistance to solvents. Since pseudocumene is flammable with a flash point at $48\,$C the electronics and sensors in the purification plants must be explosion proof to prevent electrical arcing which could ignite the vapors. The toxicity of pseudocumene also required all the plants containing scintillator to be double-contained to prevent leaks to the environment. Pseudocumene has a short term vapor exposure limit of $35\,$ppm and experiments on rats showed that the LD50 concentration is $5\,$g/kg [103, 104].

The Borexino purification plants differ significantly from typical industrial purification plants in that they had to be leak tight to air ($< 10^{-8}\,$mbar L/s for He) to prevent the

introduction of radioactive gases ^{39}Ar, ^{85}Kr, ^{222}Rn. Dust was a concern after fabrication so they were assembled and cleaned in a low particulate environment (class 100 clean room), with low radon levels to reduce the deposition of radon progeny. The internal surfaces of the purification plants were had to be smooth to eliminate crevasses that would be difficult to clean. They are also rust resistant to prevent the surface layer from oxidizing and flaking off into the scintillator. The stainless steel parts were mechanically polished and electropolished. Those that could not be electropolished were pickled and passivated making them rust resistant and giving them a smooth finish. In addition, the entire system had to be precision cleaned after it was assembled and installed at LNGS. This cleaning involved circulating of a hot detergent solution through the system and a through rinsing. These unusual requirements required a careful selection of pumps, valves, instruments, and other components. A sketch of the Borexino purification skids is shown in Figure 4.1 and a photograph taken after assembly is shown in Figure 4.2. A diagram of the columns is shown in Figure 4.3.

The purification methods in Borexino were chosen to effectively remove a wide range of radioactive isotopes. Multiple methods are used to account for the chemistry of the different elements which vary in reactiveness, solubility, polarity, and vapor pressure. Each technique is optimized to remove impurities with certain properties. The purification operations include distillation, water extraction, nitrogen stripping, and silica gel adsorption. These techniques are described in the following sections.
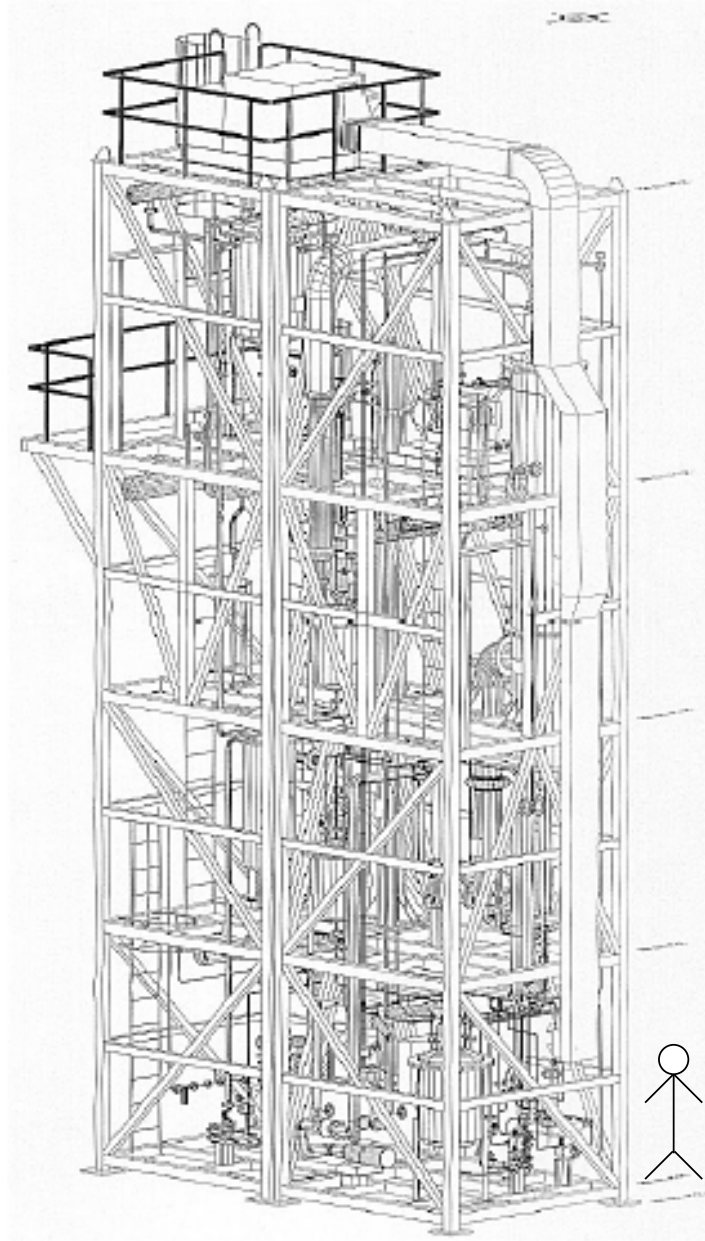
Figure 4.1: A diagram of the interior of the Borexino purification skids used to produce a high purity pseudocumene based scintillator. The four story tall unit is has been installed in Hall C at LNGS. The skids contain columns for water extraction, distillation, and nitrogen stripping. Silica gel adsorption is done in a separate plant.

Figure 4.2: A photograph of the purifications skids in the United States before they were shipped to Italy.

Figure 4.3: A diagram from the control system of Borexino purification plants showing the distillation column (C-100), water extraction column (C-200), nitrogen stripping column (C-300). Instrumentation allows the status of the plants to be monitored from the control room. The pumps and valves normally used for the purification can be operated remotely with this system.

4.1   Purification Techniques

Large-scale purification techniques are based on the preference of a contaminant to be in one phase over another. They utilize the different materials to draw contaminants into a separate phase that can then be discarded. Phases in this case can be a gas, immiscible liquid, solid, or an adsorbed or interfacial phase. The ratios of concentrations in each phase at equilibrium are typically expressed as a partitioning constant K, distribution coefficient m, or some equivalent ratio. The equilibrium partitioning constant $K_{i\alpha\beta}$ is defined as

$$K_{i\alpha\beta} = \frac{\text{Concentration of } i \text{ in phase } \alpha}{\text{Concentration of } i \text{ in phase } \beta} = \frac{C_{i\alpha}}{C_{i\beta}} \tag{4.1}$$

which is simply the ratio of the concentrations of component i in each phase. The units of the partition constants vary depending on the units the concentrations are expressed in and are not necessarily unitless. Common units for concentration are mole fraction x [unitless], mass fraction X [unitless], molar concentration C [mol/m^3], and mass concentration ρ [kg/m^3]. A mole (mass) fraction is the moles (mass) of impurity divided by the total moles (mass) of substance. By convention x and X will denote the liquid phase concentrations while y and Y will denote the gas phase concentrations. Adsorbed phase concentrations are often expressed in fractional surface coverage θ, or a surface density σ with units of [mol/m^2]. In terms of the free energy, the partition constant has the form

$$K_{i\alpha\beta} = Ae^{-\Delta G_i/RT} \tag{4.2}$$

where ΔG_i is the free energy of the transfer of i from phase α to phase β, and A is a constant. The partitioning is dependent on the chemical properties of the compounds involved as well as the temperature T. A few common purification methods are shown in Table 4.1.

In practice, large-scale purification often takes place inside tall cylindrical columns. The columns usually contain plates or packing material that create a large contact area and ensure good mixing. The columns are usually designed to achieve a specified purity, given the constraints on processing speed, space, cost, energy, material consumption, etc. These columns are modeled as having a number of stages where equilibrium is achieved. An equilibrium stage is a section of the column where a local equilibrium between the phases

Method	Property Used
Liquid Extraction	Liquid Solubility
Gas Stripping	Gas Solubility
Adsorption	Binding Energy
Distillation	Vapor Pressure
Vacuum Degassification	Gas Solubility

Table 4.1: Various methods used for large scale purification and the physical properties they rely on.

is achieved. Though equilibrium is not actually achieved in practice the idea of equilibrium stages provides a convenient way to calculate purification factors. The stage efficiency is the ratio of the achieved partitioning to what one would get in full equilibrium. It is a function of the flow rates, packing material, and mixing within the column.

Columns where two materials come into contact can be run in different configurations. The flows can be parallel to each other, perpendicular to each other at each stage in a cross-current mode, or antiparallel to each other in a counter-current mode. The rate of transfer between the two materials is maximized by having the largest concentration difference at each point of contact. This is best accomplished with a counter-current configuration. This way the solvent is purest as it enters the column mixing with the purest feed just as it leaves, and dirtiest when it contact the initial feed stream at the other end. Hence it is able to purify effectively along the entire length of the column. Counter-current flow uses less solvent than other configurations to achieve the same purity.

If all the partitioning constants are known, as well as the number of equilibrium stages then the purification factor can be calculated. In most applications, the chemical properties of the solute are known. When this is the case the appropriate purification techniques can be easily selected. In Borexino, however, the chemical forms of all the impurities except for the radioactive noble gases are unknown. This is often the case with elements that are created from a radioactive decay. In the uranium and thorium chains the progeny are produced in high energy decays. The nuclei are often created in an ionized state, and are able to ionize and excite molecules along their trajectory. This is a result of the kinetic decay energy of

the nucleus being large compared with the molecular binding energy of the surrounding particles. These decay products are often charged in a highly reactive local environment making their chemical binding difficult to predict. In addition the chemical properties of elements produced in minute quantities are poorly known. Different molecular states of the impurities can drastically affect the partitioning and thus the purification efficiency.

Borexino will use a combination of techniques to remove impurities from the scintillator including filtration, water extraction, nitrogen stripping, and distillation [105]. These target particulates, metallic impurities, dissolved gases, and chemical impurities respectively. The physical and chemical mechanisms they rely on are described below.

4.2 Thermodynamics of Phase Equilibrium

A system with multiple phases that are in equilibrium will generally have a different concentration of components in each phase. The concentration in each phase is determined by the minimization of the energy of the system. The equilibrium compositions determine the partitioning constant for the system.

Macroscopic systems are well described by thermodynamic quantities such as temperature T, pressure P, and entropy S. The change in internal energy of a system dE is the sum of the heat entering the system dQ and the work done on the system dW. The change of the system's energy given by the first law of thermodynamics is

$$dE = dQ + dW \tag{4.3}$$

where dQ is the heat added to the system and $dW = -PdV$ is the work done on the system. The second law of thermodynamics tells us that the entropy S of a system increases,

$$dS \geq \frac{dQ}{T} \tag{4.4}$$

where T is the temperature of the system. The entropy S is also proportional to the number of states accessible to a system.

$$S = k_B \ln \Omega \tag{4.5}$$

where Ω is the number of accessible states. Combining Equations 4.3 and 4.4, the change in energy of the system is

$$dE \leq TdS - PdV \tag{4.6}$$

This says that for processes where the entropy and volume are held constant, the change in energy will be negative. At equilibrium the energy will be at a minimum. In real situations it is easier to hold some variables constant than others. Free energies are useful for situations when certain parameters are particularly easy to control. The minimization of the free energies then determines the state of the system. The Helmholtz free energy F is minimized for processes done at constant T and V.

$$F = E - TS \tag{4.7}$$

The enthalpy H is the sum of the internal energy plus work done on the system. It is at a minimum for processes with constant pressure P and entropy S.

$$H = E + PV \tag{4.8}$$

The Gibbs free energy G is minimized for systems where changes occur at constant temperature T and pressure P.

$$G = E + PV - TS = H - TS \tag{4.9}$$

The Gibbs free energy is a useful quantity since experimentally it is easy to operate at a constant temperature and pressure. Water extraction and nitrogen stripping are both roughly done under these conditions. The contaminants lower the Gibbs free energy by moving out of the scintillator. The total differential for the Gibbs free energy is

$$dG = dE + PdV + VdP - TdS - SdT \tag{4.10}$$

Using equation 4.6 one finds

$$dG \leq VdP - SdT \tag{4.11}$$

The terms dP and dT are zero since P and T are constant thus

$$dG \leq 0 \tag{4.12}$$

For irreversible reactions dG will be negative and $dG = 0$ if the reaction is reversible. The Gibbs free energy of a system will be at a minimum when the system is in equilibrium. The Gibbs free energy is also a function of the composition of a system.

$$G = \sum_i n_i \mu_i \tag{4.13}$$

where μ_i is the chemical potential , and n_i is the number of molecules of component i. The chemical potential μ_i is the energy necessary to add one atom or molecule of component i to a system. It is defined as

$$\mu_i = \left[\frac{\partial G}{\partial n_i}\right]_{T,P,n_{j \neq i}}. \tag{4.14}$$

At equilibrium the chemical potential of each component in each phase will be equal.

$$\mu_{i\alpha} = \mu_{i\beta} \tag{4.15}$$

This implies the chemical potential of a species is constant throughout the system at equilibrium. For an ideal gas the chemical potential is

$$\mu_i^{gas} = \mu_i^* + RT \ln \frac{\phi_i p_i}{P} \tag{4.16}$$

where μ_i^* is the chemical potential of a reference state, often chosen to be the pure compound, and p_i is the partial pressure. The fugacity coefficient ϕ_i accounts for deviations from the ideal state. The fugacity is defined as $f_i = \phi_i p_i$. For a liquid the chemical potential is

$$\mu_i^{liquid} = \mu_i^* + RT \ln \gamma_i x_i \tag{4.17}$$

where γ_i is the activity coefficient which accounts for deviations from ideality, and x_i is the mole fraction.

The Gibbs phase rule determines how many variables are required to describe the state of a system. The Gibbs phase rule states that

$$v = c - p + 2 \tag{4.18}$$

where v is number of degrees of freedom of the system, c is the number of chemically independent species, and p is the number of phases. One variable is needed for each degree of

freedom. For example, in a binary liquid-vapor equilibrium there are two species and two phases, and thus there are two independent variables. They can be chosen from the temperature, total pressure, vapor composition, or liquid composition. Once two are selected the other two variables are determined.

4.3 Purification Rates

The speed of purification processes is limited by how quickly the phases equilibrate. It is described by a relaxation time which is the characteristic time scale for a system to approach equilibrium. The relaxation time is determined by the rate which molecules are transferred from one phase to another. The flux is driven by diffusion along concentration gradients. Any active mixing or agitation will speed up this process.

The molecules must also cross an interface to the adjacent phase. This is one instance where it can be favorable for molecules to move across an interface into a phase where there is a higher concentration. The concentration on either side of the interface is determined by the relative solubility. Mass transfer coefficients are used to describe the particle flux across interfaces. They are useful because they do not require knowledge of the precise concentration gradients at the interfaces that are difficult to measure.

4.3.1 Diffusion

Diffusive motion can be derived by assuming a random force $F(t)$ on a spherical particle in a fluid. The motion of the particle in each dimension is described by

$$m\ddot{x} = -6\pi\mu r\dot{x} + F(t) \tag{4.19}$$

where r is the radius of the particle and μ is the viscosity. The term $6\pi\mu r\dot{x}$ is a damping force proportional to the velocity. The above equation can be rewritten as

$$m\left(\frac{d}{dt}(x\dot{x}) - \dot{x}^2\right) = -6\pi\mu rx\dot{x} + xF(t). \tag{4.20}$$

Taking the time average of x and $\dot{x}$ quantities and using the facts that $\langle xF(t) \rangle = 0$ and $\frac{1}{2}m\langle \dot{x}^2 \rangle = \frac{1}{2}kT$, one finds

$$\left(\frac{d}{dt} + \frac{6\pi\mu r}{m} \right) \langle x\dot{x} \rangle = \frac{kT}{m}. \tag{4.21}$$

Defining a time scale

$$\tau = \frac{m}{6\pi\mu r} \tag{4.22}$$

the equation can be solved given the initial condition that there is no displacement at $t = 0$ to find

$$\langle x\dot{x} \rangle = \frac{kT}{6\pi\mu r}(1 - e^{-t/\tau}). \tag{4.23}$$

Since

$$\langle x\dot{x} \rangle = \frac{1}{2}\frac{d}{dt}\langle x^2 \rangle \tag{4.24}$$

the equation for $\langle x^2 \rangle$ can be integrated over time to get

$$\langle x^2 \rangle = \frac{2kT}{6\pi\mu r}\left[t - \tau(1 - e^{-t/\tau}) \right]. \tag{4.25}$$

In the limit $t \ll \tau$

$$\langle x^2 \rangle = \frac{kTt^2}{m}. \tag{4.26}$$

In the limit $t \gg \tau$

$$\langle x^2 \rangle = \frac{kTt}{3\pi\mu r} \tag{4.27}$$

which describes the process of diffusion. The diffusion constant is

$$D = \frac{kT}{3\pi\mu r}. \tag{4.28}$$

4.3.2 Mass Transfer at Interfaces

While Fick's law describes diffusive transport in a bulk material, complications arise at interfaces. The concentrations at interfaces can change rapidly in short distances and are not generally known. Due to the partitioning constant, a species can preferentially move across an interface to a phase where it is at a higher concentration. Transfer across interfaces is described by the mass transfer coefficients. It assumes diffusion occurs in small regions

Flux [mol/m²s]	Driving Potential	Mass Transfer Coefficient
Gas		
$N_A/S = k_G \Delta p_A$	p_A [Pa]	k_G [mol/m² s Pa]
$N_A/S = k_y \Delta y_A$	y_A [mole fraction]	k_y [mol/m² s mole fraction]
$N_A/S = k_c \Delta C_A$	C_A [mol/m³]	k_c [m/s]
$W_A/S = k_c \Delta Y_A$	Y_A [kg A/kg B]	k_y [mol/m² s ΔY]
Liquid		
$N_A/S = k_L \Delta C_A$	C_A [Pa]	k_L [m/s]
$N_A/S = k_x \Delta x_A$	x_A [mole fraction]	k_x [mol/m² s mole fraction]

Table 4.2: The rate laws and transfer coefficients for diffusion through a stagnant film. Conversions between the liquid coefficients are: $k_G = k_y/P_T = k_C/RT = k_y/Mp_{BM}$. The log-mean driving force is $p_{BM} = \frac{p_{B2}-p_{B1}}{\ln(p_{B2}/p_{B1})}$. For liquids $k_L C = k_x$. [106]

around the interface where the change in concentration can be approximated as linear. Assume a single film boundary such as a fluid in contact with a solid. Across that interface

$$\frac{N_A}{S} = -D\frac{dC_A}{dz} = D\frac{C_{A2} - C_{A1}}{z_F} \tag{4.29}$$

Here N_A is in moles per second of component A, S is the area, D the diffusion constant, C_{A1} the concentration in the bulk material, C_{A2} is the concentration at the surface, and z_F the effective film thickness. The diffusion constant and film thickness are combined into the mass transfer coefficient k_C.

$$\frac{N_A}{S} = \frac{D}{z_F}(C_{A2} - C_{A1}) = k_C \Delta C_A \tag{4.30}$$

where k_C has units of velocity. Depending on the concentration units, the mass transfer coefficients have the units shown in Table 4.2.

The film thickness z_F is dependent on the flow in the system. However, limits on the film thickness can be estimated. For turbulent flows, the velocity of a liquid tends to be no more than $1\,\mathrm{m/s}$ and for a gas less than $10\,\mathrm{m/s}$. Diffusion constants for gases tend to be about $10^{-5}\,\mathrm{m^2/s}$ and $10^{-9}\,\mathrm{m^2/s}$ for liquids to within an order of magnitude. The Schmidt number is a dimensionless quantity that is a ratio of the inertial to diffusive forces.

$$Sc = \frac{\mu}{\rho D} \tag{4.31}$$

where here μ is the viscosity, and ρ is the density. The Schmidt number clusters around 1 for gases and 1000 for liquids. For situation with high turbulence (large Reynolds number), the mass transfer coefficient is [106]

$$k_C = 0.036 v Re^{-0.2} Sc^{-0.67} \tag{4.32}$$

where Re is the Reynolds number. The mass transfer constant has an upper limit in gases of roughly $k_C \sim 10^{-2}$ m/s, and in liquids an upper limit of $k_C \sim 10^{-5}$ m/s for highly turbulent flow. The film thickness is related to the mass transfer coefficient by

$$z_F = \frac{D}{k_C} \tag{4.33}$$

Highly turbulent flows correspond to minimal film thickness of $z_F \sim 10^{-3}$ m in gas, and $z_F \sim 10^{-4}$ m in liquid.

To determine the rate of purification processes, the mass transfer rate between two different phases is required. Two-film theory explains the transfer between a gas and liquid phase or two immiscible liquids in terms of two film resistances. Take a gas-liquid system that is in equilibrium when

$$y_{Ai}^* = m x_{Ai}^* \tag{4.34}$$

Here the subscript i denotes the concentration at the interface, y and x represent the liquid and gas concentrations respectively, and m is the local slope of the equilibrium curve. The asterisk indicates equilibrium values. The rate law can then be expressed as

$$\frac{N_A}{S} = K_{oy}(y_A - y_A^*) \tag{4.35}$$

$$\frac{N_A}{S} = K_{ox}(x_A^* - x_A) \tag{4.36}$$

The overall mass transfer coefficients K_{oy} and K_{ox} are the amplitudes of the transfer rate. x_A^* and y_A^* indicate the values at the interface are in equilibrium with bulk concentrations of the other phase, which are generally known. The overall mass transfer coefficients are related to the individual mass transfer coefficients of each phase by

$$\frac{1}{K_{oy}} = \frac{1}{k_y} + \frac{m}{k_x} \tag{4.37}$$

$$\frac{1}{K_{ox}} = \frac{1}{mk_y} + \frac{1}{k_x} \tag{4.38}$$

The terms $\frac{1}{K_{oy}}$ and $\frac{1}{K_{ox}}$ are called the overall resistances. These resistances can be summed like electrical resistances. If $m \ll k_x$ then

$$\frac{1}{K_{oy}} \approx \frac{1}{k_y} \tag{4.39}$$

and the resistance is mostly in the gas phase. This is the case for a highly soluble gas. In the opposite case where m is large

$$\frac{1}{K_{ox}} \approx \frac{1}{k_x} \tag{4.40}$$

and the liquid resistance dominates.

4.4   Scintillator Filtration

The scintillator for Borexino is filtered to remove any particles that are suspended in the fluid. Filters are located at multiple positions within the purification plants. Borexino uses Teflon filters made by Mykrolis and Pall with a nominal pore size of 50 nm. Teflon is the trade name for polytetrafluoroethylene or PTFE, a hydrophobic material. The filters are cylinders roughly 25 cm long with an 10 cm diameter. The filters have a nominal membrane area of about $1\,\text{m}^2$, though the actual surface area resulting from the pores is many times larger.

All filters have a distribution of pore sizes. A good filter will have a narrow pore size distribution around the peak value. This will stop most of the larger particles from penetrating the filter without creating an unnecessarily large resistance to the flow. The efficiency of a filer is determined by the reduction of particles of a particular size when a fluid passes through the filter. The efficiency naturally varies with the size of the particle. The final particulate content is determined by the filter efficiency and the original size distribution of particulate in the scintillator.

The Borexino detector can tolerate at most $9\,\mu\text{g}$ of dust in the fiducial volume. The average density of dirt is $2.7\,\text{g/cm}^3$ and the activity is about $1\,\text{kBq/kg}$. A spherical piece of dust that weighed $9\,\mu\text{g}$ would have a diameter of $18\,\mu\text{m}$. Of course dust has a wide

distribution of sizes so a significant number of smaller dust particles passing through the filter is also a concern. Shape distributions also matter since particles only need to clear a pore along their two smallest dimensions. Contamination issues for the filters are discussed in Section 5.4.4.

4.5 Water Extraction

Borexino uses water extraction as one of the methods to purify the scintillator. The purification skids contain a countercurrent water extraction column where the water is added to the top and the feed of pseudocumene is inserted at the bottom. After mixing with the water, the pseudocumene separates and floats to the top of the column where it is removed. Water is drained from the bottom. The column is $25\,\mathrm{cm}$ diameter x $5\,\mathrm{m}$ tall and is filled with Koch structured stainless steel packing to increase the fluid contact area and mixing. The packing has a total surface area of roughly $100\,\mathrm{m}^2$. The water extraction column is shown in Figure 4.4.

Liquid-liquid extractions place two immiscible liquids in contact in order to to transfer a solute to the liquid with the higher affinity. The different affinities are due to the relative strengths of the intermolecular forces between an impurity and surrounding liquid. Water extraction takes advantage of the relative polarity of the molecules. Polar molecules have permanent regions that are electron-rich or electron-poor. Forces acting locally between these charged regions dominate polar molecular interactions. Nonpolar molecules are those whose primary interactions arise from van der Waals forces. Van der Waals forces are comprised of the London dispersion forces, Debye forces, and Keesom forces.

$$F_{vdW} = F_{London} + F_{Debye} + F_{Keesom} \tag{4.41}$$

Van der Waals interactions are described by the Lennard-Jones potential

$$V_{LJ} = 4\epsilon \left[\left(\frac{\sigma}{r} \right)^{12} - \left(\frac{\sigma}{r} \right)^{6} \right] \tag{4.42}$$

where ϵ and σ are constants with units of energy and distance respectively. The r^{-12} term is an empirical term that accounts for the repulsive force at short distances. The potential

is shown in Figure 4.5. The London dispersion force is an attractive force that acts on all molecules. It results from the random fluctuations of electrons. A temporary dipole results from the asymmetry caused by random fluctuations in the electronic distribution. This temporary dipole induces a dipole in adjacent molecules which results in an attractive force. The London dispersion force is weaker than the other forces and its strength increases with molecular weight. Its contribution to the constant in the $-1/r^6$ term is

$$V_{London} \sim -\alpha_1 \alpha_2 \frac{I_1 I_2}{I_1 + I_2} \frac{1}{r^6} \tag{4.43}$$

where α_i is the polarizability of the atom i and I is the ionization energy [60]. Debye forces are the result of a permanent dipole inducing a dipole moment in adjacent molecules.

$$V_{Debye} \sim -(\mu_1^2 \alpha_2 + \mu_2^2 \alpha_1) \frac{1}{r^6} \tag{4.44}$$

where μ_1 is the dipole moment and μ_2 is an induced dipole moment. Keesom forces arise from dipole-dipole interactions.

$$V_{Keesom} \sim -\frac{\mu_1^2 \mu_2^2}{3 k_B T} \frac{1}{r^6} \tag{4.45}$$

The potential energy of two dipoles a distance r apart is

$$U = \frac{\mu_1 \mu_2}{r^3} [2 \cos \theta_1 \cos \theta_2 - \sin \theta_1 \sin \theta_2 \cos \phi] \tag{4.46}$$

where θ is the dipole angle with respect to the vector between the dipoles and ϕ is the azimuthal angle of the second dipole with respect to the first [107]. The force between the dipoles is of course $F = -\nabla U$. The chemical potential can be thought of as the energy required to move a molecule subjected to this force into the system. The chemical potential will be constant throughout the system at equilibrium.
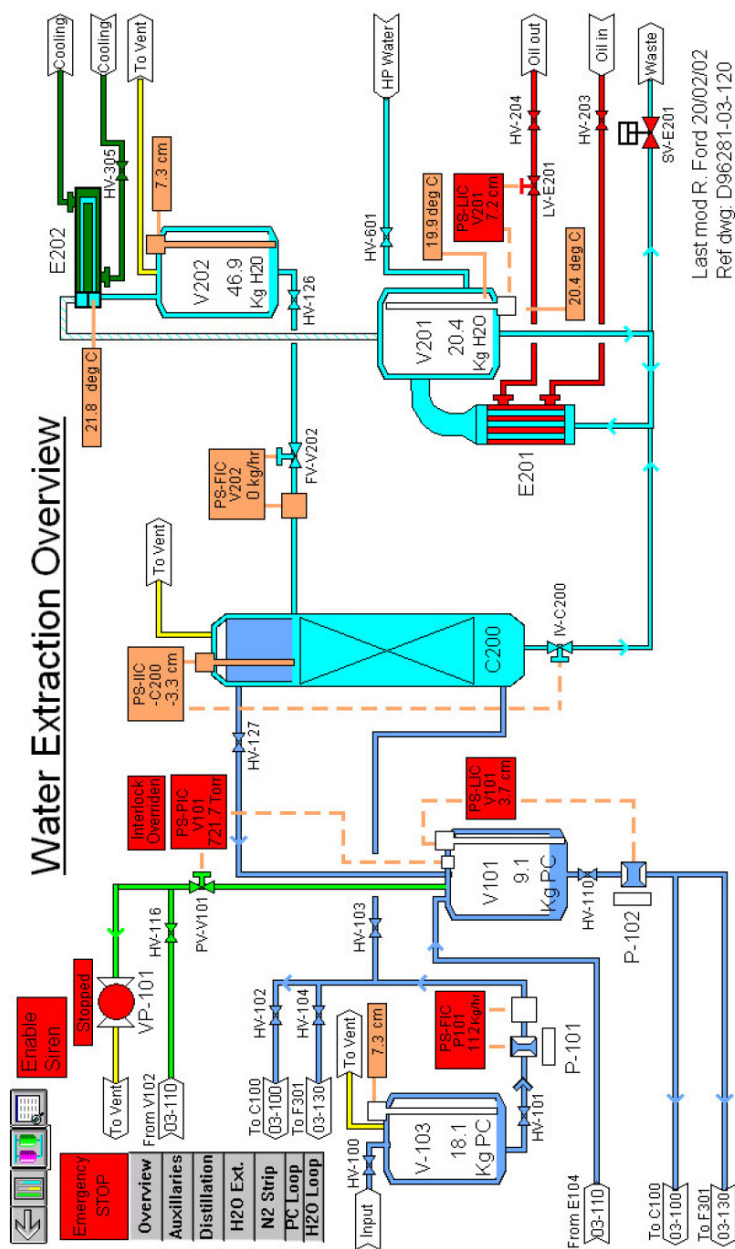
Figure 4.4: The Borexino water extraction column (C200). The extraction column can process 1000 L/h of PC. High purity water flows in near the top of the column (FV-V202) while scintillator enters at the bottom (HV-103). The purified scintillator is removed from the top of the column (HV-127) after it separates. A distillation unit (E201) continuously purifies the water used for the extraction.
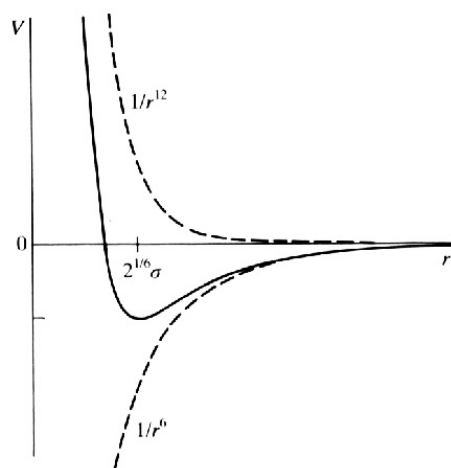
Figure 4.5: The Lennard-Jones potential which describes van der Waals interactions. $V_{LJ} = 4\epsilon \left[\left(\frac{\sigma}{r}\right)^{12} - \left(\frac{\sigma}{r}\right)^{6} \right]$. The strength of the attraction is given by ϵ and the equilibrium separation occurs at $2^{1/6}\sigma$.

Atoms and molecules that are ionic or polar prefer being surrounded by polar water molecules over nonpolar scintillator. Water extraction is thus expected to be effective in removing polar impurities such as metal ions from the scintillator. On the other hand, it is more energetically favorable for a noble gas to reside in the nonpolar scintillator over water. For example, the change in free energy to move an ion with a $10\,\text{nm}$ radius from pseudocumene to water is $\Delta G = 2.9\,\text{eV}$. This large free energy means ions strongly prefer the water phase. Radioactive decay products are often produced in an ionized state. For positive ions of lead, bismuth, and polonium, which have slightly larger radii depending on their charge state, the free energy of this transfer will be reduced by up to 40%.

From a macroscopic perspective, the molecular interactions will lead to different impurity concentrations in the two liquids. The extraction can be modeled as a mixture of scintillator, water, and an impurity. A three component system can be described by a triangular diagram shown in Figure 4.6. This type of representation is useful because for any point in the diagram, the sum of the fractional compositions of the three components equals one. In the diagram each vertex represents one component of the system. The fractional composition of each component is determined by the position in the diagram.

Partitioning between immiscible liquid-liquid systems can be conveniently represented on a triangular diagram, shown in Figure 4.7, where for clarity the grid has been left off. A triangular diagram can describe what happens in a single stage liquid-liquid extraction where the two liquids in contact have reached equilibrium. In the case of Borexino, scintillator (A) and water (B) would be represented by the bottom left and bottom right corners on the triangle. The impurity (C) that is to be removed from the scintillator is represented by the top vertex. Pairs of points on the solubility curve connected by tie-lines represent two phase mixtures. In the region above the solubility curve the system is in a single homogeneous phase. The tie-lines determine the composition of the two immiscible phases when the system has total concentration M. The lever rule states that the ratio of weights of solutions R and E is

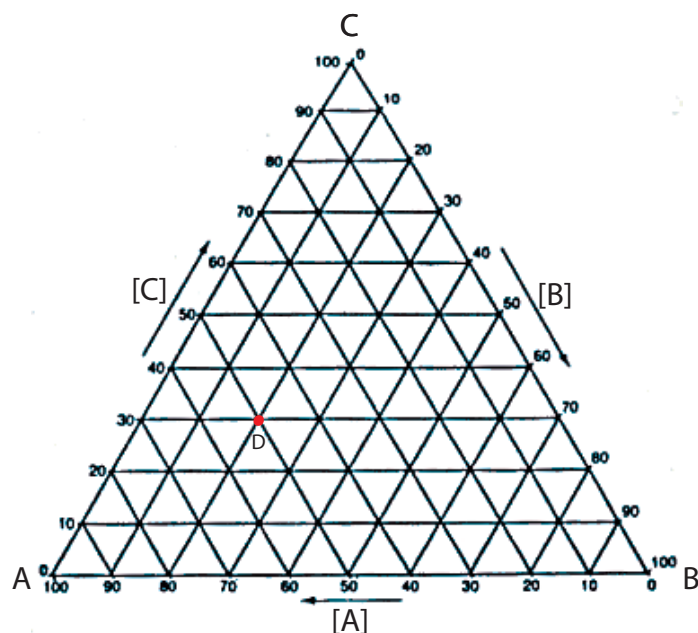$$\frac{R}{E} = \frac{\overline{RM}}{\overline{EM}} \tag{4.47}$$

Figure 4.6: A three component system can be represented by a point on a triangular diagram. Each side of the diagram is scaled from 0 to 100% representing either the mass fraction or mole fraction of the component. The corners of the triangle correspond to the pure A, B or C. The fraction of C in a mixture is found by shifting the point horizontally to the scale on left side of the diagram. The bottom side of the triangle represents solutions with 0% of C, the horizontal line above it represents mixtures with 10% C, and so on. The composition of B and C can be found in a similar manner. For example the point D in the diagram has 50% A, 20% B, and 30% C.

where points R, E, and M are shown in Figure 4.7.

The purification achieved for a multiple stage extraction can be determined from single stage partitioning. For an extraction process, the feed typically refers to the liquid stream (unpurified scintillator) containing the solute that is to be extracted. The solvent is an immiscible liquid (high purity water) that is mixed with the feed. The raffinate (purified scintillator) is the exit stream which is depleted of solute. The extract (dirty water) is the stream that is removed with a higher concentration of solute. The two most common types of extraction columns are cross current columns where the flows are perpendicular

in each stage, and countercurrent columns where the flows are anti-parallel. For liquids with different densities a countercurrent mode is often used where the flow of the feed and solvent proceed in opposite directions through a column. The heavier fluid is inserted at the top of the column and extracted at the bottom, while the lighter fluid is inserted at the bottom and removed from the top. In this case, let the flow rate of the feed be F and the flow rate of the solvent be S. Let X_f, X_r, X_s, and X_e be the mass fractions of solute in the feed, raffinate, solvent and extract, respectively. The distribution constant K_D is defined as the ratio of the concentrations between the two liquids at equilibrium.

$$K_D = \frac{X_f^*}{X_s^*} \tag{4.48}$$

where the superscript asterisk indicates the equilibrium value. For a cross current extraction column with n equivalent stages the raffinate concentration will be

$$X_r = X_f \frac{\frac{K_D S}{F} - 1}{(\frac{K_D S}{F})^{n+1} - 1} \tag{4.49}$$

assuming a pure solvent with $X_s = 0$ is used. The extraction factor E is

$$E = \frac{k_D S}{F} \tag{4.50}$$

where a higher extraction factor leads to better purification. The purification factor X_f/X_r is

$$\frac{X_f}{X_r} = \frac{(E)^{n+1} - 1}{E - 1}. \tag{4.51}$$

Higher purification is achieved with a larger partitioning constant, higher solvent flow rate, or lower feed rate. Under the normal range of operating conditions the Borexino water extraction column will have three to five equivalent equilibrium stages. The number of stages depends partly on the flow rates of scintillator and water.

For liquid extractions, the amount of mixing is determined by fluid properties like viscosity, surface tension at the interface, and density differences. Static extraction columns like the one in Borexino use gravitational energy and internal packing material to mix the two liquids. It is important to achieve the right level of mixing. Too little mixing results in

a small interfacial surface area and poor extraction efficiency. Too much mixing results in small droplets or emulsions which can take a very long time to separate.

Water extraction is a convenient method for purification because of its simplicity. However, there are limitations. Water and pseudocumene are not perfectly immiscible so there will be some water left in the pseudocumene. Though a small amount, this water will carry a relatively high concentration of impurities. When saturated with water, pseudocumene will have a mole fraction $x_{iw}^{sat} = 0.9978$ [60]. This is often stated in terms of γ_{iw}^{sat}, the aqueous activity coefficient

$$\gamma_{iw}^{sat} = \frac{1}{x_{iw}^{sat}} = \frac{1}{v_w C_{iw}^{sat}} \tag{4.52}$$

where $v_w = 0.018 \, \text{L/mol}$ is the molar volume of water, and C_{iw}^{sat} is the saturation concentration. In saturation with water, pseudocumene has an activity coefficient $\gamma_{iw}^{sat} = 1.3 \times 10^5$. The large activity coefficient indicates that pseudocumene will contain very little water when saturated. The activity coefficient for pseudocumene in water is also large.

The relative humidity of a material is the water content as the percentage of the saturation value. The relative humidity will be the same for any phases that are in equilibrium. In Borexino, the pseudocumene must be maintained at 30% relative humidity or higher to ensure the nylon vessel does not become brittle and crack.
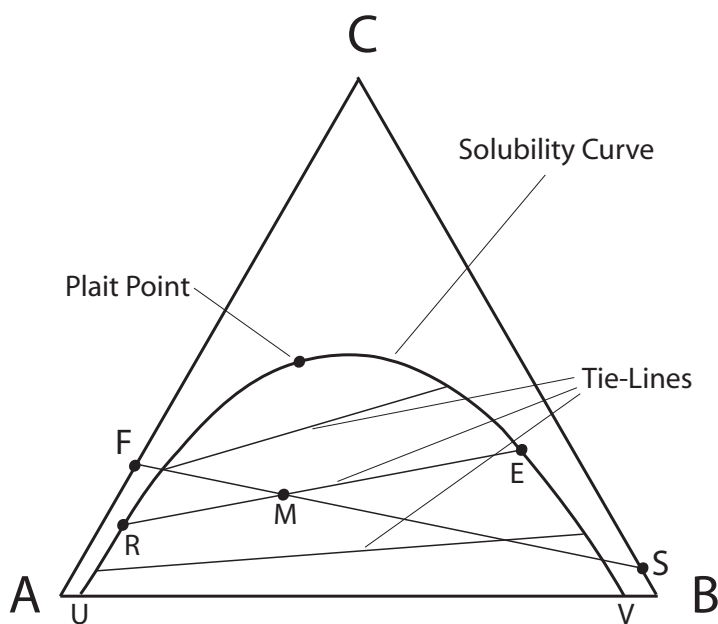
Figure 4.7: A triangular diagram representing a two immiscible liquids A and B with impurity C. Points F and S represent the concentrations of the initial liquids that will be mixed. The total concentration of the system M must lie on the line connecting the points F and S. The tie-lines are determined by equilibrating two phases with total concentration M. The points R and E then give the concentrations of the two phases once they separate. Points R and E will always lie on the solubility curve and form the endpoints of a tie-line. Tie-lines are not normally parallel and their slope is dependent on the equilibrium. The plait point P is the point where the end points of the tie-lines merge. It is a critical point above which two separate phases cease to exist. The points U and V will overlap with the bottom vertices of the triangle in the case where the liquids are perfectly immiscible [106].

4.5.1 Water Purification

A large quantity of high purity water is needed for the water extraction operation. About $2000\,\mathrm{m}^3$ is also required to fill the volume between the water tank and stainless steel sphere to act as a radiation shield and muon veto. The underground LNGS labs are located below the water table so there is a ready water supply. The drawback is that the water is highly contaminated with minerals and radioactive isotopes.

The water underground in LNGS has a radon activity of $\sim 10^4\,\mathrm{Bq/m}^3$ [108, 82]. The radon concentration is greater than what would be expected from secular equilibrium with the uranium in the water by a factor of 10^6. The high radon presence means the water will also contain ^{210}Pb which has a 22.3 year half life and produces ^{210}Bi and ^{210}Po which have decay energies in the neutrino energy window. The water used for the extraction must at a minimum be pure enough to not introduce contaminants into the scintillator that it is supposed to purify. In order to produce high purity, the mineral rich water taken from the mountain is processed with a water treatment plant in Hall C near the detector. The water plant utilizes $0.1\,\mu$m filters for particulates, reverse osmosis units for fine particles, a nitrogen stripping column to remove gases like radon, and an ion exchange resin to remove charged particles. After treatment the water has a measured resistivity near the physical limit of $18.2\,\mathrm{M\Omega}$ [92]. The water coming out of the plant has a radiopurity requirement of less than $10^{-6}\,\mathrm{Bq/m}^3$. The water used for the water extraction is also distilled.

Radon poses a particular problem because of its partitioning. The relative solubility ratio of radon from pseudocumene:nitrogen:water is 38:3.3:1 by volume. In equilibrium the concentration of radon in pseudocumene will be 38 times the radon concentration in water. This is unfortunate because the radon has a strong preference to be in pseudocumene. The Ostwald coefficient for radon in water is $K = 0.26$ at $20\,$C. The Ostwald coefficient is a dimensionless quantity equal to the ratio of the amount concentrations in the gas and in the liquid. The mole fraction of nitrogen gas (N_2) in water at saturation is $x = 1.7774 \times 10^{-5}$ [60].

4.6 Distillation

Distillation is the process of heating a solution and extracting the purified vapor phase. It uses differences in the boiling points or vapor pressures of the different species. At a given temperature, components of a solution will typically have different mole fractions in the liquid and vapor phase.

The effectiveness of a distillation is determined by the relative volatility of the two components. The relative volatility of a mixture with components i and j is

$$a_{ij} = \frac{y_i x_j}{y_j x_i} = \frac{K_i}{K_j} \tag{4.53}$$

where y_i is the mole fraction of component i in the vapor and x_i is the mole fraction in the liquid. The partition constant K_i is defined as

$$K_i = \frac{y_i}{x_i} \tag{4.54}$$

where y_i is the vapor mole fraction at equilibrium for liquid mole fraction x_i. Partitioning constants are usually determined empirically. If the partitioning constants are known along with the physical parameters of the distillation system the purification factor can be predicted. The most important variables aside from the partitioning constants are the feed rate, temperature, number of stages, reflux ratio, and bottoms removal rate.

From a theoretical standpoint the partition constant can be expressed as

$$K_i = \frac{\gamma_i \phi_i^{sat} p_i^{sat}}{\hat{\phi}_i P} e^{\frac{1}{RT} \int_{p_i^{sat}}^{P} v_i^L dP} \tag{4.55}$$

where γ_i is the activity coefficient, $\hat{\phi}_i$ is the fugacity coefficient of the vapor mixture, p_i^{sat} is the vapor pressure of pure i, ϕ_i^{sat} is the fugacity of pure vapor i, v_i^L is the molar volume of the liquid, and the exponential term is called the Poynting correction. Fugacity accounts for deviations from ideality. If the vapor obeys the ideal gas law which is valid for low pressure, high temperature systems then

$$K_i = \frac{\gamma_i p_i^{sat}}{P}. \tag{4.56}$$

If the liquid solution is ideal and Raoult's Law applies then

$$K_i = \frac{p_i^{sat}}{P}. \tag{4.57}$$

Raoult's Law states that the vapor pressure of a mixture is

$$p_i = x_i p_i^{sat} \tag{4.58}$$

where p_i is the vapor pressure of i, and x_i is the mole fraction in solution.

Pseudocumene from Borexino scintillator and an impurity can be treated as a two component system. For a binary mixture $y_j = 1 - y_i$ and $x_j = 1 - x_i$. The relative volatility a_{ij} can then be expressed as

$$a_{ij} = \frac{y_i(1 - x_i)}{x_i(1 - y_i)}. \tag{4.59}$$

The purity of the vapor phase y_i is then

$$y_i = \frac{x_i a_{ij}}{1 + x_i(a_{ij} - 1)}. \tag{4.60}$$

A high relative volatility a_{ij} makes a mixture easier to separated. The vapor pressure and the boiling point of a solution are generally a function of the mole fractions of the components in the mixture. Vapor pressures tend to decrease for substances with higher molecular polarity because it lead to stronger polar bonding. Vapor pressure also tends to decrease with increasing molecular size which leads to larger van der Waals interactions.

The equilibrium constant can be related to the temperature with the van't Hoff equation

$$\ln K = -\frac{\Delta H_{vap}}{RT} + \frac{\Delta S_{vap}}{R} \tag{4.61}$$

where ΔH_{vap} and ΔS_{vap} are the enthalpy and entropy of vaporization, and T is the temperature. For a pure liquid the equilibrium constant is equal to the vapor pressure $K = P$. The vapor pressure as a function of temperature is

$$P = \exp\left[\frac{-\Delta H_{vap}}{R}\left(\frac{1}{T} - \frac{1}{T_{bp}^\circ}\right)\right] \tag{4.62}$$

where T_{bp}° is the temperature of the normal boiling point at one atmosphere. The boiling temperature is

$$T_{bp}^\circ = -\frac{\Delta H_{vap}}{\Delta S_{vap}} \tag{4.63}$$

The distillation process can be illustrated by a plotting of the temperature versus composition as shown in Figure 4.8. The bottom curve represents the temperature where a solution will begin to boil. It is formed by bubble points at different concentrations. The top curve, made of dew points, indicates the temperature where vapor of a given concentration will condense.
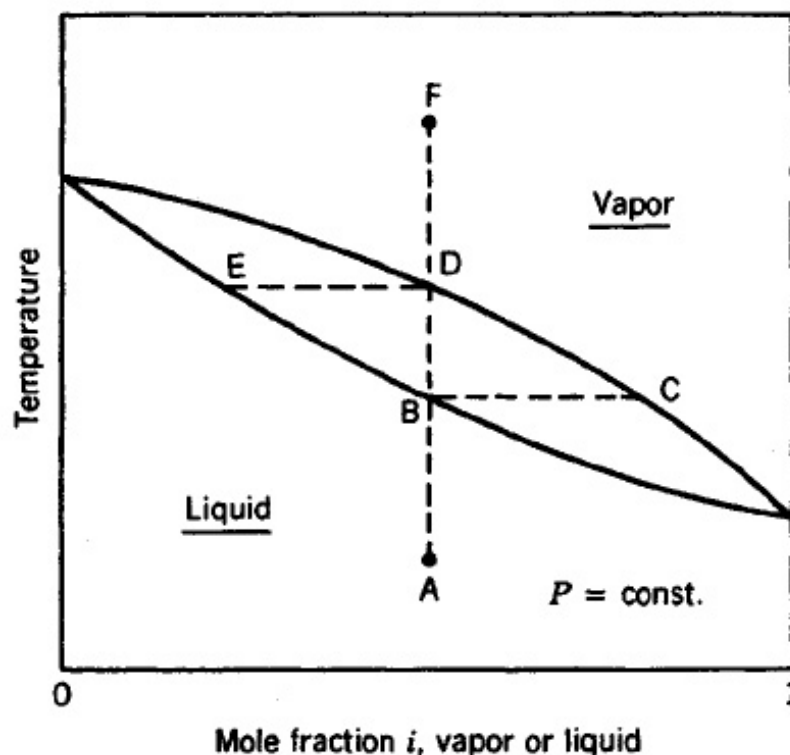

Figure 4.8: An equilibrium phase diagram of the temperature T versus mole fraction x_i for a binary system. A solution at point A can be heated to point B where a vapor with concentration C will be formed. Note that the vapor C has a different concentration than the solution at B. Distillation is the process of extracting and condensing the vapor. Figure from [109].

Distillation systems have tradeoffs between the rate of distillation, achieved purity, and amount of product recovered. The speed of a distillation is constrained by the heating power, the power of the condenser, and for large-scale systems the amount of heat that can

be released into the environment. For higher purity, the distillation temperature should be lower and the fraction of bottoms that are discarded should be higher.

The Borexino reflux distillation column is $75\,$cm diameter $\times$ $7\,$m tall and has six sieve trays. It can process $1000\,$L/h of pseudocumene. The number of equilibrium stages in a distillation unit is roughly equal to the number of trays in the column. Each tray has an efficiency that is in the range of 60-80% depending on the operating conditions. The efficiency of a distillation column is determined by the number of equilibrium stages that are reached. The reflux of product back into the distillation column will improve the efficiency of the distillation. The distillation column is shown in Figure 4.9.
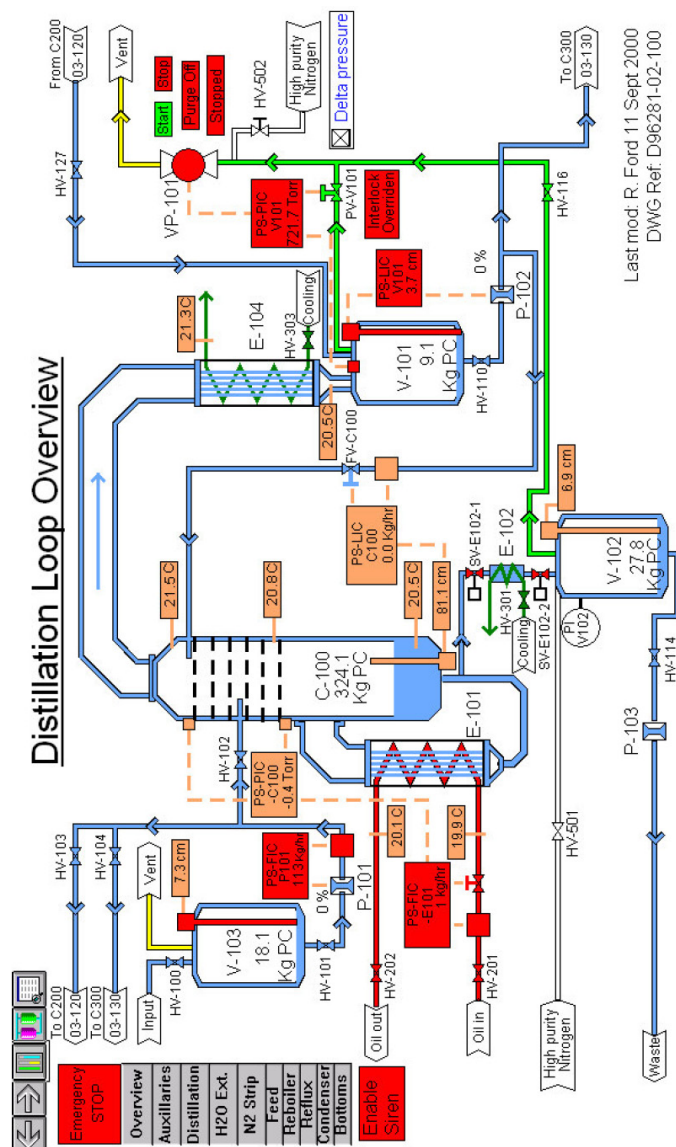
Figure 4.9: The six stage Borexino distillation column (C100). Feed from (V-103) enters the column through (HV-102) at the third stage. The boiler (E101) heats the scintillator with hot oil. Vapor is removed from the top of the column and condensed in (E104). Liquid from the condenser is stored in (V-100). Reflux from (V-100) flows back into the top tray of the column through (FV-C100). Bottoms from the column are cooled in (E-102) are drained into (V-102) before being sent to the waste tank.

4.7   Nitrogen Stripping

Stripping or sparging refers to the removal of impurities from a liquid with a gas. Absorption is the reverse process where components of a gas are transferred to a liquid phase. Both rely on the difference in solubility of a compound between a gas and liquid. Stripping is typically done in a column with countercurrents of liquid and gas. Liquid is inserted at the top and drips down through a series of packing trays while gas is inserted at the bottom and removed at the top. The packing maximizes the contact area between the two phases and ensures good mixing.

For liquid-vapor systems Henry's Law relates the vapor pressure of a component to its liquid concentration. Henry's Law states

$$p_i = K_H x_i \tag{4.64}$$

where K_H is Henry's constant, p_i is the partial pressure, and x_i is the mole fraction in liquid. Note that a normally gaseous compound will be partly dissolved in a liquid even above its condensation temperature. For example, pure nitrogen at room temperature and one atmosphere is in a purely gaseous state. But in the presence of water there will be some nitrogen dissolved in the liquid phase. The partial pressure is proportional to the mole fraction dissolved in the liquid but the constant of proportionality is Henry's constant instead of the vapor pressure in Raoult's Law. Henry's constant is a function of the temperature, pressure, solute, and solvent.

The purification factor for nitrogen stripping is analogous to that of a liquid-liquid extraction. Consider a system with liquid flow rate L and gas flow rate G. Assume the liquid feed initially has a mass fraction X_f and the gas is free of impurities. The extraction factor E will be

$$E = \frac{G}{K_H L} \tag{4.65}$$

where K_H is a unitless Henry's constant. The final purity after n stages is then

$$X_r = X_f \frac{\frac{G}{K_H L} - 1}{(\frac{G}{K_H L})^{n+1} - 1}. \tag{4.66}$$

The purification factor for nitrogen stripping is the same as in Equation 4.51.

The purification of a liquid in a stripping operation is shown in Figure 4.10. It shows a system where a final liquid purity x_1 must be achieved.
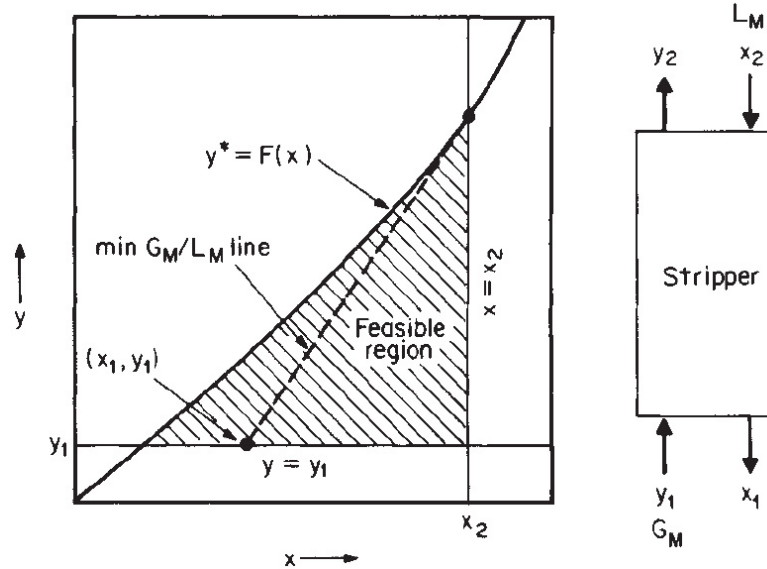

Figure 4.10: A liquid-gas concentration diagram for a stripping operation where a liquid purity x_1 is required. The equilibrium curve is $y^* = F(x)$. The gas flow rate is G_M, the liquid flow rate is L_M, the input liquid concentration is x_2, and the input gas concentration is y_1. The point (x_1, y_1) and the point where the line $x = x_2$ intersects with the equilibrium curve define the theoretical minimum gas to liquid ratio line G_M/L_M. Typically the operating ratio is 20-50% higher than the minimum value. Figure from [110].

The Borexino nitrogen stripping column is $15\,\mathrm{cm}$ in diameter $\times$ $9\,\mathrm{m}$ high. A diagram of the column is shown in Figure 4.11. It can process $1000\,\mathrm{L/h}$ of pseudocumene. The nitrogen requirement is $1500\,\mathrm{m^3/h}$. High purity nitrogen must be used to strip the scintillator. The main contaminants in the nitrogen supply are radioactive noble gases, which are a problem because they are difficult to remove. The nitrogen has an argon purity requirement of $0.4\,\mu\mathrm{Bq}$ $^{39}\mathrm{Ar/m^3(N_2)}$ or $0.31\,\mathrm{ppm}$ Ar and a krypton purity requirement of $0.14\,\mu\mathrm{Bq}$ $^{85}\mathrm{Kr/m^3(N_2)}$ or $0.14\,\mathrm{ppt}$ Kr [111]. It is expected that the efficiency for stripping radon from the scintillator will be greater than 99.3% under standard operating conditions.

	^{39}Ar	^{85}Kr	^{222}Rn
Activity	$1.4\,\mathrm{Bq/m^3}$ Ar	$1.4\,\mathrm{MBq/m^3}$ Kr	$5.6 \times 10^{19}\,\mathrm{Bq/m^3}$ Rn
Ambient Activity	$13\,\mathrm{mBq/m^3}$ air	$1.4\,\mathrm{Bq/m^3}$ air	$\sim\!30\,\mathrm{Bq/m^3}$ air
Required N$_2$ Purity	$0.4\,\mu\mathrm{Bq/m^3}$ N$_2$	$0.13\,\mu\mathrm{Bq/m^3}$ N$_2$	$6\,\mu\mathrm{Bq/m^3}$ N$_2$

Table 4.3: Nitrogen purity requirements [91]. Nitrogen is used to strip the scintillator of radioactive gases like radon. It is also used as a cover gas in the detector where it is maintained at a slight over pressure. The nitrogen supply must have low concentrations of krypton (0.16 ppt Kr) and argon (0.36 ppm Ar) which have radioactive isotopes. A supply of high purity nitrogen was shown to meet these requirement.

Figure 4.11: The Borexino nitrogen stripping column (C300). High purity nitrogen enters the bottom of the column through (F302) and scintillator is inserted at the top after being heated in (E302). The purified scintillator is removed through (P-301).

Pore Size Å	Bulk Density g/cm^3	Specific Surface Area m^2/g	Adsorption Site Density cm^{-3}
60	0.40	530	9.7×10^{20}
100	0.50	330	97.0×10^{20}

Table 4.4: Properties of Kromasil silica gel produced by Eka Akzo Nobel Chemicals.

4.8 Silica Gel Adsorption

Silica gel adsorption works by preferentially adsorbing impurities on silica that is packed in a column while allowing the scintillator to flow through. This technique utilizes the difference in surface binding energies. The materials most commonly used for adsorption are activated charcoal or silica gel. Both can be produced in a form where they have a very high surface area per unit mass. The silica gel (SiO_2) used in Borexino has a surface binding site density of 4.6 sites/nm^2 and a surface to mass ratio of 500m^2/g [112]. Properties of the silica gel are shown in Table 4.4. This results in a density of adsorption sites of $\sim 10^{21}$ /cm^3. A more detailed discussion of adsorption can be found in Chapter 5. The silica gel columns are located in Module 0, an interconnection system that links the various plants in Borexino.
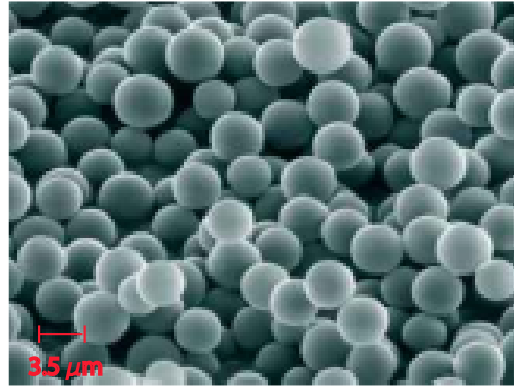

Figure 4.12: A magnified picture of the Kromasil 3.5 μm silica gel used to purify scintillator for Borexino. Each bead shown in the picture is a highly porous structure with a large internal surface area that is not visible.

Silica gel purification tests done with the CTF showed an increase in scintillator activity after the operation [113]. There was one silica gel test done in CTF I and two tests in CTF III using pseudocumene, and one silica gel test in CTF II using PXE as the scintillator. The CTF tests started with a relatively clean sample of scintillator. It is possible that the increase in contamination came from dirty transfer lines or the silica gel itself. Measurements of the radon emanation of silica gel have shown that there is not enough radium intrinsically present to contaminate the scintillator [91]. However, the exposure of the silica gel to ambient air with its high radon concentration could add a large quantity of impurities. Laboratory tests at Munich using radon loaded scintillator showed three stage silica gel purification factors of about 550 for ^{210}Po and 150 for ^{210}Pb [113]. This indicates that the silica gel effectively removes lead and polonium from scintillator when it is present at high concentrations.

The silica gel nominally comes in $3.5\,\mu$m beads, which are is highly porous and have a large internal surface area. However smaller silica fragments must also exist. There is some concern that small silica gel particles might penetrating the filters and remain in the scintillator. This would add highly contaminated particulates which would increase the background rate in the detector. It is expected that these particulates would settle out of the scintillator over time.

4.9 Purification Concerns

Designed as a small scale prototype, the $4.2\,\mathrm{m}^3$ Counting Test Facility (CTF) scintillator volume is about 25 times smaller than the Borexino fiducial volume. The CTF has gone through three different phases and had accumulated several years of low background data. The results have demonstrated the technical feasibility of several key aspects of the Borexino experiment. CTF's main achievements involve high sensitivity measurements of liquid scintillator purity. Concentrations of radioactive isotopes as low as 10^{-18} g/g of uranium and thorium have been measured by the CTF.

The CTF has exposed several difficulties with the purification methods that will be

used by Borexino. The CTF has its own purification plant on top of the detector, which is essentially a small scale version of the Borexino purification plants. The CTF skids are capable of water extraction, nitrogen stripping, and distillation.

The CTF data are taken in time segments of roughly a few days each. This allows various maintenance activities and calibrations to take place between runs. The raw data from each run is reconstructed to form a set of events each consisting of a time, energy, position, and other information. The reconstructed data is then analyzed to determine impurity levels and other relevant information. The count rate in the CTF III is shown in Figure 4.13. The energy spectrum is shown in Figure 4.14.
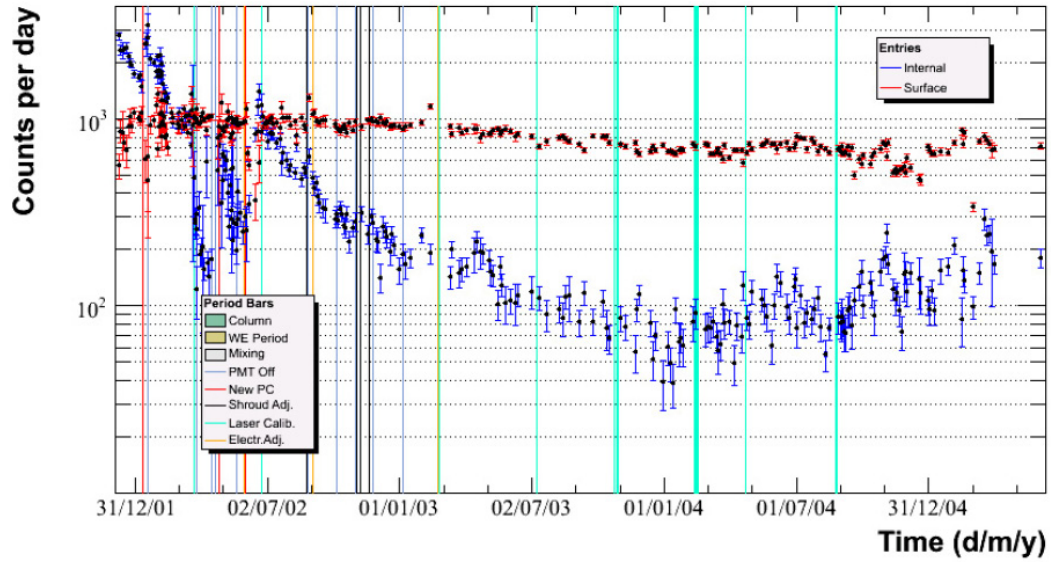

Figure 4.13: The count rate in CTF III as a function of time. Shaded regions indicate periods where various operations took place. Jumps in the rate after certain operation are a result of radon exposure. The rate on the surface of the CTF nylon vessel (red) is significantly higher than the internal rate (blue) from radioactive elements in the scintillator.

The CTF has a smaller volume and thus a worse sensitivity than the Borexino detector. For the Borexino detector to achieve one count per day from the scintillator, the CTF would have to demonstrate an internal rate of about a count per month. Due to backgrounds in the CTF from radon in the water and the nylon vessel which is close to the fiducial volume,
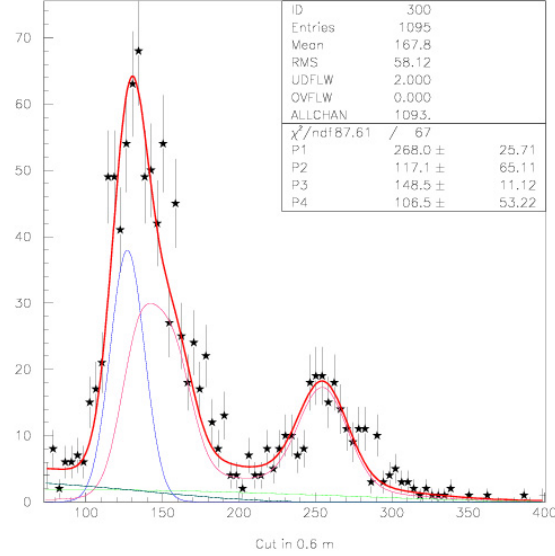
Figure 4.14: The energy spectrum of CTF III during runs 2154-5216. The x-axis is the number of photoelectrons measured. A radial cut of $r < 60\,\mathrm{cm}$ was applied to eliminate surface events. The data are fit to a spectrum with decays from ^{210}Po (blue), ^{210}Bi and ^{40}K (green), ^{222}Rn (red), and ^{85}Kr (black).

this is infeasible. However, from the internal event rate shown in Figure 4.13 two important observations can be made. The first is that the internal rate is significantly above the count per month rate required for Borexino. The measured rate is not an upper limit resulting from the sensitivity of the CTF but an actual rate statistically different from zero. The rate remains high even after the purification and external background subtraction. The internal rate in the CTF III had been at best about 50 ± 15 counts per day which would imply about 1000 background events per day in Borexino. The second observation is the purification in the CTF never achieved the large purification factors that were expected. The largest reduction in the internal count rate was roughly an order of magnitude, not the five to six orders of magnitude required to reach Borexino purities. Purification studies focused on these issues motivated the work in this thesis.

4.9.1 CTF Purification Results

A brief description of the Counting Test Facility (CTF) analysis and the results of the CTF III purification operations are summarized below. A detailed analysis of the CTF III data focusing on elements in the radon chain can be found in reference [87].

The analysis of CTF data indicate that the bulk of the internal background events in the CTF are due to ^{210}Po. The concentration of ^{210}Po in the CTF is determined as follows. The internal scintillator activity was found using a 65 cm radial cut to remove surface events. This cut provided a 35 cm buffer of scintillator from the nylon vessel and surrounding water. The volume of this cut is roughly $1\,m^3$ of scintillator or roughly a fourth of the CTF scintillator volume. The ^{210}Po concentration was found from the energy spectrum by fitting a gaussian to the ^{210}Po peak on top of an exponentially decaying background. Bi-Po coincidences were used to exclude alpha decays higher up in the radon chain and muon events were also ignored.

Before the scintillator was purified it had an activity of 313 events/day/ton from ^{210}Po. This accounted for about 80% of the events in the neutrino window. The Bi-Po coincidences which are a measure of the radon concentration were only 1.5 events/day/ton. The dominance of ^{210}Po indicates that it is out of equilibrium with its parent ^{210}Bi. This is also an indication that there is little ^{210}Pb in the scintillator which would be in equilibrium with ^{210}Bi after about a week.

The silica gel purification reduced the polonium rate to 131 events/day/ton, which corresponds to a 40% reduction when accounting for the natural decay. The purification took place from the 6th-8th of March, 2002. The total internal background rate also decrease by roughly 40% which was expected since it is dominated by ^{210}Po.

The water extraction tests occurred from the 13th-24th of April, 2002. After the test there were 22.4 events/day/ton of polonium which was half the total count rate. This was an 80% reduction of the internal polonium after accounting for its decay. This is the most successful purification operation in the CTF III. Other purification operations showed a much smaller decrease from water extraction and an increased rate from the silica gel

adsorption. However it should be noted that the analysis of these later operations was complicated by detector adjustments.

4.10 Purification Measurements

Small scale experiments were set up at Princeton University to address the scintillator purification efficiency. These bench top tests were preferable because they could be carried out relatively quickly compared to Counting Test Facility (CTF) purification operations. CTF tests were also complicated by the complexity of the system. There were a several of potential sources of contamintation in the CTF which could not be easily disentangled. Small scale tests could be better controlled, and easily modified and repeated to identify systematics. Laboratory tests also allowed the scintillator to be heavily spiked with radioactive isotopes which could clearly not be done in the CTF without ruining the detector. The scintillator spiking facilitated the examination of individual radioactive species. In the CTF a radioactive species would typically have to be identified from a low statistic energy spectrum, unless it was part of a delayed coincidence event. Finding isotope concentrations in the CTF thus required a fit to the energy spectrum with all the potential contaminants. Determining the concentration of a single dominant radioactive isotope was a much cleaner measurement.

Of particular concern was the ^{210}Po isotope due to its high concentration in the CTF measurements. The removal of ^{210}Po through different purification processes was tested. The idea was to heavily spike the scintillator with ^{210}Po. A measurement of the initial ^{210}Po concentration and the concentration after purification would determine the efficiency. The ^{210}Po concentration in the scintillator could be easily determined by observing light produced in its decay.

Scintillator made from pseudocumene with $1.5\,\mathrm{g/L}$ of PPO was used for these tests. The pseudocumene was initially stored in a sealed 55 gallon drum. During this time there was a slight exposure to oxygen and other contaminants which had to be removed. To prepare the pseudocumene it was first distilled under vacuum with a nitrogen feed using the setup

shown in Figure 4.15.

Figure 4.15: The distillation system used to prepare pseudocumene. Pseudocumene starts in the large glass vessel (upper left) and is dripped into the system. The heating mantle (lower left) heats the pseudocumene in a spherical glass vessel. The vapor travels up the vertical glass distillation column connected to the right side of the sphere. The top of the distillation column is connected to a water cooled condensing tube (top). The condensed pseudocumene then drains into a collection vessel (right). Nitrogen gas was slowly bubbled into the pseudocumene while it was heated. The distillation was carried out under a partial vacuum. Distilled pseudocumene is later mixed with PPO to make scintillator.

4.10.1 Radon Exposure

This scintillator was spiked with ^{222}Rn from a 2 MBq source made by Pylon Electronics. The flow through source that contained ^{226}Ra in a cylindrical chamber 6.7 cm in diameter $\times$ 9.9 cm long. The continuous output of the radon source is 250 Bq/minute and the source can handle flow rates up to 10 L/min. The source strength was calibrated to within 4%.

The radon exposure was done by placing about one liter of pseudocumene in a 7.5 L glass exposure jar (vacuum desiccator) connected to a three-way valve. The valve could be opened to either a vacuum pump or the radon source. The size of the exposure jar allowed for a large volume of gas above the liquid. First, the gas was pumped out of the exposure jar

creating a partial vacuum above the pseudocumene. The source which was at atmospheric pressure was then connected to the jar at vacuum. Nitrogen gas and radon from the source expanded into the exposure jar which was then sealed. The volume in the exposure jar was much larger that the volume of the radon source so most of the radon ended up in the jar. Since the radon partitions favorably to pseudocumene the majority of the radon ended up in the liquid. A diagram of the exposure setup is shown in Figure 4.16.
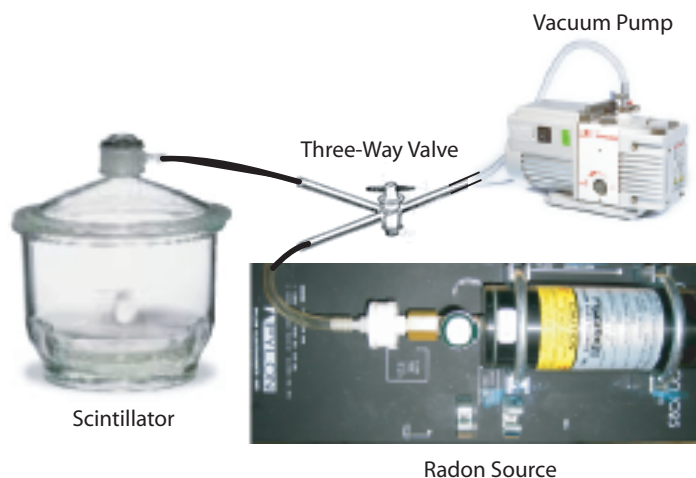

Figure 4.16: The scintillator radon exposure setup. A vacuum is created above the pseudo-cumene. Radon from the source then flows into the vacuum. The jar of scintillator and radon is then sealed. The radon in the gas is transferred to the scintillator due to favorable partitioning.

Glass bubblers were used to expose smaller quantities of scintillator ($\sim 25\,\mathrm{ml}$) to radon. This allowed the scintillator to be spiked with a higher concentration of radon as activity of the source was transferred to a smaller volume of scintillator. The bubbler used slightly pressurized nitrogen gas that was flowed through the radon source. The mixture of radon and nitrogen gas was then bubbled through the scintillator transferring the radon to the scintillator. Sometime multiple exposures were used to increase the concentration. The bubbler setup is shown in Figure 4.17.
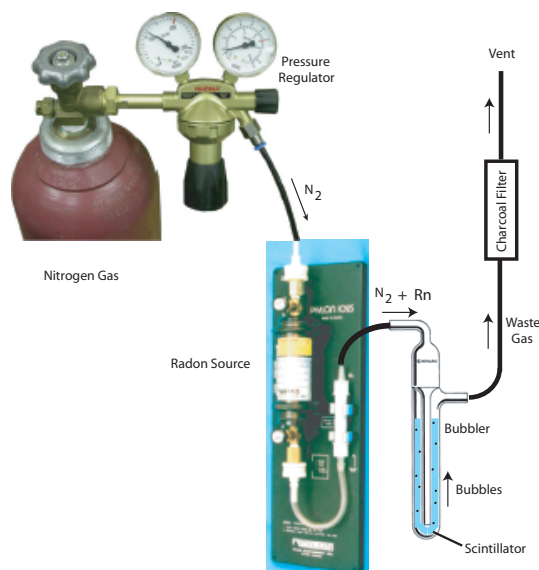
Figure 4.17: The bubbler setup used to spike scintillator with radon. Nitrogen gas picks up radon as it flows through the source. It is then released as small bubbles at the bottom of the scintillator. As the bubbles travel up through the scintillator they transfer radon to the scintillator. After the bubbles leave the scintillator the gas passes through a charcoal trap and is vented through into a fume hood.

The radon in the scintillator was allowed to decay over several radon half-lives. Radon has a half-life of 3.8 days and the other products before ^{210}Pb all have half-lives of less than one hour. After the radon had decays away there is a high concentration of ^{210}Pb in the scintillator which has a half life of 22.3 years. ^{210}Pb decays slowly eventually producing ^{210}Bi ($t_{1/2} = 5$ days), and then ^{210}Po ($t_{1/2} = 138.4$ days). The buildup of ^{210}Po as a function of time after a radon exposure is shown in Figure 4.18. Though the radon decays quickly, the buildup of ^{210}Po takes several months or about a ^{210}Po mean life. In order to get a substantial ^{210}Po rate scintillator samples had to be exposed well in advance of any measurements. The buildup of an isotope to its equilibrium value generally occurs on the time scale of its mean life when it is produce by a slowly decaying parent.
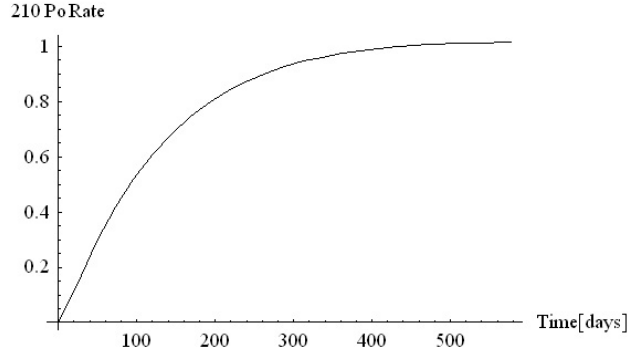
Figure 4.18: The buildup of ^{210}Po in arbitrary units as a function of time since a ^{222}Rn exposure. The time scale for ^{210}Po buildup is on the order of its mean life ($\tau = 200$ days).

4.10.2 ^{210}Po Counting

The polonium measurements were made with two $50\,\mathrm{mm}$ ($2\,\mathrm{in}$) photomultiplier tubes (PMTs). The two PMTs were placed on both sides of the scintillator sample to detected light produced by the ^{210}Po decays. Low activity lead bricks were used to shield the scintillator from external gamma activity. The entire setup was enclosed in a light-tight box to protect the PMTs when the high voltage was on. A diagram of the setup is shown in Figure 4.19.

The data acquisition system was designed with NIM modules for signal processing and CAMAC modules for acquisition. This system was designed to measure the energy of the events and distinguish between alpha and beta decays. The event energy is proportional to the total charge collected. Alpha and beta decays differ in their pulse shape, with alphas having larger tails relative to the prompt signal. Measurements of the total charge from each PMT were made by integrating the entire pulse. The tail charge was measured by starting the pulse integration after a $40\,\mathrm{ns}$ delay.

The PMT signals were amplified with a Lecroy 612AM charge amplifier. This six channel 40X amplifier has a bandwidth of $140\,\mathrm{MHz}$ and two outputs for each channel. However, three copies from signal from each PMT are required: one to produce a gate, one for the total charge, and one for the tail charge. The electronics were impedance matched at $50\,\Omega$
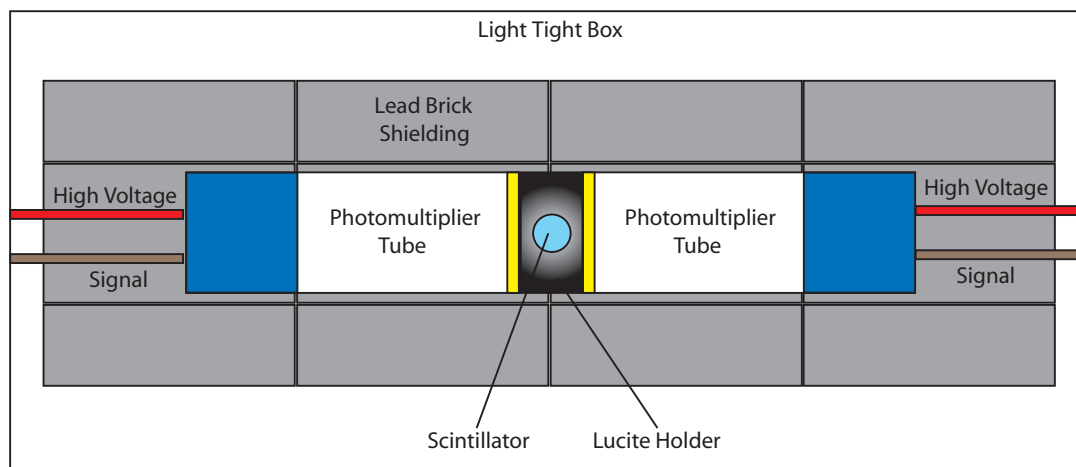
Figure 4.19: The measurement setup to count scintillator samples. Two 5 cm photomultiplier tubes (PMTs) were used to detect the scintillation light. Lucite was used to couple the light from the scintillator to the PMTs. Reflective foil was placed around the Lucite to enhance light collection. Lead bricks shielded the scintillator from external gamma activity.

to prevent reflections, so a signal could not simply be split in two. To produce an additional signal copy, one output from each amplified PMT signal was routed back into an empty amplifier input producing two additional signals. These doubly amplified signal copies were used for the total and tail charge while the singly amplified signal was used to create a gate. The gate was formed by routing one output signal from each PMT to a Phillips Scientific 706 leading edge discriminator. For signals above threshold the discriminator would produce a 20 ns gate.

A Phillips Scientific 755 quad four fold logic unit was used as an "AND" gate. When it simultaneously observed two open (20 ns) gates from the discriminator it output a 100 ns gate as a trigger. This trigger is routed to an analogue to digital converter (ADC). A Lecroy 2249A charge ADC with 12 channels and a 10 bit resolution was used to integrate the charge. Acquisition occurred whenever the gate signal was open. The ADC received the gate from the logic unit and four PMT signals from the amplifier. The tail charges were timed so only the tail was present in the gate window. The full charge was delayed so it

fell completely within the gate window. Delays were created by routing the signal through extra lengths of cable. The Jorway 73A CAMAC Crate Controller transferred the signal from the ADC to a computer over a Small Computer System Interface (SCSI) Bus. The modules used in the signal chain are shown in Figure 4.20. A diagram of the electronics is shown in Figure 4.21.
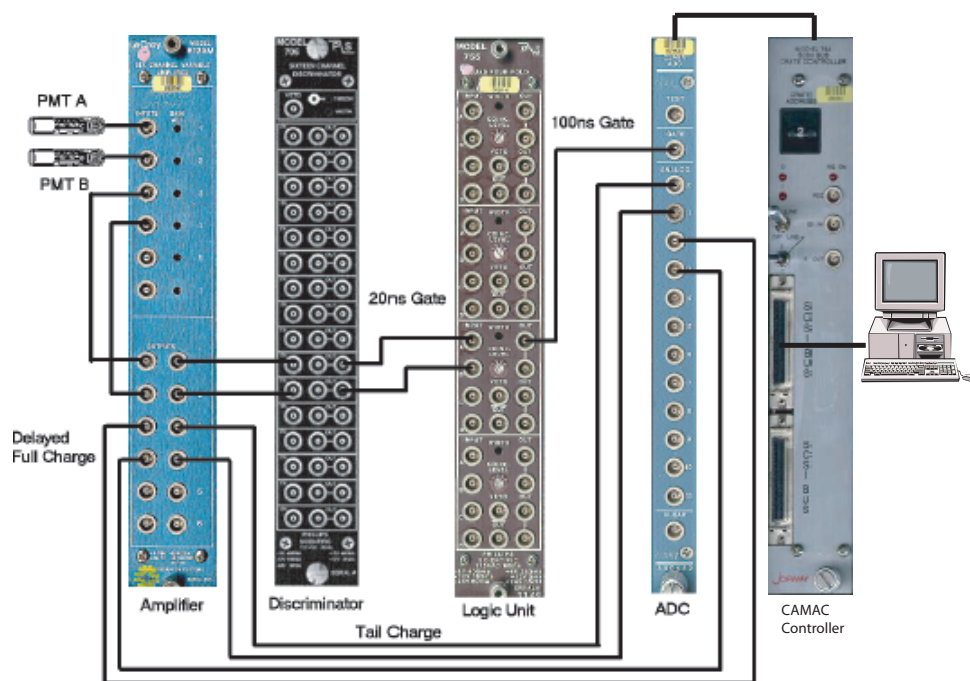

Figure 4.20: The data acquisition system for the two photomultiplier tubes used to count scintillator samples. The black lines represent wires carrying the signal between modules.

The data is displayed in real time during the measurement for diagnostic purposes and is also stored for offline analysis. Data from a scintillator sample that has recently been spiked with radon is shown in Figure 4.22.
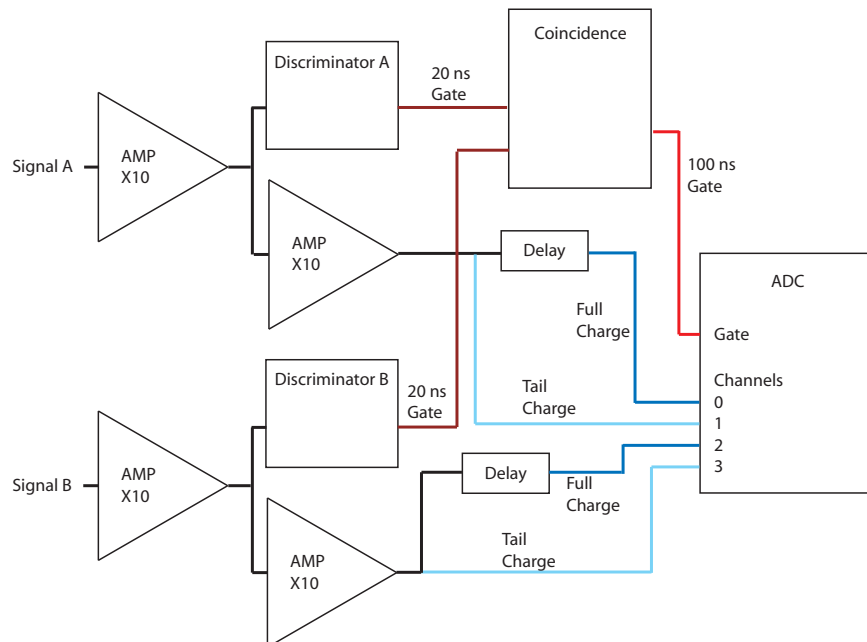
Figure 4.21: A diagram of the electronics readout for the data acquisition system. The two photomutiplier tube output are signal A and B.
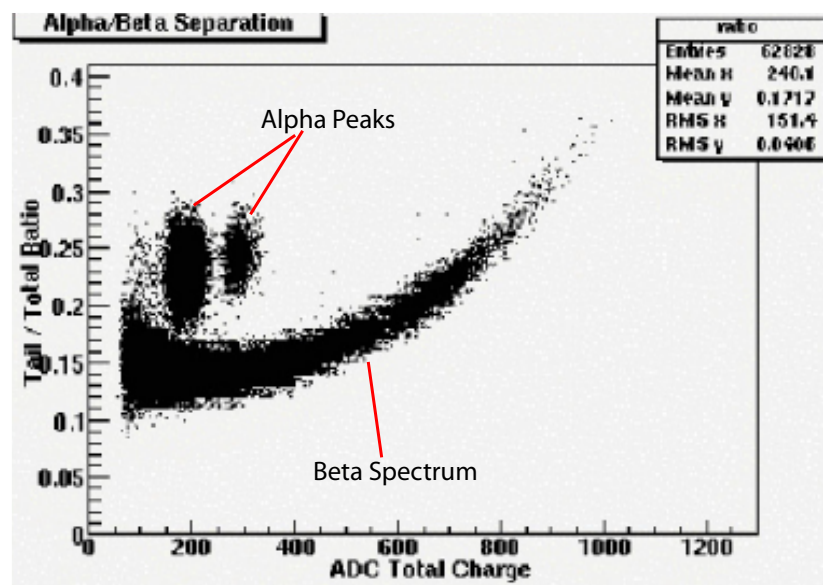
Figure 4.22: A PMT measurement of alpha/beta separation for scintillator that was recently exposed to radon. The ratio of the tail to total charge is plotted versus the total charge (energy) of the event. Alpha events which have longer decay time and whose pulse shapes have larger tails, are shifted above the continuous beta spectrum. The alpha peaks from ^{222}Rn and ^{218}Po form the large spot on the upper left, and the ^{214}Po alpha peak is visible on the right.

4.10.3 Water Extraction Measurements

After the scintillator has a good ^{210}Po concentration from radon spiking, the scintillator was purified by water extraction. Water extraction was done with equal amounts of $15\,M\Omega$ deionized water and scintillator. A separatory funnel was used to mix 10 ml of water and 10 ml of scintillator that had been previously sparged with N_2 gas. The solution was mixed and separated. After each separation a clean separatory funnel and fresh deionized water were used. Scintillator samples were placed in small test tubes each containing 7 ml of scintillator. A cylindrical piece of Lucite with a hole bored in it was used to hold the test tubes and to couple light to the two PMTs. The test tubes had the advantage of being cheap and disposable. A picture of the setup can is shown in Figure 4.23.
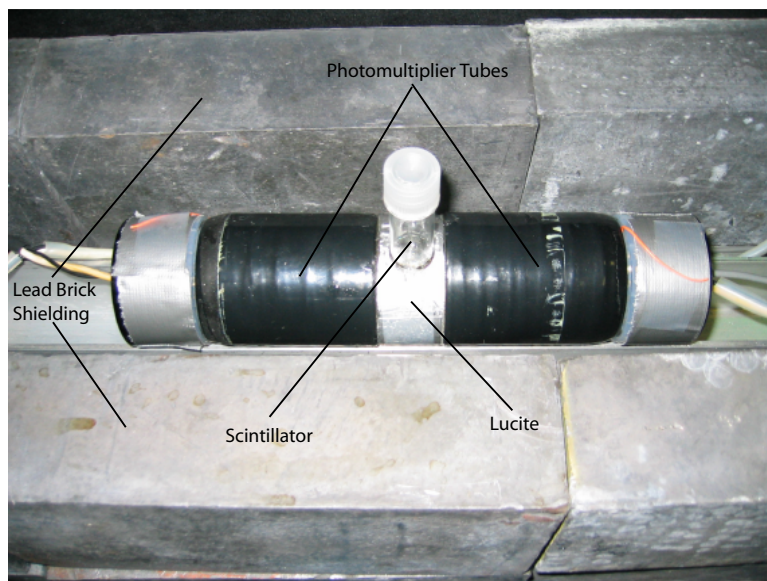
Figure 4.23: Two 5 cm photomultiplier tubes counting a scintillator sample held in a test tube with the top lead shield removed. A Lucite holder couples the light from the test tube to the PMTs. The Lucite is wrapped in foil to increase the light collection. Optical coupling grease between the test tube and Lucite, and between the Lucite and PMTs increases light transmission.

Three stages of water extraction were done under different mixing conditions. Samples were shaken vigorously by hand for 1 minute, mixed with a magnetic stir bar for 1 minute,

and mixed with a magnetic stir bar for 30 minutes. The agitation from the stir bar was much greater than from shaking the mixture by hand. This was apparent from the longer time required for the water and pseudocumene to separate. Results from the water extraction of polonium from scintillator is shown in Figure 4.24. The measured purification factors
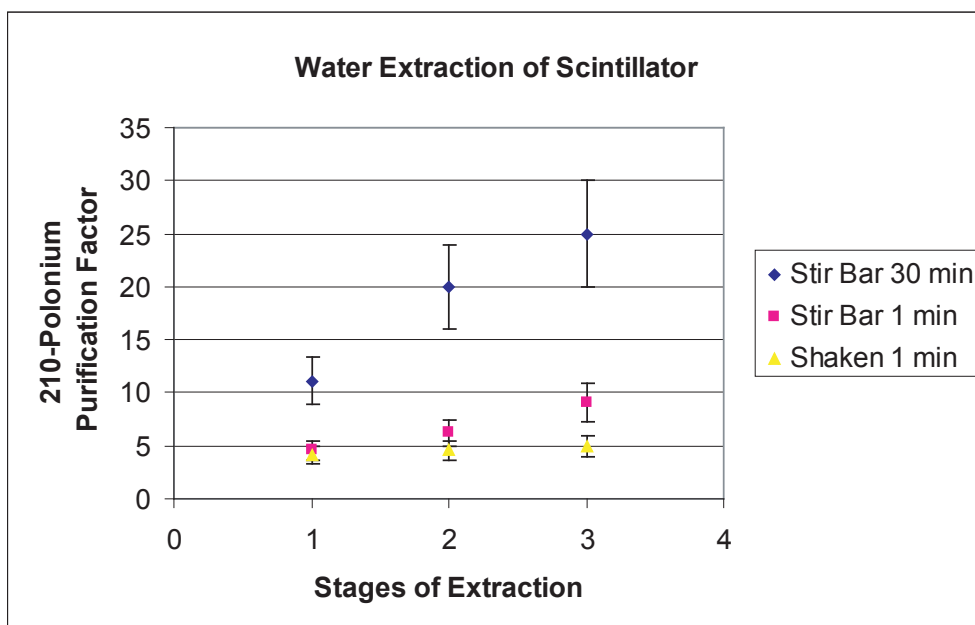
Figure 4.24: The effectiveness of water extraction for removing ^{210}Po from scintillator. Longer and more vigorous mixing lead to higher ^{210}Po removal.

were much lower than expected. Even with 3 stages of 30 minute stir bar extractions a purification factor of only 25 was achieved. The stir bar mixed the water and scintillator much more vigorously than packing material in the Borexino column. Since polonium is a very polar atom it was expected that it would prefer the water strongly yielding purification factors of several orders of magnitude. The most likely explanation is that a fraction of the polonium is bound in a nonpolar configuration which reduces the partitioning coefficient and thus the purification efficiency. The exact chemical form of polonium when produced from ^{210}Bi in pseudocumene is not known. However, there have been studies that indicate

Mixing Time	Diffusion Distance
[minutes]	[mm]
1	0.85
5	1.9
30	4.6
60	6.6

Table 4.5: The average diffusion distance $\sqrt{\langle r^2 \rangle}$ in pseudocumene.

a fraction of the polonium is in a charged state.

The water extraction data show an increase in purification with an increase in agitation or an increase in mixing time. The increase in purification with mixing time indicates that an equilibrium of polonium between the water and scintillator was not reached during the one minute extractions. The mass transfer of polonium from the scintillator to the water depends on the diffusion constant, the area of the interface which is determined by the size of the droplets, and the mass transfer coefficient. The average diffusion distance in three dimensions as a function of time is

$$\sqrt{\langle r^2 \rangle} = \sqrt{6Dt} \tag{4.67}$$

where the diffusion constant in water or pseudocumene is $D \sim 2 \times 10^{-9}\,\mathrm{m^2/s}$. The drops of pseudocumene created during mixing have to have a radius smaller than the diffusional distance if equilibrium is to be reached. Table 4.5 shows the average distance an impurity will travel due to molecular diffusion.

The mass transfer coefficient k_c in an agitated tank can be found from the Sherwood number. The Sherwood $Sh = \frac{k_c l}{D}$, Schmidt $Sc = \frac{\mu}{\rho D}$, and Reynolds $Re = \frac{l v \rho}{\mu}$ numbers which are summarized in Table 4.6. For an actively mixed liquid-liquid system the Sherwood number is related to the Reynolds and Schmidt number by [106]

$$Sh = 0.052(Re)^{0.833}(Sc)^{0.5}. \tag{4.68}$$

An effective Reynolds number can created based on system parameters such that

$$Re = \frac{d_i^2 N \rho}{\mu} \tag{4.69}$$

Name	Value
Sherwood number	$Sh = \frac{k_c l}{D}$
Schmidt number	$Sc = \frac{\mu}{\rho D}$
Reynolds number	$Re = \frac{l v \rho}{\mu}$
Peclet number	$Pe = \frac{l v}{D}$
Stanton number	$St = \frac{k_c}{v}$

Table 4.6: Dimensionless groups used in mass transfer processes. Here k_c is the mass transfer coefficient, l is a length scale, D is the diffusivity, μ is the viscosity, ρ is the density, and v is the velocity. They are related by $Pe = ReSc$ and $St = \frac{Sh}{Pe}$.

where d_i is the stir bar diameter, N is the number of revolutions per second, ρ is the density, and μ is the viscosity. The product $d_i N$ is the characteristic velocity of the system.

$$\frac{k_c d_v}{D} = 0.052 \left(\frac{d_i^2 N \rho}{\mu} \right)^{0.833} \left(\frac{\mu}{\rho D} \right)^{0.5} \tag{4.70}$$

where k_c is the mass transfer coefficient, d_v is the vessel diameter, d_i is the stir bar diameter, and [106]. The water extraction mixing was done with $d_i = 2\,\text{cm}$, $d_v = 10\,\text{cm}$, $N = 2$, $\mu = 5.9 \times 10^{-4}\,\text{kg/m/s}$, and $\rho = 876\,\text{kg/m}^3$. This gives a mass transfer coefficient of $k_c = 7 \times 10^{-6}\,\text{m/s}$ for the stir bar mixing which is roughly what is expected in a turbulent system.

Two other water extraction tests were done with a larger number of stages. The ^{210}Po concentration was measured before and after the extractions. The mixing was done by mixing equal volumes of pseudocumene and water. The waster and pseudocumene was shaken by hand in a separatory funnel for 5 minutes. The water was drained from the separatory funnel after and extraction and fresh water was added afterward for the next extraction. The separatory funnels were exchanged for clean ones after every five extraction stages. Measurements of the ^{210}Po concentration were made after 10 and 15 extractions. The ^{210}Po purification factors for 10 stages of water extraction was 3.7±0.5 and for 15 stages was 17±4.4. It is notable that the longer 5 stage extraction showed less purificaition than the shorter three stage extraction. This is possible that this is due to differences in the mixing intensity between the two extractions. It is unlikely that water purity was a

limiting factor. The main purpose of the additional extractions was to see if higher purities could be attained with further purification which does not appear to be the case. Mixing from shaking a solution of water and scintillator vigorously by hand is of similar intensity to the mixing in the Borexino water extraction column. The results from these measurement indicate that water extraction does not remove ^{210}Po from scintillator efficiently enough to meet the Borexino requirements.

The water extraction efficiency could potentially be improved by using an acidic solution since it is known that polonium is readily dissolved in acids. Acidic solutions have traditionally been used to dissolve polonium prior to plating onto a metal. An acidic solution by definition has a pH of less than 7. The pH of a solution is

$$\text{pH} = -\log[\text{H}^+] \tag{4.71}$$

where $[\text{H}^+]$ is the concentration of hydrogen ions in moles per liter. HNO_3 was used to make an acidic solution with a pH=2. This was mixed with polonium loaded scintillator in the same manner described above. The ^{210}Po purification factors for 10 stages of acid extraction was 11.8±2.1 and for 15 stages was 12.5±2.6. It is possible that the purification is reaching a plateau where further extractions have a small effect, however, more measurements are needed to test this conclusion. The main point is that purification factors for an acidic extraction are also not as large as required by the experiment. In addition 15 stages of water or acid extraction are impractical for the large volume of Borexino scintillator given the purification processing rate.

4.10.4 Distillation Measurements

A small scale distillation tested the removal of ^{210}Po from pseudocumene. Pseudocumene was exposed to radon which produced ^{210}Po over time as described in Section 4.10.1. Measurements of the ^{210}Po were made with PMTs using alpha/beta discrimination described in Section 4.10.2. The distillation was done with a three stage Snyder distillation column. This column had three floating ball valves that separate stages of the column. As the pressure built up in the lower stage the ball would be lifted and vapors would enter the higher

stage. After condensing on the walls the liquid would pool around the ball which prevented liquid from draining back down the column. The glass distillation setup for separating ^{210}Po from pseudocumene is shown in Figure 4.25. A pressure of 20 in Hg was maintained with a vacuum pump during distillation. The scintillator sample was counted with PMTs before and after being distilled to determine the ^{210}Po concentration.
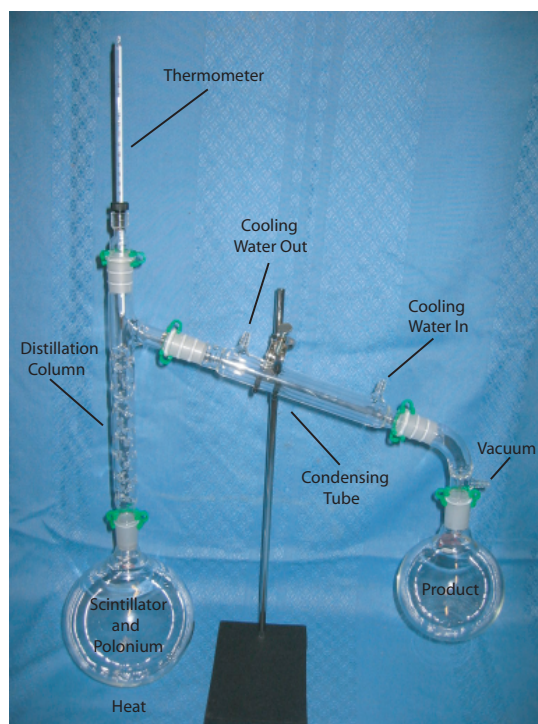
Figure 4.25: Distillation setup for pseudocumene loaded with ^{210}Po. The product is collected in the flask on the right and transfered to a quartz cell for measurement.

The scintillator was measured in cylindrical quartz cells 50 mm in diameter $\times$ 2 cm thickness shown in Figure 4.26. Quartz was chosen for its high optical transmission over the wavelengths of interest. A valve was attached to each cell to allow for nitrogen sparging of the scintillator. PMTs were placed on either side of the quartz cell for counting. Reflective foil was placed around the circumference of the cell to increase light collection.

Figure 4.26: A quartz cell that was used to hold scintillator for counting. PMTs were placed on each side of the quarts cell. The cell is about 5 cm in diameter and 1.75 cm thick. The volume to surface ratio is about 3.6 mm.

Roughly 50 ml of radon loaded pseudocumene was used for the distillation. About 80% of the solution was distilled leaving 10 ml of bottoms in. The distillation achieved a purification factor of greater than 500 ± 90 for ^{210}Po removal. The sensitivity of the measurement was limited by the initial ^{210}Po concentration which was roughly 500 times background. After distillation the ^{210}Po concentration in the scintillator was consistent with background measurements.

4.11 Wavelength Shifter and Quencher

Scintillator which will fill the inner vessel is made of pseudocumene and the wavelength shifter PPO. PPO starts as a white powder that is dissolved in the pseudocumene. The buffer solution which fills the inner and outer buffer volumes is created by mixing a quencher, DMP with pseudocumene.

The scintillator and buffer production in Borexino involves making highly concentrated master solutions with either PPO or DMP and pseudocumene. The master solutions will be mixed with pure pseudocumene at the last stage before filling so that the desired concentrations of PPO in the scintillator and DMP in the buffer are achieved. The concentration

of the scintillator master solution with PPO is $200\,\text{g/L}$. The concentration of the buffer master solution with DMP is $200\,\text{g/L}$.

Contaminants in the PPO master solutions can be a problem for the scintillator even though the master solution gets highly diluted. The PPO is exposed to air during the manufacturing process and afterward while in storage. Air exposure means it is contaminated with radon progeny which needs to be removed before it is used to make scintillator. Assuming that there is roughly $1\,\text{m}^3$ of PPO powder that will be used by Borxino there will be 8×10^4 counts of ^{210}Pb per day per year of air exposure. This number is an upper limit since the packaging around the PPO will act as a partial radon barrier. However, this worst case exposure is 10^5 times more background than the experiment can tolerate and it is unlikely the packaging which is known to be permeable to radon provides level type of protection. ^{210}Pb will produce ^{210}Bi and ^{210}Po whose decays are in the neutrino window. Water extraction for scintillator is not very effective and this is expected to be true for master solution of PPO as well.

The master solution with PPO is particularly difficult to distill. The boiling points of pseudocumene and PPO are very different. PPO has a density of $1.06\,\text{g/cm}^3$, a melting point of 72-73°C, and a boiling point of 360°C. The boiling point of pseudocumene is 169°C. Small scale distillation tests using glassware showed that all the pseudocumene from the master solution was evaporated while the PPO remained in liquid form. The PPO was later evaporated at an elevated temperature. After cooling the system to room temperature the remaining PPO that was not distilled formed a solid crystal. This was difficult to handle because it stuck to the glass and was not easily redissolved in pseudocumene at room temperature. Care must be taken that the PPO master solution distillation bottoms do not solidify and clog the large scale distillation system which would be difficult and time consuming to disassemble and clean. After several modifications a successful PPO master solution distillation was carried out using the CTF purification skids.

4.12 Emanation

Emanation of radon from the pseudocumene storage tanks is a problem for Borexino. The steel tanks built for Borexino emanate radon even though care was taken to ensure that the welds were made with special rods low in thorium. The emanation radon is a result of radium embedded in the steel.

Extensive radon emanation measurements of Borexino materials were made with high sensitivity detectors developed at Heidelberg. The sensitivity of the measurement technique for material samples is about $50\,\mu$Bq/m^2 [114]. The emanation for the different vessels used by the experiment has also been measured. These measurements were done by allowing the radon in the tanks to reach an equilibrium between the natural decay and emanation. The tanks were then flushed with high purity nitrogen. As the nitrogen left the tank it was passed through a cooled trap to collect the radon. The concentrated radon was then measured to determine the emanation rate.

The steel in the storage vessels have a ^{226}Ra concentration of $17 \pm 3\,$mBq/kg [115]. For the four large storage tanks in Hall C the residence time for purified pseudocumene is roughly three weeks before radon contamination from emanation becomes too high. This means that the pseudocumene must be purified a short time before it is inserted into the detector.

Surface Contamination

Surface contamination from radioactive isotopes is a source of background in the Borexino detector. Surface contaminants can be in the form of macroscopic dust particles that has settled on the surface or individual isotopes at the molecular or atomic level. Surface contamination is primarily a problem because the radioactive contaminants can be transferred from the surfaces to the high purity liquid scintillator. As a result, there are strict limits on the surface cleanliness of all detector components that come in contact with the scintillator.

Preventing radioactive contamination of the liquid scintillator from surfaces encountered during fluid handling operations is an essential yet difficult task. During its processing, the liquid scintillator will be transported through a series of lines, tanks, and columns, coming in contact with hundreds of square meters of surface area in each case. Most of the surface area will be stainless steel that has been either electropolished or in cases where that was not practical, pickled and passivated to prevent corrosion. There is also a large stainless steel surface area due to the packing materials in the purification columns. The packing material has a convoluted geometry making it challenging to clean. Other large non-steel surfaces come from the Teflon filters and silica gel, which are used to purify the scintillator. To a lesser extent, the scintillator will also be in contact with gasket material, nylon from the vessels, glass from the PMTs, and instrumentation used to measure fluid properties. To

minimize dust and particulates all the parts were assembled in a clean room environment. When possible, parts were also washed after the final installation by circulating a hot detergent and then rinsing thoroughly with high purity water.

The surface contamination on the inner nylon vessel poses an additional problem not only because it can contaminate the scintillator, but because of its proximity to the fiducial volume. The inner nylon vessel is located inside the water shield, and inner and outer buffers which were designed to stop gammas. As a result some gamma decays that occur on the surface of the inner nylon vessel will reach the fiducial volume where they will scatter off electrons, mimicking neutrino events. Also, alpha and beta decays on the interior surface of the inner nylon vessel will produce scintillation light. A fraction of these decays will be mistaken as events by the detector even though they occur outside the fiducial volume because the position reconstruction is not perfect. Though these contributions can often be statically subtracted they still add an uncertainty to background rate in the fiducial volume.

There are some factors that mitigate the effects of the nylon vessel contamination. Only the inner surface of the nylon vessel is in contact with the scintillator and has the potential to contaminate it. The outer surface is in contact with the buffer which is physically separated from the scintillator by the nylon. Light output in the buffer region is quenched so decays in the buffer region are not usually observed. Contamination on the outside of the vessel is thus less of a concern.

Surface decay products that are stopped in the nylon will not produce any scintillation and will not be observed. Nylon covers a roughly 2π solid angle for surface decays in the limit that the particle decay paths are small compared to the vessel radius of $4.25\,\mathrm{m}$. This results in the observation of only half the decays on the inner surface of the inner nylon vessel. However, some decays on the outside (buffer region) of the inner nylon vessel will penetrate the nylon and reach the scintillator on the other side where they will be seen. These are primarily gammas due to their longer range and betas to a smaller extent. External alphas will be absorbed by the nylon where a $9\,\mathrm{MeV}$ alpha has a range of $79\,\mu\mathrm{m}$ [116].

From an operational point of view, both the level of contamination on various surfaces

and its effect on the scintillator must be understood. To this end a number of small-scale laboratory experiments were carried out. They tested the adsorption of isotopes of the ^{222}Rn chain on materials used in Borexino. The experiments addressed the following issues:

- Surface contamination through adsorption from a dilute liquid.

- Surface contamination from the deposition of airborne contaminants.

- The rates as which surfaces become contaminated.

- Equilibrium surface contamination values.

- The rates of desorption of surface contaminants into scintillator.

- The effectiveness of cleaning methods.

5.1   Adsorption

Adsorption describes the accumulation of material at an interface. It will generally occur between any two distinct phases such as a solid-liquid, solid-gas, liquid-gas, or immiscible liquid-liquid interface. Adsorption differs from absorption because it describes a surface effect, while absorption describes transport into a bulk phase. Sorption typically refers to both adsorption and absorption.

The concentration of a particular species at an interface can differ significantly from the bulk concentrations in either of the adjacent phases. Impurities will often concentrate at an interface at a level greater than the concentration on either side. The ability of impurity concentrations to spike at interfaces makes them especially dangerous for Borexino.

The adsorption relevant for Borexino occurs at a solid-liquid or solid-gas interface. A molecule in a liquid or gaseous state has full translational freedom. Since an adsorbed molecule looses a degree of translational freedom from its unbound state, adsorption is always an exothermic process. An adsorbed molecule gains a degree of vibrational freedom. In solid-gas systems more adsorption will take place at lower temperatures and less at higher temperatures.

A flat metal surface typically has a surface binding site density $n^s = 10^{-5} \, \text{moles/m}^2$ or $6 \times 10^{18} \, \text{sites/m}^2$, which is the atomic packing density in a crystal plane. Materials made of larger atoms will typically have a lower packing density and less binding sites per area. The density of binding sites will increase with the roughness of the surface which is one of the reasons that steel used in Borexino is electropolished. Large molecules that are adsorbed on a surface may take up more than one binding site. The primary difference between liquid and gas adsorption is that with liquids all the surface binding sites are filled, while for gases this is not necessarily true.

In a solid-liquid system a species will eventually establish an equilibrium between the bulk fluid phase and the adsorbed surface phase. The concentration of impurities that reside on a surface in equilibrium depends on the surface-to-volume ratio, partitioning constant, and initial impurity concentration. A significant fraction of the total contamination may reside in the surface phase even for simple geometries which have low surface-to-volume ratios. This means surfaces such as the nylon vessel can be a relatively strong source of background. This is in fact the case in the CTF III, where the surface activity is around $700 \, \text{counts}$ per day on the $12.6 \, \text{m}^2$ nylon vessel, while the internal bulk activity from $4.2 \, \text{m}^3$ scintillator is only $80 \, \text{counts}$ per day. While the surface activity includes a relatively constant contribution from intrinsic impuritities in the nylon and external water shield, the adsorbed phase activity is still significantly outweighs the internal activity.

Adsorption is classified as either physical or chemical in nature. Physical adsorption is governed by an equilibrium between phases. Binding is due to van der Waals forces, where the bond energies are less than $\sim 0.1 \, \text{eV}$. For comparison, the thermal energy at room temperature is about $0.025 \, \text{eV}$. Physical adsorption involves the same forces that condense liquids. The rates for adsorption and desorption are similar for physical processes. Chemical adsorption is less common than physical adsorption. Chemical adsorption is an irreversible process where the binding energies are in the range of 1-$10 \, \text{eV}$. It results from the formation of chemical bonds between the adsorbate and substrate and often involves the dissociation of molecules as they bind to a surface. There is frequently an activation energy that acts as a barrier to chemical adsorption.

In the simplest case the adsorption reaction for both chemical and physical processes can be described by

$$A + * \rightarrow A* \tag{5.1}$$

where A is an atom or molecule, $*$ represents an open binding site and $A*$ is an occupied binding site. The reverse reaction for desorption (physical) is

$$A* \rightarrow A + *. \tag{5.2}$$

Equilibrium occurs for physical adsorption when the rates of the adsorption and desorption reactions are equal. This can be generalized to multicomponent systems the different species will compete for the binding sites.

5.1.1 Adsorption Isotherms

Physical adsorption in equilibrium is described by isotherms, which are plots of the adsorbed surface concentration versus the fluid concentration at a constant temperature. Typically the solute is the component that is plotted. Most isotherms can be described by one of five classes shown in Figure 5.1.

If there are a limited number of adsorption sites that can become saturated then the surface concentration c_i^s is described by the Langmuir isotherm

$$c_i^s = \frac{n^s K_{iL} c_i}{1 + K_{iL} c_i} \tag{5.3}$$

where K_{iL} is the Langmuir constant, c_i is the solution concentration of impurity i, and n^s is the number of adsorption sites per area [60]. For gas adsoprtion, the Langmuir isotherm is often represented at a fractional surface coverage θ,

$$\theta = \frac{bP}{1 + bP} \tag{5.4}$$

where b is a constant related to the temperature and Gibbs free energy, and P is the pressure.

At low concentrations, the Langmuir isotherm reduces to a Henry's Law isotherm. Henry's Law is valid in the limit $K_{iL} c_i \rightarrow 0$, where the denominator of Equation 5.3 goes

to one. The Henry's Law isotherm is

$$c_i^s = K_H c_i \qquad (5.5)$$

where K_H is Henry's constant. Henry's Law describes situations where very low solute concentrations are involved and is the most applicable to Borexino.

Adsorption becomes more complicated when a large number of sites become filled. In that case other effects come into play such as interactions between bound atoms on adjacent sites. Multiple adsorption layers can also occur. This changes the energetics because the adsorbate begins acting as a substrate. Multilayer binding results in a BET isotherm (after Brunauer, Emmett, and Teller). The BET isotherm is

$$\theta = \frac{cz}{(1-z)[1-(1-c)z]} \qquad (5.6)$$

where $z = p/p^0$, p^0 is the saturation pressure of the gas, and the c is a constant [106].

$$c = e^{(\Delta H_{des} - \Delta H_{vap})/k_B T} \qquad (5.7)$$

where ΔH_{des} is the enthalpy of desorption, ΔH_{vap} is the enthalpy of vaporization, and T is the temperature. In the limit that $c \gg 1$ ($\Delta H_{des} \gg \Delta H_{vap}$) and $z \ll 1$ ($p \ll p^0$) the BET isotherm reduces to the Langmur isotherm. Multilayer adsorption typically occurs when the temperature of the system is nears the condensation temperature of the gas.
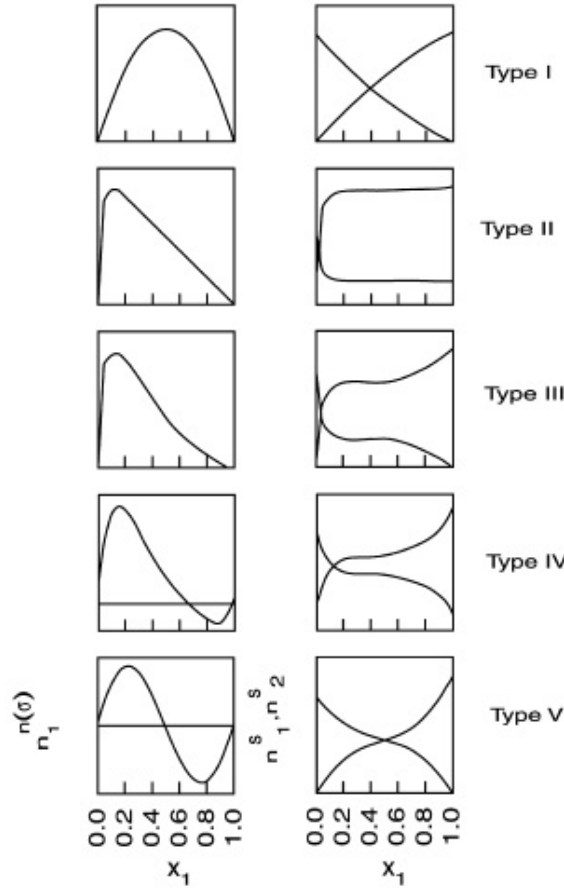
Figure 5.1: Classes of solid-liquid adsorption isotherms. The surface excess $n_1^{n(\sigma)}$ is plotted in the left column and the surface densities of the two components n_1^s, and n_2^s are plotted in the right column. The mole fraction x_1 is plotted on the horizontal axis. The surface excess is defined as $n_1^{n(\sigma)} = n_0(x_{1,0} - x_1)$, where n_0 is the total number of moles in the system, $x_{1,0}$ is the mole fraction of component 1 before the solution comes in contact with the surface, and x_1 is the mole fraction of the solution after reaching equilibrium with the surface. The surface excess is often used because it is typically composed of known quantities. The Type I isotherm describes a Henry's Law isotherm where the amount of adsorbed material is linearly dependent on its concentration in solution. Henry's Law can be used to describe any sufficiently dilute solution. The Type II isotherm is a Langmuir isotherm which accounts for the saturation of binding sites. The Type III, IV, and V isotherms describe different types of high surface area material or cases where multilayer adsorption takes place. Figure from reference [117].

5.1.2 Adsorption from a binary solution

Adsorption is relatively simple in the cases that interesting for Borexino. This is due to the extremely low levels of impurities that are present in the scintillator. Any impurity species in the scintillator can be regarded as a dilute binary solution where the scintillator is the solvent and the impurity is the solute. The concentrations in Borexino are low enough that interactions between the impurities are negligible.

Of course a dilute binary solution simply means that adsorption can be described by a Henry's Law isotherm

$$c_i^s = K_H c_i \tag{5.8}$$

where the surface concentration is linearly related to the concentration in solution. This is sometimes represented in the literature as the equivalent equation

$$s = ky \tag{5.9}$$

where s is the surface concentration, y is the fluid concentration, and k is the partitioning constant. The partition constant or Henry's constant is

$$K_H = e^{-\Delta G/k_B T} \tag{5.10}$$

where ΔG is the Gibbs free energy, k_B is Boltzmann's constant, and T is the temperature. The Gibbs free energy is a function of the components of the solution and the surface the solution is in contact with.

To summarize, physical adsorption constants for binary solutions are determined by

- The two components in the solution.

- The surface in contact with the solution.

- The temperature of the system.

For Borexino the solvents of interest are pseudocumene, water, and different detergent solutions. Pseudocumene is the main component of the scintillator and buffer. Water is important because it is used for rinsing and will initially be used to fill the detector for

calibration purposes. Detergents are used to clean the system after assembly. The low concentration solutes are elements in the radon chain or other radioactive isotopes. Surfaces of interest are stainless steel, nylon, Teflon, and silica gel. Borexino is primarily concerned with partitioning constants in a temperature range from 12-80 C. The temperature of the underground laboratories at LNGS is 12 C and the cleaning takes place at elevated temperatures up to 80 C. Higher temperatures help remove surface contamination because desorption is endothermic. Small scale laboratory experiments determined the partitioning for several of these combinations.

5.1.3 Adsorption On Glassware

Glassware was used extensively in the following experiments to store, transfer, and measure samples of scintillator. Adsorption during intermediate storage or transfer operations would reduce the final amount of polonium. Adsorbed radioactive isotopes on the measurement vessel would reduce the scintillation counting rate. This is a result of some of the surface decay products getting ejected into the glass instead of the scintillator where they would produce light.

The first indication that surface effects were a problem was that the cylindrical quartz cells used for measurements proved particularly difficult to clean. A quartz cell that held polonium-loaded scintillator was counted with the PMT setup described in Section 4.10.2. The cell shown in Figure 4.26, was emptied and dried with nitrogen gas. Pure scintillator was used to refill the cell which was counted again. After begin refilled with fresh scintillator the cell had 36% of its original ^{210}Po rate. The volume-to-surface ratio of the cell was 3.6 mm.

The partitioning constant can be found in for different scenarios. If the polonium repartitioned between the scintillator and surface after the cell was refilled then the partitioning constant would be

$$K_H = \frac{V}{S}\frac{m}{1-m} \tag{5.11}$$

where m is the ratio of the refilled rate to the original rate, V is the volume of the cell, and S is the surface area in contact with the scintillator. To simplify it was assumed that

Treatment	Percent Remaining
Refilled only	36.0±1.4%
Alconox	12.8±0.5%
Basic Solution	11.3±0.5%
Radiac	7.0±0.3%

Table 5.1: Removal of ^{210}Po from a cylindrical quartz cell using various cleaning methods at room temperature. The percent remaining is the ratio of the rate measured after the cleaning step to the initial measurement when the cell was filled with polonium loaded scintillator. The different treatments were performed sequentially starting from the top. The quartz cell has a volume $V = 24.0\,\mathrm{cm}^3$ and surface area $A = 65.8\,\mathrm{cm}^2$.

the surface decay detection 50% efficient. In the case of complete repartitioning where the ^{210}Po was removed from the cell surface to reestablish equilibrium $K_H = 2.1\,\mathrm{mm}$.

If all the polonium stayed on the surface when the quartz was refilled then the partitioning constant would be

$$K_H = \frac{V}{S}\frac{2m}{1-m} \tag{5.12}$$

where m is the still ratio of the refilled rate to the original rate. In this case where there is no desorption after the cell is refilled, $K_H = 4.2\,\mathrm{mm}$. Later measurements indicate that desorption for a surface is a relatively slow process so the partition constant is likely closer to the higher value of $4.2\,\mathrm{mm}$.

After the quartz cell had been emptied and refilled with clean scintillator, a series of tests were done to see how well the cell could be cleaned. The quartz cell was then cleaned with Alconox detergent, rinsed with deionized water, refilled with clean scintillator, and counted. The same cell was then cleaned with a basic solution with pH=11, rinsed, refilled, and counted. The process was repeated with the cleaning solution Radiacwash. The results are shown in Table 5.1. After the cell was sequentially cleaned with the previously mentioned solutions, the rate from the cell was still three times above background. This indicates that once contaminated with polonium, surfaces are very difficult to clean to their original conditions.

The measurements with the quartz cell did not fully address the partitioning when the

polonium started on a surface. A second set of measurements to further probe the polonium partitioning used disposable borosilicate test tubes for scintillation counting. Adsorption on borosilicate was also relevant because most of the glassware the scintillator came in contact with including beakers, pipettes, separatory funnels, and the distillation system was also made of borosilicate.

The borosilicate partitioning measurements began by filling and counting a test tube with polonium loaded scintillator. Transferring the scintillator into a second clean tube would show how much polonium was in the liquid, while refilling the original tube with scintillator would show how much was on the glass. To check if the polonium on the glass repartitioned in the same manner as polonium starting in the scintillator, the contents of both tubes were again transferred to clean test tubes and the original tubes refilled with scintillator. The sequence of operations is shown in Figure 5.2. The measurement setup described previously in Section 4.10. A diagram of the setup is shown in Figure 4.19 and the data acquisition system for the PMTs is shown in Figure 4.21.

At least two measurements are required to determine a partitioning constant. In the following analysis pairs of the measurements described above were used to calculate the partitioning constant. The volume-to-surface ratio of the scintillator in the test tube is $\frac{V}{A} = 0.51\,\mathrm{cm}$. The measured ^{210}Po activity of the sample i is $R_i\,[\mathrm{Bq/cm^3}]$. The measured rate R_i was the sum of the bulk activity y_i and half the surface activity s_i of the sample

$$R_i = y_i + \frac{1}{2}s_i. \tag{5.13}$$

The data from the measurements are shown in Table 5.2. It is further assumed that when the solution is in equilibrium with the surface and adheres to the relation

$$K_H = \frac{V}{A}\frac{s_i}{y_i}. \tag{5.14}$$

The Henry's constants were calculated assuming equilibrium was reached for the partitioning between the scintillator and glass test tubes for each measurement. For measurements where scintillator was transferred from one test tube to a clean tube, Henry's
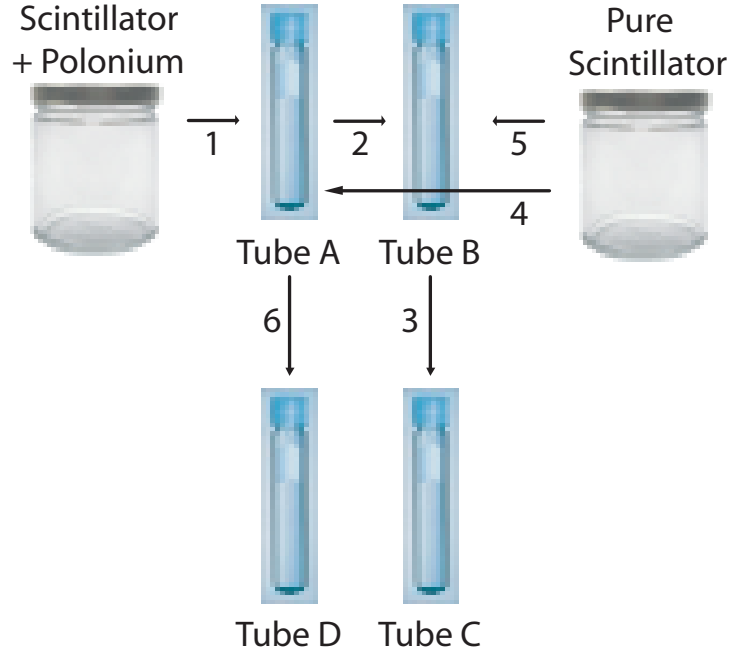
Figure 5.2: The sequence of steps performed to determine the partitioning of ^{210}Po between scintillator and borosilicate glass. In Step 1, polonium loaded scintillator is poured into Tube A for counting. In Step 2, Tube A is emptied in to Tube B which is measured, and so on. In Steps 4 and 5 the tubes are refilled with pure scintillator. In Step 6 scintillator from Tube A which has been refilled is transferred to Tube D. The test tubes with scintillator were counted with PMTs after each step. The results are shown in Table 5.2 and Table 5.4.

constant was calculated according to

$$K_H = \frac{V}{A} \frac{1-m}{m} \qquad (5.15)$$

where $m = R_n/R_o$ is the ratio of the measured rate in the new tube to the rate in the original tube, V is the volume of scintillator, and A is the glass surface area in contact with the scintillator. In the cases where the emptied tubes were refilled with clean scintillator the partitioning constant

$$K_H = \frac{V}{A} \frac{m}{1-m} \qquad (5.16)$$

where m is the measured rate after the tube is refilled over the original rate. As later tests showed the equilibrium assumption is invalid, especially for the desorption case which

Step Number	Measured ^{210}Po Rates [mBq]	Tube Counted
1	662±15	Tube A
2	496±12	Tube B
3	330±9	Tube C
4	83±4	Tube A
5	96±4	Tube B
6	31±2	Tube D

Table 5.2: The measured rates from the test tube samples. The step number refers to the sequence of operations illustrated in Figure 5.2. The counting started 30 minutes after each tube had been filled, including five minutes of nitrogen sparging. Three hours elapsed between the time the test tubes were filled and their contents were transferred (poured) into another tube. The rate consists of all the decays that occurred in the bulk scintillator plus about half the decays on the surface. A background of 2.9 mBq has been subtracted off the rates. The errors shown are statistical only. A larger systematic error from instability in the alpha/beta separation of about ∼10% is not included. The volume of scintillator in the test tubes was 20 cm^3, and the surface area was 38.9 cm^2.

occurs on time scales much greater than 30 minutes. Taking different assumptions about how the polonium repartitions, bounds for the possible values of K_H can be found. These are shown in Table 5.3.

Since the surface and solutions are the same for all the measurements each system should be described by the same partitioning constant. Pairs of measurements are used separately to find the partitioning constant. Assuming equilibrium is reached the partitioning constants derived from these measurements are shown in Table 5.4.

The K_H values shown in Table 5.4 assume equilibrium was reached before each sample was measured. Measurements started 30 minutes after the tubes were filled, during which contaminants would diffuse about 0.5 mm. This is a much shorter distance than the 1 cm diameter of the test tubes. As the diffusion distance is so short the mixing from the 5 minutes of nitrogen sparging was likely the dominant factor. Despite the mixing from the nitrogen sparging it is possible that equilibrium was not fully achieved.

A few of the samples showed slight oxygen quenching, which shifts the alpha peak into the beta spectrum when using the tail to total ratio for discrimination. Some quenching

Condition of 2nd Measurement:	Equilibrium Reached	All ^{210}Po In Liquid	All ^{210}Po On Surface
Transfer	$\frac{V}{A}\frac{1-m}{m}$	$\frac{V}{A}\frac{2(1-m)}{m}$	$\frac{V}{A}\frac{1-2m}{m}$
Refill	$\frac{V}{A}\frac{m}{1-m}$	$\frac{V}{A}\frac{2m}{1-m}$	$\frac{V}{A}\frac{2m}{2-m}$

Table 5.3: Values for Henry's constant K_H with different partitioning assumptions. The ratio of measured rates $m = R_n/R_o$, where R_n is the new measurement, and R_o is the original measurement, V is the volume of scintillator, and A is the area of the surface the scintillator is in contact with. In the case where scintillator is transferred from one tube to another the actual value of K_H is between the equilibrium value and the limit where all the polonium remains in the liquid, $\frac{V}{A}\frac{1-m}{m} < K_H < \frac{V}{A}\frac{2(1-m)}{m}$. For the transfer case all the polonium sticking to the surface after the transfer is unphysical. In the case where a test tube is refilled with clean scintillator, the value of K_H is between the equilibrium value and the limit where all the polonium remains on the surface, $\frac{V}{A}\frac{2m}{2-m} < K_H < \frac{V}{A}\frac{m}{1-m}$. For the refill case all the polonium going to the liquid is unphysical.

Ratio of Samples	Relative Measured Rates [Percent]	K_H [cm]
(2) / (1)	75±3	0.17
(3) / (2)	67±3	0.25
(5) / (1)	13±5	0.077
(6) / (2)	19±5	0.12
(7) / (5)	37±8	0.88

Table 5.4: Measurements of scintillator with ^{210}Po in test tubes to determine partition of polonium between the scintillator and glass. The number in parenthesis in the left column refer to the steps in the sequence of operations illustrated in Figure 5.2. The ratio of the measured rates are shown in the center column. Henry's constants in the right column are calculated assuming perfect equilibrium partitioning in each case. The errors are statistical only and do not include errors of from the alpha/beta separation. Data for each measurement are shown in Table 5.2.

occurred despite nitrogen sparging before the samples were measured. The quenching produced an uncertainty in the polonium rate of about 10% when the α/β cuts are made. A plot of alpha/beta separation using the tail-to-total ratio is shown in Figure 4.22. While the partitioning of polonium from scintillator to the glass was a fast process, the partitioning from glass to scintillator was slower. Equilibrium was not reestablished when the polonium contaminated tubes were refilled with clean scintillator. However, the slower rate of desorption is an indication that chemical adsorption is occurring. For physical adsorption processes the rates of adsorption and desorption should be similar.

For glassware in contact with ^{210}Po loaded scintillator these experiments show a partitioning constant roughly in the range of

$$0.1 < K_H < 1 \tag{5.17}$$

in units of [cm] after contact time on the order of an hour.

5.1.4 ^{210}Pb Partitioning

When pseudocumene is delivered for the experiment, it contains relatively high concentrations of contaminants, including ^{210}Pb. Lead is present because of radon exposure from air contact and radon emanation from stainless steel vessels. Before the pseudocumene can be purified, it comes in contact with pipes, storage tanks, and some column packing material. These stainless steel structures have an area of about $100\,\text{m}^2$ each and this steel has the potential to adsorb a significant fraction of the contaminants. The concern is that these surface contaminants could later be released into the pseudocumene after it had been purified.

A laboratory test was done to determine the equilibrium constant for the partitioning of ^{210}Pb between an electropolished stainless steel surface and pseudocumene. This was accomplished by measuring the ^{210}Pb concentration in pseudocumene and the ^{210}Pb concentration on the surface of a steel sample in contact with the pseudocumene. To increase the decay rates and reduce the counting time, the pseudocumene was exposed to a high

concentration of radon gas, which was allowed to decay, producing ^{210}Pb. The electropolished stainless steel sample ($3\,cm \times 3\,cm$) was then soaked in the lead enriched pseudocumene ($\sim500\,ml$) for about a month. The steel sample was counted with a planar germanium detector, which observed the $46.5\,keV$ ^{210}Pb gamma. This gamma has a 4.25% branching ratio. The lead concentration in pseudocumene was found indirectly through scintillation counting.

A scintillation detector made with a $5\,cm$ photomultiplier tubes was used to measure the ^{210}Po concentration using a pulse shape discrimination technique. PPO was added to the pseudocumene at a concentration of $1.5\,g/L$ to make a scintillator solution which was counted with the detector. The ^{210}Po concentration was measured by separating the alpha decays with the tail/total charge method. The ^{210}Pb concentration was found from the ^{210}Po concentration by knowing the time since the radon exposure. ^{210}Po will increase linearly after a radon exposure for times significantly less than the polonium half-life. The actual buildup of ^{210}Po as a function of time after a radon exposure is shown in Figure 4.18. Data was acquired from the PMT with a high speed digitizer. An Acqiris PCI digitizer card was used to sample PMT pulses at $2\,Gs/s$ recording the entire waveform for each event. Data was dumped to the computer once the onboard card memory was filled. A PMT measurement of radon exposed scintillator showing alpha/beta separation is shown in Figure 4.22.

A gamma detector was used to directly measure ^{210}Pb on steel to find partitioning constant. A diagram of the gamma detector is shown in Figure 5.3. It is a high purity P-type germanium planar detector made by Princeton Gamma Tech, which operates at -1000 V. The active detector area is $10\,cm^2$ and the crystal is $1\,cm$ thick with a dead layer of $0.1\,\mu m$. To reduce the noise, the detector must be cooled with liquid nitrogen supplied by a $7.5\,L$ insulated dewar, which is located above the detector. There is a thin $0.381\,mm$ thick Beryllium window in front of the crystal, which holds vacuum for thermal insulation while minimizing gamma attenuation. A room temperature preamp amplifies the signal from the detector. Data from the germanium detector is acquired with a multichannel analyzer made by Princeton Gamma Tech with 16000 channels and 14 bit resolution. Data

is transferred to a computer over RS-232. The detector was calibrated with ^{57}Co and
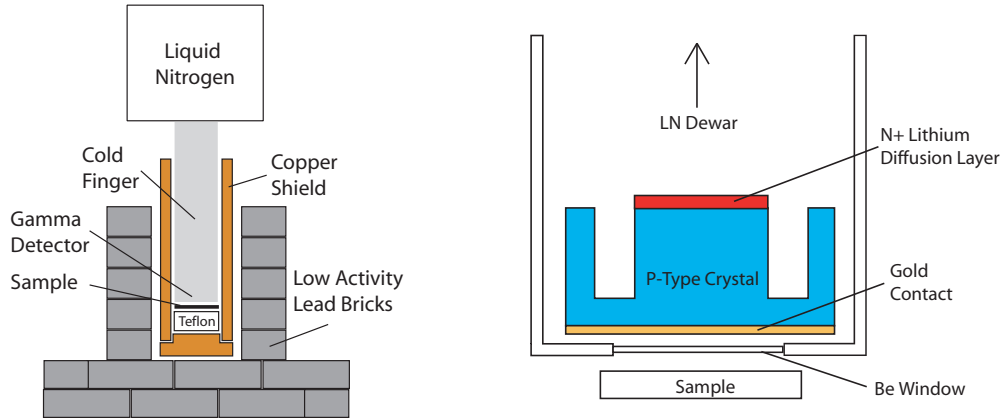

Figure 5.3: The gamma detector used for measuring ^{210}Pb on surface samples. Left: The shielding for the detector. Low radioactivity lead bricks were used for the outer layer of shielding with a cylindrical copper shield inside. A piece of Teflon shielded was placed inside the copper. Right: The P-type high purity germanium crystal above the sample.

^{55}Fe sources, which emit gammas at 122.07 keV and 5.895 keV respectively. The FWHM resolution at 122.07 keV is 620 eV and at 5.895 keV is 391 eV. A gamma spectrum from one of the samples is shown in Figure 5.4.

Shielding for the germanium detector was required to block gamma radiation from the room. The outer most layer of shielding was constructed with low activity bricks which had a low concentration of ^{210}Pb. Low activity lead is often attained from sunken ships where the lead is old enough that the ^{210}Pb component has decayed away. ^{210}Pb has a 22.3 year half-life. Lead is a dense, high Z material so it is ideal for adsorbing gammas. The second layer of shielding was made of copper which is one of the purest metals. This was designed to stop any remaining ^{210}Pb gammas emitted from the lead bricks. The thickness of the copper shield was optimized to block lead activity, while not over producing Bremstralung radiation from muon interactions in the copper. The third layer of shielding was a made of Teflon which is relatively pure compared to the metal. The gamma attenuation from these
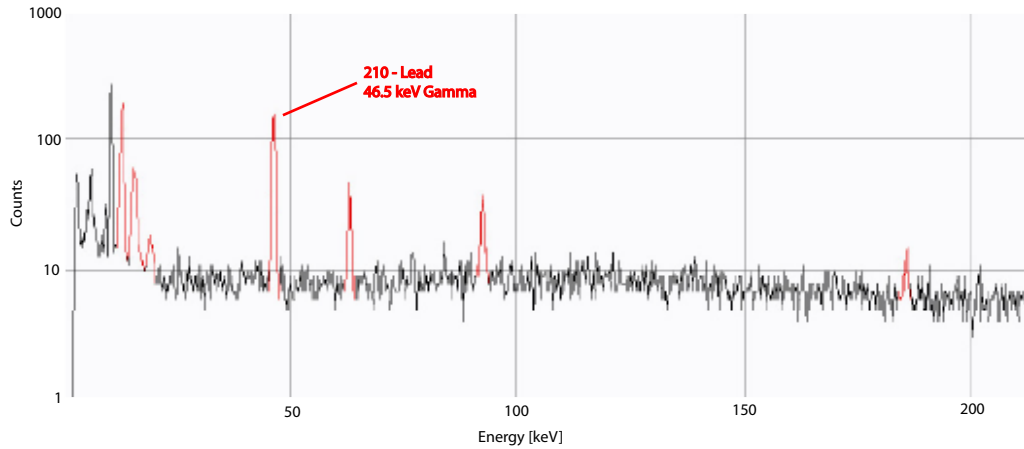
Figure 5.4: The gamma spectrum showing the 46.5 keV gamma peak from ^{210}Pb. The gamma detector has a resolution of about 500 eV at this energy.

shielding material, and the beryllium window is shown in Figure 5.5.

Partitioning measurements were also made for ^{210}Po by measuring its concentration on a surface and in solution. A silicon alpha detector was used to directly measure ^{210}Po on surfaces to find partitioning constants. A picture of the alpha detector is shown in Figure 5.6. On the top of the vacuum chamber is an Ortec ULTRA-AS ion-implanted-silicon detector. The circular active area is 12 cm^2. The front contact of detector is implanted with 50 nm of boron and the active depth is ∼100 µm. The resolution of the detector for alpha particles is 37 keV FWHM at 5.486 MeV. The intrinsic detector activity is < 15 counts per day between 3-8 MeV and the detector operates at -50 V. In order to prevent the absorption of the alpha particles in air before they reached the detector, the chamber was placed under vacuum during measurements. The measurement chamber was pumped out with a rotary vane pump with an inline filter to prevent the backflow of pump oil. The signal from the detector was amplified with an Ortec charge shaping amplifier. A CAMAC based ADC was used to read the charge. An alpha spectrum from one of the samples is shown in Figure 5.7.

The density of scintillator is $c_1 = 7.3 \times 10^3$ mol/m^3, and stays essentially constant
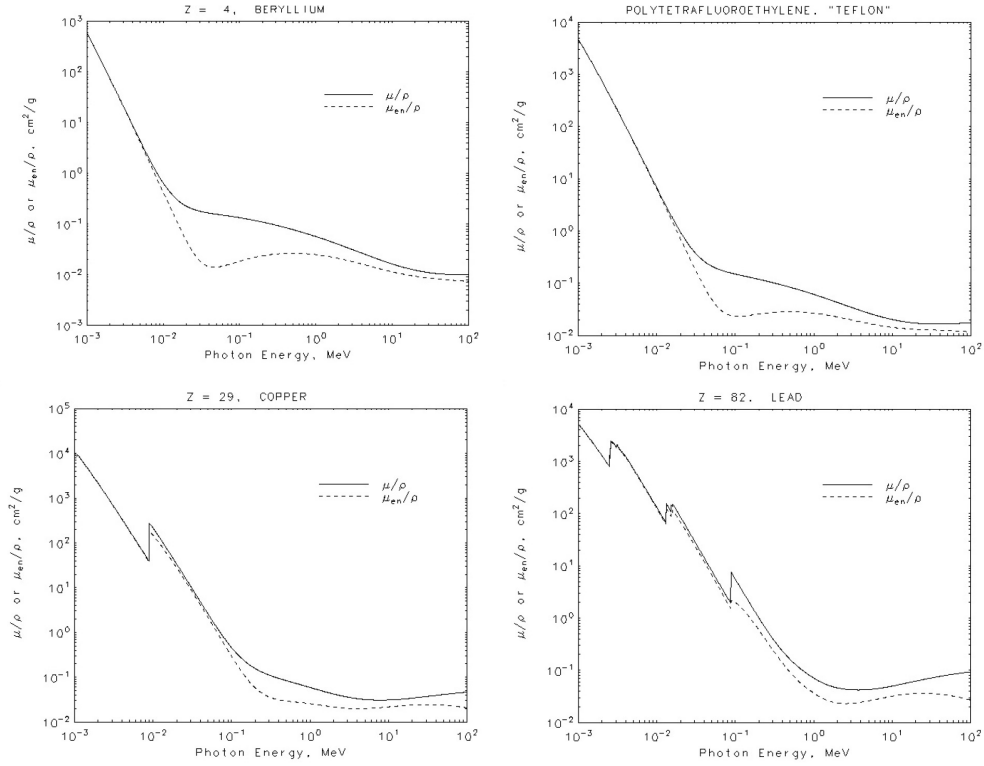
Figure 5.5: The xray mass attenuation coefficients for the shielding materials and the beryllium window as a function of energy. The density of Teflon is $2.2\,\mathrm{g/cm^3}$, copper $8.9\,\mathrm{g/cm^3}$, lead is $11.3\,\mathrm{g/cm^3}$, beryllium is $1.85\,\mathrm{g/cm^3}$. The attenuation is exponential with thickness x, is given by $I/I_0 = e^{-(\mu/\rho)x}$. Plots from [118].

since the solution is dilute. The lead and polonium concentrations in solution are of order $c_2 \sim 10^{-10}\,\mathrm{mol/m^3}$ (or fractional concentration $x_2 \approx 10^{-14}$). The surface concentrations for lead and polonium are on the order of $c_2^s \sim 10^{-11}\,\mathrm{mol/m^2}$ (surface coverage $\theta_2 \approx 10^{-6}$). This is safely in a regime where the surface concentration is linearly related to the bulk concentration by Henry's Law. Henry's constants found from the measurements are shown in Table 5.5.

This experiment resulted in a higher value for the Henry's constant on glass than the measurements with the test tubes. It is proposed that this is due to differences in the exposure of the surface. With the test tubes the radon in the scintillator had decayed away

Figure 5.6: The alpha detector used for measuring ^{210}Po decays on the surfaces of samples. The detector is attached to the top of the chamber.

before it came in contact with the glass. The only elements present were ^{210}Pb, ^{210}Bi, and ^{210}Po and the surface exposure lasted about 30 minutes. With the direct surface activity measurements the samples were in contact with the scintillator for about a month. Another difference was the presence of radon in the scintillator during the exposure. This allowed radon's immediate decay products like ^{218}Po, ^{214}Pb, ^{214}Bi, and ^{214}Po to bind to the surface in addition to the ^{210}Pb, ^{210}Bi, and ^{210}Po. For each decay there was a 50% probability that the nucleus would recoil into the material. This could cause the element to become embedded in the solid or increase the probability of chemical adsorption due to the large decay energies involved. Both these effects would increase the Henry's constant. However, further measurements are necessary to test this hypothesis.
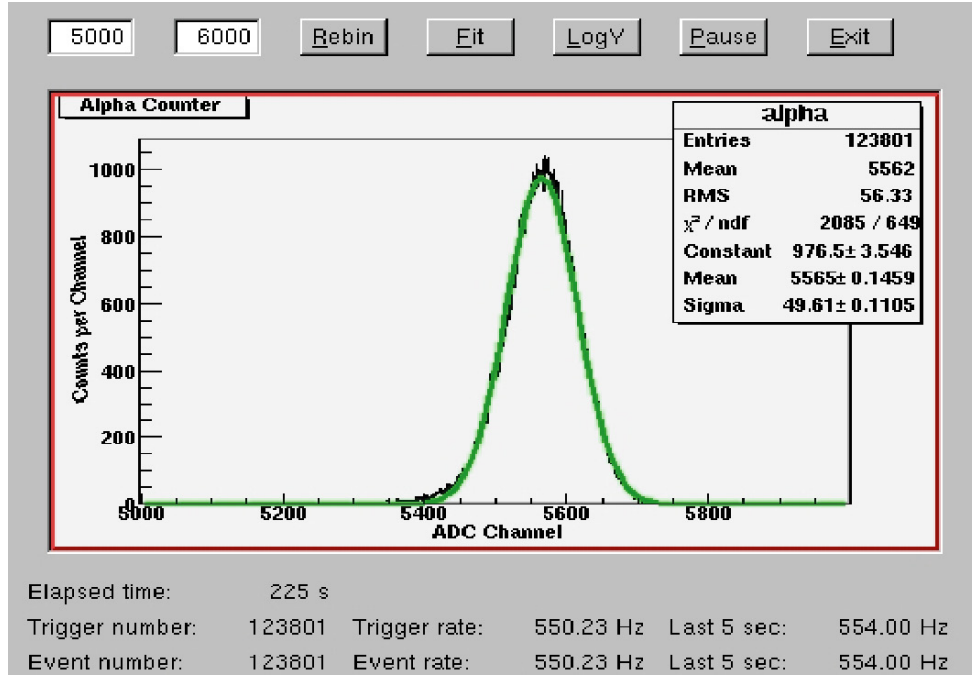
Figure 5.7: The alpha spectrum measured for ^{210}Po. Alpha decays occur at discreet energies producing distinct energy peaks. The energy resolution of alpha detectors is typically much poorer than for gamma detectors.

Material	$K_H(^{210}\text{Po})$ [cm]	$K_H(^{210}\text{Pb})$ [cm]
Steel	14	22
Nylon	3.9	-
Glass	2.8	-

Table 5.5: Henry's constants K for different elements ^{210}Po and ^{210}Pb at 20°C between pseudocumene and the material surface. Henry's Law states $c_i^s = K_H c_i$. It is not known exactly which chemical form the elements are in. The chemical form in these measurements should be similar to their chemical form in the unpurified Borexino scintillator.

5.1.5   Charged State of Polonium

Scintillator measurements with the Counting Test Facility have shown ^{210}Po contamination. Polonium is reactive and likely to bind to other molecules when in scintillator, though little in known about its actual molecular configurations. The following measurements were done to determine if the molecules were in an ionic state and if so, what the sign of the charge was.

^{210}Po is produced from the decay of ^{210}Bi. Bismuth beta decays with an energy of 1.17 MeV, resulting in a nucleus with an extra proton. The electrons will reconfigure themselves in response to the increased nuclear change. The probability of a given ionization state is determined by squaring the overlap of the initial and final electron wave functions. In practice this is hard to calculate due to the effect of the adjacent scintillator molecules.

Measurements were made to see if the molecules were charged by placing 15 volts across two samples of stainless steel and immersing them in a pseudocumene solution containing polonium. A third steel sample was inserted with a floating voltage. The polonium decay rate on each of the three steel samples was measured with an alpha counter after two and nine hours of exposure. Charged molecules are preferentially attracted to the plates with a voltage across them. The samples at 0 and +15 volts were oriented parallel to each other with ∼10 cm separation and the inward facing sides were counted. The floating sample was off to the side. A diagram of the setup is shown in Figure 5.8.
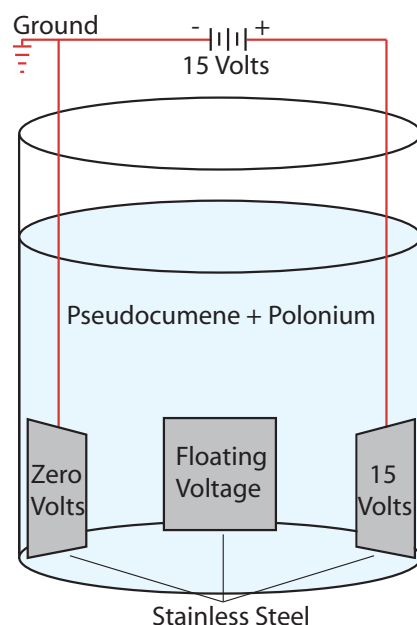
Figure 5.8: The setup for testing the charge state of ^{210}Po in scintillator. Three stainless steel samples were immersed in polonium loaded scintillator. The samples were held at $0\,\mathrm{V}$, $+15\,\mathrm{V}$, or left at a floating voltage.

The results are shown in Figure 5.9. The sample at $+15$ volts showed highest polonium adsorption, indicating the majority of the polonium is negatively charged. The sample at 0 volts (ground) had less adsorption than the sample at a positive voltage, but more than the steel sample left at a floating voltage. This seems to indicate a smaller fraction of the ^{210}Po is in a positively charged ionic state. Different experiments are needed to determine what the exact molecular configurations are. Note that when radon alpha decays in air, the ^{218}Po is produced primarily in a positively ionized state.
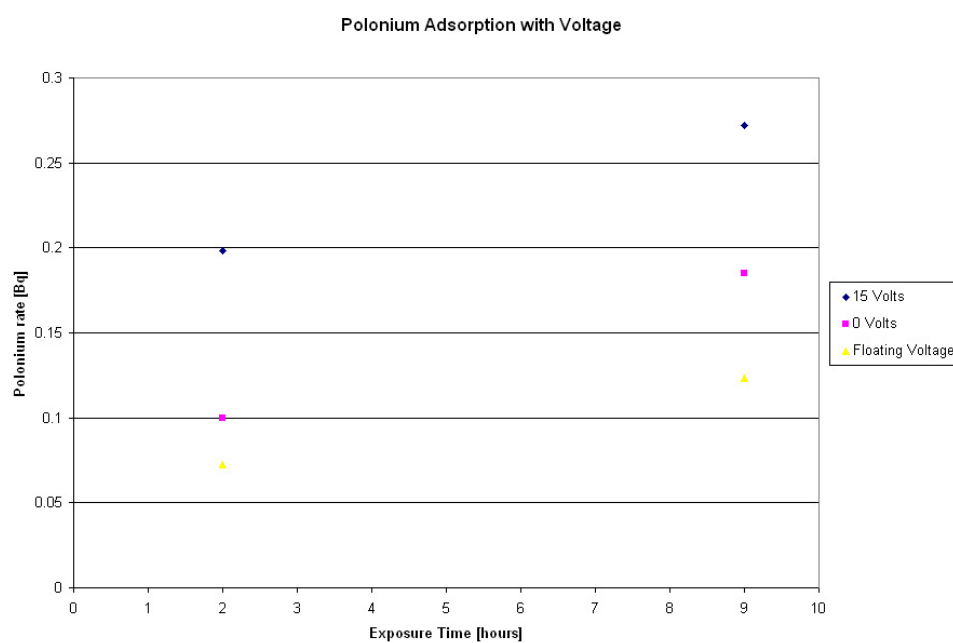
Figure 5.9: The ^{210}Po rate on stainless steel samples after being exposed to polonium loaded pseudocumene. The polonium decay rate on the steel samples was measured with an alpha detector. The data indicate that the polonium is in a negatively charged state.

5.2 Reaction Rates

From a pragmatic point of view, Borexino is concerned with how quickly surfaces become contaminated, or if contaminated, how quickly contaminants will leach into the scintillator. The rates constants for adsorption and desorption are not necessarily the same. While it was found that contaminants adsorbed quite rapidly, desorption was a much slower process. The energy required for desorption is at least the enthalpy of adsorption and possibly more if the adsorption is activated. Desorption occurs when phonons in the material break the surface bonds of the adsorbed molecules. Desorption can also occur through an external stimulus like an incident photon or electron. This is typically a much faster process, though the electrons or photons of sufficient energy must be present for it to occur.

A set of measurements was made to determine the time scale for desorption of ^{210}Pb on steel. A sample of electropolished stainless steel ($3\,\mathrm{cm} \times 3\,\mathrm{cm}$) was soaked in pseudocumene loaded with ^{210}Pb. The lead was attained by exposing the peudocumene to a high concentration of radon and allowing it to decay. The ^{210}Pb on the steel was measured with the gamma detector described in the previous section. The piece of steel was then soaked in deionized water at $50^{\circ}\,\mathrm{C}$ for a period of time after which the ^{210}Pb on the steel was remeasured.

The results of the desorption measurements are shown in Figure 5.10. The graph shows that the fractional surface concentration decreases linearly when plotted on a logarithmic time scale. This is unfavorable for cleaning processes that involve flushing or soaking pipes and tanks with water because removal of surface contaminants is slow. The desorption rate is generally a function of the substrate, adsorbed species, contact fluid, and temperature.

The rate of change of the surface concentration of ^{210}Pb can be described by

$$\frac{dc^s}{dt} = -kc^s \tag{5.18}$$

where C^s is the surface concentration of ^{210}Pb, and k is the rate constant. The logarithmic time dependence indicates that in this case desorption is a first order reaction and the rate is linearly dependent on the concentration. The surface concentration would then decay
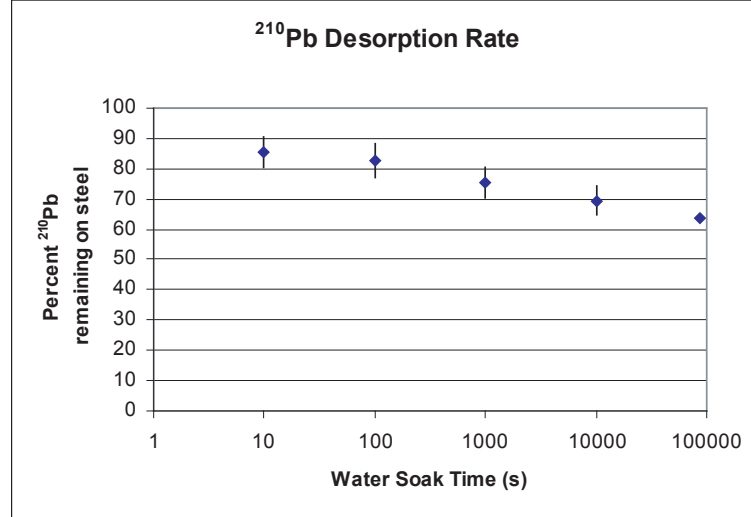
²¹⁰Pb Desorption Rate

Figure 5.10: The desorption of ^{210}Pb from stainless steel into water as a function of time. The steel ($3\,\text{cm}\times3\,\text{cm}$) was soaked in one liter of $10\,\text{M}\Omega$ deionized water at $50°\,\text{C}$. The first four data points were made with the same sample that was repeatedly soaked and counted. A separate sample was measured with higher statistics after a one day soak for the data point on the right. The desorption mean life $\tau \sim 100\,\text{days}$ [119].

exponentially according to

$$c^s = c_0 e^{-kt} \tag{5.19}$$

where C_0 is the initial surface concentration. The rate of removal can be described by a mean life $\tau = 1/k$. For ^{210}Pb desorption from steel into water $\tau \sim 100\,\text{days}$.

The desorption of ^{210}Po from nylon into water has also been measured and shown to be a first order reaction [120]. Nylon samples were exposed to high concentrations of airborne radon gas. The progeny were deposited on the surface and allowed to decay. Samples were then soaked in deionized water for different amounts of time to remove the ^{210}Po. The ^{210}Po remaining on the nylon was then measured using an alpha detector to observe the ^{210}Po decays. The data are shown in Figure 5.11. The mean life for ^{210}Po desorption from nylon into water is $\tau \sim 22\,\text{hours}$.

Several measurements have been done to test the effects of aggressively cleaning stainless
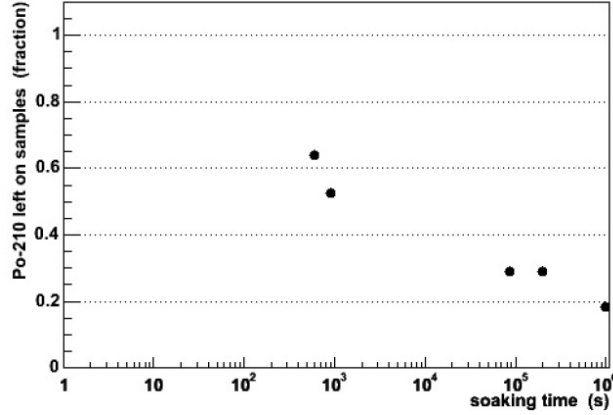
Figure 5.11: The desorption of ^{210}Po from a nylon surface into deionized water as a function of time. Plotted is the ^{210}Po rate on nylon versus the logarithmic soak time. The nylon samples were originally exposed to airborne radon. The mean life for desorption $\tau \sim 1$ day. Figure from [121].

steel detergent solutions. Data are shown in Table 5.6. With out a detergent cleaning, ^{210}Pb desorption is a problem for Borexino. These measurements also show that the desorption rate of ^{210}Pb from steel into pseudocumene is a very slow process. Elevated temperatures were used because for some cleaning operations to speed desorption.

Several additional measurements of ^{210}Po removal from stainless steel were made [122]. They used stainless steel samples exposed to high concentrations of radon gas. The ^{210}Po on

Soak Treatment	Temperature	Time	Percent Remaining
Pseudocumene	20° C	10 Hours	96.1±1.1%
Pseudocumene	20° C	1 Day	95.9±0.8%
Water	50° C	1 Day	63.7±0.9%
Brulin Detergent	50° C	1 Day	16.0±0.6%
Brulin Ultrasonic	20° C	1 Hour	11.7±0.5%

Table 5.6: ^{210}Pb removal from on stainless steel through various cleaning methods. These results are representative of the relative efficiencies of each method. They are also indicative of the desorption rate for each process.

the surface was measured before and after treatment with and alpha detector. The samples were cleaned with several detergents including a chelating agent, Ecoinox, Alconox, and Ecoclean for a time of 1-5 hours. The cleaning was done mostly at temperatures 80 C and with a few samples washed at 20 C. The cleaning agents removed 50-55% of the ^{210}Po from the surface in all cases. Secondary cleaning of the steel showed no further removal of ^{210}Po to within 5%. Samples of stainless steel that were soaked in pseudocumene for 13 hours after washing were also showed no ^{210}Po removal within the experimental errors.

5.3 Polonium Partitioning in the CTF

An analysis was done for the ^{210}Po partitioning between the scintillator and nylon vessel in the CTF III. The diameter of the nylon vessel in the CTF is 1 m, thus the surface area is 4π m^2, the volume is $\frac{4\pi}{3}$ m^3, and the volume to surface ratio is 0.33 m.

The CTF partitioning analysis used a radial cut $r > 85$ cm to find the surface events. Events from the scintillator in the volume from $85 < r < 100$ cm were subtracted from the data. The is only water for $r > 1$ m. The internal scintillator rate was determined by finding the activity at $r < 65$ cm where surface events were negligible. Other alpha activity from the radon chain was shown to be low by observing the Bi-Po coincidences.

In the CTF III the total radioactive contamination partitioning between the nylon and the scintillator has a constant $K_H \approx 3$ m, which is larger than expected. This large partitioning constant can be partly explained by a concentration of surface events at the bottom of the vessel likely due to the settling of heavy particulates. Also adding to the surface component is the pipe activity at the north and south pole. For ^{210}Po on the vessel the partitioning constant was in the range of 2-10 m depending on the time period, which is also higher than expected.

The surface counts in the CTF were not distributed evenly over the vessel. The poles of the vessel are hotter than the rest of the vessel, mainly due to the extra nylon material in those regions. The south pole also had a higher event rate than the north. It is suspected that the asymmetry is caused by radioactive particulates settling out of the scintillator. An

asymmetry parameter is defined as

$$A = \frac{s - n}{s + n} \tag{5.20}$$

where s is the count rate on the southern hemisphere and n is the rate on the northern hemisphere. The asymmetry is defined so that A is positive when the south pole is hotter. For the CTF III runs the asymmetry parameter is in a range

$$0.10 < A < 0.25 \tag{5.21}$$

with fluctuations occurring over time.

The time for contaminants to reach equilibrium between the nylon surface and bulk scintillator in the CTF is dominated by the rate of diffusion in the vessel when there is no fluid motion. The time it takes for a molecule to diffuse across the $1\,\mathrm{m}$ radius vessel full of scintillator is about 3 years. Any fluid motion will reduce the equilibrium time. It is believed that the scintillator in the vessel is stationary for over two years between 2003-2005 when operations were stopped. The only possible fluid motion during this time would have resulted from thermal convection currents and temperature measurements indicate that there was a relatively stable vertical temperature gradient making this unlikely.

During the later portion of the CTF III when operations were stopped, a column of contaminants formed from the top of the vessel. It is suspected that these contaminants were in the form of heavy particulates because the column did not exhibit significant diffusional broadening. These particles likely originated in the north end pipe and settled gravitationally. This also indicates that particulates were present and settled to the bottom of the vessel. Surface events that have settled out due to particulates are not distinguishable from contaminants attached to the nylon vessel in the current analysis. For a more detailed discussion see Reference [87].

5.4 Radon Progeny Deposition

One of the most prevalent radioactive backgrounds is from radon gas, which is naturally present in air. Each year about 20000 people die from lung cancer due to radon. Typical

indoor radon activities are from 10-100 Bq/m^3, though they can increase to several thousand Bq/m^3 in mines and caves where low background experiments are usually located to shield cosmic rays. The half-life of radon is 3.8 days, but it is continually replenished by emanation from the ground where deposits of ^{266}Ra reside. While the radium deposits are stationary, radon is a noble gas which is highly mobile and can diffuse to the surface. To reduce radon activity, buildings are typically ventilated with clean outside air.

Properties of radon and its progeny have been extensively studied to understand human radiation exposure from their inhalation. Many of the associated measurements and models are also of interest to low background experiments that must deal with surface contaminants. An excellent review of the literature can be found in *Radon And Its Decay Products In Indoor Air* by W. Nazaroff and A. Nero [123]. For low background experiments, radon is a problem because of the ^{210}Pb isotope. Because the ^{210}Pb half-life is long compared to the lifetime of a typical experiment, it is not practical to wait for ^{210}Pb to decay away. ^{210}Pb beta decays to produce ^{210}Bi which beta decays to ^{210}Po and ^{210}Po alpha decays to ^{206}Pb which is stable. Thus, the deposition of radon progeny results in the presence of three radioactive isotopes that persist long after the surfaces are isolated. The radon decay chain is shown in Figure 5.12.

Though radon is a noble gas and does not react, its progeny readily stick to surfaces. The rate of gas adsorption is given by

$$R_{ads} = A_{ads}Pe^{-E_{ads}/k_BT} \tag{5.22}$$

where A_{ads} is a constant for adsorption, P is the partial pressure, T is the temperature, and E_{ads} is the activation energy for adsorption. The rate of desorption is

$$R_{des} = A_{des}Ne^{-E_{des}/k_BT} \tag{5.23}$$

where A_{des} is a constant for desorption, N is the surface concentration of the adsorbed species, and E_{des} is the energy of desorption. The adsorption enthalpy is

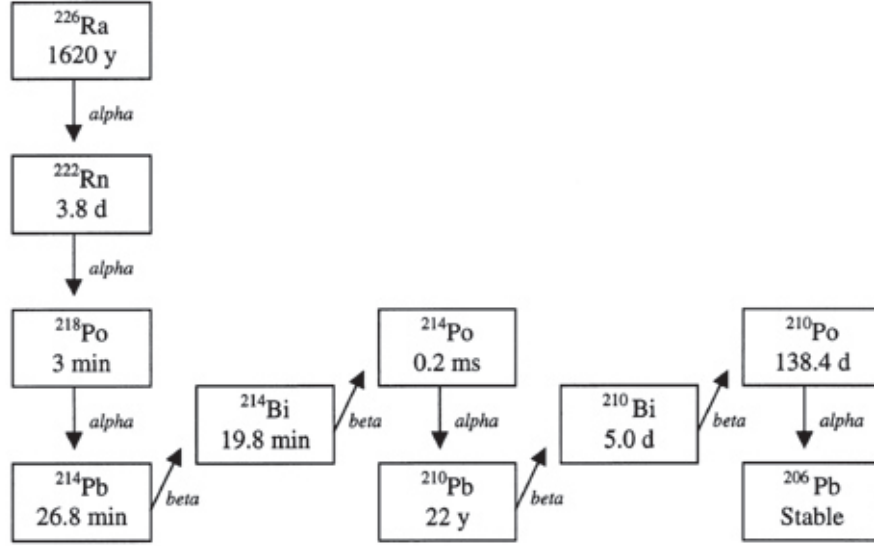$$H_{ads} = E_{ads} - E_{des}. \tag{5.24}$$

Figure 5.12: The radon decay chain is part of the ^{238}U decay chain. Once radon decays, the progeny have short half-lives of less than an hour each until ^{210}Pb is reached. The 22 year half-life of ^{210}Pb and the subsequent decays of ^{210}Bi and ^{210}Po are a problem for low background experiments like Borexino.

The constants for adsorption and desorption are related by

$$\frac{A_{ads}}{A_{des}} = e^{-\frac{S_{ads}}{k_B}} \qquad (5.25)$$

where S_{ads} is the entropy of adsorption. At equilibrium the rates of adsorption and desorption are equal. In addition to normal physical desorption through phonon interactions, radioactive elements may also break free from a surface when they decay.

The adsorption rate can be alternatively described as

$$R_{ads} = J \cdot S \qquad (5.26)$$

where J is the flux and S is the sticking probability. The flux is

$$J = \frac{P}{\sqrt{2\pi m k T}} \qquad (5.27)$$

where P is the partial pressure of the gas, and m is the mass. The sticking probability is

$$S = f(\theta)e^{-E_{ads}/RT} \qquad (5.28)$$

Particle Diameter	0.1μm	0.2μm	0.3μm	0.5μm
Class 1	1240	265	106	35.3
Class 10	12400	2650	1060	353
Class 100	124000	26500	10600	3530

Table 5.7: Maximum number of particles per m^3 equal to or greater than the specified size for various classes of clean rooms. The class refers to the number of particles per cubic foot with a diameter of at least $0.5\,\mu$m.

where $f(\theta)$ is some function of the surface coverage. In the case where $E_{ads} = 0$, and interactions between adjacent adsorbed molecules can be ignored the sticking probability is

$$S = 1 - \theta \tag{5.29}$$

where θ is the fractional surface coverage.

The deposition rate of ^{210}Pb is slow due to the low concentration of radon progeny and the large number of surface adsorption sites. For reference a flat surface has $\sim 10^{19}$ adsorption sites per square meter. Both fixed surfaces and aerosol particles provide sites for radon progeny to bind to. Aerosol particles with attached radon progeny can also adhere to fixed surfaces. In a low particulate environment such as a class 100 clean room few progeny will be attached to aerosols and the amount of ^{210}Pb deposited on a surface will be about 10^6 atoms/m^2/year. Specification for different classes of clean rooms are shown in Table 5.7. A high particulate environment which is more typical will have a ^{210}Pb deposition rate of 10^5 atoms/m^2/year due to the slower deposition of aerosols. In ambient conditions almost all the radon progeny will be attached to aerosol particles. At equilibrium the rate of ^{210}Pb deposition will equal the rate of ^{210}Pb decay and there will be a surface concentration of $\sim 10^7$ atoms/m^2. The surface activity from ^{210}Pb as a function of exposure time is shown in Table 5.8.

Radon progeny are formed in energetic decays, allowing them to ionize and react with molecules in the environment. The exact chemistry is difficult to predict as it is strongly dependent on various pollutants in the atmosphere. Reactions have been observed to be highly dependent on the concentrations of specific contaminants.

Time	Surface Activity [Bq/m^2]
Minute	3×10^{-9}
Hour	2×10^{-7}
Day	5×10^{-6}
Week	4×10^{-5}
Month	2×10^{-4}
Year	2×10^{-3}

Table 5.8: The typical surface activity from ^{210}Pb due to the deposition of radon progeny in a low particulate environment. This assumes a deposition velocity of $2\,$mm/s, and a radon activity of $30\,$Bq/m^3. As a rule of thumb a surface will acquire about $\sim 1\,$mBq/m^2 of ^{210}Pb activity per year of air exposure. Surfaces in equilibrium with ^{210}Pb will have an activity of $\sim 10\,$mBq/m^2.

The concentration of radon progeny in a room is relatively constant when measured sufficiently far from the walls. Near the walls, the concentration of the progeny decreases because the walls act like a sink. The surface concentration σ is the integral of the flux J towards the walls over the time of exposure t. The flux is found from the diffusion equation

$$J(x,t) = -D\nabla C(x,t) \tag{5.30}$$

where D is the effective diffusion constant, and $C(x,t)$ is the concentration at position x and time t. However, if the concentration is constant in time and space (away from surfaces), it is convenient to instead represent the flux J as the product of the room concentration C and a deposition velocity v_d. The deposition velocity, which is a mass transfer coefficient, is

$$v_d = \frac{D}{z_o} \tag{5.31}$$

where D is the diffusion constant and z_o is the boundary layer thickness. The boundary layer z_o is the region near a surface where the air is essentially static and convection is negligible. Boundary layer diffusion near a wall is illustrated in Figure 5.13.

The deposition velocity can be thought of as the rate at which particles diffuse towards
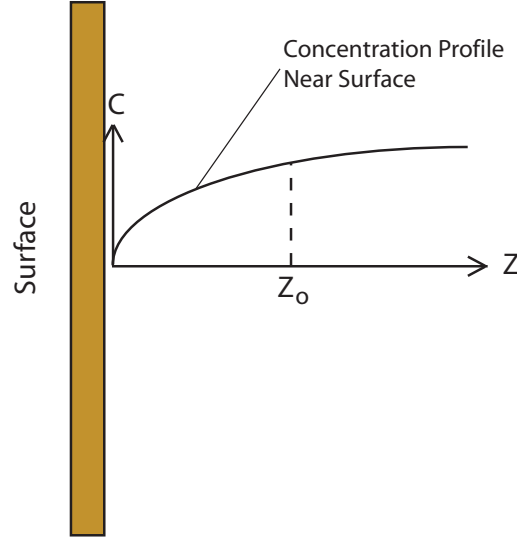
Figure 5.13: The concentration profile of radon progeny near a surface. The concentration in a room is roughly constant at distance larger than z_o away from a surface. The deposition rate is relatively independent of orientation of the surface. Near a surface the concentration decreases due to adsorption. The thickness of the boundary layer z_o is determined by the air flow in a room. In a typical room the boundary layer would range from $4\,\mathrm{cm}$ to a few millimeters.

a surface. The deposition of radon progeny can then be described by

$$\sigma(^{210}\mathrm{Pb}) = \sum_{i=1}^{5} C_i v_d t \tag{5.32}$$

where:

$\sigma(^{210}\mathrm{Pb}) =$ the surface density of ^{210}Pb atoms [atoms/m^2];

$C_i =$ the concentration of ith radon daughter [atoms/m^3];

$i =$ index denoting specific progeny $\{1, 2, 3, 4, 5\} \rightarrow \{^{218}\mathrm{Po},\ ^{214}\mathrm{Pb},\ ^{214}\mathrm{Bi},\ ^{214}\mathrm{Po},\ ^{210}\mathrm{Pb}\}$;

$v_d =$ the deposition velocity [m/s];

$t =$ the exposure time [s].

The ^{210}Pb does not appear immediately, but is produced after the radon and short lived precursors that stick to the surface decay. For time scales longer than several hours, the time for these quickly decaying isotopes to become ^{210}Pb can be safely neglected.

Variable	Deposition Velocity
Air Velocity	Increased
Aerosol Attachment	Decreased
Charged Fraction	Increased
Negative Ion Density	Decreased
Surface Roughness	Increased

Table 5.9: Factors influencing the deposition velocity v_d. A higher air velocity reduces the boundary layer near a surface z_o, increasing the deposition velocity. Aerosol attachment slows deposition because aerosols diffuse more slowly than individual atoms. The fraction of charged progeny is determined by the air composition. A higher fraction of charged progeny will increase the deposition velocity if static charges are present on surfaces. A high negative ion density will reduce the fraction of charged progeny which are usually positive ions.

Studies have found that for progeny are not attached to aerosols the deposition velocity $v_d = 4 \times 10^{-3}$ m/s in an average room [124]. This number can fluctuate by a factor of two in either direction depending on the local conditions. The deposition velocity depends mostly on the local air flow and airborne particulate concentration.

The deposition velocity is significantly reduced by the attachment of radon progeny to aerosols. Surface charges, if present, can also be a dominant factor in the deposition rate. Insulators are very susceptible to static charge buildup on their surface, while metals can be grounded to keep them neutral. A partial list of the factors influencing the deposition velocity is given in Table 5.9.

The concentration of each radon progeny is determined by its half life, the concentration of its parent, the ventilation rate of the room, the total surface area which acts as a sink, filtration, and surface recoils which can free attached progeny. The Jacobi Model (which is not discussed here) uses these parameters to describe the steady state progeny concentrations with a set of coupled differential equations [125]. Some interactions that influence the concentration of radon progeny are shown in Figure 5.14.

Aerosols usually have the biggest impact on the deposition velocity. Generally the fraction of progeny attached to aerosols increases with aerosol density, though it is also dependent on the size distribution of the aerosols. Attachment of radon progeny to aerosol

particles will reduce the deposition velocity by roughly a factor of 10. A typical distribution of aerosol particle sizes is shown in Figure 5.15. Environments that are particularly dusty due to construction of machining or are especially clean due to filtering will have distributions that differ significantly. A large number of deposition velocity measurements have been made under a variety of conditions. Some measurements of deposition velocities are shown in Figure 5.16.

The deposition rate can be broadly classified into two categories, one for unattached progeny, and another for the deposition of aerosols with attached progeny. Aerosol deposition is a slower process due to the larger mass of the particles. The deposition of neutral aerosol particles occurs either from diffusion or gravitational forces. For particles greater that about $1\,\mu$m sedimentation due to gravity dominates. For smaller particles less that about $0.1\,\mu$m diffusion tends to dominate. Stokes Law says the drag force F_d on a particle with small Reynolds numbers (Re < 1) is

$$F_d = 6\pi\mu rv \tag{5.33}$$

where r is the radius of the particle, and v is the velocity, and μ is the dynamic viscosity of air. The settling velocity of a particle is calculated from Stokes Law [126].

$$v_s = \frac{\rho_p d_p g C}{18\mu} \tag{5.34}$$

where ρ_p is the particle density, d_p is the particle diameter, $g = 9.81\,\text{m/s}^2$ is the gravitational acceleration, and C is the slip correction factor.

$$C = 1 + 2.592\frac{\lambda}{d_p} + 0.84\frac{\lambda}{d_p} + e^{-0.435\frac{\lambda}{d_p}} \tag{5.35}$$

where $\lambda = 6.52 \times 10^{-8}\,\text{m}$ is the mean free path in air. A $1\,\mu$m particle will have a settling velocity of about $5 \times 10^{-5}\,\text{m/s}$ as shown in Figure 5.17.

The diffusion constant of an aerosol particle is

$$D = \frac{k_B T C}{3\pi\mu d_p} \tag{5.36}$$

where T is the temperature. The average diffusion constant of an atom in air at STP is $0.054\,\text{cm}^2/\text{s}$. The average velocity of an atom is found from the Maxwell-Boltzmann

distribution

$$f(v) = 4\pi \left(\frac{m}{2\pi k_B T}\right)^{\frac{3}{2}} v^2 e^{-\frac{mv^2}{2k_B T}} \tag{5.37}$$

resulting in

$$\bar{v} = \sqrt{\frac{8k_B T}{\pi m}} \tag{5.38}$$

In air at room temperature the average velocity is $450\,\mathrm{m/s}$, which is similar to the speed of sound.

If present, static charges will be the dominant factor in the adsorption rate. The motion from electric forces between charged particles will overwhelm the diffusive motion. ^{218}Po and ^{214}Pb that are formed from decays in air are positively charged ions, though the fraction of the ^{214}Pb that is charged is lower. The charged state of radon progeny can be partly explained by the interactions that take place shortly after the decay.

When a ^{222}Ra alpha decays to forms ^{218}Po, it releases $5.49\,\mathrm{MeV}$ of energy. Since this is a two body decay, the energy of the ^{218}Po ion can be found by conserving energy and momentum. The energy of the ^{218}Po ion is $101\,\mathrm{keV}$. This ion is positively charged due to the stripping of electrons by the alpha particle. The singly charged state is most common and is empirically found to occur 88% of the time [129]. The velocity of the particle found from its energy is $v = 3 \times 10^5\,\mathrm{m/s}$. The recoil range in air is about $R_c = 50\,\mu\mathrm{m}$ [67]. The stopping times T is

$$T = 1.2 \times 10^{-7} R_c \sqrt{\frac{m}{E}} \tag{5.39}$$

with m in [amu] and E in [MeV]. This gives a stopping time of $T = 2.8 \times 10^{-10}\,\mathrm{s}$. During this time the polonium will undergo roughly 10^{12} collisions. Once thermalized the collision frequency is about 10^9 collisions/s.

When a ^{218}Po ion is created, it undergoes one of three processes: neutralization, aerosol attachment, or a chemical reaction. For neutralization the positive polonium ion will combine with a negative ion or free electron. The half life of neutralization $\tau_{1/2}$ is

$$\tau_{1/2} = 0.693 \frac{\epsilon_0}{NeB} \tag{5.40}$$

where N is the number density of negative ions, $e = 1.6 \times 10^{-19}\,\mathrm{C}$ is the electron charge, $B \sim 1.6 \times 10^{-4}\,\mathrm{m^2/V/s}$ is the ion mobility, and $\epsilon_0 = 8.85 \times 10^{-12}$ is the permittivity of free

space [130]. The mobility and diffusion constants are related by

$$\frac{B}{D} = \frac{e}{k_B T} \tag{5.41}$$

For a typical negative ion concentration of $N = 2 \times 10^8/\mathrm{m}^3$ the neutralization half life $\tau_{1/2} = 20\,\mathrm{minutes}$ [131]. This is much longer than the $3.1\,\mathrm{minute}$ half life of $^{218}\mathrm{Po}$. The polonium ions can also transfer their charge to neutral atoms in the atmosphere. This will most likely happen with molecules that have an ionization energy less than the $8.34\,\mathrm{eV}$ of polonium. It is proposed that the primary mechanism for neutralization is the reaction with oxygen, which has a high electron affinity [132, 133].

The high ionization fraction of radon progeny allows them to be easily removed with electrostatic methods. For example a wire with a large negative voltage will effectively remove charged progeny within a $\sim 1\,\mathrm{m}$ radius.
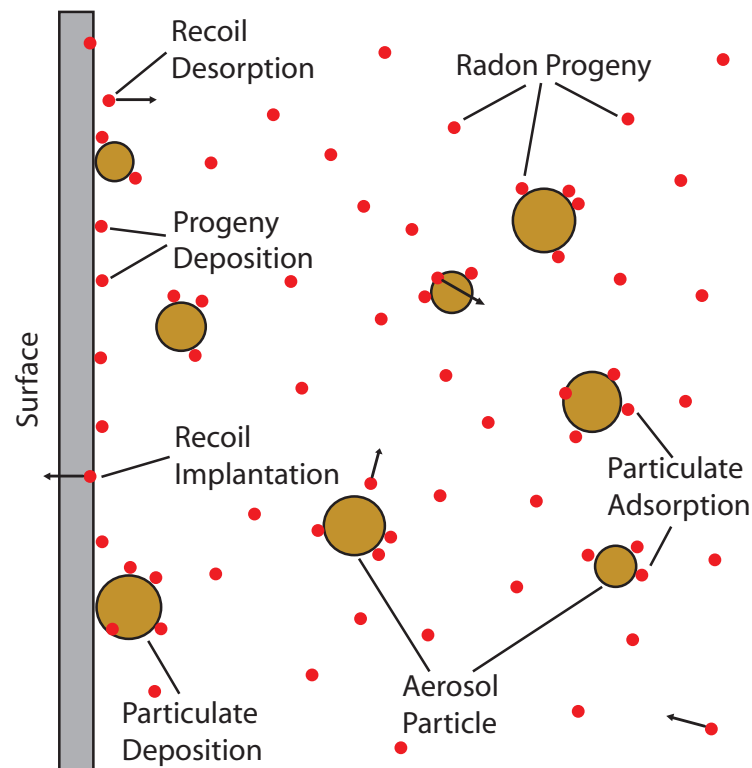
Figure 5.14: The concentration of radon progeny is determined by the rate of a several of mechanisms. Progeny can attach to fixed surfaces or to aerosol particles. The rate of aerosols deposition on surfaces is slower than the deposition rate of unattached progeny. Nuclear recoils resulting from the decay of adsorbed progeny can lead to implantation in the surface or desorption depending on the direction. Implanted ions are stationary though they can be freed by the recoil from a subsequent decay. Most radon progeny will decay to ^{210}Pb after several hours.
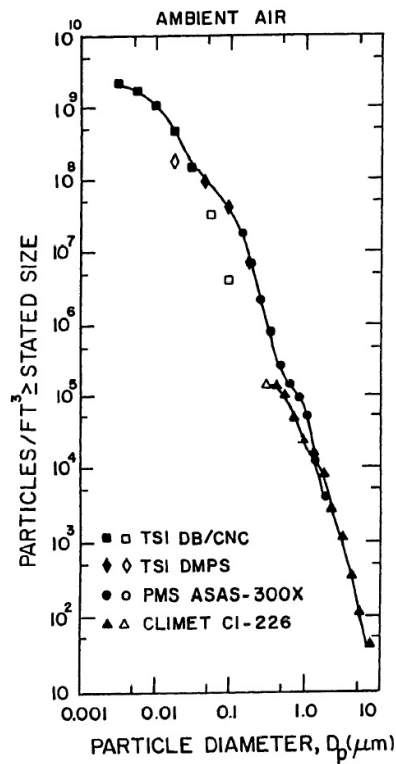
Figure 5.15: A typical size distribution of aerosol particles in ambient air. These particular measurements were taken in Minneapolis. The distribution is known as a Jung distribution where the slope is -3 for sizes larger than $0.1\,\mu$m on a logarithmic plot. This corresponds to an eight fold concentration decrease when the particle size doubles, or a thousand fold reduction when the particle size increases a factor of 10. Figure from [126].
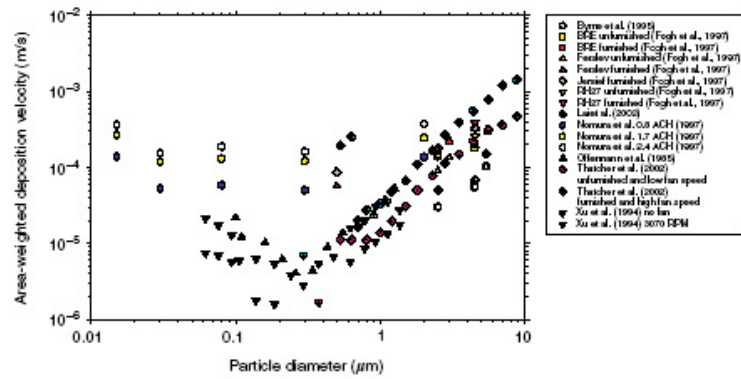
Figure 5.16: The area averaged deposition velocity of aerosol particles in a room sized chamber. The minimum deposition velocity occurs for particles with a diameter of about 200 nm. Figure from [127].
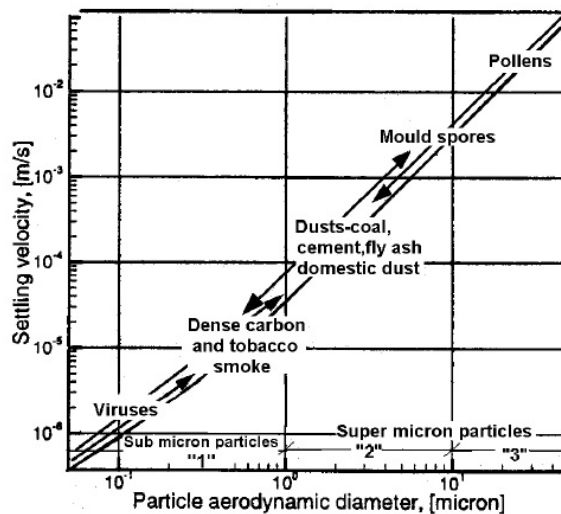

Figure 5.17: The settling velocity of aerosol particles [128].

5.4.1 Deposition Measurements

The nylon vessels in Borexino remain in direct contact with the liquid scintillator and are the nearest component to the fiducial volume, making a high level of vessel cleanliness essential. Measurements were performed to test the build up of ^{210}Pb on a nylon surface in a clean room environment [134]. A small test clean room ($2\,\text{m} \times 2\,\text{m} \times 3\,\text{m}$) was built to simulate the full scale class 100 clean room where the Borexino nylon vessels were fabricated. A clean room environment differs significantly from a typical room because the aerosol concentration is small enough that the attachment of radon progeny is negligible. The air flow in a clean room due to the high filtration rate is also significantly higher than normal. Though the clean room filters do little to remove radon gas, they remove the radon progeny quite efficiently. It is worth noting that the test clean room was different from a standard clean room in that it was well sealed to retain radon during the exposure. This resulted in a small ventilation rate, while maintaining a high filtration rate.

A clean room class is defined by the maximum number of particles per cubic foot with a diameter $0.5\,\mu$m or larger. The maximum number of particles greater than a certain size for different clean room classes is shown in Table 5.7. The particle distribution in a class 10 clean room is shown in Figure 5.18.

To measure the effective deposition velocity, nylon film samples ($5\,\text{cm} \times 5\,\text{cm}$) were placed in the test clean room. A $2\,\text{MBq}$ radon source was used to expose the room and nylon samples to a high radon concentration. The radon concentration in the test clean room was monitored over time using a RAD7 radon detector. The samples of nylon were then removed and the ^{210}Pb surface contamination was measured. The actual measurement was of the ^{210}Po α decays with a silicon detector. The ^{210}Pb rate was calculated by accounting for the build up time of ^{210}Po. Since only the radon concentration was measured and not that of the progeny, the ^{210}Pb surface contamination is expressed as

$$\sigma(^{210}\text{Pb}) = [\sum_{i=1}^{5} C_i]v_d t = [kC_0(t)]v_d t \tag{5.42}$$

where we take the sum over progeny to be proportional to the radon concentration $C_0(t)$ at time t. The constant k, which is dominated by the filtration rate, is incorporated into
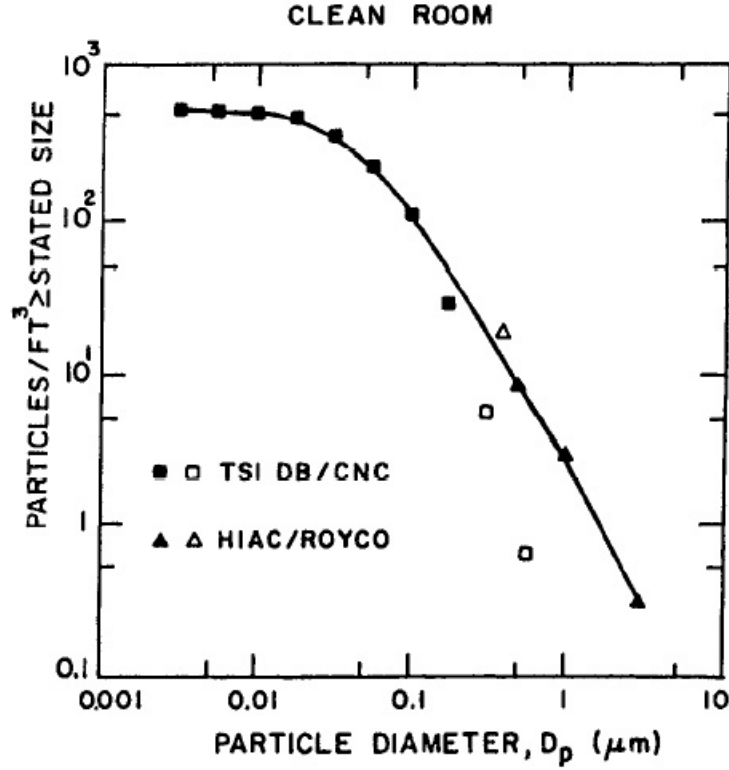
Figure 5.18: A typical size distribution of aerosol particles in a class 10 clean room. Figure from [126].

an effective deposition velocity $v_0 = k v_d$. The ^{210}Pb surface contamination is then

$$\sigma(^{210}\mathrm{Pb}) = C_0(t) v_0 t \qquad (5.43)$$

where $C_0(t)$ is the radon concentration at time t and v_0 is an effective deposition velocity. The test clean room experiment provided the integrated radon exposure and ^{210}Pb surface contamination. It showed that in a clean room environment the effective deposition velocity is

$$v_0 = 3 \times 10^{-8}\,\mathrm{m/s}. \qquad (5.44)$$

This effective deposition velocity is roughly three orders of magnitude smaller that the average deposition velocity for an unattached radon progeny in a typical room. The most

Parameter	Value
Volume	$770\,\mathrm{m}^3$
Filters	84 HEPA
Flow Type	Laminar
Relative Humidity	50%
Temperature	$290\,\mathrm{K}$
Ventilation Rate	$0.024\,\mathrm{m}^3/\mathrm{s}$
Filtration Rate	$28\,\mathrm{m}^3/\mathrm{s}$
Particulates $d > 0.5\,\mu\mathrm{m}$	$< 3530/\mathrm{m}^3$
Radon Activity	$1\,\mathrm{Bq}/\mathrm{m}^3$

Table 5.10: Specification for the class 100 clean room where the Borexino nylon vessels were fabricated. Modifications were made to reduce the deposition of radon progeny. The filtration constant $\lambda_f = 0.036/\mathrm{s}$.

likely explanation is that the high filtration rate removed the radon progeny from the air before they reached the nylon samples. If this is indeed the case then the effective deposition velocity should scale inversely with the filtration constant λ_f, which is defined as the number of volumes filtered per time.

5.4.2 Borexino Nylon Vessel Fabrication Precautions

The Borexino nylon vessels were fabricated in a customized class 100 clean room in Princeton, NJ. This clean room used a radon filter to provide low radon air for ventilation. The filter was a vacuum swing adsorption system, which could supply up to $170\mathrm{m}^3/\mathrm{h}$ of air with a radon activity of $<0.3\,\mathrm{Bq}/\mathrm{m}^3$ [135]. The clean room was sealed to minimize the makeup air required to keep an over pressure and to prevent the back diffusion of radon. Clean rooms are typically not well sealed. Inside the clean room the radon activity was reduced to about $1\,\mathrm{Bq}/\mathrm{m}^3$ during fabrication. The clean room specifications are shown in Table 5.10.

During the vessel fabrication the nylon film was discharged with anti-static rods to prevent charged progeny from being attracted to the vessel. It was also kept well covered when not in use. Only the edges, where the joints were made, saw significant air exposure. Since the nylon vessels will be filled with water for many weeks during commissioning, it

is expected that much of the deposited contamination will be removed. Details about the nylon vessel fabrication can be found in reference [120].

5.4.3   Steel Cleaning

Stainless steel parts are pretreated before installation in the detector. This process begins by cleaning the steel to remove oils and hydrocarbons that are stuck to the surface. Cleaning is done with a detergent or solvent. The next step involves electropolishing or pickling and passivating when electropolishing is impractical.

Electropolishing is accomplished by placing the part in an ionic solution and applying a voltage. As current flows, metal from the surface is removed and deposited into the solution. It is essentially electroplating in reverse. Electropolishing preferentially removes protrusions and sharp edges from a metal surface. This makes the surface smooth and highly reflective giving electropolished pieces a bright finish. The main drawback of electropolishing is that it can not be used on sharp sealing surfaces for applications where a tight tolerance is required.

Pickling removes scale from heating and rust, and takes off a layer of low chromium material from the surface of the steel. Pickling is usually done chemically with nitric and hydrofluoric acids. At weld sites a strong pickling paste is used. Pickling creates a clean chromium rich layer at the metal surface. Passivation speeds the formation of a protective passive film by removing iron from the surface layer. Passivation is done with a nitric or citric acid solution.

After pickling and passivation or electropolishing the metal is washed in an ultrasonic bath or rinsed in deionized water to get rid of any remaining acids, solutions, or particulates that are attached to the surface. Theses processes remove the outer layer of steel and any ^{210}Pb that has been deposited. Contamination is minimized by limiting air exposure after treatment.

5.4.4 Teflon Filter Contamination

The surface of the Teflon filters can be contaminated by radon gas deposition. The nominal surface area is $1.3\,\mathrm{m}^2$, but the actual surface area including the pores is a few orders of magnitude larger. The filter packaging is made of a material which is permeable to radon and does not act as a good barrier against diffusion. Assuming the radon concentration inside the filters is not affected by the packaging, the activity of ^{210}Pb on the filters can be calculated. For a one year exposure to air, the filters will have $\sim$200 counts/day of ^{210}Pb. If lead on the filter then desorbs into the scintillator with which it comes in contact, it will produce an unacceptably large background for the experiment. As a result of the ^{210}Pb will wash off, the filters need to be cleaned before installation. Proper storage to prevent further radon deposition after cleaning is also needed. It is suggested that parts are stored either under a nitrogen atmosphere or in vacuum.

The large filter surface can also hold contaminants adsorbed from contaminated liquid and release them into the scintillator as it passes through. Since Teflon is a hydrophobic material it cannot be easily wetted. Cleaning must be done carefully since contaminants on the Teflon will preferentially go into scintillator over water.

5.4.5 Deposition Summary

The deposition of radon progeny is a major concern for Borexino. Radon progeny including ^{210}Pb, ^{210}Bi, ^{210}Po are often the dominant contribution from surface activity in low background experiments due to the prevalence of radon and the long half life of ^{210}Pb. Various methods can be employed to suppress the level of radon progeny in the air. These can take the form of filtration with HEPA units, radon scrubbers such as the vacuum swing adsorption system which supplied air for the Borexino clean room, or adsorption systems where the residency time of radon in the system is longer than its half-life so the radon decays before it passes through. Aged air that is pressurized and stored in cylinders can also be used if the volume required is not too great. Various electrostatic methods for the removal of charged progeny using high voltages are also possibilities.

When possible, parts should be stored in a highly isolated environment where no radon is present. It is best to place parts under vacuum or in a radon free atmosphere. Often, a sealed container slightly over pressured with a pure gas like nitrogen is convenient. If isolation is not practical, parts should be kept covered and electrically grounded to be free of static charge. Storage in metallic bags that are impermeable to radon is also an option. Minimizing surface contamination from radon progeny deposition must be a governing principle in the design and construction of an experiment if low backgrounds are to be achieved.

Scintillator Flow Modeling

Borexino is capable of online scintillator purification while the detector is in operation. The purification efficiency will be determined by how effectively the purification plant removes contaminants and by the mixing of scintillator in the nylon vessel. Since the scintillator cannot be purified unless it is removed from the vessel, the flow patterns within the vessel affect the overall purification efficiency. Flow patterns in the Counting Test Facility (CTF) and Borexino inner vessel were determined with numerical simulations.

The geometry of the CTF vessel and the Borexino vessel are similar. Both are spheres with pipes attached to the north and south poles to add and remove fluid. The main differences are in the diameters of the spherical vessels, the diameters of the pipes that they are connected to, and the geometry around the end regions where the connections are made. A picture of the Borexino inner vessel is shown in Figure 6.1.

Typical online purification involves draining scintillator from the bottom of the detector, purifying the scintillator, and reinserting it at the top of the vessel. This method is called loop purification as the scintillator travels in a closed path through the purification plants. Mixing in the vessel can either assist or hinder the purification. This depends on whether the scintillator being removed from the vessel is mostly unpurified scintillator or mostly scintillator that has already been purified and reinserted into the vessel. The best case scenario is when there is no mixing and only unpurified scintillator is removed for
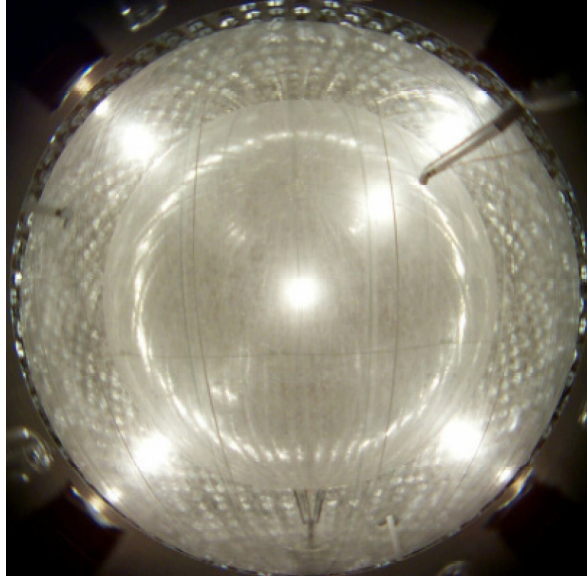
Figure 6.1: The inner and outer nylon vessels after installation in the stainless steel sphere. This picture was taken prior to filling when the vessels were inflated with nitrogen gas. Photomultiplier tubes mounted on the sphere are visible. Connections to the inner nylon vessel are made at the north and south poles.

purification. The worst case scenario also involves no mixing. In this case the same volume scintillator keeps being repurified while the bulk of the unpurifed scintillator remains in the vessel. Clearly diffusion will cause any real system to be somewhere between theses two limits. However, one should note that increasing mixing will reduce the purification efficiency in the first case and improve it in the second.

A preferable method to a loop purification is batch purification where the scintillator from one vessel is purified and placed in a second vessel after purification. In this way all the scintillator is purified exactly once and no mixing of purified and unpurified scintillator take place. During the filling of the Borexino detector scintillator from the storage tanks will be batch purified as it is inserted into the detector. Unless the detector is drained, any purification done after the detector is filled must be done in a loop mode where the efficiency is reduced. Draining the Borexino detector is a major operation that would take several months and is not foreseen under normal operating conditions.

The purification in a batch operation is determined by the efficiency of the purification process that is used. A batch process suffers no reduction of efficiency from mixing. A loop purification is more complicated because the mixing will reduce the purification efficiency. Purifying one volume of scintillator in a loop mode will always be less efficient than a batch purification of the same volume. The loop mode efficiency will approach the batch mode efficiency in the limit where no mixing occurs and only unpurified scintillator is removed from the system.

Perfect mixing means that the scintillator is instantaneously mixed when it is reinserted into the detector and any impurities are uniformly spread throughout the volume. For purification in a perfectly mixed system with impurity concentration $C(t)$ where the purification process removed all contaminants from the fluid the concentration is described by

$$\frac{dC}{dt} = -\frac{Q}{V}C \tag{6.1}$$

where V is the total volume of the fluid in the system and Q is the volume flow rate. The solution to the equation is

$$C(t) = C_0 e^{-\frac{Q}{V}t} \tag{6.2}$$

where C_0 is the initial concentration at $t = 0$. Thus in the case of perfect mixing there would be a 1/e reduction of contaminants each time a volume of scintillator was purified.

6.1 Fluid Dynamics

The flow patterns within the CTF and Borexino detectors are determined by a set differential equations and the systems boundary conditions. The boundary conditions in this case are the walls of the vessels and the input and output flow rates. The flow rates in Borexino are determined by the capacity of the purification plants. Below is an overview of the equations used to describe fluid motion.

Fluid flow is governed by three conservation laws that state

- Fluid mass is conserved.

- The change in momentum is the equal to the sum of the forces on the fluid.

- The change in energy is the sum of the work done and heat added to the fluid.

Take a fluid with density ρ [kg/m^3], pressure p [N/m^2], velocity $\mathbf{v}$ [m/s], dynamic viscosity μ [kg/m/s], body force $\mathbf{f}$ [kg m/s^2], and internal energy e [J]. The kinematic viscosity is defined as $\nu = \mu/\rho$ [m^2/s]. The equations that describe fluids are simply the mathematical expression of these conservation laws. Mass conservation is described by the continuity equation

$$\frac{\partial \rho}{\partial t} + \nabla \cdot (\rho \mathbf{v}) = 0 \tag{6.3}$$

where the partial derivative is with respect to time t [136, 137]. This says the change in density $\frac{\partial \rho}{\partial t}$ from any sources or sinks in the system which are described by the divergence term $\nabla \cdot (\rho \mathbf{v})$. Most liquids can be well approximated as having constant density and the last term can be written as $\rho \nabla \cdot \mathbf{v}$. The momentum conservation equation is

$$\frac{\partial (\rho \mathbf{v})}{\partial t} + \mathbf{v} \cdot \nabla (\rho \mathbf{v}) = -\nabla p + \nabla \cdot \mathbf{T_{ij}} + \mathbf{f} \tag{6.4}$$

where $\mathbf{T_{ij}}$ is the viscous stress tensor. The substantial derivative on left hand side of the equation describes the acceleration of an element of fluid while the right hand side represents all the forces acting on the fluid element. Forces can arise from a pressure difference ∇p, stress $\nabla \cdot \mathbf{T_{ij}}$, or body force $\mathbf{f}$ such as gravity. The viscous stress tensor is defined as

$$\mathbf{T_{ij}} = \mu \left(\frac{\partial v_i}{\partial x_j} + \frac{\partial v_j}{\partial x_i} \right) \tag{6.5}$$

where v_i are the velocity components, and the x_i derivatives are with respect to the spatial components. In the literature the total stress $\sigma_{\mathbf{ij}}$ is sometimes used

$$\sigma_{\mathbf{ij}} = -p\delta_{\mathbf{ij}} + \mathbf{T_{ij}} \tag{6.6}$$

so that the first two terms on the right hand side of the momentum equation can be combined. The energy conservation equation is

$$\rho \frac{\partial e}{\partial t} + \rho \mathbf{v} \cdot \nabla e = K_H \nabla^2 T - p \nabla \mathbf{v} + \nabla (\mathbf{T_{ij} v}) \tag{6.7}$$

where K_H is the thermal conductivity. It states the change in internal energy of the system arises from the flow of energy though temperature gradients and the motion of the fluid.

Often a number of simplifications can be made depending on the particular situation. Liquids are often approximated as incompressible since their bulk modulus K is usually large.

$$K = -V\frac{dp}{dV} = \rho\frac{\partial p}{\partial \rho} \tag{6.8}$$

For a typical liquid the bulk modulus is $K \sim 10^9\,\text{N/m}^2$. An incompressible fluid implies that

$$\frac{\partial \rho}{\partial t} = 0. \tag{6.9}$$

The incompressibility approximation holds when the velocity of the fluid is much less than the speed of sound in a steady state condition.

If the flow is steady then the fluid motion at any point is constant in time.

$$\frac{\partial \mathbf{v}}{\partial t} = 0 \tag{6.10}$$

For irrotational flow where there is no circulation

$$\nabla \times \mathbf{v} = 0. \tag{6.11}$$

For Newtonian fluids the sheer stress is proportional to the strain rate.

$$\sigma_{ij} = \mu\frac{\partial v_i}{\partial x_j} \tag{6.12}$$

Laminar flow is slow moving and steady. Turbulent flow is unsteady and produce eddies of different sizes. These eddies convert the translational energy of the flow into heat. In a pipe there is a transition between laminar and turbulent flow that occurs as velocity or pipe diameter increases. The type of flow is determined by the Reynolds number Re which is a ratio of the inertial force to the viscous force of a fluid.

$$\text{Re} = \frac{\rho v d}{\mu} = \frac{v d}{\nu} \tag{6.13}$$

For flow in a pipe, a Reynolds number less than 2100 means the flow is laminar and for Reynolds number greater than 2100 the flow is in a transitional state that is partly turbulent.

Flow in a pipe with Re>4000 are fully turbulent. The Reynolds numbers that governs turbulents for flow past an object are generally different. In Borexino flow is laminar within the vessel and turbulent in the north and south end pipes for a flow rate of $1\,\mathrm{m^3/h}$.

The Navier-Stokes equations in an inertial reference frame for an incompressible fluid where ρ is constant are

$$\frac{\partial \mathbf{v}}{\partial t} + (\mathbf{v} \cdot \nabla)\mathbf{v} = -\frac{1}{\rho}\nabla p + \nu \nabla^2 \mathbf{v} + \frac{\mathbf{f}}{\rho} \tag{6.14}$$

along with the continuity and energy concervation equations. The kinematic viscosity is defined as $\nu = \mu/\rho$. The Navier-Stokes equations describe most flows of interest but are difficult to solve. For laminar flows the Navier-Stokes equations are sufficient, but for turbulent flows a Reynolds average form of the equations is often used. The Reynolds Averaged Navier Stokes (RANS) equations for incompressible flow are

$$\rho\frac{\partial \mathbf{v}}{\partial t} + (\mathbf{v} \cdot \nabla)\mathbf{v} = -\nabla p + \mu \nabla \mathbf{v} + \rho \nabla \cdot \mathbf{R} + \mathbf{f} \tag{6.15}$$

$$\nabla \cdot \mathbf{v} = 0 \tag{6.16}$$

where $\mathbf{R}$ is the Reynolds stress tensor. For the k-ϵ model of turbulent flow

$$\mathbf{R} = -\frac{2}{3}k\mathbf{I} + \nu_T(\nabla \mathbf{u} + \nabla \mathbf{u}^T) \tag{6.17}$$

$$\nu_T = c_\mu \frac{k^2}{\epsilon} \tag{6.18}$$

where $c_\mu = 0.09$, k is the turbulent kinetic energy, and ϵ is the dissipation of k [138]. The equations for laminar flow are recovered if an effective viscosity $\nu_{\mathrm{eff}} = \nu + \nu_T$ and effective pressure $p_{\mathrm{eff}} = p + \frac{2}{3}k$ are used. The equations for k and ϵ are

$$\frac{\partial k}{\partial t} = \mathbf{v} \cdot \nabla k - \nabla \cdot (D_k \nabla k) + \gamma_k k = F_k \tag{6.19}$$

$$\frac{\partial \epsilon}{\partial t} = \mathbf{v} \cdot \nabla \epsilon - \nabla \cdot (D_\epsilon \nabla \epsilon) + \gamma_\epsilon \epsilon = F_\epsilon \tag{6.20}$$

where the diffusion coefficients are

$$D_k = \frac{\nu_T}{\sigma_k} + \nu \tag{6.21}$$

$$D_\epsilon = \frac{\nu_T}{\sigma_\epsilon} + \nu \tag{6.22}$$

the reaction coefficients are

$$\gamma_k = \frac{\epsilon}{k} \tag{6.23}$$

$$\gamma_\epsilon = c_2 \frac{\epsilon}{k} \tag{6.24}$$

and the source terms are

$$F_k = \frac{\nu_T}{2} |\nabla \mathbf{u} + \nabla \mathbf{u}^T|^2 \tag{6.25}$$

$$F_\epsilon = \frac{c_1 k}{2} |\nabla \mathbf{u} + \nabla \mathbf{u}^T|^2 \tag{6.26}$$

where $c_1 = 0.126$, $c_2 = 1.92$, $\sigma_k = 1.0$ and $\sigma_\epsilon = 1.3$ are empirical constants. For physical solution k and ϵ will be positive numbers. These Reynolds Averaged Navier Stokes equations were used to model the flow patterns in the CTF and Borexino.

6.2 Computational Fluid Dynamics

In most situations there is no analytical solution to the Navier Stokes equations. Instead the flow is solved by an iterative process. Computational Fluid Dynamics (CFD) encompasses the mathematical methods and computational techniques for this procedure. CFD typically works by dividing a system into a number of small domains. The conservation equations are then discretized and applied in each of the regions. After a sufficient number of iterations the parameters of the system converge and a solution is attained.

To begin a CFD computation, the geometry of the system in which the fluid flows must be defined. After the geometry is designed, the volume must then meshed into small cells. These cells can be different shapes and sizes however, they should be small compared to the length over which the parameters of the system vary. Each cell is used as a control volume over which the conservation equations are applied.

The geometry of the detectors were modeled with the Gambit preprocessor. Gambit was also used to form a mesh within the volumes. There is a tradeoff between the number of cells which provides a higher resolution of the flow and the larger computing time needed

for the solution to converge. To attain good resolution in areas of fast flows, the mesh was fine around the inlet and outlet pipes and the mesh increased in size towards the interior of the vessel where the velocities were slower.

Simulations were done using Fluent, a commercially available flow modeling software package based on the finite volume method. The finite volume method uses the integral form of the conservation equations which are applied to the control volumes formed by the mesh. Computational nodes are located at the centroid of each control volume. Once the mesh is generated and operating conditions are defined, a solution to the flow patterns was found by solving the Navier Stokes equation iteratively with a RANS k-ϵ turbulence model. Convergence was required for the velocity, continuity, k, and epsilon. The criteria for convergence was that changes in the residuals for each quantity has to be less than $1/1000$ between successive iterations.

Simulations were run primarily on a $1\,\text{GHz}$ dual processor Xenon server with $1\,\text{Gb}$ of RAM. Computing time was also borrowed from a faster cluster with more processors to speed up time varying simulations.

6.3   Borexino Inner Vessel Model

The mesh of the Borexino detector is shown in Figure 6.2. The tubes leading into the inner vessel at the north and south poles have diameters of $10.16\,\text{cm}$ and the vessel diameter is $8.5\,\text{m}$. The top of the upper pipe was set as a mass flow inlet and the bottom of the lower pipe was defined as a pressure outlet. The nylon vessel is taken to be a perfect sphere except around the north and south poles where rigid nylon structures support the vessels. The vessel in its filled state is designed to be neutrally buoyant. However, there are ropes that hold the vessel in place for the small buoyant forces that arise due to temperature fluctuations. This will slightly deform the vessel along lines of latitude and longitude. The slight deviation in the sphericity of the vessel due to the ropes was neglected in these simulations.

The velocity profile in the detector is shown in Figures 6.3 and 6.4. The flow rate of
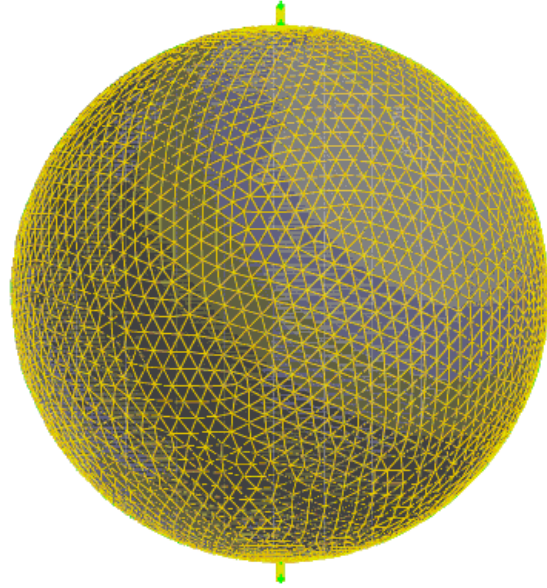
Figure 6.2: A mesh of the volume if the inner vessel of the Borexino detector. Only the surface mesh is shown here for clarity. The diameter of the nylon sphere is 8.5 m with 10.16 cm diameter pipes entering the top and bottom. The mesh contains 100422 tetrahedral cells with 19155 nodes, 9050 wall faces, 58 mass flow inlet faces, 58 pressure outlet faces, and 196261 interior faces.

$1\,\mathrm{m}^3/\mathrm{h}$ of scintillator is limited by the speed of the purification plants. The viscosity of pseudocumene is $\mu = 5.9 \times 10^{-4}\,\mathrm{kg/m/s}$. For a flow rate of $1\,\mathrm{m}^3/\mathrm{h}$ the Reynolds number in the pipes is 5200, so the flow is turbulent. Inside the nylon vessel the Reynolds number is ~100, so the flow is laminar. Flow within the vessel is rotationally symmetric about the vertical y-axis. It is obvious from the velocity profile that there is no circulation in the detector implying $\nabla \times \mathbf{u} = 0$.

Pathlines are the lines traced by fluid particles. For steady flows, pathlines are the same as streamlines which are lines tangent to the velocity field. In Figure 6.5 particles were released from the inlet of the Borexino inner vessel and tracked until they left the vessel.
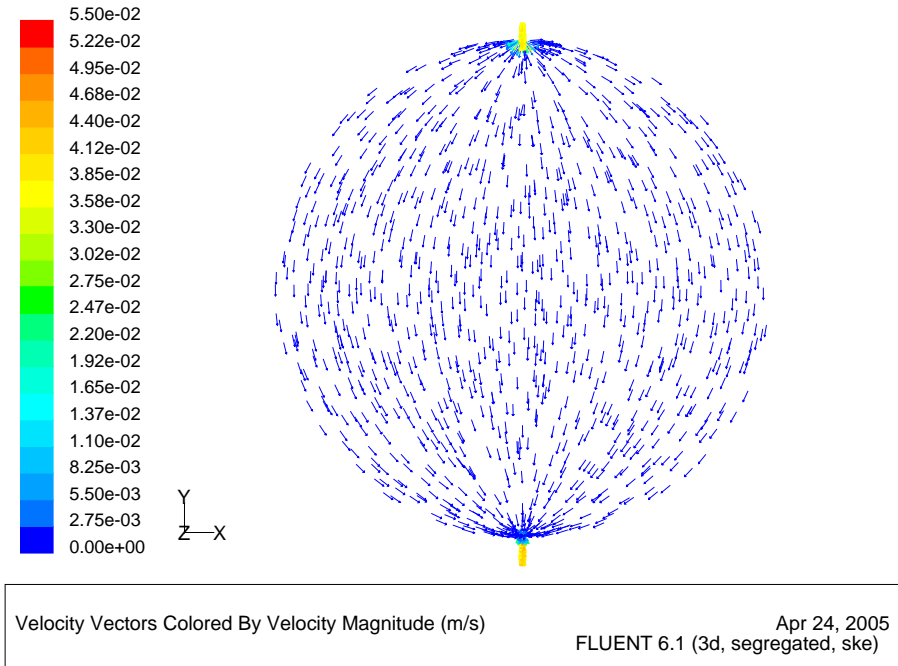
Figure 6.3: The steady state velocity vectors in the Borexino inner vessel for a flow rate of $0.24 \, \text{kg/s}$ or $1 \, \text{m}^3/\text{h}$. This is the maximum purification rate of the skids. Vectors are shown in a vertical cross section of the detector. The flow is completely laminar within the vessel.

It is clear that the velocity is much slower near the edges of the detector. While particles starting from the top going down the center of the detector take about 4.5 days to reach the bottom, a particle that travels along the edge of the detector will take about 23 days. The transit time of particles near the edge of the vessel means it take on the order of weeks to exchange scintillator in this region. For reference the diffusion of an atom during this time is about 15 cm. So despite the relatively long time required to flush the detector, contaminants will only diffuse a short distance during this time.

There is the potential for significant improvement in the purification efficiency if the scintillator in the detector can be separated with a thermal gradient. There is a natural vertical temperature gradient in the underground labs of a few degrees Kelvin though it is
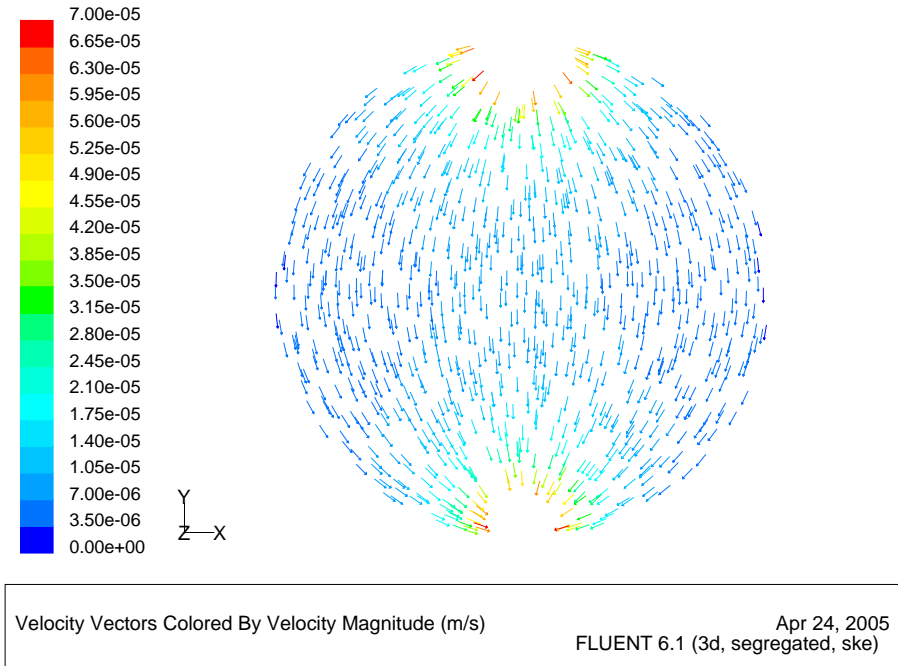
Figure 6.4: The steady state velocity vectors in the Borexino inner vessel for a flow rate of $0.24\,\mathrm{kg/s}$ or $1\,\mathrm{m}^3/\mathrm{h}$. This is the same data as in Figure 6.3 but scaled to show more detail in the interior of the vessel. The maximum velocity in this figure was limited to $0.1\,\mathrm{mm/s}$. This limit excludes the velocity profile near the top and bottom of the vessel where the flow is fast. Flow is visibly faster in the center of the vessel and slower at the edged as expected.

not known if this temperature gradient will exist inside the inner volume which is shielded by the water tank and inner and outer buffer. However, if a temperature gradient exists in the inner vessel, fluid separation might be maintained by heating the pseudocumene before it is inserted in the top of the detector. The thermal expansion coefficient of pseudocumene is $\alpha = 8 \times 10^{-4}\,\mathrm{g/cm}^3/\mathrm{K}$ which gives a change in density of $\sim 0.1\%$ per degree K. Scintillator can be heated during the purification process and inserted in the top of the detector with a slightly elevated temperature. The buoyant force from its smaller density would be enough to make the purified fluid float above the unpurified scintillator.
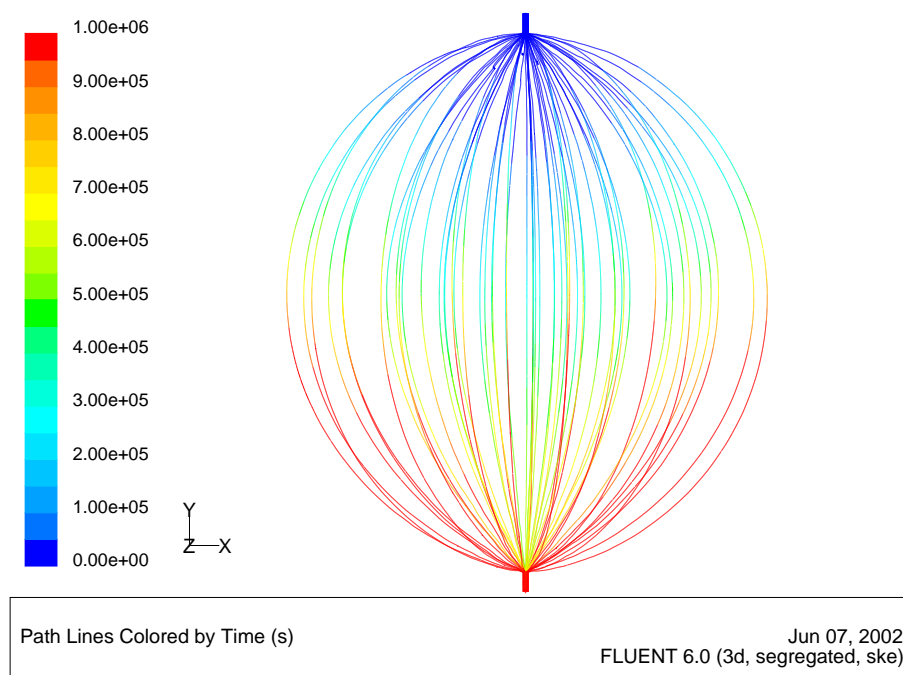
Figure 6.5: Pathlines of particles released at the inlet of the Borexino inner vessel. They are propagated for 10^6 seconds. As expected, the flow slows significantly near the walls. The time is indicated by the color of the particle track. The transit time of a particle that starts at the top of the vessel and proceeds straight down to the drain is 4.5 days.

6.4   Counting Test Facility Model

Simulations were run for the Counting Test Facility (CTF) vessel to determine mixing during purification. The CTF vessel is a sphere 1 m in diameter with a 5.1 cm inlet on top and a 2.5 cm outlet on the bottom. The CTF vessel is surrounded by water so it has a positive buoyancy. Deformation from the ropes holding the vessel in place are not included in this model. As a historical note the experiment was shut down from August 2002 through mid 2005 due to a pseudocumene spill. During this time routing maintenance activity for the CTF could not be performed. As a result the vessel obtained significant deviations from sphericity during this period. The CTF mesh is shown in Figure 6.6.
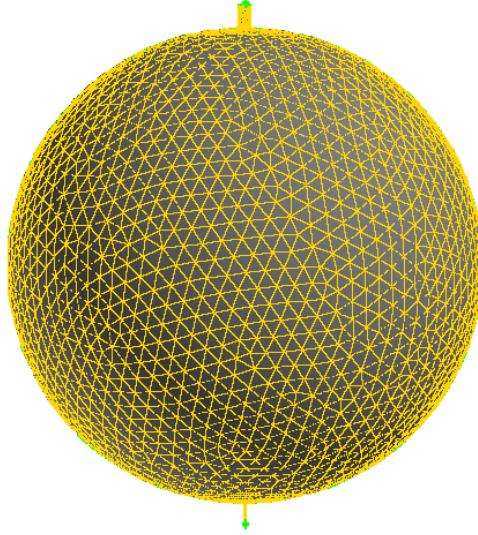
Figure 6.6: A mesh of the volume of the inner vessel of the CTF detector. Only the surface mesh is shown here for clarity. The diameter of the nylon sphere is 1 m. The mesh contains 65626 tetrahedral cells with 12779 nodes, 6742 wall faces, 20 mass flow inlet faces, 120 pressure outlet faces, and 127805 interior faces. The main difference between the CTF and Borexino inner vessel shown in Figure 6.2 aside from their size is the geometry of the pipes and the regions at the north and south pole. Though these small differences are not obvious in this picture they have a significant effect on the flow patterns.

Velocity vectors for a flow rate of 300 L/h are shown in Figure 6.7. The steady state flow in the CTF is rotationally symmetric about the vertical y-axis. A jet from the inlet extends into the vessel creating recirculation loops. These loops form a toroidal pattern with flow going up the sides of the vessel and down through the middle. These loops imply $\nabla \times \mathbf{u} \neq 0$. The axis of rotation is a horizontal circle with a 33 cm radius that is 10 cm below the equator. The strength of the jet is enhanced by the geometry of the inlet which is a sharp right angle where the pipe transitions to the vessel. If the opening was tapered outwards as in the case of the Borexino inner vessel transition the formation of the jet can be suppressed.

Pathlines of particles released at the inlet of the CTF detector are shown in Figure 6.8. When operated at a flow rate of 300 L/h, 80% of the scintillator inserted flows directly

Velocity Vectors Colored By Velocity Magnitude (m/s)   Apr 25, 2005
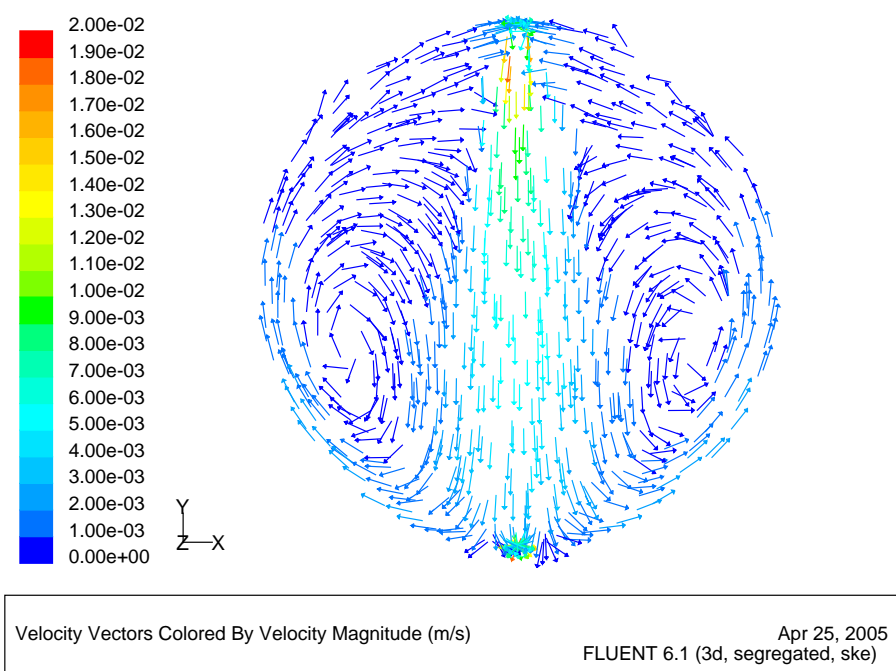FLUENT 6.1 (3d, segregated, ske)

Figure 6.7: Velocity vectors in a vertical cross section of the CTF for a constant flow rate of 300 L/h which is the typical purification rate of the CTF skids. A jet is visible from the inlet on top that extends to the drain on the bottom. Notable are the toroidal recirculation loops that form within the vessel. The fluid in these loops does not mix well with the incoming flow. The poor mixing of these loops has an adverse effect on the overall purification in loop mode.

across the vessel into the drain at the bottom without mixing. In other words, only 20% of the scintillator in the CTF is removed for every volume change. A particle that enters the top of the vessel and goes straight to the drain takes about 10 minutes to traverse the detector.

CTF pathlines of particles starting in the $z = 0$ plane are shown in Figure 6.9. The particles were tracked for 1500 s. The color of the particle track indicate the passage of time. In steady state recirculation loops are fairly stable and do not mix much. The symmetry of the detector is the main cause of the stability. Simulations showed that adding asymmetry
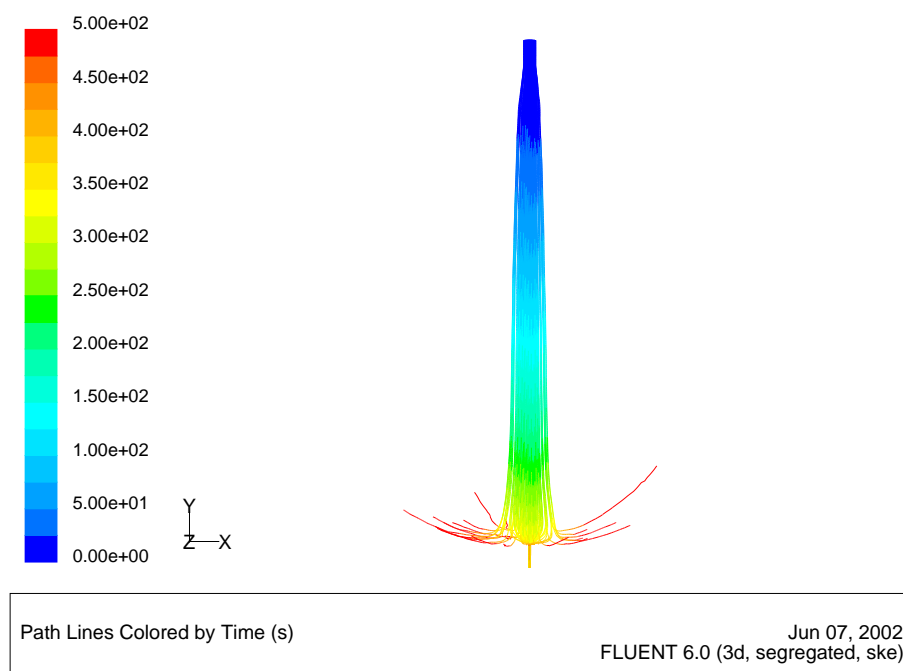
Figure 6.8: Pathlines of particles released from the inlet with a steady state flow at a rate of 300 L/h. They are propagated for 500 s. Of the 132 particles that were released, 105 went into the drain. The efficiency due to poor mixing in the CTF is $\sim 20\%$ when running in a steady state loop mode.

to the geometry aided the mixing greatly.

Contours of constant velocity in the CTF are shown in Figure 6.10. The looping circulation pattern exists but is not visible. The flow in the inlet of the CTF has a Reynolds number of about 3100, indicating turbulence in the pipe. The outlet which has a smaller diameter and a Reynolds number of 6250 will also have turbulent flow. Within the vessel the Reynolds number is ~ 160 so the flow is laminar.

Simulations were done to test the CTF flow patterns at a reduced flow rate. By lowering the flow rate the recirculation loops can be eliminated which improves the mixing efficiency greatly. The velocity profile for the CTF at a flow rate of 215 L/h is shown in Figure 6.11.
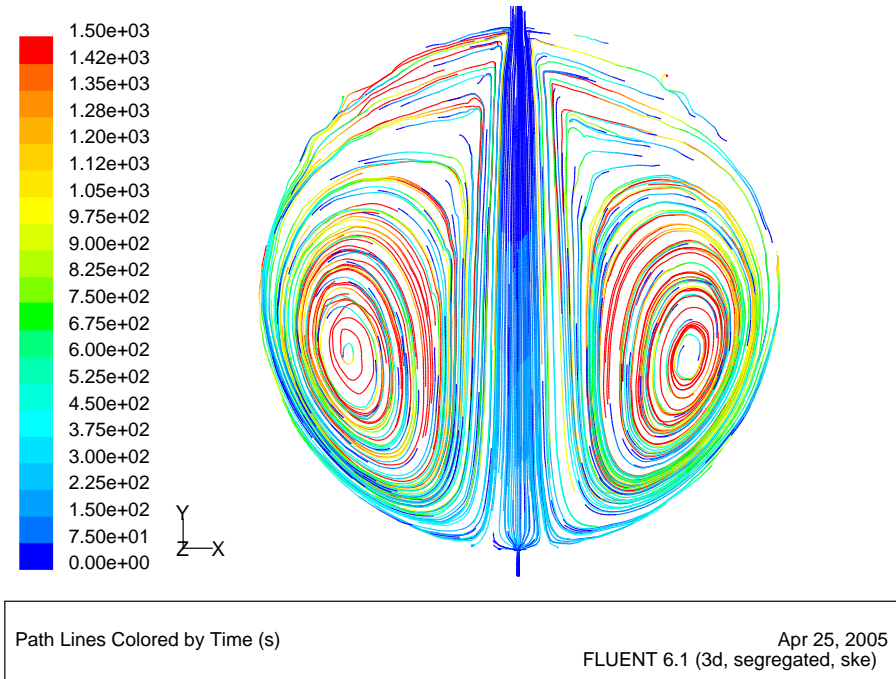
Figure 6.9: Pathlines of particles released in a vertical plane of the CTF. Of the 320 particles released 60 went into the drain, however this is not representative of the CTF mixing efficiency since it is only a vertical cross section where particles were released and not the whole volume. These pathlines show the fluid loops are relatively stable and do not mix well with the flow through the center of the detector.

While it is generally desirable to purifiy at as high a rate possible the flow patterns show that the over all purification can be improved by reducing the rate. This allows for a greater protion of the unpurified scintillator to be removed from the vessel for every volume exchange. When recirculation loops are present most of the effort is spent repeatedly purifying the same scintillator.

2.50e-02	
2.25e-02	
2.00e-02	
1.75e-02	
1.50e-02	
1.25e-02	
1.00e-02	
7.50e-03	
5.00e-03	
2.50e-03	
0.00e+00	

Contours of Velocity Magnitude (m/s)

Jun 07, 2002
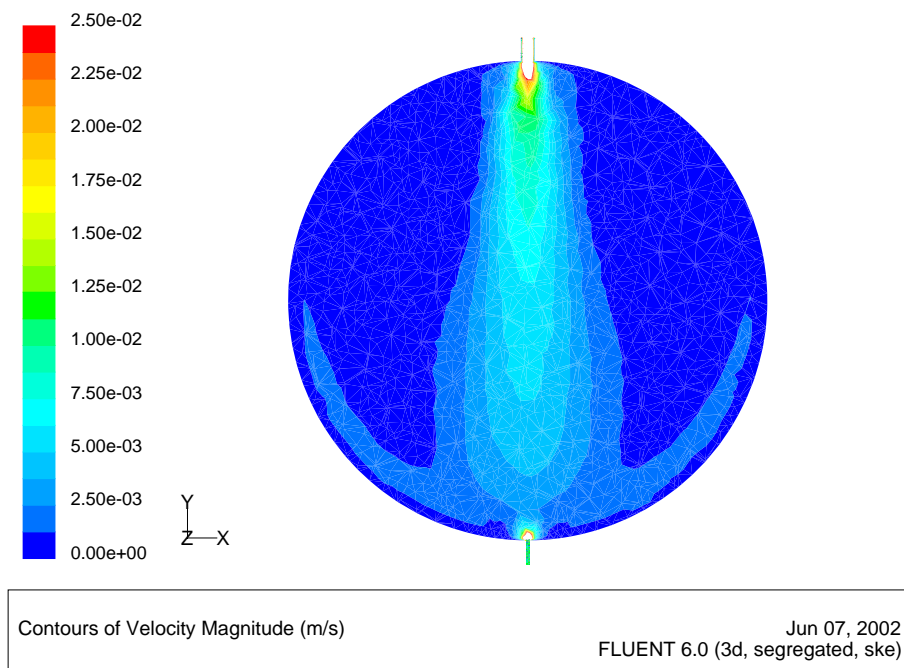FLUENT 6.0 (3d, segregated, ske)

Figure 6.10: Contours of constant velocity in a cross section of the CTF. Fast moving fluid from the inlet penetrates the length of the vessel. This fast inlet stream is driving flow up the bottom edges of the vessel. The looping recirculation pattern still exists but is not as apparent because only the magnitude of the velocity is shown. These contours are for a flow rate of $300\,\mathrm{L/h}$.

Velocity Vectors Colored By Velocity Magnitude (m/s)   Jun 25, 2002
                                                    FLUENT 6.0 (3d, segregated, ske)
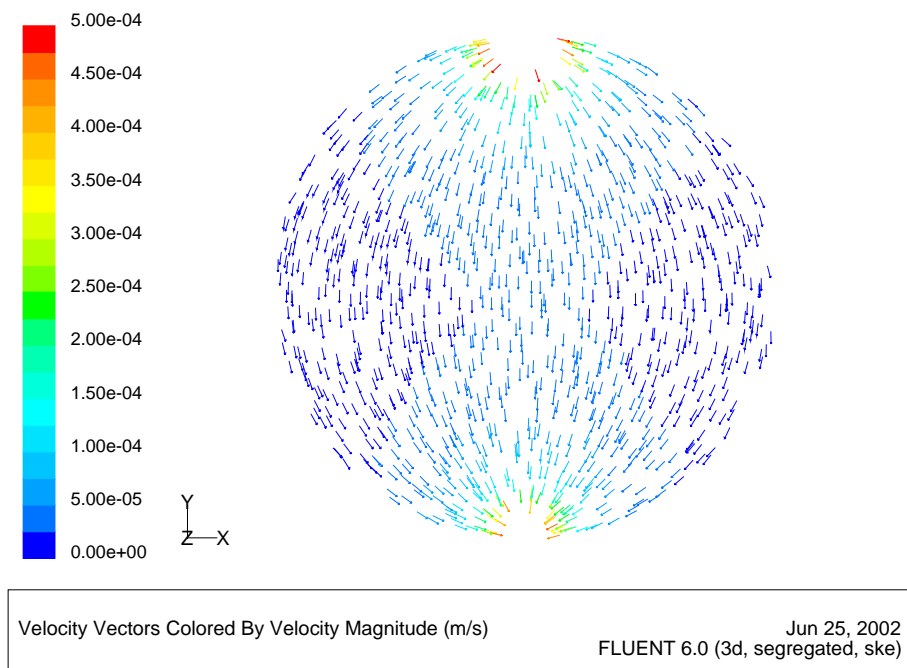
Figure 6.11: Velovity vectors in the CTF. This are for a flow rate of 215 L/h. The flow around the inlet and drain is off scale in order to show detail about the interior flow. At this reduced flow rate no recirculation loops are present. Purification with this flow pattern will be greatly improved.

6.4.1 Time Varying Flow

One method of increasing mixing in the detector is to start and stop the flow. Simulations were done starting flow from a fully static condition. This was done by iterating in $0.25\,\mathrm{s}$ time steps. The solution approached convergence at each time step but the number of iterations was limited. In this manner a reasonabe convergance was achieved at each time step though the convergence criteria were not strictly met. Modeling unsteady flows was more computationally intensive than the steady state models. Simulations show that from a full stop the flow pattern in the CTF takes about a half hour to form.

A simulation of stopping flow from a CTF steady state condition was also run. They showed that fluid became mostly static in about 15 minutes. However, the flow pattern was broken very quickly once the flow was stopped. The momentum from the jet set the fluid in the detector rotating about a single straight axis. This provided good mixing in the detector well before the motion was damped out due to viscous forces.

As a result of these simulations the CTF was run in a start-stop mode during a water extraction tests which lasted about two weeks. The loop purification was run for 2-5 hours before it was stopped. After stopping fluid operations, a period of at least an hour passed before purification resumed. A detailed schedule of the operations can be found in Reference [113]. The start-stop times were longer than the simulation showed was necessary to eliminate the recirculation pattern due to the difficulty of starting and stopping the purification plants.

Just over five detector volumes of scintillator were purified during this period. The last $5323\,\mathrm{kg}$ of scintillator was mixed with an an acidic solution with 0.2% HNO_3 for the water extraction process. The total start-stop water extraction operation resulted in a 38% reduction of the total number of internal events. Alpha decays were originally 86% of the total internal events. The total alpha reduction was $\sim 36 \pm 10\%$ while the beta reduction was $\sim 55 \pm 25\%$ where the errors are statistical only.

6.4.2 Geometric Considerations

Several simulations were done to understand how the geometry around the pipe-vessel transition would modify the flow patterns. This was done for the input pipe on the top of the vessel only. As currently built the CTF has a sharp transition at this junction where the input pipe opens at a 90° angle. The flow patterns were shown to be sensitive to this geometry. Various tapered openings that flared outward at the end of the pipe permitted a higher flow rate before recirculation loops appeared. Changing the angle of the input flow also helped break up the recirculation loops.

Potential modifications involve making a baffle to redirect the inflow or smoothing the transition so that the opening flared outwards. Both were shown to increase the velocity where recirculation loops began to form. However, it was concluded that structural modifications to the CTF would be too difficult to make.

The Borexino detector currently has a wide angle taper where the scintillator enters the vessel. This prevents the formation closed circulation loops withing the detector.

6.5 Flow Conclusions

Purification of the scintillator in the CTF was severely hindered due to poor mixing when running at $300\,\text{L/h}$. This was the result of closed circulation loops which were essentially stagnant and were not removed from the vessel under steady state operating conditions. Mixing is improved by reducing the flow rate or repeatedly starting and stopping the flow. Simulations have showed that mixing in the CTF would be improved by having a gradual transition where the inlet pipe opened smoothly to the vessel. Adding asymmetry to the detector will also disrupt the flow loops and aid mixing in the vessel. A summary of techniques to improve mixing is given in Table 6.1.

The flow patterns in the Borexino detector are favorable for efficient purification. Flow in the Borexino detector in at a constant $1\,\text{m}^3/\text{h}$ does not loop and the entire volume of scintillator is accessible. According to the flow patterns, the time required to remove the full volume of scintillator for purification is on the order of a month. Ideally the scintillator

Parameter	Modification
Inlet pipe diameter	Increased
Inlet pipe transition	Tapered opening
Flow rate	Decreased
Geometry	Asymmetric

Table 6.1: Detector properties that will improve mixing by suppressing recirculation loop formation. These should be taken into account when designing a system that will be purified in a continuous loop mode. Ideally there should be no looping flow circulation in the volume as these regions are not easily removed from the system for purification.

solution will be purified sufficiently during filling so that no further purification is needed once the detector is full.

Bibliography

[1] W. Pauli, "Letter to physical society of tubingen" (December 1930).

[2] C. Cowan, F. Reines, et al., "Detection of the free neutrino: A confirmation", *Science* **124** (1956) 3212.

[3] B. Cleveland, et al., "Measurement of the solar electron neutrino flux with the homestake chlorine detector", *The Astrophysical Journal* **496** (1) (1998) 505.

[4] The Super-Kamiokande Collaboration, Y. Fukuda, et al., "Evidence for oscillation of atmospheric neutrinos", *Phys. Rev. Lett.* **87** (1998) 1562.

[5] The SNO Collaboration, Q. Ahmad, et al., "Measurement of the rate of $\nu_e + d \rightarrow p + p + e^-$ interactions produced by ^{8}B solar neutrinos at the Sudbury Neutrino Observatory", *Phys. Rev. Lett.* **87** (2001) 071301.

[6] The KamLAND Collaboration, K. Eguchi, et al., "Evidence for reactor anti-electron neutrino disappearance", *Phys. Rev. Lett.* **90** (2003) 021802.

[7] V. Kopeikin, "Components of antineutrino emission in nuclear reactor", *Physics of Atomic Nuclei* **67** (11) (2004) 1963.

[8] R. Lopez, et al., "Precision detection of the cosmic neutrino background", *Phys. Rev. Lett.* **82** (20) (1999) 3952.

[9] G. Fiorentini, et al., "Kamland, terrestrial heat sources and neutrino oscillations", *Phys. Rev. B* **558** (2003) 15.

[10] A. Zalewska, "Topical questions in the experimental neutrino physics", *Acta Physica Polonica B* **34** (11) (2003) 5249.

[11] S. Dodelson, *Modern Cosmology*, Academic Press, 2003.

[12] O. Elgaroy, O. Lahav, "Neutrino masses from cosmological probes", *New Journal of Physics* **7** (2005) 61.

[13] R. Fardon, et al., "Dark energy from mass varying neutrinos", *J. Cosmol. Astropart. Phys.* **10** (2004) 005.

[14] S. Eidelman, et al., "Review of Particle Physics", *Phys. Lett. B* **592** (2004) 1.

[15] C. Weinheimer, B. Degenddag, et al., "High precision measurement of the tritium β spectrum near its endpoint and upper limit on the neutrino mass", *Phys. Rev. B* **460** (1999) 219.

[16] K. Assamagan, C. Brönnimann, M. Daum, et al., "Upper limit of the muon-neutrino mass and charged pion mass from momentum analysis of a surface muon beam", *Phys. Rev. D* **53** (1996) 6065.

[17] The ALEPH Collaboration, R. Barate, et al., "An upper limit on the tau neutrino mass from three- and five-prong tau decays", *Eur. Phys. J. C* **2** (1998) 395–406.

[18] R. Allen, et al., "Study of electron-neutrino electron elastic scattering at LAMPF", *Phys. Rev. D* **47** (1993) 11–28.

[19] D. Krakauer, R. Talaga, et al., "Limits on the neutrino magnetic moment from a measurement of neutrino-electron elastic scattering", *Phys. Rev. B* **252** (1990) 177.

[20] C. Bennett, M. Halpern, G. Hinshaw, et al., "First year Wilkinson Microwave Anisotropy Probe (WMAP) observations: Preliminary maps and basic results", *The Astrophysical Journal* **148** (2003) 1–27.

[21] Particle Data Group, C. Caso, et al., "Review of particle physics", *Eur. Phys. J. C* **3**.

[22] J. Peltoniemi, "Appendix to quantum field theory" (2001).

[23] S. Mikheev, A. Smirnov, "Resonance enhancement of oscillations in matter and solar neutrino spectroscopy", *Sov. J. Nucl. Phys.* **42** (1985) 913–917.

[24] L. Wolfenstein, "Resonance enhancement of oscillations in matter and solar neutrino spectroscopy", *Phys. Rev. D* **17** (9) (1978) 2369.

[25] P. de Holanda, W. Liao, A. Smirnov, "Toward precision measurements in solar neutrinos", *Nucl. Phys. B* **702** (1-2) (2004) 307.

[26] J. Bahcall, C. Peña-Garay, "Solar models and solar neutrino oscillations", *New Journal of Physics* **6** (2004) 63.

[27] M. Tanimoto, "Search for CP violation with a neutrino factory", *Phys. Rev. B* **462** (1999) 115.

[28] J. Bahcall, "Neutrinos from the sun", *Scientific American* **221** (1) (1969) 28–37.

[29] J. Bahcall, M. Kamionkowski, A. Sirlin, "What do we (not) know theoretically about solar neutrino fluxes?", *Phys. Rev. Lett.* **92** (12) (2004) 121301.

[30] J. Bahcall, A. Serenelli, S. Basu, "New solar opacities, abundances, helioseismology, and neutrino fluxes", *The Astrophysical Journal* **621** (1) (2005) L85.

[31] J. Bahcall, A. Ulmer, "Temperature dependence of solar neutrino fluxes", *Phys. Rev. D* **53** (8) (1996) 4202.

[32] E. Bugaev, et al., "Atmospheric muon flux at sea level, underground, and underwater", *Phys. Rev. D* **58** (1988) 054001.

[33] The SAGE Collaboration, V. Gavrin, et al., "Measurement of the solar neutrino capture rate in SAGE and the value of the *pp* neutrino flux at the earth", *Nucl. Phys. B* **138** (2005) 87.

[34] The SNO Collaboration, B. Aharmim, et al., "Electron energy spectra, fluxes, and day-night asymmetries of ^{8}B solar neutrinos from the 391-day salt phase SNO data set", *Phys. Rev. C* **72** (2005) 055502.

[35] T. Gaisser, "Talk: Comments on atmospheric muon and neutrino backgrounds in neutrino telescopes" (July 2003).

[36] V. Agrawal, et al., "Atmospheric neutrino flux above 1 Gev", *Phys. Rev. D* **53** (3) (1996) 1314.

[37] The Super-Kamiokande Collaboration, S. Fukuda, et al., "^{8}B and *hep* neutrino measurements from 1258 days of Super-Kamiokande data", *Phys. Rev. Lett.* **86** (2001) 5651–5655.

[38] L. Mikaelyan, "Investigation of neutrino properties in experiments at nuclear reactors: Present status and prospects", *Physics of Atomic Nuclei* **65** (2002) 1173–1187.

[39] The KamLAND Collaboration, T. Araki, et al., "Measurement of neutrino oscillation with KamLAND: Evidence of spectral distortion", *Phys. Rev. Lett.* **94** (8) (2005) 0031–9007.

[40] M. Apollonio, et al., "Limits on neutrino oscillations from the CHOOZ experiment", *Phys. Rev. B* **466** (1999) 415–430.

[41] F. Boehm, et al., "Final results from the Palo Verde neutrino oscillation experiment", *Phys. Rev. D* **64** (2001) 112001.

[42] A. Morales, "Review on double beta decay experiments and comparison with theory", *Nucl. Phys. B* **77** (1999) 335.

[43] APS Members, "The neutrino matrix" (2004).

[44] E. Adelberger, et al., "Solar fusion cross sections", *Reviews of Modern Physics* **70** (4) (1998) 1265.

[45] J. Bahcall, "Be-7 solar-neutrino line - a reflection of the central temperature distribution of the sun", *Phys. Rev. D* **49** (8) (1994) 3923.

[46] D. Williams, "Earth fact sheet", NASA Goddard Space Flight Center.

[47] J. Benziger, F. Calaprice, et al., "A proposal for participation in the Borexino solar neutrino experiment", Princeton University (1996).

[48] J. Bahcall, "The luminosity constraint on solar neutrino fluxes", *Phys. Rev. C* **65** (2002) 025801.

[49] J. Bahcall, "Solar models and solar neutrinos: Current status", hep-ph/0412068 (December 2004).

[50] C. Galbiati, et al., "Cosmogenic ^{11}C production and sensitivity of organic scintillator detectors to *pep* and CNO neutrinos", *Phys. Rev. C* **71** (2002) 055805.

[51] M. Balata, et al., "CNO and *pep* neutrino spectroscopy in Borexino: measurement of the cosmogenic ^{11}C background with the Counting Test Facility", Version 3.0 (2006).

[52] P. Antonioli, et al., "SNEWS: The SuperNova Early Warning System", *New Journal of Physics* **6** (2004) 114.

[53] L. Cadonati, et al., "Supernova neutrino detection in Borexino", *Astropart. Phys.* **16** (4) (2002) 361.

[54] G. Fiorentini, M. Lissia, et al., "Geo-neutrinos: a new probe of Earths interior", http://arxiv.org/abs/physics/0508019 (2004).

[55] R. Raghavan, "Measuring the global radioactivity in the earth by multidetector antineutrino spectroscopy", *Phys. Rev. Lett.* **80** (3) (1998) 635.

[56] V. Barger, et al., "Solar mass-varying neutrino oscillations", *Phys. Rev. Lett.* **95** (2005) 211802.

[57] F. Sergiampietri, "Geometric data on LBL neutrino beams towards the ICANOE detector at the LNGS" (September 1999).

[58] J. Bahcall, M. Kamionkowski, A. Sirlin, et al., "Solar neutrinos: Radiative corrections in neutrino-electron scattering experiments", *Phys. Rev. D* **51** (11) (1995) 6146–6158.

[59] E. Wilhelmi, *Separacion Gamma/Hadron con el telescopio MAGIC*, Ph.D. thesis, Universidad Complutense de Madrid (2001).

[60] R. Schwarzenbach, P. Gschwend, D. Imboden, *Environmental Organic Chemistry*, John Wiley & Sons Inc., 2003.

[61] M. Johnson, *Scintillator Purification and Study of Light Propagation in a Large Liquid Scintillation Detector*, Ph.D. thesis, Princeton University (1998).

[62] J. Birks, *Organic Molecular Photophysics: Volume 2*, John Wiley & Sons Ltd, 1975.

[63] L. Cadonati, *The Borexino Solar Neutrino Experiment and its Scintillator Containment Vessel*, Ph.D. thesis, Princeton University (2001).

[64] P. Helfrey, *Isobaric Heat Capacities at Bubble Point of Pseudocumene and n-HEPTANE*, , California Institution of Technology (1957).

[65] P. Linstrom, W. Mallard, "NIST Chemistry WebBook", Standard Reference Database 69 (June 2005).

[66] J. Birks, *Photophysics of Aromatic Molecules*, John Wiley & Sons Ltd, 1970.

[67] J. Birks, *The Theory and Practice of Scintillation Counting*, Pergamon Press, 1964.

[68] J. Birks, A. Cameron, "Energy transfer in organic solutions I: Photofluorescence of terphenyl-toluene solutions", *Proc. Phys. Soc.* **72** (1958) 53–64.

[69] J. Birks, J. Nafisi-Movaghar, et al., "Energy transfer in organic solutions IV: Diffusion, solvent excitation migration and quenching in p-xylene solutions", *Proc. Phys. Soc.* **91** (1967) 449–458.

[70] J. Birks, et al., "Energy transfer in organic systems V: Lifetime studies of anthracene-perylene transfer in benzene solutions", *J. Phys. B: Atom. Molec. Phys.* **1** (1968) 266–273.

[71] J. Birks, "Energy transfer in organic systems VI: Fluorescence response fimctions and scintillation pulse shapes", *J. Phys. B: Atom. Molec. Phys.* **1** (1968) 946–957.

[72] J. Birks, et al., "Energy transfer in organic systems IX: Effect of diffusion on transfer efficiency", *J. Phys. B: Atom. Molec. Phys.* **3** (1970) 513–525.

[73] J. Birks, H. Najjar, M. Lumb, "Energy transfer in organic solutions XI: Temperature dependence of singlet excitation transfer and quenching in toluene solutions", *J. Phys. B: Atom. Molec. Phys.* **4** (1971) 1516–1522.

[74] J. Maneira, *Calibration and Monitoring for the Borexino Solar Neutrino Experiment*, Ph.D. thesis, University of Lisboa (2001).

[75] J. Birks, J. Conte, G. Walker, "The fluorescence excitation spectra of aromatic liquids and solutions", *J. Phys. B: Atom. Molec. Phys.* **1** (1968) 934.

[76] R. Mathad, N. Umakantha, "Effects of dilution, temperature and viscosity on intermolecular energy transfer in scintillators", *J. Phys. D: Appl. Phys.* **19** (1986) 1381–1387.

[77] T. King, R. Voltz, "The time dependence of scintillation intensity in aromatic materials", *Proceedings of the Royal Society of London* **289** (1966) 424–439.

[78] M. Neff, "Internal note on the laboratory measurements of quenching factors", Munich University of Technology (1996).

[79] G. Ranucci, A. Goretti, P. Lombardi, "Pulse-shape discrimination of liquid scintillators", *Nucl. Instr. Meth. A* **412** (2-3) (1998) 374.

[80] M. Chen, "Quenching of undesired fluorescence in a liquid scintillator particle detector", *Nucl. Instr. Meth. A* **420** (1-2) (1999) 189.

[81] J. Prochaska, *The Design and Fabrication of Optimal Light Collectors for the CTF Upgrade*, Senior Thesis, Princeton University (1993).

[82] The Borexino Collaboration, G. Alimonti, et al., "Science and technology of Borexino: a real-time detector for low energy solar neutrinos", *Astropart. Phys.* **16** (2002) 205.

[83] A. Ianni, P. Lombardi, G. Ranucci, O. Smirnov, "The measurements of 2200 ETL9351 type photomultipliers for the Borexino experiment with the photomultipliers testing facility at LNGS", PMT characteristics (2004).

[84] F. Gatti, et al., "DAQ electronics for Borexino experiment", *Nucl. Phys. B* **78** (1999) 111.

[85] Electronics Group, "Handbook for Borexino electronics", Version 1.0 (2000).

[86] F. Gatti, et al., "The Borexino read out electronics and trigger system", *Nucl. Instr. Meth. A* **461** (1-3) (2001) 474.

[87] K. McCarty, *The Borexino Nylon Film and the Third Counting Test Facility*, Ph.D. thesis, Princeton University (2005).

[88] D. Manuzio, M. Pallavicini, "Results from air run VIII", Borexino scintillator calibration source (2003).

[89] Thomas Jefferson National Accelerator Facility - Office of Science Education, "It's elemental", http://education.jlab.org/itselemental/index.html (2005).

[90] National Council on Radiation Protection and Measurements (NCRP), "Ionizing radiation exposure of the population of the United States", Washington DC, NCRP Report No. 93 (1987).

[91] H. Simgen, G. Heusser, G. Zuzel, "Highly sensitive measurements of radioactive noble gas nuclides in the Borexino solar neutrino experiment", *Applied Radiation and Isotopes* **61** (2003) 2–3.

[92] The Borexino Collaboration, M. Balata, et al., "The water purification facility for the low background Counting Test Facility of the Borexino experiment at Gran Sasso", *Nucl. Instr. Meth. A* **370** (1996) 605.

[93] The Borexino Collaboration, "Borexino: A real time liquid scintillator detector for low energy solar neutrino study", National Science Foundation Proposal (December 1992).

[94] J. Hubbell, "Photon mass attenuation and energy-absorption coefficients from $1\,keV$ to $20\,MeV$", *Applied Radiation and Isotopes* **33** (11) (1982) 1269.

[95] G. Knoll, *Radiation Detection And Measurement*, John Wiley & Sons Inc., 1989.

[96] J. Motz, H. Olsen, H. Koch, "Pair production by photons", *Reviews of Modern Physics* **41** (4) (1969) 581.

[97] W. Jones, "The slow neutron cross section of H", *Phys. Rev.* **74** (4) (1948) 364–369.

[98] C. Galbiati, *Data taking and analysis of the Counting Test Facility of Borexino*, Ph.D. thesis, Universita a degli Studi di Milano (1998).

[99] J. Benziger, et al., "The nylon scintillator containment vessels for the Borexino solar neutrino experiment", Internal Princeton University Borexino memo (2005).

[100] M. Saito, et al., "Determination of radon solubilities to 1,2-Dimethylbenzene, 1,3-Dimethylbenzene, 1,4-Dimethylbenzene, 1,3,5-Trimethylbenzene, 1,2,4-Trimethylbenzene and 1-Isopropyl-4-methylbenzene", *Nihon Kagakkai Shi* **6** (1999) 363.

[101] M. Wojcik, G. Zuzel, "Radon permeability through nylon at various humidities used in the Borexino experiment", *Nucl. Instr. Meth. A* **524** (1-3) (2004) 355.

[102] M. Wojcik, "Radon diffusion through polymer membranes used in the solar neutrino experiment Borexino", *Nucl. Instr. Meth. A* **449** (1-2) (2000) 158.

[103] J. Jarnberg, et al., "Toxicokinetics of inhaled trimethylbenzenes in man", *Toxicology and Applied Pharmacology* **140** (2) (1996) 281.

[104] E. Janik-Spiechowicz, et al., "Genotoxicity evaluation of trimethylbenzenes", *Mutation research - Genetic Toxicology and Environmental Mutagenesis* **412** (3) (1998) 299.

[105] J. Benziger, "A scintillator purification system for a large scale solar neutrino experiment", *Nucl. Instr. Meth. A* **417** (1988) 278–296.

[106] D. Basmadjian, *Mass Transfer, Principles and Applications*, CRC Press, 2004.

[107] A. Adamson, A. Gast, *Physical Chemistry of Surfaces*, John Wiley & Sons Inc., 1997.

[108] M. Deutch, "Borexino note concerning radon diffusion", Internal MIT Borexino memo (1992).

[109] R. Rouseau, *Handbook of Separation Process Technology*, John Wiley & Sons Inc., 1987.

[110] R. Perry, *Perry's Chemical Engineers' Handbook*, McGraw Hill, 1997.

[111] G. Zuzel, G. Heusser, H. Simgen, "^{39}Ar and ^{85}Kr in gaseous nitrogen for the solar neutrino experiment Borexino", *Applied Radiation and Isotopes* **61** (2004) 197–201.

[112] L. Neidermeier, et al., "Scintillator purification by silica gel - chromatography in the context of low counting rate experiments", 8th ICATPP Conference, Como (2003).

[113] L. Niedermeier, *High Efficiency Purification of the Liquid Scintillators for the Solar Neutrino Experiment Borexino*, Ph.D. thesis, Munich University of Technology (2001).

[114] W. Rau, G. Heusser, "^{222}Rn emanation measurements at extremely low activities", *Applied Radiation and Isotopes* **53** (2000) 371–375.

[115] The Borexino Collaboration, C. Arpesella, et al., "Measurements of extremely low radioactivity levels in Borexino", *Astropart. Phys.* **18** (2002) 1.

[116] M. Berger, et al., "Stopping-power and range tables for electrons, protons, and helium ions", National Institute of Standards and Technology (2005).

[117] J. Toth, *Adsorption Isotherms*, Encyclopedia of Surface and Colloid Science, Marcel Drekker, Inc., 2002.

[118] J. Hubbell, S. Seltzer, "NIST X-ray attenuation databases", National Institute of Standards and Technology (2005).

[119] M. Leung, "Surface contamination from radon progeny", in: Topical workshop on low radioactivity techniques: LRT 2004, Vol. 785, *AIP Conference Proceedings*, 2004, p. 184.

[120] A. Pocar, "Low background techniques for the Borexino nylon vessels", in: Topical workshop on low radioactivity techniques: LRT 2004, Vol. 785, *AIP Conference Proceedings*, 2004, p. 248.

[121] A. Pocar, "^{210}Pb and ^{210}Po wash-off from nylon, stainless steel, and teflon surfaces in water", Internal Princeton University Borexino memo (2004).

[122] E. Harding, "Radon daughter wash-off from stainless steel", Internal Princeton University Borexino memo (2002).

[123] W. Nazaroff, A. Nero, *Radon And Its Decay Products In Indoor Air*, John Wiley & Sons Inc., 1998.

[124] G. Schiller, *A theoretical convective-transport model of indoor radon decay products*, Ph.D. thesis, University of California Berkeley (1984).

[125] W. Jacobi, "Activity and potential alpha energy of ^{222}Rn and ^{220}Rn daughters in different air atmospheres", *Health Physics* **22** (1972) 441–450.

[126] D. Tolliver, *Handbook of Contamination Control in Microelectronics - Principles, Applications and Technology*, William Andrew Publishing, 1988.

[127] A. Lai, "Particle deposition indoors: A review", *Indoor Air* **12** (4) (2002) 211.

[128] G. Einberg, S. Holmberg, "Particle filtration in a ventilated room", *Indoor Air* **21** (2002) 1070.

[129] E. Wellisch, "Experiments of the active deposit of radium", *Philosophical Magazine* **28** (1914) 417.

[130] R. Gunn, "Diffusion charging of atmospheric droplets by ions, and the resulting combination coefficients", *Journal of Meteorology* **11** (5) (1954) 339.

[131] O. Raabe, "Concerning interactions that occur between radon decay products and aerosols", *Health Physics* **17** (2) (1969) 177.

[132] A. Busigin, et al., "The nature of unattached RaA (Po-218) particles", Health physics **40** (3) (1981) 333.

[133] S. Goldstein, et al., "Environmental neutralization of polonium-218", Environmental science technology **19** (2) (1985) 146.

[134] T. Shutt, "Radon plateout program", Internal Princeton University Borexino memo (2000).

[135] A. Pocar, *Low Background Techniques and Experimental Challenges for Borexino and its Nylon Vessels*, Ph.D. thesis, Princeton University (2003).

[136] G. Emanuel, *Analytical Fluid Dynamics*, CRC Press, Inc., 1994.

[137] H. Lomax, T. Pulliam, D. Zingg, *Fundamentals of Computational Fluid Dynamics*, Springer, 2004.

[138] A. Lew, et al., "A note on the numerical treatment of the k-epsilon turbulence model", *International Journal of Computational Fluid Dynamics* **14** (3) (2001) 201.